# The chemistry of AGB and post-AGB stars

**by**

*Paul M. Woods*


**A thesis submitted to the University of Manchester Institute of Science and Technology for the degree of Doctor of Philosophy.**

Department of Physics
UMIST
PO Box 88
Manchester M60 1QD
United Kingdom.

**June 2004**

# Abstract

I have studied the chemistry of (mainly carbon-rich) AGB and post-AGB stars using millimetre-wave observations and chemical models. I present a comprehensive overview of past and present research into this area, followed by four different case studies: Firstly, I investigate a number of carbon stars with high mass-loss rates in both the northern and southern skies. These stars are compared to each other and found to be very similar chemically. Moreover, they are very similar to carbon stars with low mass-loss rates. This result makes the chemical modelling of such stars simpler. Differences occur in stars' $^{12}C/^{13}C$ ratios, which reflect different nucleosynthesis histories, and in abundances of SiO, which can indicate the passage of shocks through the inner wind of the star. The second study is of the molecule-rich proto-planetary nebula (PPN), CRL618. I construct a chemical model of the warm, dense torus, which shows that complex molecules form in high abundances. The most notable of these complex molecules is benzene, which is found to form via a previously undiscovered reaction scheme, and matches the column density calculated from observations closely. In contrast, the next two chapters deal with two molecule-poor PPNe. Observations reveal that only simple molecules (CO, CN, HCN) are abundant. The lack of sufficient shielding of UV radiation from the increasingly hot star and the interstellar medium is a possible reason for this. The final study looks at the final stage of stellar evolution, and surprisingly finds that molecules are detected in what one would expect to be very diffuse and highly irradiated material. The first detections in a planetary nebula (PN) of formaldehyde ($H_2CO$) and carbon sulphide (CS) are made. The chemical model of a clump in various post-AGB scenarios shows that clumps cannot support many of the molecules detected in PNe; some other form of shielding and/or reformation is necessary. Overall, this thesis shows that the post-AGB is a period of great transition, not only from a large, cool star to a small, hot star, but also from a stage where there is a chemical conformity (among carbon stars) to one in which there is diversity (molecule-rich/molecule-poor PPNe), back once again to conformity (among planetary nebulae). Several questions about post-AGB chemistry are raised, and I briefly go on to mention the importance of further research into the formation of polycyclic aromatic hydrocarbons and of clumps.

# Acknowledgements

*My thanks go to my supervisors and close collaborators, Tom Millar, Lars-Åke Nyman and Albert Zijlstra.*

*And also to those others with whom I have had the pleasure of working, Eric Herbst, Hans Olofsson and Fredrik Schöier.*

—

*I am grateful to the European Southern Observatory (ESO) for hosting me in Santiago de Chile for more than two years, and for the opportunity to get to know that beautiful country. Best wishes to the ESO Santiago students, for whom a mid-morning pisco is never an inviable option ('Emergency break!'). Thanks to the (former) SEST team who helped entertain me during my stays on a 2,500 m-high mountain in the middle of the barren desert...*

*Thanks also to Fiz, Calamity, Spicyhot, Morganna, Baidh, Confusion and many, many others. To Pilar, Beck and Bevan, Ian, Lucy, Rachel, Ivana, Johnny, Patrick, Sharon and all others who passed through the gates of SCC, and made life so much more enjoyable.*

—

*For fun, frolics and, er, food parcels, thanks to Anna, Bert, Christopher, Em, Jessie, Matthew, Mike, Mum & Dad, and the Magic posse.*

*I came upon a child of God, walking down the road.*
*I asked him, where are you going?*
*And this he told me.*

*He said I'm going down to Yasgur's Farm,*
*Just join in a rock and roll band.*
*Get back to the land and set my soul free.*

*(He said) we are stardust, we are golden,*
*And we got to get ourselves back to the garden.*

*So can I walk beside you?*
*I've come here to lose the smog,*
*I feel like I'm a cog in something turning round and round.*

*Maybe it's just the time of year,*
*Maybe it's the time of man.*
*I don't know who I am,*
*But life is for learning.*

*(And then) we are stardust, we are golden,*
*And we got to get ourselves back to the garden.*

*We are stardust, we are golden,*
*And we got to get ourselves back to the garden.*

*By the time we got to Woodstock,*
*We were half a million strong.*
*Everywhere you look there was a song and hope and a celebration.*

*And I dreamed I saw the bomber death planes*
*Riding shotgun in the sky,*
*Turning into butterflies above our nation.*

*We are stardust, we are golden,*
*And we got to get ourselves back to the garden.*

*We are stardust, we are a billion year old carbon, we are golden.*
*We just got caught up in some devil's bargain*
*And we got to get ourselves back to the garden.*

*To some semblance of a garden.*

— Joni Mitchell.

*To Kate*

*(soft-head)*

# Declarations

No portion of the work referred to in this thesis has been submitted in support of an application of another degree or qualification of this or any other university, or other institution of learning.

Some parts of the work presented in this thesis may have been included in the following articles:

**Molecules in bipolar proto-planetary nebulae.**
Paul M. Woods, L.-Å. Nyman, F.L. Schöier, A.A. Zijlstra, T.J. Millar, H. Olofsson, 2004, A&A, submitted.

**Molecular abundances in carbon-rich circumstellar envelopes.**
Paul M. Woods, F.L. Schöier, L.-Å. Nyman, H. Olofsson, 2003, A&A, 402, 617

**The chemistry of proto-planetary nebulae.**
Paul M. Woods, T.J. Millar, E. Herbst, A.A. Zijlstra, 2003, A&A, 402, 189.

**Very Large Telescope spectra of carbon stars in the Large Magellanic Cloud and their metallicity dependence.**
M. Matsuura, A.A. Zijlstra, J.Th. van Loon, I. Yamamura, A.J. Markwick, Paul M. Woods, L.B.F.M. Waters, 2002, ApJ, 580, L133.

**The synthesis of benzene in the proto-planetary nebula CRL618.**
Paul M. Woods, T.J. Millar, A.A. Zijlstra, E. Herbst, 2002, ApJ, 574, L167.

**The chemistry of CRL618.**
Paul M. Woods, T.J. Millar, A.A. Zijlstra, E. Herbst, IAU Symposium 209, Planetary nebulae: Their evolution and role in the universe, Kwok, S., Dopita, M., Sutherland, R. (Eds), ASP, 279.

# Contents

# List of Figures

# List of Tables

# Chapter 1

# Introduction

## 1.1 Preamble

When you tell people that you're an astronomer their eyes light up with romantic notions of nights spent reclining under the eyepiece of a large optical telescope, shooting stars occasionally passing through the frame. When you then tell them that nowadays computers do all that, and generally you work in the daytime like everybody else, their faces fall somewhat. When you go on further to explain that you actually study the chemistry of stars, and that requires the use of "radio" waves and no pretty pictures whatsoever, you're generally met with complete blankness, or a switch in conversation topic to what the weather's doing, or what the latest bunch of oddballs are currently up to in the Big Brother house. However, sometimes astronomy can be fun (fun enough for the Sun newspaper! See Fig. 1.1), and perhaps as this thesis will show, astronomy can even be interesting...

## 1.2 Overview

This thesis is organised into seven chapters and an appendix containing two sections. This first chapter serves as a general introduction to the topic of evolved stars and concentrates on those areas referred to later in the thesis. It covers stellar evolution, the different characteristics of the Asymptotic Giant Branch (AGB),

ROWN ALE

# Boffins find huge cloud of alcohol in space

*ET foam home . . . how movie favourite would look enjoying a pint of outer-space ale*

By DAVID WOODING, Spaced-Out Correspondent

**STARGAZERS have found a boozers' paradise in outer space — a gigantic mass of pure alcohol.**

They stumbled across a mystery cloud while peering through their telescopes at a distant constellation.

Now after months of research they have learned the mystery object is the final front-beer . . . enough alcohol to make **400 TRILLION, TRILLION** pints of beer.

That's 300,000 pints a day for every person on Earth for the next **BILLION** years. It would fill the world's oceans tens of thousands of times over.

## Frozen

But star-trekkers who want to beam up for a quick one had better think again — the bar at the end of the Universe is 10,000 light years away — or 58,656,960,000,000,000 miles.

Last night, the three British astronomers who made the discovery were raising their glasses in a more down-to-Earth toast.

Geoff Macdonald and Rolf Habing, of the University of Kent and Tom Miller, of the University of Manchester Institute of Science and Technology, were the boffins who spotted the cloud.

They were looking through the powerful James Clerk Maxwell Telescope on Hawaii at a newly-formed star called G34.3 in the constellation of Aquila. Further studies revealed that heat from the new star is producing alcohol faster than all the world's breweries and distilleries put together.

At minus 148°C the cloud is warm by space standards — but the brew could be comfortably drunk without ice.

As Captain Kirk might say if he stumbled across the alcoholic haze: "Booze me up, Scotty."

Only one problem in outer space, though . . . the pubs have no atmosphere.

## 10 STOUT OF THIS WORLD DRINKS

1 Interstellar Artois
2 Carling Black Hole Label
3 Tennants Extra Terrestrial
4 Adnams Alien
5 Mars-tons Pedigree
6 Watneys Red Planet
7 Miller Lite Years
8 Rolling Rocket
9 Castlemoon XXXX
10 Red Spock Cider

Figure 1.1: Prof. T.J. Millar's most critically acclaimed work.

proto-planetary nebula (PPN) and planetary nebula (PN) evolutionary stages, and circumstellar chemistry during these three stages.

Chapter 2 looks at a sample of six carbon-rich AGB stars and determines their molecular abundances, finding all the stars in the sample somewhat chemically identical.

Chapters 3, 4 and 5 examine the chemistry during the PPN stage. Chapter 3 models the dense torus of a chemically *rich* PPN, CRL618, whilst Chapter 4 contains observations of two molecule-*poor* PPNe, IRAS16594-4656 and IRAS17150-7112. Chapter 5 then goes on to show that this molecular deficiency is the result of little shielding of complex molecules. Hence shielding of the intense UV fields during the PPN stage is crucial to the survival of larger molecules.

Three PNe are studied in Chapter 6, and observations show that only a few small molecules are present in reasonable quantity. However, $H_2CO$ and CS are detected, for the first time in a planetary nebula. Distributions of several molecules are mappped, and fractional abundances are calculated. A simple model of a clump in a planetary nebula shows that small molecules such as CO, HCN, CN and CS will survive from the AGB phase given enough shielding.

Conclusions are drawn and summarised in Chapter 7, and possible avenues of further investigation are given. Appendix A contains a literature study of the stars studied in this thesis, whilst Appendix B is a compendium of the molecular line observations of the stars.

## 1.3 Stellar evolution

### 1.3.1 Main sequence and red giant branch evolution for low- and intermediate-mass stars

A star will spend up to 90% of its life on the Main Sequence (MS) of the Hertzsprung-Russell (H-R) diagram (see Figure 1.2), converting a central hydrogen reserve into helium. Eventually, the hydrogen core of the star becomes exhausted and leaves behind an inert helium core. Hydrogen-burning continues in a shell around the core, and the hydrogen envelope outside this shell expands in mass. The portion of the circumstellar envelope (CSE) able to 'move' hydrodynamically (the convective envelope) will extend inwards to "dredge up" (see Sect. 1.4.3) the ash from hydrogen-burning. This process is aptly named "the first dredge up".

Low mass stars (defined as stars that develop an electron-degenerate helium core,

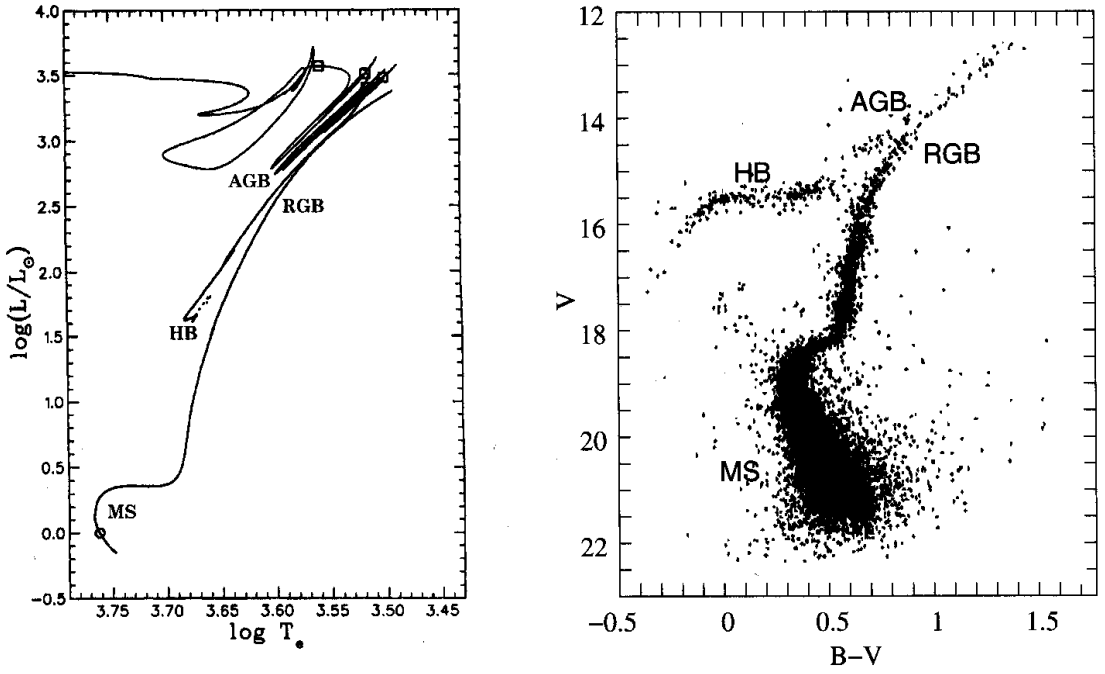


Figure 1.2: **Left** Hertzsprung-Russell diagram with the computed long-term evolution of the sun. The current luminosity and temperature are indicated by a circle (from Sackmann et al. 1993). **Right** Observed colour-magnitude diagram of the globular cluster M3 (from Buonanno et al. 1994).

hence with masses less than about 2.5 $M_\odot$) ascend the Red Giant Branch (RGB), a well defined evolutionary track in the H-R diagram (see Fig. 1.2). Intermediate mass stars (defined as stars which ignite helium non-degenerately, but develop an electron-degenerate *carbon-oxygen* core following the exhaustion of helium at the centre, and hence with masses less than about 8 $M_\odot$) do not populate the RGB, but are slightly bluer, and only populate the Asymptotic Giant Branch (AGB, so called because it asymptotically approaches the giant branch of the H-R diagram). 95-98% of stars in general pass through these two stages in evolution (Habing 1996). Following the RGB initially, a star will increase in luminosity and decrease in effective temperature until the central helium ignites in a very quick and very luminous "helium flash". This marks the end of the RGB, and from here the star moves onto the Horizontal Branch, during which helium burns quiescently at the core. The core will then become inert yet again, this time being composed of mostly carbon and oxygen. Accompanying the (re-)formation of the degenerate core is the second dredge up (see Sect. 1.4.3). The temperature in the rapidly-contracting core increases as the result of the release of gravitational potential energy, and then decreases as energy is lost through escaping neutrinos. Expansion of the outer H-

envelope leads again to the formation of a red giant, which this time ascends the AGB. RGB stars and AGB stars are very similar in appearance, but in general the AGB star is much more luminous – RGB stars have a maximum luminosity of 2 900 $L_\odot$, whereas AGB stars can have a luminosity of around 10 000 $L_\odot$. There is some overlap in luminosity range, but AGB stars can be distinguished by their pulsating nature, or by larger mass-loss rates. All stars less than 8 $M_\odot$ find themselves at the AGB stage of evolution. Following the exhaustion of central helium, both low mass and intermediate mass stars behave qualitatively similarly, as if at the same stage of nuclear evolution.

### 1.3.2 AGB evolution

Once on the AGB, a star produces energy in the helium shell around the inert core, all of which is encased in a thin H-shell. This is a very unstable arrangement. Periodically, and usually for short periods only, the He-shell ignites. The liberated energy raises the local pressure, and produces expansion of the envelope. Eventually this leads to double-shell burning, since the heat of the helium-burning shell ignites the outer, hydrogen-shell. Once the expansion has progressed far enough, cooling causes the helium-burning to die down. Often, the expansion takes the hydrogen shell out to distances where the hydrogen-burning is shut off. It starts up again when helium-burning has reduced to such a level that material falls inward again and the hydrogen is reignited. After a period of quiescent double-shell burning, the helium-burning flares up once again. These phases are called "shell flashes" or "thermal pulses". Thus AGB stars are often divided into early-AGB stars (E-AGB, which have not yet begun to pulse) and thermally-pulsing AGB stars (TP-AGB). These flashes produce much more carbon than oxygen (reaching a ratio of 2:1, finally), and can be a source of C-enhancement in the envelope if the products can be convected to the stellar surface (i.e., the third dredge-up, see Sect. 1.4.3).

### 1.3.3 Post-AGB evolution

Many of the stars on the Asymptotic Giant Branch will become planetary nebulae – hot stellar remnants, surrounded by diffuse nebulae of gas and dust (see Sect. 1.3.3.3). This involves a transition which leaves the central star at an effective temperature of 30 000–200 000 K, with a luminosity of 1 000–10 000 $L_\odot$ and surrounded by a nebula of ionised and molecular gas. The method of ejecting the gas and dust which constitutes a planetary nebula is far from understood. It is

known that large-amplitude pulsations occur, but the theory is not well developed enough to convincingly explain the ejection process. However, a series of stages from AGB star to PN is evident, even though the finer details may not be established.

#### 1.3.3.1 The end of the AGB

As an AGB star increases in luminosity, so also the rate at which mass is ejected from the star increases (the mass-loss rate). Eventually there comes a point when the circumstellar shell is completely detached from the contracting stellar core because there is no material left to eject. This occurs when the stellar mantle becomes $\lesssim 0.01\,\mathrm{M}_{\odot}$ in mass. This detachment is most likely due to inflation of the CSE, by pulsation-driven shocks, and then due to radiation pressure on dust grains, forcing the gas (which is coupled to the dust) away from the star. The core remnant continues to burn hydrogen or helium in a shell, depending on what stage of a flash cycle the final detachment occurred (Iben 1984).

There is expected to be no change in kinematics as the shell expands, and this is confirmed by observations (e.g., Bujarrabal et al. 1992; Nyman et al. 1992; Volk et al. 1993; Omont et al. 1993a). For this particular reason it is assumed that the non-spherical shapes of proto- and planetary nebulae arise from asymmetries already present in the AGB star. However, outflow velocities tend to be higher for post-AGB objects than for objects on the AGB (e.g., Nyman et al. 1992; Volk et al. 1993), which suggests the development of jets.

#### 1.3.3.2 Proto-planetary nebulae

The most popular theory to describe the structures seen in post-AGB objects is called the "interacting stellar winds" model, first proposed by Kwok et al. (1978). The P Cygni profiles of central stars of planetary nebulae show evidence of winds at speeds of up to $4\,000\,\mathrm{km\,s^{-1}}$; at the end of the AGB this fast wind catches and overtakes the slow-moving AGB wind, and the region of interaction of these two winds determines the site of formation of the nebula (see Sect. 1.5.3). The fast wind also shapes the nebula, and bipolarity in nebulae is common, with the nebular axis either coinciding with the spin angular momentum or magnetic moment axis of the remnant. The hot, high-velocity wind that proceeds from some early proto-planetary nebulae (e.g., CRL618 and CRL2688) has been studied, for example, by Neri et al. (1992, CRL618) and Young et al. (1992, CRL2688). Wind velocities in these two objects reach $\approx 200\,\mathrm{km\,s^{-1}}$ and $\approx 100\,\mathrm{km\,s^{-1}}$, respectively.

Also during this stage of evolution, the stellar remnant increases in temperature, from several thousand degrees Kelvin on the AGB to ten or even thirty thousand Kelvin (e.g., CRL618). The surface temperature of this remnant has an effect on its nebula. If the temperature is high enough, photons from the surface will ionise a portion of the nebula, causing it to fluoresce optically. This fluorescence is tempered by how much of the nebular mass is self-shielding.

The youngest planetary nebulae (PNe) appear to be on the order of a few thousand years old (that is, they appear in the classical PN form a few thousand years after the AGB stage). Thus the stage in between, the proto-planetary nebula (PPN) stage, involves a rapid transition. It seems that the form of stars in this stage is highly dependent on the physical characteristics of their precursors – on the mass-loss rate, the stellar wind velocity, thermal pulses, the variation of UV flux. The time taken for the stellar remnant to drop in luminosity by an order of magnitude from the end of the AGB, the fading time, also plays a crucial role in determining the properties of the PN. This time is on the order of 10 000 yr.

#### 1.3.3.3 Planetary nebulae

After time, the hot remnant will cool due to the cessation of nuclear burning, and become a white dwarf. The nebula will expand, and eventually disperse into the interstellar medium (ISM). The white dwarf may experience some sort of rebirth, experiencing a final helium shell flash and retracing the steps along the AGB, or a final hydrogen shell flash to become a self-induced nova.

The photodissociation of the envelope now is dominated by the UV field of the star. Whereas before it was dominated by the interstellar UV field, during the PPN-phase the importance of the stellar UV field has become more pronounced, and by the PN-stage is much stronger than the ambient interstellar UV field. Hence most of the surviving molecules will be those that self-shield, i.e., CO and $H_2$. In fact, CO emission from the former AGB CSE dominates the emission in these objects.

## 1.4 Processes on the AGB

### 1.4.1 Pulsation and variability

Whilst on the AGB, a star will suffer 'variability', due to instabilities in the hydrodynamics of the star. It will experience radial pulsations and opacity changes in the ionised hydrogen region. Pulsation will start at a critical luminosity, and the

initial period will depend on the mass of the star. The amplitude and the period of pulsation will increase as the star evolves, and pulsations cease at the tip of the AGB. The pulsating stars found on and around the AGB can be divided into several groups:

Firstly, Miras (Mira variables) have a large visual amplitude change - from 2.5 to 6-7 mags. An increase in absorption of $C_2$ and CN (or TiO in O-rich stars) as temperature diminishes, permits a greater association of atoms into molecular form. Well-studied stars of this type are S Cep and Mira. Pulsation periods are 300 days and above.

OH/IR stars are thought to be descendants of Mira variables, and can have periods of up to 2 000 days (Herman & Habing 1985a). The most extreme OH/IR stars seem to be non-variable (Herman & Habing 1985b), and may have moved off the AGB (Habing et al. 1987).

Semi-regular variables are split into three sub-groups. SRa stars have a wider range of period but a smaller amplitude than Miras (less than 2.5 mag). They are regular in both amplitude and in the interval between maxima. SRb stars have poorly defined intervals between maxima. SRc stars have a very wide range of intervals between maxima (30 – few thousand days) and have a small visual amplitude variation.

Slow, irregular variables (Lb) are stars that show no pattern and have low amplitudes. The difference between these stars and SRb stars is not well defined, but Lbs tend to be more luminous.

### 1.4.2 Luminosity

Luminosity varies on four distinct timescales: one due to the dynamical oscillations of the envelope, a second one due to thermal pulse instabilities, a third is the thermal pulse relaxation timescale (the timescale for a return to quiescence) and finally, the timescale which describes the period between helium ignitions. During pulses, luminosity doubles for a short time, and then slowly decreases to roughly 3 times below pre-flash level for about 200 years. The pre-flash luminosity is regained after about 10 000 years (10% of inter-pulse time.) This inter-pulse time is only dependent on core mass ($M_c$):

$$\log \tau_{ip} = 4.5 \left(1.68 - \frac{M_c}{M_\odot}\right) \text{ yr.}$$

For a typical core mass of $0.6\,\mathrm{M}_\odot$, the inter-pulse time is 70 000 years. After a few initial pulses, luminosity also is dependent on core mass, and goes as:

$$L = 59000\,\left(\frac{M_\mathrm{c}}{\mathrm{M}_\odot} - 0.5\right)\,\mathrm{M}_\odot\,\mathrm{yr}^{-1}.$$

The maximum luminosity possible is 50 000 solar luminosities, since the core mass is restricted to $<1.4\,\mathrm{M}_\odot$. At the start of thermal pulsing, the core mass is dependent on the star's Main Sequence mass,

$$\frac{dM_\mathrm{c}}{dt} = 8\;10^{-7}(\frac{M_\mathrm{c}}{\mathrm{M}_\odot} - 0.5)\,\mathrm{M}_\odot\,\mathrm{yr}^{-1}$$

and increases as

$$M_\mathrm{c} = 0.95 + 0.075(M_{MS} - 7)\,\mathrm{M}_\odot$$

so that the timescale for a luminosity increase is about 1.2 million years. Since this is a tenth of time a star spends on the AGB, no dramatic increases in core mass or luminosity are expected for an individual star.

### 1.4.3 Dredge-up

The composition of the photosphere of an AGB star is determined by dredge-ups. To re-iterate, dredge-up is the cycling of "burnt" material through a convective region.

The first dredge-up occurs as the star becomes a red giant for the first time, following the exhaustion of hydrogen. This results in a doubling of the surface $^{14}$N abundance, a reduction in surface $^{12}$C abundance by about 30%, the development of a surface $^{12}\mathrm{C}/^{13}\mathrm{C}$ ratio of about 20–30, a reduction in surface Li and Be by several orders of magnitude, and practically no change at all in the surface abundance of $^{16}$O (Becker & Iben 1980; Iben 1967, 1977).

The second dredge-up only occurs for stars greater than $4\text{–}5\,\mathrm{M}_\odot$ and comes after the exhaustion of central helium, accompanying the formation of the electron-degenerate core. The dredged-up material can be as much as $1\,\mathrm{M}_\odot$ for the most massive intermediate-mass stars, and contains no hydrogen (which has entirely become helium), and an almost complete lack of $^{12}$C and $^{16}$O (which have become $^{14}$N). Meanwhile, in the helium-exhausted core temperatures rise as a result of the release of gravitational potential energy, and then decrease as energy-loss via neutrinos becomes important. The end result is a low temperature degenerate core, which

cannot start to burn carbon until the core mass approaches the Chandrasekhar mass of $1.4\,M_\odot$. However, only the most massive intermediate-mass stars will experience a change in surface composition.

To illustrate the variation in surface composition over these two dredge-ups, let us assume a ratio of C:N:O of $\frac{1}{2}$:$\frac{1}{6}$:1 before any dredge-ups have taken place. After the first dredge-up the ratio becomes $\frac{1}{3}$:$\frac{1}{3}$:1, independent of stellar mass. Finally, after the second dredge-up, the ratio is approximately 0.33:0.55:1.

Following the second dredge-up the chemical makeup of the star is determined by thermal pulses; an AGB star will thermally pulse for $\sim 10^5 - 10^6\,$yr. Since the dominant energy source for a thermal pulse is the triple-$\alpha$ reaction[1] then it is not surprising that the most abundant element produced is $^{12}$C. The $^{16}$O that follows from the addition of another $\alpha$-particle is produced at an abundance an order of magnitude smaller than that of $^{12}$C. At the end of helium burning the final abundances of $^{12}$C and $^{16}$O are in the ratio 2:1, approximately. During the inter-pulse phase almost all the $^{12}$C and $^{16}$O which enter the hydrogen-burning shell is converted to $^{14}$N and subsequently to $^{22}$Ne.

The third dredge-up occurs during the thermally-pulsing stage. Again, the convective envelope extends down into processed material and brings up newly synthesised $^{12}$C in addition to neutron-rich isotopes. This occurs after every thermal pulse, and the depth to which the convective envelope descends is dependent on the pulse amplitude (Iben 1975), which in turn is dependent on stellar envelope mass. More massive stars experience a deeper dredge-up.

#### 1.4.3.1 Formation of carbon stars

Carbon stars were first identified by Father Angelo Secchi in 1868, and some 88 years later they were still something of an enigma (Bidelman 1956). Progress has been made since then, but they still remain somewhat mysterious, often due to the thick cloak of dust many of them use to conceal themselves. A recent review by Wallerstein & Knapp (1998) and the IAU Symposium on 'The Carbon Star Phenomenon' (Wing 2000) are both useful references.

Carbon stars are classified as stars with [C]/[O] ratios of greater than one. They are recognised through molecular bands of $C_2$, CN and CH. Furthermore, those with a thick dust envelope are distinguished by SiC emission at $11.4\,\mu$m. They make up $\approx 10\%$ of AGB stars in the Milky Way (Houk 1963), yet produce about 50% of the

[1] $3\alpha \longrightarrow {}^{12}\mathrm{C} + \gamma$

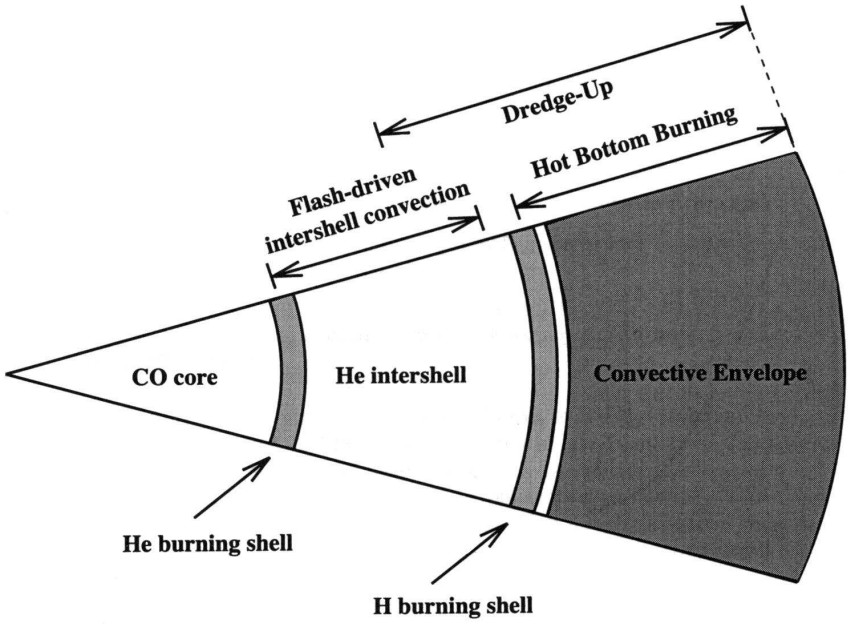


Figure 1.3: A schematic view of the inner regions of an AGB star (Lattanzio & Forestini 1999).

material ejected into the ISM (Kastner 1990).

Stars on the Main Sequence have initial $^{12}C/^{13}C$ ratios of 50-90. The source of $^{12}C$ in carbon stars is the triple-$\alpha$ reaction inside the star. The problem has been how the $^{12}C$ is brought to the surface in order to produce carbon stars, especially since the wide range of $^{12}C/^{13}C$ ratios suggests that in some cases the $^{12}C$ must have reacted with protons on the way to the surface.

For a low mass star ($M_\star \lesssim 1.7\,M_\odot$) the triple-$\alpha$ reaction occurs in the degenerate core, with a rate that increases until the rising temperature removes the degeneracy. This creates an unstable temperature gradient which may entirely mix the star. Eventually all the matter between the stellar core and surface will be ejected, halting any further carbon-enrichment.

For a more massive star, a different process is required because there is no degenerate core. After helium ignites at the top of the RGB and settles down to quiescence, a C-O core is produced, surrounded by burning double-shells (see Figure 1.3). The helium shell burns by shell flashes (like the core flash of the lower mass stars) and the shell flashes produce more carbon than oxygen. The mixing of this excess carbon to bring it to the surface of the star has been a persistent problem since it seems clear that photospheric convection zones do not reach deeply enough to bring $^{12}C$-enhanced material up as a steady process. Suffice to say that if "enough"

dredge-up occurs, a carbon star will form.

For the most massive stars, a process called hot-bottom burning prevents carbon star formation. The high temperatures at the H-He border cause a hot-bottom convection zone. The high velocities in the zone during a thermal pulse means that the entropy barrier which exists between the H and He regions may be broken, and mixing may occur (Frost et al. 1998a,b; Sackmann & Boothroyd 1991; Boothroyd et al. 1993). This produces four times as much carbon as a normal thermal pulse which does not break the barrier. A result of hot-bottom burning is that carbon is burned into nitrogen and oxygen before it reaches the photosphere (Iben & Renzini 1983). If carbon is not burned, it would require about $10^6$ years of evolution before the carbon abundance at the surface could exceed the oxygen abundance. Since observations indicate that intermediate-mass stars spend about $10^5$ years or less as TP-AGB stars, such stars will not become carbon stars whether or not dredged-up carbon is converted to nitrogen. Hot-bottom burning is experienced by stars more massive than $4.5\,M_\odot$, and hence carbon stars are only formed from stars with an initial AGB mass less than $4.5\,M_\odot$. Since lower mass stars are less effiecient in dredging up material (Lattanzio 1993), a lower limit also exists.

The transition from oxygen- to carbon-rich is fast, on the scale of the envelope mixing time (a few tens of years). The oxygen-rich outer layers will continue to expand with a typical expansion velocity, and underneath a carbon-rich layer will start to build. This seems to explain the observations of carbon stars with oxygen-rich envelopes (e.g., Willems & de Jong 1986; Little-Marenin 1986), although there are doubts, since these stars do not exhibit OH emission (see the "discussions" of Zuckermann & Maddalena 1989; de Jong 1989).

### 1.4.4 Masers

Masers (microwave amplification by stimulated emission of radiation) are often observed in late-type stars, and can be differentiated from thermal radiation by several characteristics. Masers generally have a large intensity, very narrow linewidths and abnormal line ratios, indicating deviations from equilibrium. They are produced by a population inversion in the relevant levels, which is generally caused by infra-red or collisional pumping mechanisms in circumstellar environments.

The three most widespread masering molecules are OH, $H_2O$ and SiO, although other molecules such as SiS, HCN, CS and CO also mase. OH, $H_2O$ and SiO masers are pumped differently, they emanate from different sized regions ("maser spots"),

and are found at different radii. SiO maser regions are generally found closest to the star ($10^{14}$ cm), $H_2O$ masers require slightly lower temperatures, and hence are found further out ($10^{15}$ cm) and come from regions of $\approx 5\,10^{14}$ cm in size, and OH maser spots are found further out still and have sizes of $\approx 5\,10^{15}$ cm.

### 1.4.5 Mass-loss

White dwarfs are the end-points of stellar evolution for AGB stars. Typically they have fairly constrained masses of $\approx 0.6\,M_\odot$. There is evidence that white dwarf progenitors have a main-sequence mass of up to $8\,M_\odot$ (Weidemann & Koester 1983). This implies that approximately $7\,M_\odot$ are lost on the RGB and AGB in the most extreme cases.

In general it is found that most mass-loss occurs towards the end of the AGB. This ejection of matter produces a circumstellar envelope of gas and dust, which obscures the star. The obscuration is linked to the optical depth of the envelope; this is given approximately by:

$$A_V = 10 \left( \frac{\dot{M}_w}{10^{-6}\,M_\odot\,\mathrm{yr}^{-1}} \right) \left( \frac{10^{14}\,\mathrm{cm}}{R_i} \right) \mathrm{mag},$$

where $R_i$ is the inner radius of the dust envelope and $\dot{M}_w$ the mass-loss rate of the wind (Bohlin et al. 1978). This CSE will initially appear as a small infrared excess, but as mass-loss grows, the emission of the CSE will dominate that of the star. The light from the star itself will usually only become visible after the AGB, when the CSE detaches itself from its source.

The knowledge that mass-loss exists is now firm and established. However, the reasons behind it are less clear, largely because the photosphere of the star, which is the region where mass-loss is thought to start, is not easy to observe. The current scheme of thought is that pulsations of the star initiate the mass-loss, and the expanding envelope is pushed outwards by radiation pressure on the circumstellar dust. Neither pulsations nor radiation pressure seems able to produce the required amount of mass-loss alone (Bowen & Willson 1991).

In this scenario, pulsations of the star cause shock waves in the surrounding matter, and this elevates an atmosphere in which dust can readily form (Bowen 1988). Models mimicking this show correct values of $\dot{M}_w$ and $v_w$ (the wind velocity), and there is also circumstantial evidence to support this: it seems that pulsation implies mass-loss and mass-loss implies pulsation in observations of AGB stars (e.g.,

Jura 1986; Habing et al. 1987). The mass-loss rate is also in some way related to the pulsational period (e.g. Degioia-Eastwood et al. 1981; Vassiliadis & Wood 1993) and the pulsational period in turn is related to the pulsational amplitude (Ukita 1982).

Dust then absorbs radiation from the central star, is heated and radiates isotropically in the infrared. The photons from the star carry momentum as well as energy, and when radiation is absorbed by the dust, this momentum is transferred. This results in a force upon the dust, greater than that due to the gravity of the central star, and the dust is rapidly accelerated outwards. Collisions between dust and gas in turn accelerate the gas outwards. The dust is accelerated by radiation until the drag force from the gas equals the radiative force (e.g., see Tielens 1983). This mechanism means that dust drift velocity (the velocity with which the dust moves in relation to the gas) increases rapidly with distance, and also that the gas is rapidly accelerated beyond the point where dust forms. The crucial parameter here seems to be the dust condensation radius. All but the coolest stars form dust very close to the star. However, a mechanism is needed to bring material up from the photosphere to a level where dust can form and drive the gas away to infinity.

The mass-loss rate is given by,

$$\begin{aligned}
\frac{dM}{dt} &= \frac{dM}{dr}\frac{dr}{dt} = v_{\rm exp}\frac{dM}{dr} \\
\frac{dM}{dr} &= \frac{d(\frac{4}{3}\pi r^3\rho)}{dr} \\
&= \frac{4\pi}{3}(2m_{\rm H}\mu n)\frac{dr^3}{dr} \\
&= 8\pi m_{\rm H}\mu n r^2 \\
\Rightarrow \frac{dM}{dt} &= v_{\rm exp}(8\pi m_{\rm H}\mu n r^2) \\
\dot{M} &= 8\pi m_{\rm H}\mu v_{\rm exp} n(r) r^2 \ {\rm M_\odot\,yr^{-1}}, \qquad (1.1)
\end{aligned}$$

where $v_{\rm exp}$ is the (assumed constant) expansion velocity, $\mu$ the mean molecular weight (taken as 2 for molecular hydrogen), $\rho$ the density and $n$ the number density of particles. This expression is not valid in the inner regions of the envelope, where the expansion velocity is not constant. This implies that the number density distribution of hydrogen is given by,

$$n_{\rm H_2} \sim 10^6 \left(\frac{\dot{M}}{10^{-6}\,{\rm M_\odot\,yr^{-1}}}\right)\left(\frac{15\,{\rm km\,s^{-1}}}{v_{\rm exp}}\right)\left(\frac{10^{15}\,{\rm cm}}{r}\right)^2,$$

where $n_{\mathrm{H_2}}$ is per cubic centimetre. Thus for an "average" AGB star, $n_{\mathrm{H_2}}$ varies from $10^9\,\mathrm{cm}^{-3}$ at $10^{14}\,\mathrm{cm}$ to $10^3\,\mathrm{cm}^{-3}$ at $10^{17}\,\mathrm{cm}$.

Observations of extended CSEs show that AGB mass-loss is close to isotropic. When the star leaves the AGB, a high-velocity (super)wind begins to blow, which may be inherently bipolar or may be channelled by some sort of dense equatorial torus. This type of structure shown in young PNe may indicate that AGB mass-loss becomes non-symmetric during the very last mass-loss period. The high-velocity wind and the expansion of the HII region will enhance the density contrast. Eventually the molecular gas is left only in a fragmented ring or shell, with the final structure relying on the initial density contrast in the AGB CSE. The fragments consist of lumps, or groups of lumps, which have been compressed by the pressure of the developing nebulosity.

In the majority of cases, mass-loss is spherically symmetric on the large scale. However, it seems that high-resolution work shows the presence of clumps in the outflow, and that they are a common phenomenon, rather than just peculiarities. The vast majority of mass-loss models assume a smooth outflowing wind. Olofsson (1994a; see also Olofsson 1996a; Olofsson et al. 1996) proposes a scenario for the evolution of an AGB CSE through to the white dwarf stage by modelling a clumpy outflow. A crude estimate of the number of lumps emitted per unit time is given by:

$$\dot{N} = 1 \left( \frac{M_{\mathrm{lump}}}{10^{-6}\,\mathrm{M}_\odot} \right) \left( \frac{10^{-6}\,\mathrm{M}_\odot\,\mathrm{yr}^{-1}}{\dot{M}} \right) \mathrm{yr}^{-1}.$$

Thus only a few lumps per cycle will be ejected. As examples, a small, $H_2O$ or OH maser-emitting, region would have 10 and 100 clumps per region. A single dish CO observation ($\approx 5\,10^{16}\,\mathrm{cm}$) would encompass 1000 clumps. Clumps would quite rapidly reach their terminal velocity, and would expand at the sound speed, as they receded from the star. This may explain the increasing spot size as one goes from SiO to $H_2O$ to OH masers, which emanate from regions increasingly further out in the envelope.

Besides the problem of a clumpy outflow, there are a number of indications that mass-loss is not spherically symmetric on the AGB (see A.1.1), although there are no large departures from spherical symmetry. This asymmetric mass-loss on the AGB is thought to produce the prevalent bipolarity seen in PPNe and PNe.

There are a number of methods of estimating mass-loss rates from observations. Some are more reliable than others, and in general errors are likely to be a factor of 5 or so.

1. Far-infrared emission from dust can be used, and the large amount of information from the IRAS satellite, for one, makes this a very practical approach. There are several ways of calculating rates - crude methods include estimating the mass-loss rate from a particular flux, i.e., $\dot{M}_{\rm w} = {\rm f}(F_{\lambda 1})$ using the 60 $\mu$m IRAS flux (Jura 1987), or using the ratio of two fluxes, i.e., $\dot{M}_{\rm w} = {\rm f}(F_{\lambda 1}/F_{\lambda 2})$ (van der Veen 1989). These are dependent on the gas-to-dust ratio, which is often hard to determine accurately, and the former is also dependent on the distance to the star, which is another highly uncertainly quantity. Another method would be to use the strength of silicate emission features at 9.7 $\mu$m and 11.2 $\mu$m (Skinner & Whitmore 1988a,b). However, for high mass-loss objects this method cannot be used since the silicate emission features become absorption features. A slightly more complex method is then adopted (Schutte & Tielens 1989).

2. Another IR-based method is the comparison of the full IR spectrum of a star with a model spectrum (Bedijn 1987; Schutte & Tielens 1989). This method again relies on the uncertain gas-to-dust ratio, and also on the emitting properties of the dust. Furthermore, the expansion velocity of the envelope must be obtained by some independent means. However, if this information can be obtained then models can produce quite accurate results.

3. The majority of CSEs consist of a high degree of molecular hydrogen. Unfortunately this molecule has no lines in the millimetre-wave regime, and infra-red lines tend to fall inside regions of high atmospheric contamination. The next most abundant species is CO, which has observable lines. This molecule has uncomplicated emission, forms in the photosphere of the star, and is very stable to photodissociation. Hence it is an ideal tracer of a stellar wind. However, its often faint emission means that only a few hundred CSEs have been detected in CO. The first good attempt to calculate mass-loss using CO was made by Knapp & Morris (1985), although their model has been shown to be lacking for higher mass-loss rates (e.g., Olofsson 1989).

4. For O-rich stars the OH molecule can be used to estimate mass-loss (e.g., Netzer & Knapp 1987). Although the OH molecule seems to be found in a thin shell rather than spread throughout the envelope, the radius of the OH-shell is determined by the UV optical depth of the CSE and hence by the mass-loss rate. The radius of the shell is an observable quantity. This

Table 1.1: Representative mass-loss rates and lifetimes on and beyond the AGB (Olofsson 1990).

| Phase | $\dot{M}_{\rm w}$ ($\rm M_\odot\,yr^{-1}$) | Lifetime (yr) |
|---|---|---|
| O-rich AGB star | — | $\sim 10^6$ |
| O-rich Mira variable | $1\,10^{-6}$ | 50 000 |
| OH/IR-star | $5\,10^{-5}$ | 8 000 |
| Extreme OH/IR-star | $2\,10^{-4}$ | — |
| Bright C-star | $3\,10^{-7}$ | 50 000 |
| IR C-star | $2\,10^{-5}$ | 16 000 |
| Planetary nebula | — | 15 000 |

method works for quite distant objects because the emission of OH is often maser amplified.

Table 1.1 shows representative mass-loss rates on the AGB and in the post-AGB phase as a summary (Olofsson 1990). OH/IR stars have a spectral energy distribution (SED) which peaks between 6–10 $\mu$m, with an absorption at 9.7 $\mu$m and an OH maser at 1612 MHz. IR stars are strong in the infra-red (especially the $K$-band at 2.2 $\mu$m), but fainter at visual wavelengths. Carbon stars have an SED which peaks around 10 $\mu$m.

The study of how mass-loss changes with time is an on-going one. Episodic mass-loss can clearly be seen in the multiple rings around IRC+10216, for instance (see Fig. 1.4). The reasons for such rings are less than clear, however. More drastically, detached envelopes have also been observed on the AGB (Olofsson et al. 1990a). Especially striking is the case of TT Cyg (Olofsson et al. 2000). The detached shells represent drops in mass-loss rate of more than an order of magnitude over as short a time as 10 000 yr. It is likely that both these occurances are related to thermal pulses in some way, but the mechanism is not as yet known.

The average mass-loss evolution can be simply determined by combining the radial density distribution of the CSE with the kinematics, to give the mass-loss rate at a retarded time. For example,

$$\dot{M}_{\rm w}(t - r/v_{\rm w}) = 4\pi r^2 \rho(r) v_{\rm w}. \tag{1.2}$$

A more elaborate method uses the fact that a CSE provides a large range in physical conditions. Emission at different wavelengths and from different molecular species have a different dependence on these properties, and hence sample $\dot{M}_{\rm w}$ at different retarded epochs (using Eq. 1.2). For instance, for a mass-loss rate of $10^{-6}\,\rm M_\odot\,yr^{-1}$,

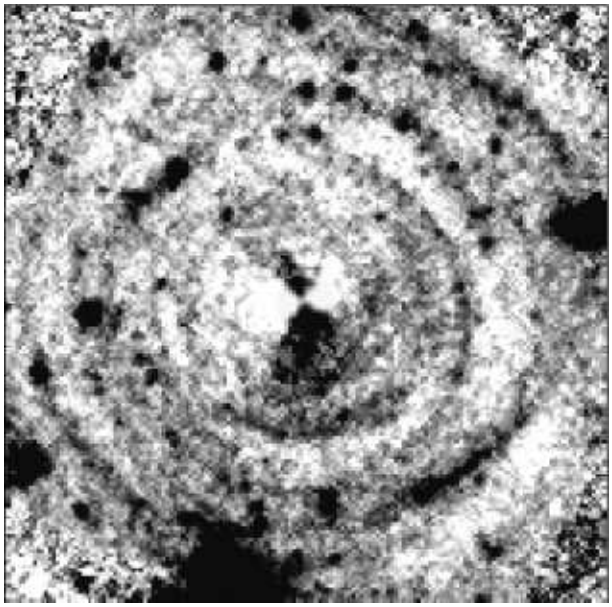

Figure 1.4: Composite V-band images of IRC+10216, taken from the Canada-France-Hawaii Telescope, and from the HST (Mauron & Huggins 2000). The multiple shells around the source can be clearly seen, as can a distinctly bipolar feature at the centre.

the 12 $\mu$m emission, the 60 $\mu$m emission, OH (1612 MHz) and CO ($J$=1-0) give results for retarded times of $\approx$10, $\approx$100, $\approx$100, $\approx$1 000 yr ago, respectively. Unfortunately the uncertainties in the derived mass-loss rates are presently too large to make this a useful approach.

Mass-loss rates appear to increase as stars reach the end of the AGB. At the tip, mass-loss suddenly reduces drastically (Bedijn 1987; Volk & Kwok 1989), although does not cease altogether (van der Veen et al. 1989; Trams et al. 1989). The reason behind this seems due to the stellar H-envelope reaching such a low mass as to inhibit pulsations. Observations show that many post-AGB objects have *high* mass-loss rates (e.g., Loup et al. 1990), although it is questionable whether the CO emission samples present-day mass-loss.

### 1.4.6 Physical characteristics of the envelope

On the AGB stars lose huge proportions of their mass, ejecting it into the interstellar medium. Rates of mass-loss can be as much as $10^{-4}\,\mathrm{M}_{\odot}\,\mathrm{yr}^{-1}$. This mass-loss, which is initiated by pulsations and/or radiation pressure, forms a CSE. Gas and dust stream outward from the star in a stellar wind, often at speeds as high as 20 or 30 $\mathrm{km\,s}^{-1}$. As this matter becomes diluted (becomes less dense) it is exposed to the

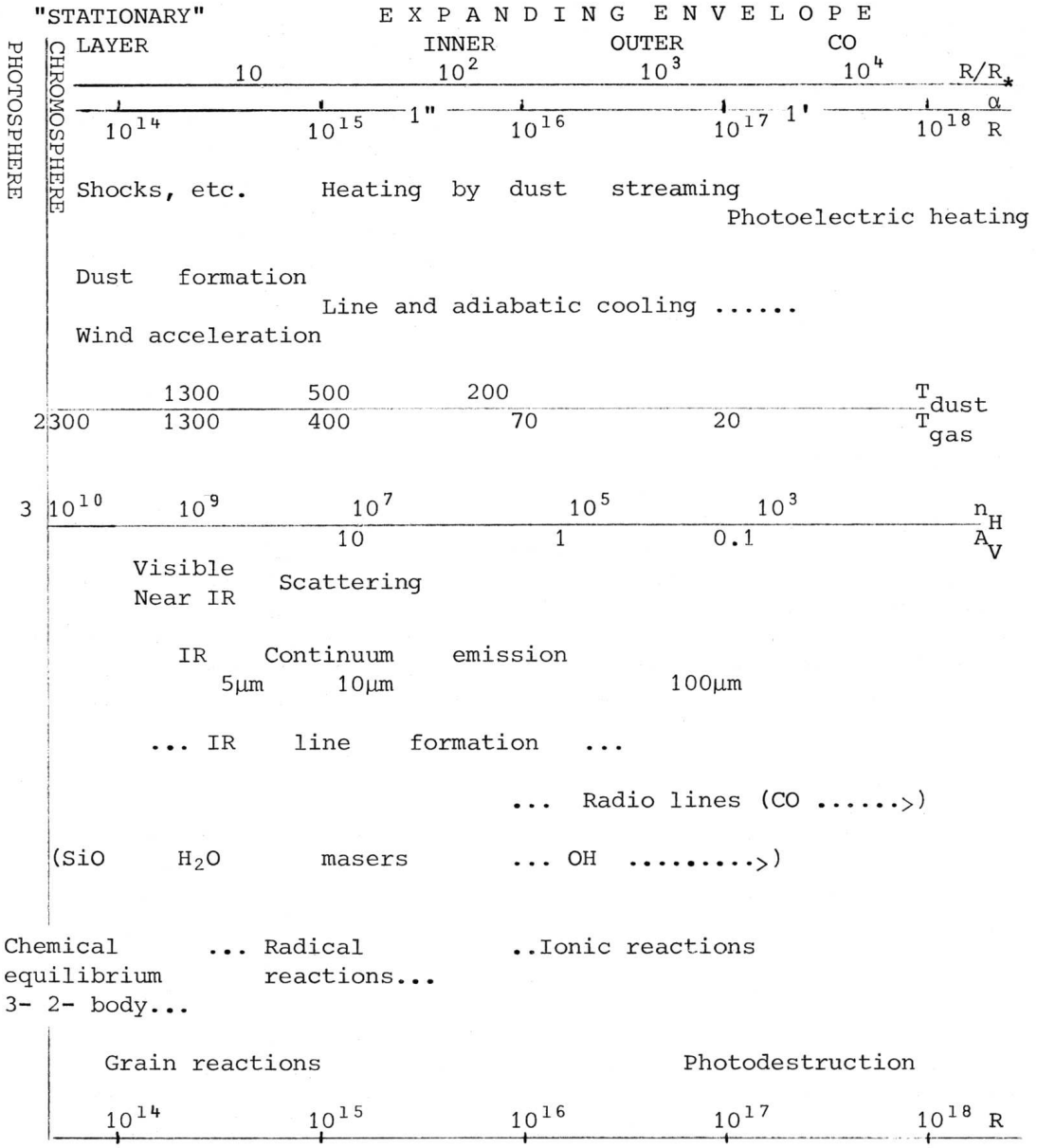


Figure 1.5: Structure of an AGB envelope (IRC+10216). Assumed parameters: $d = 200\,\mathrm{pc}$, $R_\star = 1\,000\,\mathrm{R}_\odot = 7\,10^{13}\,\mathrm{cm}$, $\dot{M} = 4\,10^{-5}\,\mathrm{M}_\odot\,\mathrm{yr}^{-1}$. In outer envelope, $n_\mathrm{H} = 5\,10^{37} r^{-2}\,\mathrm{cm}^{-3}$, $A_\mathrm{V} = 2.5\,10^{-22} N_\mathrm{H}$. The range of maser emission is only applicable to oxygen-rich envelopes (Omont 1985).

interstellar radiation field, and also to photons from the star itself.

Closest to the stellar core there is a region where nuclear burning is occurring – hydrogen becoming helium and helium becoming heavier elements. Outside this is the stellar atmosphere, where pulsations usually occur. Pulsations raise masses of gas, some of which partly returns to the photosphere and some of which continues outwards. The levitated gas cools, allowing dust to form. Working outwards, next comes the inner circumstellar envelope, then the main circumstellar envelope, and finally the outer circumstellar envelope, which terminates in the ISM. It is on the main circumstellar envelope that most millimetre astronomers concentrate – it is here that the stellar wind has reached a steady velocity, and solids have condensed.

Temperature and density progressively decrease with radius. Temperature is found to follow a power law, $r^{-a}$, with $a$ in the region 0.6–0.8 (Kwan & Linke 1982). It is very difficult to accurately ascertain the temperature of an envelope, and generally models of the kinetic temperature distribution are used. From a detailed treatment by Huggins et al. (1988), the temperature distribution in a C-rich CSE with a mass-loss rate of $10^{-5}\,\mathrm{M_\odot\,yr^{-1}}$ was found to follow,

$$T_\mathrm{k}(r) \sim 300 \left(\frac{10^{15}\,\mathrm{cm}}{r}\right)^{0.7} \mathrm{K}.$$

In regions which are not exposed to the interstellar UV field (i.e., shielded regions), the main heating process is friction, due to grains streaming through the outflowing gas. Cooling is provided by adiabatic expansion of the envelope, and by CO rotational lines. Other possible heating and cooling mechanisms are discussed by Truong-Bach et al. (1990).

The density of a spherically symmetric envelope is assumed to drop as $1/r^2$, although there is strong evidence for clumps of matter rather than a homogeneous distribution, as mentioned above. Recent calculations using a combination of hydrodynamical and stellar evolutionary codes have shown that the final AGB density drops off more steeply than $1/r^2$ (Schönberner & Steffen 2001), due to density variations during thermal pulses. Observations have led Sahai et al. (1998) and Volk et al. (2000) to estimate density profiles for various AGB and post-AGB stars in the region of $\rho \sim r^{-2.2\ldots-3}$.

The radiation field in an AGB CSE comes from three sources. Firstly, the star, which is either luminous ($10^4\,\mathrm{L_\odot}$) and cool ($2\,500\,\mathrm{K}$) or less luminous ($10^2\,\mathrm{L_\odot}$ or less) but hot ($10^5\,\mathrm{K}$ or more). Dust scatters starlight, and also emits heat. Finally, the interstellar radiation field, which plays a large part in determining the size of

the molecular envelope.

Envelope expansion velocity is seen to range from $\sim 3$ to $30\,\mathrm{km\,s^{-1}}$. The survey of Lewis (1991) shows that the average expansion velocity of O-rich stars is approximately $15\,\mathrm{km\,s^{-1}}$. A similar survey by Olofsson et al. (1993b) of carbon stars shows a peak in the distribution of $v_{\mathrm{exp}}$ at about $12.5\,\mathrm{km\,s^{-1}}$. Generally, it seems that $v_{\mathrm{exp}}$ increases with Main Sequence mass (Lindqvist et al. 1992; Barnbaum et al. 1991). Terminal outflow velocity is thought to be reached at $\approx 10^{15}\,\mathrm{cm}$ from the star, according to studies of maser activity (Bowers 1992).

## 1.5 Processes in the post-AGB phase

Once a star leaves the Asymptotic Giant Branch, many changes occur which leave the end product virtually unrecognisable from the initial red giant. The central star heats up, and becomes exposed, blowing off its dusty envelope. The ejected matter may be morphed into various shapes: spheres, ellipses, bipolar, hour-glass structures. These post-AGB objects are characterised by ionised regions, extended nebulosities and often high-speed winds, which appear as jets, highly collimated outflows or other exotic structures (FLIERs, etc.). The chemistry of these objects is often very different from their predecessors: typical AGB species are (photo-) destroyed and re-formed into other species.

### 1.5.1 Proto-planetary nebulae

Proto-planetary nebulae are the transition objects between the end of the AGB and planetary nebulae. A rigorous categorisation of PPNe has been given by Kwok (2001) for example, but it is usually generally accepted that PPNe are classified as objects after the cessation of mass-loss, yet before ionisation of nebulous material. This first condition is relatively difficult to ascertain observationally. However, doubly-peaked spectral energy distributions (SEDs) are usually taken as evidence for this, since the more intense infra-red peak is due to dust (Woolf & Ney 1969; Gilman 1969; Treffers & Cohen 1974). This dust cannot be stationary since the high opacity of dust grains implies that significant radiation pressure will be exerted upon them. Ionisation of the nebula is indicated by recombination lines of H and He, plus the forbidden lines of metals.

The infra-red properties of PPN can be distinctive; there are several ways in which PPNe infra-red spectra are different to either AGB spectra or PNe spectra.

Firstly, PPN continuum colour temperatures are expected to lie between those of AGB stars and PNe, that is to say in the region 150-300 K. Colour temperatures are differences in flux magnitudes at specific wavelengths. The 10 $\mu$m silicate feature in O-rich PPNe is expected to be less prominent than in AGB stars due to the decline of dust temperature and the shift of the spectral peak out to longer wavelengths. "Silicate" here is taken to mean a molecule containing $SiO_x$, for example, enstatite ($MgSiO_3$) and fosterite ($Mg_2SiO_4$). There are unidentified infra-red (UIR) emission features in the 3.4-3.5 $\mu$m range which are strongest in PPNe. They are also present in PNe, but are weaker. A suggestion for their source is the vibration of various side groups on polycyclic aromatic hydrocarbon (PAH) molecules. A surprising 21 $\mu$m feature is seen, but only in a handful of PPNe, seemingly. It is often accompanied by a 30 $\mu$m feature which is also seen in PNe and AGB stars. The 21 $\mu$m feature is of uncertain origin: several carriers have been suggested, from nanodiamonds to urea. Since this feature is seen in only C-rich objects, it seems fairly certain that the feature is organic rather than inorganic in origin. von Helden et al. (2000) tentatively suggest that the origin of this feature is TiC.

### 1.5.2 The central star

As a star proceeds along the AGB, the core is in the process of forming a hot white dwarf. The mass of this core has great implications upon the evolution of the star as a whole so much to say that further evolution is independent of the envelope (as long as thermal equilibrium is maintained; Schoenberner 1990).

At some point between the tip of the AGB and the PN phase dust-driven mass-loss will cease, and at a certain temperature (approximately 5 000–6 000 K) a radiatively-driven wind will begin. This transition is little understood. However, the evolution of the central star seems little affected by mass-loss (Schoenberner 1990).

What does seem to affect post-AGB evolution greatly is the phase of the thermal pulse cycle during which the AGB star leaves the AGB (Iben 1984). The post-AGB phase will continue relatively smoothly if the final thermal pulse (TP) occurs well before the departure of the star from the AGB. However, if the final TP occurs in close proximity to departure from the AGB, then three scenarios have been identified, and these are labelled with the acronymns AFTP, LTP and VLTP. AGB Final TP (AFTP) is the designation given to the scenario where the star leaves the AGB immediately after the final TP. If the final TP occurs early in the post-

AGB phase, then it is called a Late TP (LTP), and if it occurs much later, then it is named the Very Late TP (VLTP). Thermal pulses occur on a timescale of approximately $10^4$–$10^5$ yr, and are independent of mass-loss rate.

In the AFTP case, the final TP occurs when the envelope mass is already very close to the critical envelope mass which marks the departure of the star from the AGB. During the dredge-up, since the dredged-up mass is comparable to the envelope mass, considerable mixing occurs. If the star is O-rich at this point, the dredge-up is enough to convert it to a C-rich object. However, the carbon star formed at this point will be more C-rich than those which have become C-rich at an earlier stage. Also, a star emerging from an AFTP episode is likely to be hydrogen-deficient, with the degree of deficiency dependent on the final dredge-up process and on the final envelope mass (Herwig 2001).

The late thermal pulse (LTP) can occur up to 5 000 yr after the departure of the star from the AGB. The LTP causes a series of events which lead to the star being "born again" onto the AGB. Since, in this case, hydrogen-burning is still ongoing during the final TP, the star will not experience the violent mixing of the H-rich envelope and the He-flash convection zone. The mass-loss scenario during the second passage along the AGB is not clear. Drastic changes in abundance, and the rise of C and O to the surface could initiate an increase in dust formation and hence rapid mass-loss.

The very late thermal pulse (VLTP) is very similar to the LTP, except that events conspire to mix the H-rich material and the He-rich material, leading to violent mixing of the envelope. The timescale is longer, usually more than 5 000 years after departing the AGB. Hydrogen burning has stopped by this time, and the convective region extends throughout the whole envelope. It may be that this path explains the prescence of the [WC] central stars of planetary nebulae (Iben & MacDonald 1995). Chemical abundances in these objects are reviewed by van Winckel (1999).

### 1.5.3 The interacting stellar winds model

Several models were proposed before the present "accepted" model for the formation of planetary nebulae was introduced. The problem posed by observations of PN was: "Why don't PN fall in on themselves once ejected?". Pressure from an ionisation front (Capriotti 1973; Wentzel 1976) and radiation pressure on grains (Ferch & Salpeter 1975) were suggested, but found lacking. Mathews (1966) introduced an

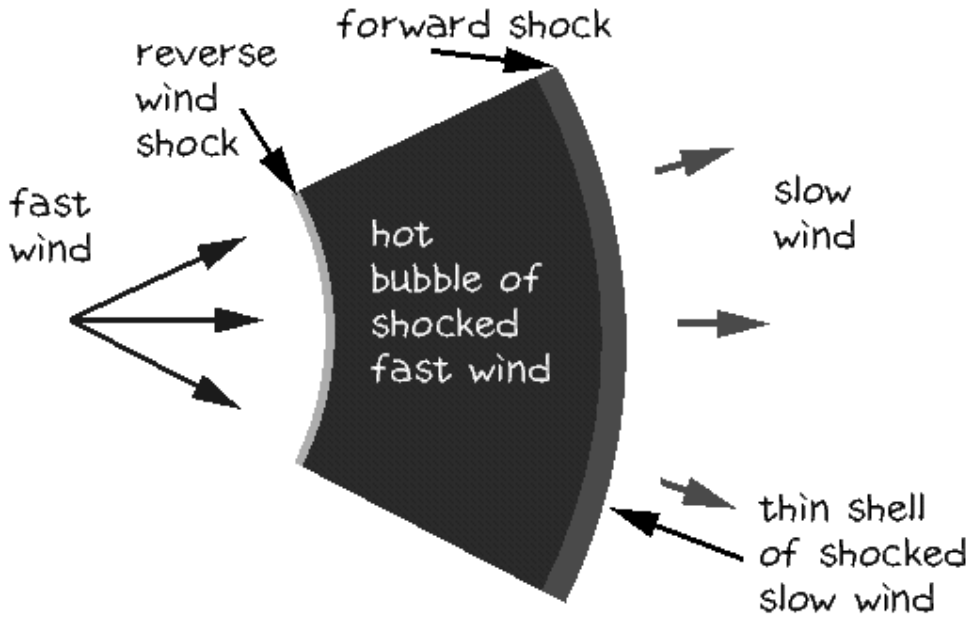


Figure 1.6: A cartoon version of the interacting stellar winds model.

idea of gas pressure as the driving force of the expansion, and a continued mass-loss to avoid the backfill.

None of these ideas completely explained the observational evidence, which was:

1. The observed expansion velocities are (much) higher than the wind velocities of AGB stars.

2. The observed densities in PN are greater than those in AGB stars

3. PNe seem to have well-defined shells with sharp inner and outer boundaries, whereas AGB stars tend to have more smooth, diffuse structures.

The most complete and henceforth accepted model was that of Kwok et al. (1978). This model was dubbed the 'interacting stellar winds' model (ISW model; Figure 1.6), for reasons which will become obvious.

Kwok et al. (1978) suggested that a planetary nebula was not a new ejection of matter, it was simply a rearrangement of matter previously ejected. This new arrangement would be due to a hot, fast wind, proceeding from the star. This wind would form only once the central star reached the required temperature for radiation pressure to drive the outflow. Since the radius of a star is now so much smaller than it was on the AGB, the terminal velocity (and also the escape velocity) will be that much higher. This new high-speed wind will collide with the AGB wind, sweeping it up into a high density ring. This is the site of the planetary nebula. The high velocity wind could have a typical velocity of $2\,000\,\mathrm{km\,s^{-1}}$.

Renzini (1981) suggested the idea of a superwind: a short phase of large mass-loss on the tip of the AGB. This was expounded in the hydrodynamical simulations of Schmidt-Voigt & Koppen (1987), which predict large nebular shell masses in the early stages of the PN. Hence the hot, ionising wind from the star would impact the superwind AGB material, which would in turn impact the AGB stellar wind. This is supported observationally by Baessgen & Grewing (1989).

Originally the ISW model was formulated for a momentum-conserving case, i.e., it is assumed that all the excess energy of the fast wind is radiated away. However, this may not be the case for all nebulae, especially when shocks are present. So the ISW model was updated for an energy-conserving case by Kwok (1982, 1983), Kahn (1983) and Volk & Kwok (1985). Shocks are present at the boundaries between the three mass components. An outer shock between the swept-up shell and the AGB wind moves outward, whilst there is an inward-moving shock between the shell and the fast wind. Since the velocity of the hot wind is so high, the inner shock also moves rapidly, and the shocked material will have a very high temperature. Cooling is very inefficient at these high temperatures. The outer shock, since the disparity in velocity is very much smaller, causes a small temperature rise, which can be efficiently cooled by the forbidden-line emission of metal ions. In general it is assumed that the region within the shell is adiabatic and the region outside is isothermal.

The density of the shell is affected by its thermal surroundings. The density jump across an adiabatic shock is small; however that across an isothermal shock depends on the square of the shock velocity and hence can be very high. This produces a dense, thin shell. In general the situation is simplified by assuming that the shell only consisits of the swept-up slow wind, and none of the hot, secondary wind.

There have been confirmations of several of the features of the ISW model. In addition to density, expansion velocity and shell structure, the model predicts: a faint halo, high velocity winds from PN central stars and thermal X-ray emission from the high-temperature bubble.

1. The halo is an AGB remnant, and has been seen in many PNe. Several haloes have been observed optically and kinematics can come from spectroscopy (e.g., Baessgen & Grewing 1989). Also, the molecular line profiles from PNe show great similarity to those from AGB stars, suggesting a common origin.

2. High speed winds were observed quite rapidly after the suggestion of the ISW

model (e.g., Heap et al. 1978).

3. X-ray emission is harder to find, largely due to the limitations of the earlier X-ray satellites. Up until recently only three PNe were observed to have X-ray emission congruous with a hot bubble. However, work by Chu et al. (2001, also see references within) with Chandra/XMM-Newton/FUSE data has produced images of X-ray emission in PNe exactly where a hot bubble would be expected to lie.

In the ISW model the central star plays an important role. Not only does it interact radiatively with the matter outside it, it mechanically pumps energy into the nebula. The central star is required to feed the energy for the dynamical evolution of the nebula.

### 1.5.4 Transition from spherical to bipolar envelopes

The morphology of post-AGB objects is a complex subject, largely because PPNe and PNe cannot be seen in three dimensions: only their projection in the plane of the sky is seen. PPNe seem to be entirely bipolar (Hrivnak et al. 2001b), whereas three general morphologies are claimed for planetary nebulae: spherical, bipolar (axially symmetric PNe having two lobes and an equatorial waist between them) and elliptical. However, bipolar and elliptical PNe may appear as spherical if seen end-on. Bipolar PNe amount to some 10–15% of all PNe (Corradi & Schwarz 1995), and are characterised by fast expansion velocities. Bipolar PNe are strongly believed to be formed from binary systems (Soker 1998a). Some percentage of elliptical PNe may also be due to binary systems.

The confounding question is how PNe become so drastically non-spherical when their AGB precursors are so uniformly spherical (at least on large scales). Opinion seems divided on whether or not the ISW model can successfully reproduce the observed morphologies. Frank & Mellema (1994) and also Frank (1999) believe that the ISW model can produce the range of shapes seen, with the hot wind amplifying asymmetries. In these models, an equatorial region of enhanced density (a disk or torus) collimates the bipolar lobes (see Fig. 1.7.a.1). Such a collimating disk has been observed in IRAS17106-3046 (Kwok et al. 2000), amongst other PPNe. Explanations of the rise of the toroidal disk come from Soker and collaborators. Soker, (Soker 1998b; Soker & Clayton 1999; Soker & Harpaz 1999) suggests that dust forms more densely over cool (AGB) stellar spots due to a weak magnetic

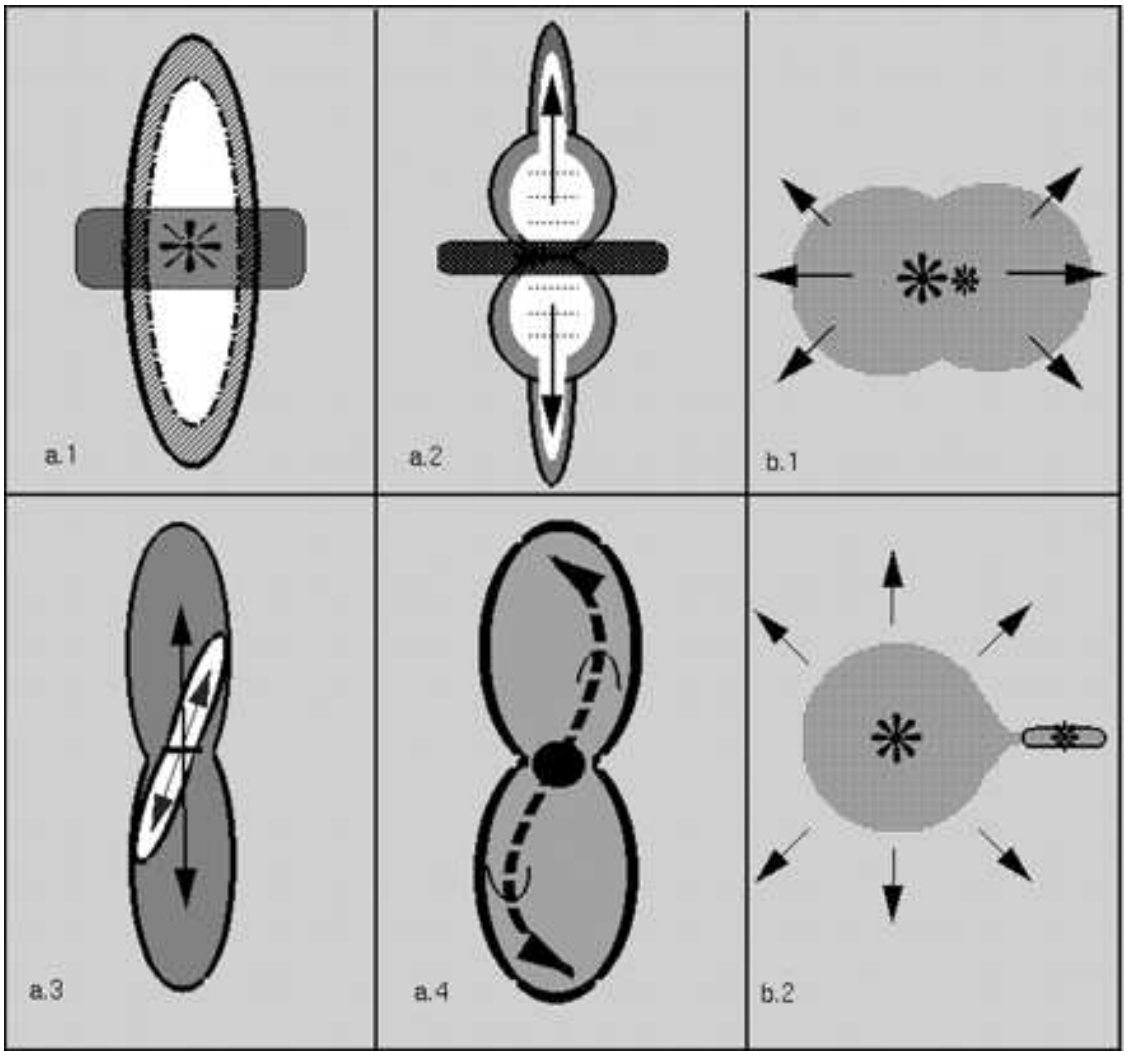


Figure 1.7: Figure from the review of Balick & Frank (2002), summarising main ideas about the shaping of PPNe. **a.1** shows a version of the ISW model, with a fast wind expanding into a slow toroid. **a.2** represents the Magnetized Wind Blown Bubble, in which a fast wind with a weak magnetic field expands into an asperical density distrubtion. **a.3** shows a disk/star magneto-centrifugal model. **a.4** represents outflows driven by episodic jets. The two panels on the right show the formation of the toroidal slow wind - **b.1** represents the common envelope evolution for short-period binaries, and **b.2** shows accretion disk formation. See Balick & Frank (2002) for further explanation and references.

field, thus enhancing the mass-loss rate in certain areas. Rotation of the AGB star concentrates these weak magnetic spots around the equator of the stellar surface, and this leads to a deviation from spherical mass-loss. The dust-enhanced areas shield radiation from material above them in the superwind phase (Soker 2000), and hence these areas become relatively cool, enabling more dust to form in the shielded regions. This mechanism is only effective when the mass-loss rate is high, i.e., in the superwind phase at the end of the AGB. This explains the appearance of non-spherical structures after the end of the AGB, rather than during. Stronger magnetic fields may be appended to this model, which result in the formation of the loops and arcs which are seen in several PNe (Soker & Harpaz 1999).

An alternative is suggested by García-Segura et al. (1999). Their work centres on the effect of a magnetic field and stellar rotation on collimation of outflows. They are able to achieve the majority of PNe morphologies with their model, and can produce ansae and jets with sufficiently strong fields. They can also produce cometary knots, as seen in the Helix nebula.

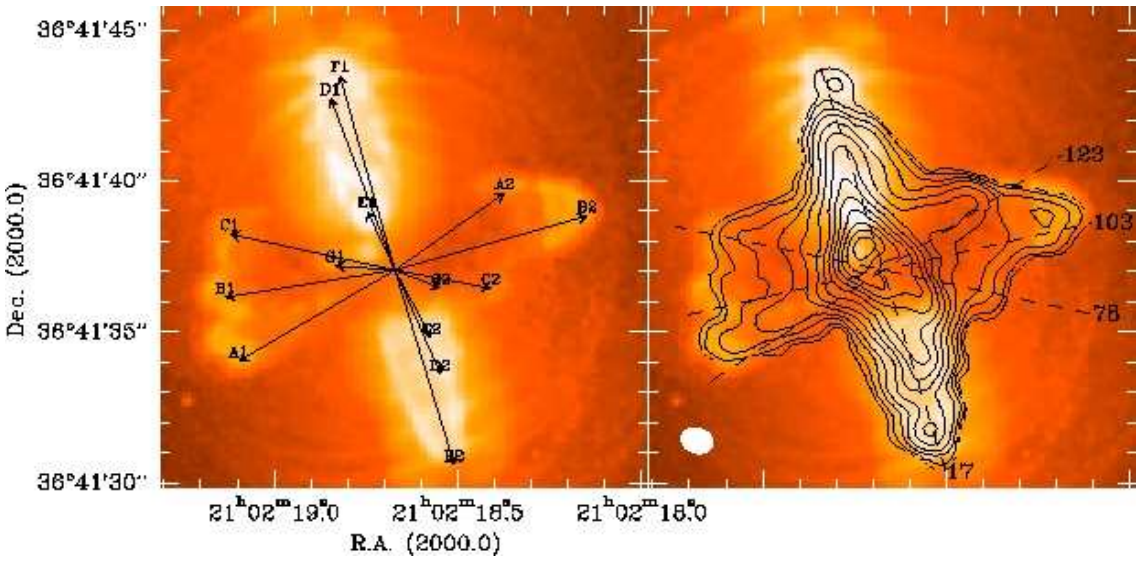


Figure 1.8: Images of the Egg nebula. For details, see Cox et al. (2000).

In addition to axisymmetric structures (such as bipolarity, etc.), point-symmetric structures are common in several PPNe. Some of the most impressive images are of the quadrupolar structure of the Egg Nebula, CRL 2688 (Fig. 1.8). This object has up to eight equatorial lobes, which are most likely to be due to four jets (Cox et al. 2000, 2001) emanating from the central star rather than an expanding, rotating equatorial disk or torus (Bieging & Nguyen-Quang-Rieu 1988b, 1996). A model

by Kastner et al. (2001), which treats equatorial expansion and rotation about the polar axis cannot account for the detailed kinematics derived from observations of $H_2$ and CO emission.

Also seen, but not so prolifically, are complete departures from symmetry in post-AGB objects. This occurs in two ways, either by jets being asymmetric (perhaps through a one-sided jet) or by departures from symmetry in the progenitor AGB envelope. Asymmetric jets require the presence of a close binary companion. In this case the outflows may be accretion disk-driven (e.g., Morris 1987; Soker 1996; Soker & Livio 1994) or magneto-hydrodynamically collimated by a sufficiently strong toroidal magnetic field (e.g., Garcia-Segura 1997; Rozyczka & Franco 1996). In the accretion disk scenario the jet may precess due to a radiation-driven instability, which warps the accretion disk (Livio & Pringle 1997).

The search for binary companions in post-AGB stars has been progressing. No binary PPNe have been detected, although this may be due to selection effects (Hrivnak et al. 2001b). This study was carried out as a radial velocity search. Bond (2000) claims that some 10% of PNe have a binary central star, with a period as short as three days. This leads from his investigation into the 16 known PNe binary systems.

### 1.5.5 Physical characteristics of the envelopes

For proto- and planetary nebulae envelope structure is somewhat different to the relatively simple AGB envelope. Mass-loss has ceased, and matter continues to expand outward from the star due to 'sweeping up' by a fast moving ionised wind. After some transition time the star heats up to $\sim$30,000 K and produces a UV flux much stronger than the ambient interstellar flux. This ionises hydrogen on the inner edge of the remnant AGB envelope, and creates a more reactive environment than in the earlier AGB phase. However this drives a rich chemistry, due to the high densities caused by the sweeping up of the remnant.

The remnant AGB CSE is generally only seen in CO emission in post-AGB sources. This is due to the fact that CO lines are the strongest and that CO is a hardy molecule, surviving long into the post-AGB phase. The CO emission from the AGB remnant remains strong enough to dominate CO emission from any other part of the star well into the PN phase.

High-speed winds are seen in several post-AGB objects (e.g., see Section A.2.1), and are seen as broad, low intensity wings in spectra. The range in velocities of these

winds is large. CRL2688, the Egg nebula, seems to have two winds with velocities of $\approx 40\,\mathrm{km\,s^{-1}}$ and $\approx 100\,\mathrm{km\,s^{-1}}$ (Young et al. 1992). This is in comparison with the AGB CSE expansion velocity of $\approx 18\,\mathrm{km\,s^{-1}}$. Incidentally, the entire structure of CRL2688 seems to be rotating at $\approx 1\,\mathrm{km\,s^{-1}}$ (Bieging & Nguyen-Quang-Rieu 1988b; Nguyen-Q-Rieu & Bieging 1990). The bipolar object OH231.8+4.2 also has high-velocity outflows. Morris et al. (1987) measure the projected outflow at $\approx 100\,\mathrm{km\,s^{-1}}$. Bowers (1991) follows the OH 1667 MHz emission throughout the star, and calculates a velocity of $\approx 10\,\mathrm{km\,s^{-1}}$ in the equatorial plane which increases to $\approx 200\,\mathrm{km\,s^{-1}}$ along the poles.

One recently-discovered feature of post-AGB objects is the presence of arcs of a spherical shape in the outer extremities. Circumstellar arcs have been discovered around eleven PNe – NGC7027, NGC 6543, Hb 5 (Bond 2000; Terzian & Hajian 2000; Balick et al. 2001), NGC3918 (Corradi et al. 2003), IC2448, NGC40, NGC1535, NGC3242, NGC6881, NGC7009, NGC7026, NGC7662 (Corradi et al. 2004) and several PPNe – CRL2688 (Sahai et al. 1998), IRAS16594-4656 (Hrivnak et al. 2001a), IRAS17150-3224 (Kwok et al. 1998), IRAS17441-2411 (Su et al. 1998), IRAS20028+3910 (Hrivnak et al. 2001a) and Roberts 22 (Sahai et al. 1999b). These arcs are circular on the sky, suggesting that they are remnants from the AGB phase of mass-loss. The arcs are seen as regions of high density, and thus are thought to be related to periods of intense mass-loss, perhaps induced by thermal pulses towards the end of the AGB, but perhaps also due to dust-gas instabilities (Deguchi 1997) or the presence of a binary companion (Mastrodemos & Morris 1999). The separation of the arcs determine a timescale of a few hundred years between each of the events which formed them.

Another type of structure found in the environs of post-AGB stars is the cometary globule. These are clumps of gas and dust which have the appearance of cometary bodies, with tails pointing away from the central star. The clearest example of these is seen in the Helix Nebula (Malin 1982; Meaburn et al. 1992). None have been seen in AGB stars, but this may just be due to the fact that they are most clearly seen against a background of ionised gas. Recent work by Huggins et al. (2003), and also Huggins et al. (1992) has used detections of CO in the most prominent globule in the Helix to determine an accurate size for these structures.

A study of maser emission as star leaves the AGB and enters the post-AGB phase is given by Lewis (1989, 1990).

## 1.6 The chemistry of AGB stars

Glassgold (1996) is a definitive starting place for learning about the processes which occur around late-type stars. Another useful reference is the review of circumstellar chemistry given by Millar (1988) in *Rate Coefficients in Astrochemistry*. Also, Omont (1991) presents a useful review. Further to those, there are individual papers which seem to come mainly from two distinct groups: that of Millar & Herbst (and Co.) and that of Glassgold & Huggins (and Co.). Both groups have developed very large chemical reaction databases which are freely available (visit, for example, `http://www.rate99.co.uk` for the latest UMIST database). These databases were intended for use in interstellar clouds, but have been, and can be, adapted for circumstellar cases. Longer chained, and more complex molecules have been added so that now models can include fullerenes, cyclic molecules (Ruffle et al. 1999), and hydrocarbon and cyanopolyyne chains of up to 23 carbon atoms (Millar et al. 2000). In the circumstellar environment recent publications have included pathways to the formation of benzene, which was the first cyclic molecule to be detected in a circumstellar envelope (Cernicharo et al. 2001b).

### 1.6.1 Chemical description of an AGB star

It is worthwhile defining what is actually meant by 'a circumstellar envelope', and why the chemistry which occurs in a CSE is so important. All stars have some circumstellar matter and hence some circumstellar chemistry (whether it be high temperature dust-formation, or low-temperature photochemistry). The most dramatic events, however, occur during the outflow of matter which occurs on the AGB. During the expansion the matter cools, and hence a more active chemistry is able to take place. This chemistry favours molecules over atoms and ions. Hence complex molecules are able to form, often at high enough abundances to be observed. The longest molecule detected in a CSE thus far is $HC_{11}N$, in the envelope of IRC+10216 (Bell et al. 1982). However, this detection has more recently been refuted by laboratory measurements of Travers et al. (1996). $HC_9N$ was first detected by Matthews et al. (1985) in the same object.

The physical characteristics of a CSE are described above. What follows is a description of a CSE with reference to the chemistry. For simplicity a spherically symmetric AGB star is usually assumed. The region of chemical interest is defined, for the purposes of this illustration, to be between $10^9$cm and $10^{19}$cm in radial distance from the centre of the star. Inside this thick shell is the core of the star,

and outside is the diffuse interstellar medium.

As an inner radius to the CSE something in the region of $3\,10^{15}$ cm is taken, which corresponds to approximately $100\,R_\star$. The outer radius is harder to define, since most observable molecules are destroyed inside the envelope, but the work of Mamon et al. (1988) has done a lot to define photodissociation radii and outer envelope radii using the properties of CO. This molecule has strong self-shielding and hence is relatively abundant at large distances. $H_2$ is not directly observable, but would be a better tracer of a circumstellar outflow since it is destroyed close to the leading edge of the wind (Glassgold & Huggins 1983).

High-frequency photons ($90 > \lambda > 300$nm) play the most important part in circumstellar chemistry. CSEs become optically thin at large distances, and hence molecules are exposed to destructive radiation. Shielding is related to mass-loss rate, in that molecules in large (massive) outflows are protected (by dust, primarily) more than those in lesser outflows. Also, for abundant molecules such as $H_2$ and CO, self-shielding may exceed that due to dust.

At some point during a molecule's path from the inner envelope to the ISM it will be photodestroyed, with a likelihood that depends on the photodissociation cross-section. This point is called the photodissociation radius. Dissociation products will then engage in chemical reactions. Chemical models of the CSE involve the 'injection' of parent molecules (typically $H_2$, He, CO, $C_2H_2$, $CH_4$, HCN, $NH_3$, $N_2$, $H_2S$, CS) at an initial radius, and their subsequent outflow. During the outflow these will be destroyed and undergo further reactions before being expelled into the ISM.

What follows is a brief description of chemistry in the stellar photosphere, which feeds the circumstellar chemistry. Three-body reactions (i.e., gas-grain reactions) are only of importance near the stellar photosphere, and therefore will only be briefly touched upon. Two- and one-body reactions can be separated into ion-molecule reactions, neutral-neutral reactions and photo-reactions (see 1.5).

#### 1.6.1.1 Photospheric chemistry

Photospheric chemistry is effectively a chemistry of high temperatures (1 000–2 000 K) and densities ($10^{12}\,\mathrm{cm}^{-3}$), and local thermodynamic equilibrium (LTE) can be fairly safely assumed. LTE occurs when chemical reaction times between all species are faster than the evolution time constants of the medium. The high temperatures overcome activation energies and the large densities allow fast three-body association reactions. Molecular abundances are dependent on elemental abundances in

the star and on heats of formation. LTE calculations of abundances have been carried out for both C-rich and O-rich stars (traditionally, Tsuji 1973) and are reliable for stable species such as CO, $H_2O$, HCN and $N_2$. CO is important since its strong bond means that the majority of carbon in O-rich stars and oxygen in C-rich stars are in the form of this molecule. Hence in the photosphere of a C-rich star the abundant molecules are CO, followed by $C_2H_2$, $N_2$, HCN and $CH_4$, while in O-rich stars they are $H_2O$, CO and $N_2$ (excluding $H_2$).

Photospheric molecules are usually observed in the infra-red, but also can be observed in millimetre studies (e.g., Cernicharo & Guelin 1987). These studies also give information on which molecules condense onto grains further out in the envelope. For instance, the Letter of Cernicharo & Guélin details detections of NaCl, AlCl, KCl. However, these molecules (and also SiS and SiO) are not detected in the main circumstellar envelope, suggesting that they condense onto dust grains.

#### 1.6.1.2 C-stars and O-stars

As mentioned in the previous section, there is a difference between the chemistry in C-rich stars and in O-rich stars. O-rich stars are relatively poorly observed compared to carbon stars because there are no massive O-rich CSEs in the close vicinity of the Sun. In O-rich stars all the available carbon is in CO, and hence it does not contribute to the formation of grains (which are primarily silicates). Yet, O-rich stars show the anomalous presence of simple organic molecules such as HNC, HCN, $H_2CO$, CN and CS (Bujarrabal et al. 1994). Also, O-bearing molecules have been found in C-rich proto-planetary nebulae (Herpin & Cernicharo 2000). No entirely sufficient explanations for these anomalies have been forthcoming, although some possible contributing factors are discussed later.

Observationally, whether a star is carbon- or oxygen-rich seems best determined by observations of HCN and SiO lines. Rather than determine abundances from the lines, which has a large degree of inaccuracy, it seems possible just to take the ratio of line intensities as an indicator. In O-rich CSEs SiO is abundant, while there is little HCN due to the lack of carbon, which is tied up in CO molecules. In C-rich environments the opposite is expected: HCN is abundant, and SiO is scarce due to all the oxygen being part of CO. Observations confirm this and produce quite a nice result: in papers by Olofsson et al. (1998) and Bujarrabal et al. (1994) some 19 O-rich objects and 6 C-rich objects were surveyed. The $I_{\mathrm{HCN},J=1-0}/I_{\mathrm{SiO},v=0,J=2-1}$ ratio produced two clear and distinct groups, such that the O-rich stars had a ratio in the range 0.05-0.3, and the C-rich stars had a ratio in the range 3-10. To determine

the actual C/O ratio is more difficult, and can not yet be effectively done from circumstellar data.

Models of O-rich envelopes usually focus on the masering molecules, $H_2O$, OH and SiO. Results of models (e.g., Nejad & Millar 1988) show the importance of neutral-neutral reactions in comparison to C-rich envelopes. Neutral chemistry is more important because OH is the most abundant reactive species in the envelope. Since neutral chemistry is so pronounced, the temperature profile of the CSE and activation energies for the reactions become all the more important. OH is produced mainly by the photodissociation of $H_2O$. Water has a large photodissociation cross-section, and hence also self-shields. A summary is given by Mamon et al. (1987). As radial distance increases, the external radiation field becomes important, and OH becomes predominant. OH can react with a large number of species: its reaction with O produces $O_2$, and its reaction with CO produces $CO_2$. The latter reaction has an energy barrier, and can only proceed in favourable conditions. Similarly SO reacts to give $SO_2$. SiO is formed by the gas-phase reaction between Si and the OH radical.

In addition to OH, $C^+$ is important in O-rich envelopes. It is formed in the photodissociation of CO. CO is fairly unreactive with gas-phase species, and its loss can be assumed to be solely due to photodissociation (Mamon et al. 1988). $C^+$ helps to explain the observations of HCN in O-rich envelopes. For instance,

$$\begin{aligned} C^+ + NH_3 &\longrightarrow H_2NC^+ + H \\ N + CH_3 &\longrightarrow HCN + H_2 \end{aligned}$$

produce some of the species observed. Appreciable abundances of HCN can only arise if $CH_4$ is also abundant, and the photodissociation rate of $N_2$ is large. Other carbon-containing species do form, and a recent Letter (Duari et al. 1999) shows that this may be due to shock chemistry in the inner envelope.

In the inner envelope, before abundances of OH build up, cosmic ray ionisation produces $H_3^+$, and hence $HCO^+$ and $H_3O^+$ (through reactions with CO and $H_2O$, respectively). The abundance of $H_3O^+$ is heavily dependent on mass-loss rate (Mamon et al. 1987).

Carbon-rich CSEs show a greater variety of molecules, due to the ease that the excess carbon atoms form bonds. This fact also explains the presence of long carbon chain molecules: polyacetylenes (e.g., $C_8H$; Cernicharo & Guelin 1996), cyanopolyynes (e.g., $HC_9N$; Bell et al. 1992) and sulfuretted chains (e.g., $C_3S$;

Cernicharo et al. 1987; Bell et al. 1993), to name but a few.

The CSEs of many carbon stars have been accurately mapped, and show 'shells' of molecules, for example, of cyanopolyynes. In this family the smaller molecules (e.g., $HC_3N$) are found closer to the star, with the larger molecules (e.g., $HC_9N$) further out, with abundance peaks which proceed from inner to outer as the number of C atoms increases (see Sect. 1.6.2.5).

To summarise, although cosmic-rays and UV photons play an active part in the chemistry of an O-rich envelope, large amounts of OH radicals make neutral chemistry important. In general, the chemistry of a C-rich CSE is very similar to that which occurs in a dark interstellar cloud. Ion-molecule and photo-reactions dominate chemical processes.

### 1.6.2 Carbon chemistry and IRC+10216

Carbon, which is usually able to form four bonds per atom, makes carbon-rich circumstellar environments sites of more varied chemistry than their oxygen-rich counterparts. The prototypical carbon star is IRC+10216, which because of its proximity (some 200 pc) and brightness (the brightest C-star at 5 $\mu$m) is the best studied carbon star. Over 50 species have been detected in this object, not including isotopomers or isomers (see Sect. A.1.1 and also Glassgold 1999). This far surpasses the number detected in any other late-type star. For this reason, the term "carbon chemistry" is used with implied but unmentioned reference to IRC+10216 (this is justified further in Chapter 2). Its chemical 'peculiarities' include a high degree of unsaturated hydrocarbons, high fractional abundances of complex molecules, and a very low HNC/HCN ratio. Also, there has been only one ion and one methyl-containing species detected in the CSE, despite sensitive searches.

Carbon chemistry in the outer parts of the envelope is assumed to begin with a handful of parent species, which are 'injected' from the inner regions of the star, where LTE conditions are present. These species are assumed to be, in approximate order of abundance, $H_2$, He, CO, $C_2H_2$, $N_2$, HCN, $CH_4$, $NH_3$. Others, such as $H_2S$, may also be parent species. The initial abundances of these molecules are difficult to determine, and are taken from infrared observations or LTE calculations.

For a C-rich envelope such as that of IRC+10216, the species $C_2H_2$ and $C_2H_2^+$ play a crucial role. These two species are the basis for the reactions which form the $C_3$- and $C_4$-bearing hydrocarbons, as well as longer chains. The production of large chains involves carbon-insertion reactions with $C^+$, fixation reactions involving C

and condensation reactions involving acetylene and its ion. Also, the methyl ion is useful because its slow reaction with $H_2$ means that it is abundant enough to react with the more minor species in the envelope. Methyl cyanide, the single methyl-containing species detected, is formed by the reaction between $CH_3^+$ and HCN. $HCO^+$ is the only ion detected, and formed by proton-transfer reactions. It is very sensitive to the cosmic-ray ionisation rate (see Glassgold et al. 1987). The low HNC/HCN ratio seems to be due to the ion-molecule chemistry rather than initial LTE abundances (Nejad & Millar 1987).

#### 1.6.2.1 Hydrocarbons

Hydrocarbons usually make up the vast majority of molecules in a carbon-rich environment, and their formation is largely due to acetylene, $C_2H_2$, its ion, $C_2H_2^+$ and its daughter, $C_2H$ and their reactions with $C_2H$ and $C_2$ (for instance in Eqs. 1.3 and 1.4). These pathways lead to higher abundances of even-numbered hydrocarbons ($C_{2n}H_m$) over odd-numbered hydrocarbons ($C_{2n+1}H_m$). The even-numbered hydrocarbons then react to produce cyanopolyynes, making the abundance of cyanopolyynes dependent on the initial abundance of $C_2H_2$. Also, reactions of $C_2H_2$ and $C_2H$ with atomic carbon lead to the formation of bare carbon clusters, which are important in the synthesis of long chains. Below are listed the general synthesis reactions for larger hydrocarbons.

$$C_2H + C_nH_2 \longrightarrow C_{n+2}H_2 + H \quad (1.3)$$

$$C_2 + C_nH \longrightarrow C_{n+2} + H_2 \quad (1.4)$$

$$C_n^- + C_m \longrightarrow C_{n+m}^- + h\nu \quad (1.5)$$

$$C_2H_2^+ + C_nH_m \longrightarrow C_{n+2}H_{m+1}^+ + H \quad (1.6)$$

Methane, $CH_4$, is another parent molecule involved in hydrocarbon formation. Synthesis proceeds via $C^+$ insertion reactions or condensation reactions, e.g.

$$CH_4 + C^+ \longrightarrow C_2H_2^+ + H_2$$

$$CH_4 + C^+ \longrightarrow C_2H_3^+ + H$$

$$CH_4 + CH_3^+ \longrightarrow C_2H_5^+ + H_2$$

Chain-lengthening then proceeds via further condensation reactions with $C_2H_2$ and $C_2H$, plus reactions with C and $C^+$. The methyl ion, $CH_3^+$, reacts slowly with $H_2$,

and thus is relatively long-lived. This leaves it available to react with more minor species, for instance, with HCN in the following reaction,

$$CH_3^+ + HCN \longrightarrow CH_3CNH^+ + h\nu. \tag{1.7}$$

This leads to methyl cyanide, which is the only methyl-bearing species detected in IRC+10216 to date. This is expected, since reaction 1.7 is the most rapid of the methyl ion reactions.

#### 1.6.2.2 Cyanopolyynes

Acetylene ($C_2H_2$) and both HCN and its radical, CN, initiate cyanopolyyne synthesis. The high abundance of acetylene implies that the fundamental reaction is:

$$CN + C_2H_2 \longrightarrow HC_3N + H \tag{1.8}$$

$HC_3N$ is also a product of the reaction between HCN and $C_2H$, i. e.,

$$HCN + C_2H \longrightarrow HC_3N + H$$

Further reactions with $C_2H$ produce long carbon-chain molecules, in a reaction that can be generalised as:

$$HC_nN + C_2H \longrightarrow HC_{n+2}N + H,$$

for $n \geq 3$. Also reactions between CN and hydrocarbons,

$$CN + C_nH_2 \longrightarrow HC_{n+1}N + H$$

result in cyanopolyynes.

The cyanopolyynes in the series up to $HC_9N$ have been detected in IRC+10216, all with very high column densities, showing that a very efficient formation mechanism must exist in such late-type stars. Howe & Millar (1990) found that reaction (1.8) was the most effective of those above.

#### 1.6.2.3 $HCO^+$ and HNC

Both $HCO^+$ and HNC appear in CSEs as the result of proton-transfer reactions. $HCO^+$ is indicative of the amount of high-energy ionisation in a CSE since it is a descendant of $H_3^+$, which is itself a product of the ionisation of $H_2$:

$$H_3^+ + CO \longrightarrow HCO^+ + H_2.$$

Similarly, HNC arises from the dissociative recombination of $HCNH^+$, which is produced via

$$MH^+ + HCN \longrightarrow HCNH^+ + M$$

where the $MH^+$ could be any of these protonated species: $H_3^+$, $N_2H^+$, $HCO^+$, $C_2H_2^+$ and $C_2H_3^+$. Also the reaction

$$C^+ + NH_3 \longrightarrow HNCH^+ + H$$

leads to HNC production (and not to HCN). IRC+10216 has a low HNC/HCN ratio compared to dense interstellar clouds, due to the ion-molecule chemistry of the outflow, which allows HNC formation only over a limited region.

#### 1.6.2.4 Benzene

Benzene formation in IRC+10216 is negligible (Millar et al. 2000); the low abundance of atomic hydrogen means that the formation route assumed for interstellar clouds (McEwan et al. 1999) is not efficient under the conditions present in carbon stars on the AGB. The interstellar formation mechanism is:

$$C_4H_2^+ + H \longrightarrow C_4H_3^+ + h\nu \quad (1.9)$$

$$C_4H_3^+ + C_2H_2 \longrightarrow c\text{-}C_6H_5^+ + h\nu \quad (1.10)$$

$$\text{or} \quad C_4H_3^+ + C_2H_3 \longrightarrow c\text{-}C_6H_5^+ + H \quad (1.11)$$

$$c\text{-}C_6H_5^+ + H_2 \longrightarrow c\text{-}C_6H_7^+ + h\nu \quad (1.12)$$

$$c\text{-}C_6H_7^+ + e \longrightarrow c\text{-}C_6H_6 + H \quad (1.13)$$

Benzene is destroyed by reactions with a number of positive ions, including $He^+$, $N_2H^+$, $H_3^+$, $HCO^+$, $C_2H_3^+$, $CH_5^+$ and $C_3H_5^+$.

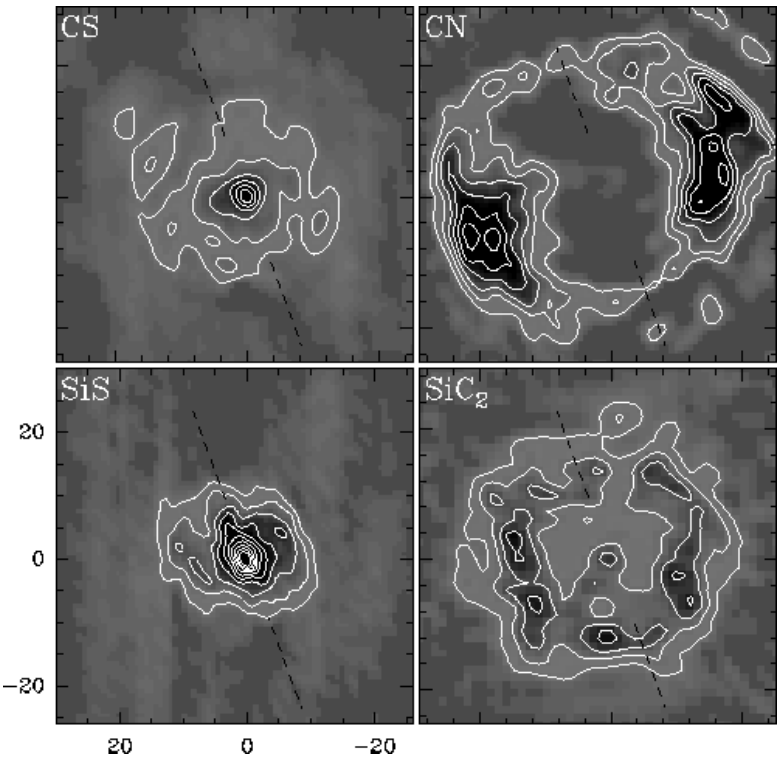


Figure 1.9: The distribution of various molecules in IRC+10216, obtained with the IRAM interferometer.

#### 1.6.2.5 Spatial distributions

The spatial distribution of a particular molecule is a very good constraint for chemical modelling. However, observationally, this requires telescopes or arrays of telescopes which are able to resolve the object in question. At present, single-dish radio telescopes do not have the sub-arcsecond resolution required, and even interferometers such as the IRAM array are limited by the proximity of suitable targets. Having said this, much of our understanding of the distribution of species throughout a CSE has come from interferometer observations, mostly of IRC+10216. Bieging & Nguyen-Quang-Rieu (1988a) used the Hat Creek Interferometer to look at IRC+10216, and found hollow shells of molecules ($C_2H$, HNC, $C_3N$ and $HC_3N$), proving that these molecules are mainly formed in the outer regions of the CSE. This work has been supplemented by Guélin and Lucas (Lucas & Guélin 1999; Guélin et al. 2000; Lucas et al. 1995, see Figures 1.9, 1.10, 1.11).

#### 1.6.2.6 Timescales

Timescales are very important to circumstellar chemistry. Two timescales are useful: a dynamic timescale, dependent on the physical properties of the envelope, and

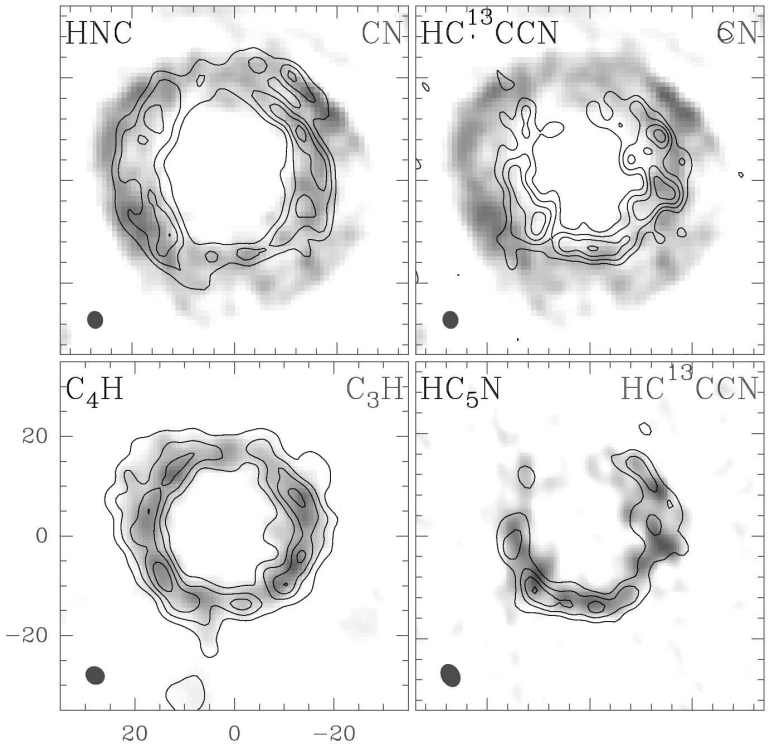


Figure 1.10: The distribution of various molecules in IRC+10216, obtained with the IRAM interferometer. Grayscale corresponds to the species in the upper right corner of each panel, contours to the species in the upper left (Lucas & Guélin 1999).

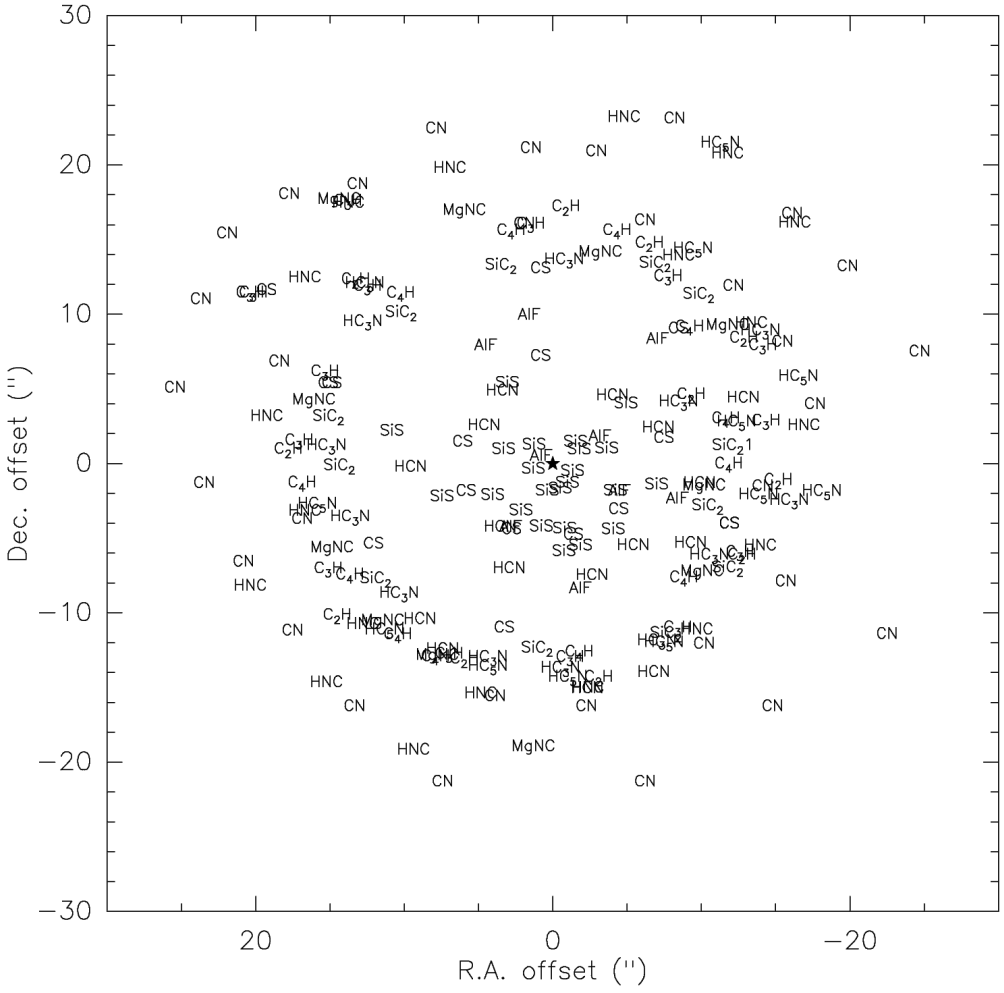


Figure 1.11: A plot of the distribution of various molecules in IRC+10216, where the maximum in emission of each species is labelled with the name of that species (Lucas & Guélin 1999).

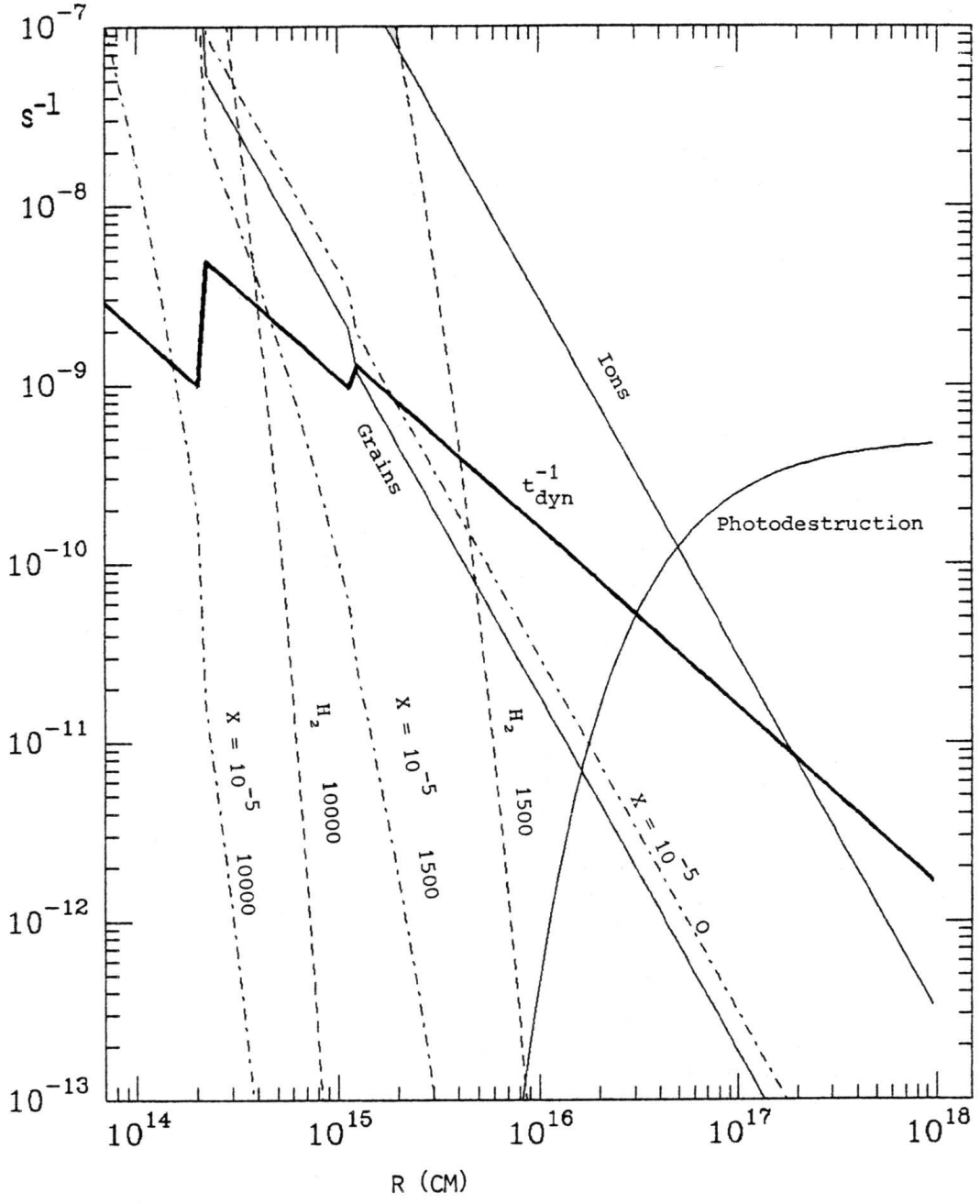


Figure 1.12: $\tau_{\rm chem}$ versus radius for the envelope of IRC+10216. For details of the model, see Omont (1985). Various time constants and reaction rates ($s^{-1}$) are shown. Assumed typical rates are the following: photodissociation, $5 \times 10^{-10} \exp(-7 \times 10^{16}/r)$; grains, $6 \times 10^{-17}\, n_{\rm H}$; ions, $10^{-9}\, X\, n_{\rm H}$ with $X = 10^{-5}$; reactions with $H_2$, $5 \times 10^{-12}\, n_{\rm H} \exp(-T/T_{\rm B})$ with $T_{\rm B} = 1\,500$ and $10\,000$ K; reactions with other abundant species (e.g., $C_2H_2$), $10^{-11}\, X\, n_{\rm H} \exp(-T/T_{\rm B})$ with $X = 10^{-5}$ and $T_{\rm B} = 0, 1\,500$ and 10 000K, and with $X = 10^{-4}$ and $T_{\rm B} = 0$.

a chemical timescale, dependent on chemical properties. The dynamical timescale is usually taken to be the expansion time of the envelope, i.e.,

$$\tau_{\rm dyn} = \tau_{\rm exp} = \frac{r}{v_{\rm exp}}$$

The chemical timescale depends on the reactants: for a photoprocess,

$$\tau_{\rm chem} \approx \frac{1}{G},$$

where $G$ is the local photorate (c.f., $G_0$, the interstellar ionisation rate, $1.3{\times}10^{-17}\,{\rm s}^{-1}$). For a reaction between two species, species A destroys species B on a timescale which is

$$\tau_{\rm chem} \approx \frac{1}{k_{\rm AB} n_{\rm A}}.$$

where $k_{\rm AB}$ is the rate coefficient for the reaction and $n_{\rm A}$ the density of species A relative to the number of hydrogen nuclei.

Typically, the chemistry of the envelope occurs where these two timescales, $\tau_{\rm dyn}$ and $\tau_{\rm chem}$, are of the same order of magnitude. Commonly this order of magnitude is $10^{10}\,{\rm s}$, and hence the 'chemical zone' is at intermediate distances from the star (Fig. 1.12). In order to be important, chemical processes must occur on a timescale faster than that of the expansion. The expression $\tau_{\rm chem} \lesssim \tau_{\rm dyn}$ defines a radius, $r_f$, outside of which destruction reactions can be considered 'frozen out'. Explicitly it is given by:

$$\begin{aligned} r_f &= 1.3\,10^{56}\,{\rm cm}\ \dot{M}_{\rm H}\ k\ x_i\ /\ v_{exp}^2 \\ &= 1.3\,10^{16}\,{\rm cm}\ \dot{M}_{\rm H-5}\ k_{-10}\ x_{i-5}\ /\ v_{exp\,15}^2. \end{aligned}$$

$x_i$ is the abundance of the reactant $i$, and $\dot{M}_{\rm H-5}, k_{-10}, x_{i-5}$ and $v_{exp\,15}^2$ are in typical units, e.g., $v_{exp}$ in units of $15\,{\rm km\,s}^{-1}$. The interplay of the various factors in calculating $r_f$ are shown in Fig. 1.12 for the envelope of IRC+10216.

## 1.7 The chemistry of post-AGB stars

The basis of the chemistry of post-AGB stars is the chemistry of AGB stars, without the complexity of large species. The expansion of the AGB circumstellar envelope means that matter is diluted, and thus exposed to dissociating UV radiation from the interstellar medium, and also from the increasingly hot central star. The stellar UV radiation field will reach at least $10^5$ times the ambient interstellar flux during

the PPN phase, but this will decrease to 10–100 times in the fully evolved PN stage, due to the decrease in luminosity of the star.

The molecules seen in PPNe and PNe give information on various processes which have occurred in the history of the particular object.

### 1.7.1 General trends

There are several species which are abundant in AGB envelopes, but are rarely observed (if at all) in PNe. CS is abundant in AGB envelopes, and although it can be enhanced by shocks in PPNe (Kasuga et al. 1997; Mitchell 1984) is generally of lower abundance, and unobserved in PNe until recently (Chapter 6). $HC_3N$, SiO and $SiC_2$ demonstrate the same sort of behaviour, decreasing in abundance going into the PPNe phase. Bachiller et al. (1997a) show that the species CS, $HC_3N$, SiO and $SiC_2$ are present in PPNe, but have been destroyed in all the PNe in their sample.

Carbon monoxide, the major gas-phase molecule after hydrogen in AGB envelopes, is not as widely seen in PNe as in earlier stages of evolution. Some 44 PNe have been detected in CO, whereas another 80 remain undetected, according to the review of Bachiller (1997). The 44 include some evolved PNe, showing that molecular gas does survive for some time in a highly-ionising environment.

Acetylene, $C_2H_2$, which is abundant in the envelopes of AGB stars is not seen in any large quantities in post-AGB objects. The $C_2H_2$ molecular band observed in carbon star spectra is not seen in post-AGB sources, implying chemical changes in the gas, perhaps incorporation into polycyclic aromatic hydrocarbons (PAHs).

In contrast, $HCO^+$ becomes greatly enhanced in the PPNe phase, and yet it is very difficult to explain why. Theoretical models of post-AGB objects all fail to produce enough $HCO^+$ by at least an order of magnitude, if not more (e.g., Woods et al. 2003a; Howe et al. 1994). $HCO^+$ is only efficiently formed by ionising radiation, and yet the levels of cosmic ray ionising radiation required to produce the desired levels of $HCO^+$ result in the destruction of most other molecules. This is due to the fact that cosmic rays induce UV photons in their interaction with $H_2$; these photons dissociate and ionise molecules. It seems that perhaps soft X-rays, as suggested by Deguchi et al. (1992), may contribute to $HCO^+$ levels in PNe, but this cannot be the complete solution due to the lower X-ray fluxes found in evolved PNe, compared to younger objects. Woods et al. (2003a) (also see Chapter 3) considered whether X-rays might be the responsible for the high level of $HCO^+$. Their treatment was

quite general – a treatment where X-rays are solely responsible for ionisation (and not dissociation) might prove interesting. This approach was taken in the chemical model explained in Chapter 5. However, a still more thorough treatment needs to be made. Another contribution may be from some sort of surface-surface interaction, as investigated by Viti et al. (2002).

CN abundances show an upward trend with increasing evolutionary status, as do HNC abundances. HNC is formed by the dissociative recombination of $HCNH^+$, and hence should be present at higher levels in more evolved objects, where the ionisation level is higher. HCN is more or less constant, and $HCO^+$ only becomes abundant in PNe.

### 1.7.2 Abundance ratios

HCN and CN can be used to give an idea of the evolutionary status of a PPN. In AGB stars, HCN is usually more abundant than CN. However, as HCN becomes increasingly photodissociated, its daughter, CN, becomes increasingly abundant; i.e., one would expect the CN/HCN ratio to increase with evolutionary age, in the early post-AGB phase (see Fig. 5.2 in Chapter 5). A similar effect is seen in the comparison of HCN and HNC. In CRL618, for example, the column densities of HCN and HNC are comparable (Herpin & Cernicharo 2000), whereas in IRC+10216 (a less evolved object) HCN is far more abundant that HNC. Average ratios in PNe by Bachiller et al. (1997a) are given as CN/HCN = 9, HNC/HCN = 0.5 and $HCO^+$/HCN = 0.5. In AGB stars these ratios are approximately 0.5, 0.005 and 0.0005, respectively.

The HCN/CO ratio should also give some indication of age, since CO self-shields to some degree, and HCN is photodissociated in preference. This would cause the HCN/CO ratio to decrease with time. However, it may be difficult to compare a number of objects which includes a mixture of O-rich and C-rich stars, since they may have had a different HCN/CO ratio when they started to move off the AGB.

The $^{12}CO/^{13}CO$ is low ($< 10$) in several PPNe (e.g., Kahane et al. 1992) compared to $10 < {}^{12}CO/{}^{13}CO < 25$ in evolved PNe (Palla et al. 2000; Bachiller et al. 1997a), $10 < {}^{12}CO/{}^{13}CO < 40$ in compact PNe (Josselin & Bachiller 2003) and $10 < {}^{12}CO/{}^{13}CO < 50$ in AGB stars (e.g., Kahane et al. 1988). A similar, although slightly narrower, range for AGB stars is found by Greaves & Holland (1997). As examples, the carbon-rich AGB star IRC+10216 has a $^{12}CO/^{13}CO$ ratio of 45 (Woods et al. 2003b), CRL618 has a $^{12}CO/^{13}CO$ ratio of 5 (Balser et al. 2002)

and OH231.8+4.2 has a ratio of ∼10 (Morris et al. 1987; Bujarrabal et al. 1994), NGC7027 (a young PN) has a $^{12}CO/^{13}CO$ ratio of 31 (Balser et al. 2002) and NGC2346 (an evolved PNe) has a $^{12}CO/^{13}CO$ ratio of 23 (Palla et al. 2000). This ratio may be an indicator of evolution (since $^{13}CO$ self-shields less than $^{12}CO$), but it is more likely to be an indicator of a star's nucleosynthesis history (e.g., Kahane et al. 1992, 1988). The significance of this ratio, and the related $^{12}C/^{13}C$ ratio, is discussed by Schöier & Olofsson (2000).

### 1.7.3 Shock chemistry

$HCO^+$ and SiO can indicate shocked gas (e.g., Mitchell & Watt 1985), and although the presence of high levels of $HCO^+$ do not necessarily imply shocks (see above), the presence of high levels of SiO does give a much better indication of shocked gas. The theory behind shock formation of SiO is discussed for the case of interstellar clouds by Hartquist et al. (1980), and supported by observations by Ziurys & Friberg (1987). SiO abundances can be substantially enhanced by shocks by many orders of magnitude in cold environments such as OMC-1: shocks are thought to destroy silicate grains, releasing Si atoms, which then become locked up in SiO molecules. A similar situation can be found in bipolar outflows, and a particular case is discussed by Gueth et al. (1998).

Molecules such as $NH_3$, and $H_2O$ in CRL618 (Herpin & Cernicharo 2000) and in NGC7027 (Liu et al. 1996), are also shock-formed and are seen at high abundances in post-AGB objects.

### 1.7.4 Chemically interesting objects

As far as particular objects go, the carbon-rich PPNe CRL2688 and CRL618 are chemically abundant. CRL2688 has been detected in 22 species, with CRL618 having a similar number of observed species (see Sect. A.2.1). OH231.8+4.2 is an interesting O-rich PPN (Morris et al. 1987; Sanchez Contreras et al. 1998).

NGC7027 is the most well-studied PN, simply because most other PNe have relatively weak lines. NGC7027 has been detected in lines of HCN, CN, $C_3H_2$, $HCO^+$, $N_2H^+$ and $CO^+$ (see Bachiller 1997, and references therein). HCN, HNC, $HCO^+$ and CN have been seen in a handful of other sources: NGC2346 (not CN, Bachiller et al. 1989), NGC6072 and IC4406 (Cox et al. 1992). M1-16 is also somewhat chemically rich (Sahai et al. 1994). Apart from these few objects, PNe are not particularly abundant in molecules other than CO and $H_2$.

### 1.7.5 Molecular line observations of post-AGB objects

The work of Herpin & Cernicharo and others (Herpin & Cernicharo 2000; Cernicharo et al. 2001a,b, also, various papers in preparation) has done a lot for the study of the chemical nature of PPNe. Their detections of new molecules in CRL618 prompted the work of Woods et al. (2002, 2003b, see Chapter 3). Also, an observational study of evolutionary stage (Herpin et al. 2001, 2002) shows that the importance of the role of UV flux increases with age, whereas the importance of shocks decreases, with the strongest shocks occurring just after leaving the AGB phase. It seems that most of the $^{12}$CO, $^{13}$CO and HCN emission in the early post-AGB stages comes from these shock regions (Herpin et al. 2002).

The paper of Bachiller et al. (1997a) did much to improve the lack of observations of molecular lines in PNe: Their overview of AGB stars, PPNe and PNe includes observations of CRL2688 and CRL618, and also NGC7027, NGC6720 (the Ring nebula), M4-9, NGC6781 and NGC7293 (the Helix nebula). Their survey included new detections of CN, HCN, HNC, $HCO^+$ and CS in these objects. They showed that abundances of most species are approximately constant throughout the PNe phase, regardless of evolutionary status, and that the following ratios are reached: CN/HCN=9, HNC/HCN=0.5, $HCO^+$/HCN=0.5.

Josselin & Bachiller (2003) performed a survey of 7 compact PNe and found very similar (column density) ratios: CN/HCN=2.6, HNC/HCN=0.4, $HCO^+$/HCN=0.5. The CN/HCN ratio seems to be a good indicator of evolutionary status, since compact PNe are thought to be intermediate between PPNe and evolved PNe (like the Ring or Helix, for example).

Various other papers have looked at individual objects: Sahai et al. (1994) looked at the PPN M1-16, Cox et al. (1992) looked at the two PNe IC4406 and NGC6072, for example. Bujarrabal et al. (2001) catalogued CO emission from all the known PPNe.

### 1.7.6 Chemical models of post-AGB objects

The study of the chemistry of proto-planetary nebulae is still somewhat preliminary. Models are necessarily simplistic, and have not managed to accurately describe all observations. Useful observations are sparse, partly due to lack of input from models. It seems clear that to progress in this field, models which combine shock chemistry, X-rays, and a high UV flux from the central star are needed. And even these considerations may not be enough: it may be necessary to tackle boundaries

between torus and wind, and clump and wind, to really reproduce PPNe chemistry accurately.

Attempts to date to describe post-AGB chemistry have taken several different approaches. Following a theoretical approach, initial papers focusing on somewhat "abstracted" aspects from Howe et al. (1992, 1994) have been complimented by more "holistic" approaches from Hasegawa et al. (2000), Ali et al. (2001), Redman et al. (2003) and Cernicharo (2004). Observationally, papers from Josselin & Bachiller (2003), Herpin et al. (2002), Bachiller et al. (1997a) and Cox et al. (1992) have helped further present knowledge in this area.

The approach of Howe et al. was first to tackle the interaction of the AGB superwind with the AGB envelope (Howe et al. 1992), and the effect of the shocks inherent in that interaction. The conclusions were that the interplay of ionisation and shocks produced many small species, and that larger molecules survived (from the AGB) either due to heavy clumping, or via grain-surface reactions. The follow up (Howe et al. 1994) was to investigate the formation of molecules in clumps – in this case in PNe. They showed that CO and $H_2$ would survive heavy photon-bombardment, and that the daughter-products of ionisation (viz. $C_2$ and CN) should be abundant.

Hasegawa et al. (2000) decided to follow the work of Yan et al. (1999), and look at NGC7027, a young PN. Yan et al. (1999) used a thin, dense shell model to try and reproduce *ISO* observations. Again, these authors invoked the interaction of the superwind with envelope (ISW model) and shocks to explain the CO lines seen with *ISO*. They find that many of the small ions and molecules observed with *ISO* are from a hot (1 000 K) central PDR, but others are also from the cooler (200 K) shocked regions. The Hasegawa et al. (2000) model adopts a thin, high-density shell (of constant density), but surrounds this with an outer region, with an inverse-square law density profile. These authors manage to explain the presence of small molecules and ions (e.g., CH, $CH^+$, OH), without needing shock chemistry; a high temperature (800 K) and photoionisation is all that is required. Also, the high abundances of $HCO^+$ seen in NGC7027, which is in general a problem for post-AGB chemistry, are reasonably well explained through photon-dominated region (PDR) chemistry[2]. The formation chain of $HCO^+$ is determined to be $O \longrightarrow OH \longrightarrow CO^+ \longrightarrow HCO^+$, followed by recombination to form CO and then destruction to give O. The oxygen-bearing molecules seen in NGC7027 are a side-

[2]The neutral gas in PDRs has been studied by Hollenbach & Natta (1995) and Sternberg & Dalgarno (1995)

effect of this chain, explaining the presence of oxygen-bearing molecules in some carbon-rich environments. Hasegawa & Kwok followed up their model with an observational paper on NGC7027 (Hasegawa & Kwok 2001).

Ali et al. (2001) have developed models for various PNe, and find the same abundance of small molecules as Howe et al. (1992). They treat X-rays (as an enhancement of cosmic-ray ionisation) and clumps. One success of the model is a fairly accurate calculation of the $HCO^+$ abundance, something unusual in post-AGB chemical models.

Redman et al. (2003) model the chemistry in a slow wind in the transition from the AGB phase through to the PN phase. They model both a smooth wind and a clumpy wind, and find that molecules are destroyed rapidly in the smooth wind, whereas in a clumpy wind larger species survive until the PN phase. They also identify molecules which could be "tracers" of clumps, for example, CS. Redman et al. (2003) conclude that clumps must form early, in the AGB phase.

Some work as yet unpublished by Cernicharo (2004) attempts to explain the detection of complex species in the PPN, CRL618. The model is composed of three different zones at different radial distances, with different temperatures, densities and chemical compositions. These three zones represent the pre-PDR of CRL 618. The model does a good job of explaining the observed abundances of $H_2CO$, OH, $H_2O$, $CO_2$ and [OI], again through the liberation of atomic oxygen from the dissociation of CO. It also predicts that the fractional abundance of $HC_3N$ will be similar to that of HCN in the early stages of post-AGB evolution. Woods et al. (2003b, also Chapter 3) find, however, that $HC_3N$ can be up to order of magnitude greater in abundance than HCN at a specified radial distance. The model of Cernicharo (2004) also has problems producing benzene in the required amount, something which is not found in Woods et al. (2003b). The Cernicharo model predicts abundances of $10^{-7}$ for $CH_2CHCN$, a species recently detected in CRL 618 (Cernicharo et al., in prep.). Woods et al. (2003b) only predict a peak abundance of $10^{-10}$ for this species. Timescales are very short in this model: Peak abundances are reached in 0.2 years, consecutive polyynes have equal abundances after a few years. All species in the inner zone are photodissociated within 2 years.

What seems to be common to a lot of post-AGB chemical models is a drastic over-abundance of CS. This is true of Hasegawa et al. (2000), Ali et al. (2001) and Woods et al. (2003b). There seems to be some destruction mechanism that is unaccounted for, or a destruction rate which is imprecise. Further problems, identified by Josselin & Bachiller (2003) are that $HCO^+$ abundances are higher

than those predicted by models (this seems to be general to post-AGB models), and that the calculated CN/HCN ratio is a factor $\sim$5 higher than the observed value (in compact PNe).

# AGB stars

# Chapter 2

# The chemistry of carbon stars

## 2.1 Introduction

The study of Asymptotic Giant Branch (AGB) stars is interesting because the processing of a star from a red giant to a white dwarf is so dramatic: many different processes are working at changing, say, the central star from a temperature of around 3 000 K to something approaching 100 000 K, or changing a physically large star into something rather small. The chemistry during this transition, too, is interesting, and perhaps the most interesting since a star's formation. The matter driven out from the star in the form of mass-loss, via the complex process of radiation pressure upon dust grains, which in turn are coupled to gases, cools enough to allow complex molecules to form, and to allow the interaction of these molecules with each other, and with external radiation to form new species.

In many cases the most interesting period of chemical activity does not happen until the end of the AGB phase. It is here that the thermal pulses of a star's atmosphere will determine whether it finishes its life as a carbon-rich (C-rich) object, or an oxygen-rich (O-rich) one. C-rich stars show a greater variety of molecules, probably due to the way the carbon atom bonds (the carbon atom being able to form four covalent bonds, the oxygen atom only two). Carbon atoms are also found to bond together, to form long chains.

Many long chain molecules, and other complex carbon- and also oxygen-bearing

species, are found in what has become the prototypical C-rich star, IRC+10216 (CW Leo). This star lies at a very close proximity to the solar system, which makes it an ideal C-rich object for study: observationally, molecular lines are strong, and the close proximity allows high-resolution interferometric maps of molecular distributions to be made (e.g., Bieging & Tafalla 1993; Dayal & Bieging 1993, 1995; Gensheimer et al. 1995; Guelin et al. 1993, 1996; Lucas et al. 1995; Lucas & Guélin 1999, some examples are given in Chapter 1). Good quality data in turn lends itself to the construction of good quality models: dust models (see Men'shchikov et al. 2001) and chemical models (e.g., Millar et al. 2000) have been developed for IRC+10216 for over 30 years.

There have been many surveys of the chemical nature of AGB stars, but most tend to concentrate on whether stars are C-rich or O-rich, or neither, or whether stars are $^{13}$C-rich, or poor. Olofsson et al. (1993a) observed some 40 stars and detected a handful of species other than CO. The sample of Bujarrabal et al. (1994) included 16 carbon stars, with up to ten molecular lines observed in each. A more recent survey by Olofsson et al. (1998) detected 22 carbon stars in up to 6 molecular lines. Very few surveys gauge the similarity of say, carbon stars, or oxygen stars. The following investigation of reasonably high-mass-losing carbon-rich AGB stars in both the northern and southern skies attempts to test the use of IRC+10216 (which is included in the survey) as a chemical "benchmark" of C-richness - can chemical models of IRC+10216 really be applied to other C-rich stars, or is each carbon star unique?

## 2.2 Investigation

To answer this question, up to 51 molecular lines were observed (of which 47 were clearly detected) in the sample of 7 high-mass-losing carbon stars. The surveyed stars are listed in Table 2.1; a literature study of each star is available in Appendix A. Observations were made during the period 1987 – 1996 with the Onsala Space Observatory (OSO) 20 m telescope in the northern hemisphere, and the Swedish-ESO Submillimetre Telescope (SEST) in the southern hemisphere. IRC+10216 was observed with each telescope to give a strong basis of comparison throughout the whole sample.

The SEST was equipped with two acousto-optical spectrometers (HRS, 86 MHz bandwidth with 43 kHz channel separation and 80 kHz resolution; LRS, 500 MHz bandwidth with 0.7 MHz channel separation and a resolution of 1.4 MHz). The re-

Table 2.1: Positions, periods ($P$), calculated distances ($D$), modelled stellar and dust temperatures ($T_\star$, $T_\mathrm{d}$) and luminosities ($L_\star$, $L_\mathrm{d}$), of the sample of carbon stars.

| IRAS No. | Other cat. name | J2000 Co-ords. |
|---|---|---|
| 07454-7112 | AFGL4078 | 07:45:02.8 −71:19:43 |
| 09452+1330 | IRC+10216 | 09:47:57.4 +13:16:44 |
| 10131+3049 | CIT6 | 10:16:02.3 +30:34:19 |
| 15082-4808 | AFGL4211 | 15:11:41.9 −48:20:01 |
| 15194-5115 | — | 15:23:05.0 −51:25:58 |
| 23166+1655 | AFGL3068 | 23.19.12.4 +17:11:35 |
| 23320+4316 | IRC+40540 | 23:34:28.0 +43:33:02 |

| Name | $P$ [days] | $L$ [$\mathrm{L}_\odot$] | $D$ [pc] | $T_\star$ [K] | $T_\mathrm{d}$ [K] | $L_\mathrm{d}/L_\star$ |
|---|---|---|---|---|---|---|
| IRAS07454-7112 | — | 9 000[a] | 710 | 1 200 | 710 | 4.3 |
| IRC+10216 | 630 | 9 600 | 120 | — | 510 | — |
| CIT6 | 640 | 9 700 | 440 | 1 300 | 510 | 6.7 |
| IRAS15082-4808 | — | 9 000[a] | 640 | — | 590 | — |
| IRAS15194-5115 | 580 | 8 800 | 600 | 930 | 480 | 2.2 |
| AFGL3068 | 700 | 7 800 | 820 | — | 1 000 | — |
| IRC+40540 | 620 | 9 400 | 630 | 1 100 | 610 | 6.6 |

(a) Assumed value.

ceivers used were dual polarisation Schottky receivers at both 3 and 1.3 mm wavelength. Typical system temperatures above the atmosphere were 400–500 K and 1000-1800 K, respectively.

The OSO 20 m telescope uses two filter banks (MUL B, 64 MHz bandwidth with a channel width of 250 kHz; MUL A, 512 MHz bandwidth and a channel width of 1 MHz). The receiver used was a horizontally, linearly polarised SIS receiver with a typical system temperature of 400–500 K above the atmosphere.

All observations were performed using the dual beam switching method, which places the source alternately in two beams, and yields very flat baselines. Beam separation was in both cases about 11′.5. Calibration was done with the standard chopper-wheel method. Main-beam efficiencies and FWHM beam widths are given in Table 2.2 for both telescopes.

A total of 196 lines were detected in the sample. 47 transitions of 24 molecular species were detected, and upper limits for another 95 relevant transitions were also obtained, including another three species ($C_2S$, $C_3S$ and SO). Table 2.3 lists the de-

Table 2.2: Beam widths and efficiencies of the SEST and OSO 20 m.

| | SEST 15 m | | Onsala 20 m | |
|---|---|---|---|---|
| Frequency [GHz] | FWHM ['] | $\eta_{\rm mb}$ | FWHM ['] | $\eta_{\rm mb}$ |
| 86 | 57 | 0.75 | 44 | 0.58 |
| 100 | 51 | 0.73 | 39 | 0.53 |
| 115 | 45 | 0.70 | 33 | 0.48 |
| 230 | 23 | 0.50 | — | — |
| 265 | 21 | 0.42 | — | — |

tections in all seven sources, together with their peak and integrated intensities. If a line has a hyperfine structure, the frequency and intensity of the strongest component is listed, and the integrated intensity is the sum over all hyperfine components. Values of $T_{\rm mb}$ (the corrected antenna temperature, $T_{\rm A}^{\star}$, divided by the main-beam efficiency, $\eta_{\rm mb}$) for lines where no detection was made are the rms noise values; these are indicated by a "less than" sign in the table. Integrated intensities of lines which were not clearly detected are calculated using the following expression,

$$I_{\rm v} \leq 3\sigma \left(\sqrt{2}\,\sqrt{2\frac{{\rm v}_{\rm exp}}{\Delta {\rm v}_{\rm res}}}\right) \Delta {\rm v}_{\rm res} = 3\sigma (2n)^{1/2} \Delta {\rm v}_{\rm res}. \qquad (2.1)$$

where $\sigma$ is the rms noise in the spectrum, ${\rm v}_{\rm exp}$ the expansion velocity, $\Delta {\rm v}_{\rm res}$ the velocity resolution of the spectrum and $n$ the number of channels covering the line width. This gives a somewhat optimistic view of the integrated intensity of the line, and hence any fractional abundance calculation using this value will be strictly an upper limit.

Almost all lines observed in IRC+10216 by the SEST were observed in the same source with the OSO 20 m telescope. The majority of those which were not are due to the lack of a 1.3 mm receiver at OSO. A large proportion of these lines were observed in the remaining six sources. Some example spectra are shown in Figs. 2.1-2.2; the remaining spectra are available online (see Appendix B).

Table 2.3: Detected lines in the sample of carbon stars

| Molecule | Transition | Frequency | IRC+10216 (SEST) | | IRC+10216 (OSO) | | IRAS15194-5115 | | IRAS15082-4808 | |
|---|---|---|---|---|---|---|---|---|---|---|
| | | | $T_{\rm mb}$ | $\int T_{\rm mb}{\rm d}v$ | $T_{\rm mb}$ | $\int T_{\rm mb}{\rm d}v$ | $T_{\rm mb}$ | $\int T_{\rm mb}{\rm d}v$ | $T_{\rm mb}$ | $\int T_{\rm mb}{\rm d}v$ |
| | | [MHz] | [K] | [K km s$^{-1}$] | [K] | [K km s$^{-1}$] | [K] | [K km s$^{-1}$] | [K] | [K km s$^{-1}$] |
| $HC_5N$ | J=32–31 | 85201.348 | 0.15 | 4.78 | — | — | < 0.01 | < 0.13 | < 0.01 | < 0.10 |
| $C_3H_2$ | $2_{1,2}$–$1_{0,1}$ | 85338.905 | 0.11 | 2.49 | — | — | 0.02 | 0.84 | < 0.01 | < 0.10 |
| $C_4H$ | N=9–8, J=19/2–17/2 | 85634.00 | 0.20 | 9.60 | — | — | — | — | < 0.01 | < 0.05 |
| $C_4H$ | N=9–8, J=17/2–15/2 | 85672.57 | 0.20 | 9.60 | — | — | — | — | < 0.01 | < 0.05 |
| $C_2S$ | 6(7)–5(6) | 86181.413 | < 0.03 | < 0.46 | < 0.04 | < 0.76 | < 0.07 | < 0.11 | < 0.04 | < 0.06 |
| $H^{13}CN$ | J=1–0 | 86340.184 | 3.23 | 87.20 | 3.86 | 114.14 | 0.57 | 20.93 | 0.09 | 3.06 |
| $C_3S$ | J=15–14 | 86708.379 | < 0.02 | < 0.30 | < 0.03 | < 0.65 | < 0.01 | < 0.08 | < 0.01 | < 0.06 |
| SiO | J=2–1 | 86846.998 | 0.71 | 20.40 | 0.95 | 24.48 | 0.16 | 5.33 | 0.07 | 1.84 |
| $HN^{13}C$ | J=1–0 | 87090.859 | < 0.04 | < 0.62 | — | — | 0.02 | 1.11 | < 0.01 | < 0.11 |
| $C_2H$ | N=1–0 | 87316.925 | 0.52 | 41.60 | 0.66 | 49.48 | 0.13 | 11.50 | 0.04 | 4.04 |
| HCN | J=1–0 | 88631.847 | 7.80 | 190.93 | 9.14 | 214.04 | 0.55 | 15.33 | 0.37 | 11.26 |
| $C_3N$ | N=9–8, J=19/2–17/2 | 89045.59 | 0.31 | 9.19 | — | — | < 0.01 | < 0.07 | < 0.01 | < 0.09 |
| $C_3N$ | N=9–8, J=17/2–15/2 | 89064.36 | 0.31 | 9.19 | — | — | < 0.01 | < 0.07 | < 0.01 | < 0.09 |
| $HC_5N$ | J=34–33 | 90525.892 | 0.16 | 2.58 | < 0.03 | < 0.67 | — | — | < 0.01 | < 0.10 |
| $HC^{13}CCN$ | J=10–9 | 90593.059 | 0.09 | 1.98 | < 0.03 | < 0.34 | 0.02 | 0.76 | < 0.01 | < 0.05 |
| $HCC^{13}CN$ | J=10–9 | 90601.791 | 0.09 | 1.98 | < 0.03 | < 0.34 | 0.02 | 0.76 | < 0.01 | < 0.05 |
| HNC | J=1–0 | 90663.543 | 0.74 | 26.49 | 0.58 | 17.22 | 0.08 | 3.72 | 0.05 | 1.70 |
| SiS | J=5–4 | 90771.546 | 1.14 | 35.54 | 1.07 | 39.47 | 0.05 | 2.78 | 0.03 | 1.58 |
| $HC_3N$ | J=10–9 | 90978.993 | 2.42 | 64.59 | 2.00 | 52.63 | 0.09 | 3.71 | 0.11 | 4.15 |
| $^{13}CS$ | J=2–1 | 92494.299 | 0.07 | 2.97 | — | — | 0.06 | 2.67 | < 0.01 | < 0.10 |
| $SiC_2$ | $4_{0,4}$–$3_{0,3}$ | 93063.639 | 0.46 | 14.60 | — | — | — | — | 0.03 | 0.40 |
| $HC_5N$ | J=35–34 | 93188.127 | 0.12 | 5.50 | — | — | — | — | < 0.01 | < 0.10 |
| $C_4H$ | N=10–9, J=21/2–19/2 | 95150.32 | 0.19 | 6.08 | 0.18 | 8.75 | 0.04 | 1.95 | 0.02 | 0.47 |
| $C_4H$ | N=10–9, J=19/2–17/2 | 95188.94 | 0.19 | 6.08 | 0.18 | 8.75 | 0.04 | 1.95 | 0.02 | 0.47 |
| $SiC_2$ | $4_{2,2}$–$3_{2,1}$ | 95579.389 | 0.32 | 10.73 | — | — | — | — | < 0.01 | < 0.08 |
| $C^{34}S$ | J=2–1 | 96412.982 | 0.15 | 5.66 | — | — | — | — | — | — |
| CS | J=2–1 | 97980.968 | 2.92 | 81.23 | 4.06 | 118.89 | 0.37 | 15.21 | 0.25 | 8.44 |
| $C_3H$ | $^2\Pi_{1/2}$,9/2–7/2 | 97995.450 | 0.18 | 11.27 | 0.28 | 14.54 | 0.01 | 0.64 | < 0.01 | < 0.11 |
| SO | J=3–2 | 99299.879 | < 0.02 | < 0.25 | — | — | — | — | — | — |
| $HC_3N$ | J=11–10 | 100076.389 | 2.21 | 53.84 | — | — | — | — | — | — |
| $HC^{13}CCN$ | J=12–11 | 108710.523 | 0.09 | 2.34 | 0.14 | 1.22 | 0.01 | 0.39 | < 0.01 | < 0.03 |
| $HCC^{13}CN$ | J=12–11 | 108721.008 | 0.09 | 2.34 | 0.14 | 1.22 | 0.01 | 0.39 | < 0.01 | < 0.03 |
| $^{13}CN$ | N=1–0 | 108780.201 | 0.11 | 8.56 | 0.24 | 6.07 | 0.02 | 2.18 | < 0.01 | < 0.05 |
| $C_3N$ | N=11–10, J=23/2–21/2 | 108834.27 | 0.39 | 11.76 | 0.64 | 18.00 | 0.01 | 0.68 | 0.02 | 0.63 |
| $C_3N$ | N=11–10, J=21/2–19/2 | 108853.02 | 0.39 | 11.76 | 0.64 | 18.00 | 0.01 | 0.68 | 0.02 | 0.63 |
| SiS | J=6–5 | 108924.267 | 1.10 | 30.00 | 1.86 | 52.40 | 0.05 | 2.44 | 0.04 | 1.14 |
| $HC_3N$ | J=12–11 | 109173.634 | 2.03 | 52.39 | — | — | 0.07 | 3.16 | 0.08 | 2.79 |
| $C^{18}O$ | J=1–0 | 109782.160 | 0.02 | 0.76 | — | — | — | — | < 0.01 | < 0.17 |
| $^{13}CO$ | J=1–0 | 110201.353 | 1.69 | 26.62 | 2.50 | 36.40 | 0.31 | 14.93 | 0.06 | 1.82 |
| $CH_3CN$ | 6(1)–5(1) | 110381.404 | 0.09 | 4.77 | < 0.05 | < 1.42 | < 0.01 | < 0.18 | < 0.01 | < 0.23 |
| $C_2S$ | 8(9)–7(8) | 113410.207 | < 0.03 | < 0.48 | < 0.07 | < 1.96 | < 0.02 | < 0.53 | < 0.01 | < 0.11 |
| CN | N=1–0 | 113490.982 | 3.43 | 238.43 | 3.88 | 310.20 | 0.13 | 16.43 | 0.19 | 14.71 |
| CO | J=1–0 | 115271.204 | 10.29 | 269.43 | 20.83 | 542.71 | 1.27 | 55.86 | 1.11 | 36.71 |
| $SiC_2$ | $5_{0,5}$–$4_{0,4}$ | 115382.38 | 0.80 | 21.43 | 1.60 | 39.38 | 0.07 | 2.66 | 0.03 | 0.82 |
| $C^{18}O$ | J=2–1 | 219560.319 | 0.15 | 4.21 | — | — | — | — | — | — |
| $^{13}CO$ | J=2–1 | 220398.686 | 3.85 | 79.62 | — | — | 0.90 | 35.58 | 0.15 | 5.76 |
| $CH_3CN$ | 12(0)–11(0) | 220747.268 | 0.17 | 2.80 | — | — | < 0.05 | < 1.01 | < 0.03 | < 0.48 |
| CN | N=2–1 | 226874.564 | 2.55 | 231.18 | — | — | 0.15 | 17.06 | 0.20 | 11.32 |
| CO | J=2–1 | 230538.000 | 34.60 | 799.00 | — | — | 4.20 | 150.00 | 2.54 | 69.40 |
| CS | J=5–4 | 244935.606 | 16.57 | 405.53 | — | — | 0.77 | 32.34 | 0.47 | 10.89 |
| HCN | J=3–2 | 265886.432 | 45.10 | 1010.24 | — | — | 4.69 | 139.76 | 0.88 | 20.83 |

Table 2.3: (*cont.*) Detected lines in the sample of carbon stars

| Molecule | Transition | Frequency | IRAS07454-7112 | | CIT6 | | AFGL3068 | | IRC+40540 | |
|---|---|---|---|---|---|---|---|---|---|---|
| | | | $T_{\rm mb}$ | $\int T_{\rm mb}{\rm d}v$ | $T_{\rm mb}$ | $\int T_{\rm mb}{\rm d}v$ | $T_{\rm mb}$ | $\int T_{\rm mb}{\rm d}v$ | $T_{\rm mb}$ | $\int T_{\rm mb}{\rm d}v$ |
| | | (MHz) | (K) | (K km s$^{-1}$) | (K) | (K km s$^{-1}$) | (K) | (K km s$^{-1}$) | (K) | (K km s$^{-1}$) |
| $C_2S$ | 6(7)–5(6) | 86181.413 | $<0.01$ | $<0.07$ | $<0.02$ | $<0.36$ | $<0.02$ | $<0.44$ | $<0.01$ | $<0.28$ |
| $H^{13}CN$ | J=1–0 | 86340.184 | 0.07 | 1.45 | 0.15 | 3.13 | 0.13 | 3.76 | 0.13 | 3.85 |
| $C_3S$ | J=15–14 | 86708.379 | $<0.01$ | $<0.07$ | $<0.01$ | $<0.23$ | $<0.02$ | $<0.47$ | $<0.01$ | $<0.21$ |
| SiO | J=2–1 | 86846.998 | 0.03 | 0.52 | 0.17 | 3.16 | $<0.02$ | $<0.47$ | 0.04 | 0.94 |
| $HN^{13}C$ | J=1–0 | 87090.859 | $<0.01$ | $<0.08$ | $<0.01$ | $<0.23$ | $<0.02$ | $<0.47$ | $<0.01$ | $<0.25$ |
| $C_2H$ | N=1–0 | 87316.925 | $<0.01$ | $<0.09$ | 0.10 | 5.81 | 0.09 | 5.94 | $<0.01$ | $<1.78$ |
| HCN | J=1–0 | 88631.847 | 0.19 | 4.43 | 0.77 | 18.07 | 0.39 | 8.97 | 0.26 | 8.24 |
| $C_3N$ | N=9–8, J=19/2–17/2 | 89045.59 | $<0.01$ | $<0.07$ | — | — | — | — | — | — |
| $C_3N$ | N=9–8, J=17/2–15/2 | 89064.36 | $<0.01$ | $<0.06$ | — | — | — | — | — | — |
| $HC_5N$ | J=34–33 | 90525.892 | 0.02 | 0.06 | $<0.01$ | $<0.21$ | $<0.01$ | $<0.21$ | $<0.02$ | $<0.37$ |
| $HC^{13}CCN$ | J=10–9 | 90593.059 | 0.01 | 0.13 | $<0.01$ | $<0.11$ | $<0.01$ | $<0.10$ | 0.08 | 0.35 |
| $HCC^{13}CN$ | J=10–9 | 90601.791 | 0.01 | 0.13 | $<0.01$ | $<0.11$ | $<0.01$ | $<0.10$ | 0.08 | 0.35 |
| HNC | J=1–0 | 90663.543 | 0.02 | 0.50 | 0.13 | 2.95 | 0.06 | 1.18 | 0.09 | 1.42 |
| SiS | J=5–4 | 90771.546 | 0.03 | 1.07 | 0.04 | 0.59 | 0.04 | 0.59 | 0.15 | 4.11 |
| $HC_3N$ | J=10–9 | 90978.993 | 0.06 | 1.39 | 0.19 | 5.17 | 0.12 | 3.37 | 0.19 | 6.16 |
| $^{13}CS$ | J=2–1 | 92494.299 | $<0.01$ | $<0.04$ | — | — | — | — | — | — |
| $SiC_2$ | $4_{0,4}$–$3_{0,3}$ | 93063.639 | 0.01 | 0.13 | — | — | — | — | — | — |
| $HC_5N$ | J=35–34 | 93188.127 | $<0.01$ | $<0.04$ | — | — | — | — | — | — |
| $C_4H$ | N=10–9, J=21/2–19/2 | 95150.32 | $<0.01$ | $<0.03$ | $<0.01$ | $<0.13$ | — | — | — | — |
| $C_4H$ | N=10–9, J=19/2–17/2 | 95188.94 | $<0.01$ | $<0.03$ | $<0.01$ | $<0.13$ | — | — | — | — |
| $SiC_2$ | $4_{2,2}$–$3_{2,1}$ | 95579.389 | $<0.01$ | $<0.06$ | — | — | — | — | — | — |
| CS | J=2–1 | 97980.968 | 0.13 | 2.53 | 0.67 | 16.91 | 0.14 | 3.93 | 0.30 | 9.56 |
| $C_3H$ | $^2\Pi_{1/2}$,9/2–7/2 | 97995.450 | $<0.01$ | $<0.09$ | $<0.02$ | $<0.55$ | $<0.01$ | $<0.31$ | $<0.02$ | $<0.45$ |
| $HC^{13}CCN$ | J=12–11 | 108710.523 | 0.01 | 0.08 | 0.05 | 0.44 | $<0.01$ | $<0.14$ | $<0.01$ | $<0.09$ |
| $HCC^{13}CN$ | J=12–11 | 108721.008 | 0.01 | 0.08 | 0.05 | 0.44 | $<0.01$ | $<0.14$ | $<0.01$ | $<0.09$ |
| $^{13}CN$ | N=1–0 | 108780.201 | 0.01 | 0.73 | 0.05 | 4.21 | $<0.01$ | $<0.28$ | $<0.01$ | $<0.18$ |
| $C_3N$ | N=11–10, J=23/2–21/2 | 108834.27 | 0.01 | 0.23 | 0.10 | 2.19 | 0.05 | 1.34 | 0.03 | 0.70 |
| $C_3N$ | N=11–10, J=21/2–19/2 | 108853.02 | 0.01 | 0.23 | 0.10 | 2.19 | 0.05 | 1.34 | 0.03 | 0.70 |
| SiS | J=6–5 | 108924.267 | 0.03 | 0.88 | 0.19 | 3.62 | 0.15 | 2.23 | 0.07 | 1.91 |
| $HC_3N$ | J=12–11 | 109173.634 | 0.06 | 1.48 | — | — | — | — | — | — |
| $^{13}CO$ | J=1–0 | 110201.353 | 0.09 | 2.10 | 0.40 | 5.90 | 0.17 | 9.33 | 0.22 | 4.39 |
| $CH_3CN$ | 6(1)–5(1) | 110381.404 | $<0.01$ | $<0.12$ | $<0.01$ | $<0.29$ | $<0.03$ | $<0.83$ | $<0.03$ | $<0.72$ |
| $C_2S$ | 8(9)–7(8) | 113410.207 | $<0.01$ | $<0.10$ | $<0.03$ | $<0.89$ | $<0.02$ | $<0.53$ | $<0.02$ | $<0.64$ |
| CN | N=1–0 | 113490.982 | 0.17 | 10.30 | 1.12 | 61.84 | 0.09 | 5.97 | 0.41 | 21.84 |
| CO | J=1–0 | 115271.204 | 1.16 | 25.57 | 3.52 | 105.00 | 2.08 | 47.08 | 1.94 | 41.88 |
| $SiC_2$ | $5_{0,5}$–$4_{0,4}$ | 115382.38 | $<0.01$ | $<0.24$ | 0.23 | 6.71 | $<0.02$ | $<0.62$ | $<0.03$ | $<0.75$ |
| $^{13}CO$ | J=2–1 | 220398.686 | 0.25 | 7.34 | — | — | — | — | — | — |
| $CH_3CN$ | 12(0)–11(0) | 220747.268 | 0.04 | 0.67 | — | — | — | — | — | — |
| CN | N=2–1 | 226874.564 | 0.41 | 20.59 | — | — | — | — | — | — |
| CO | J=2–1 | 230538.000 | 2.60 | 50.00 | — | — | — | — | — | — |
| CS | J=5–4 | 244935.606 | 0.49 | 8.12 | — | — | — | — | — | — |
| HCN | J=3–2 | 265886.432 | 0.50 | 8.82 | — | — | — | — | — | — |

## 2.3 Data analysis

These data were put to two primary uses: firstly, a non-LTE radiative transfer model was used to calculate mass-loss rates and expansion velocities from the CO line emission. Secondly, the calculated mass-loss rates, expansion velocities, and the integrated intensities taken from the data were used to calculate the fractional abundances of molecular species.

### 2.3.1 Radiative transfer modelling

In order to further constrain the radiative transfer modelling, the JCMT public archive was searched for complementary CO and $^{13}$CO line observations (generally, higher $J$ transitions). In addition, interferometric observations of the CO($J$=1–0) brightness distribution around some of the sample stars have been performed (Neri et al. 1998) using the Plateau de Bure interferometer (PdBI), France.

The Monte Carlo method (Bernes 1979) is used to determine the steady-state level populations of the CO molecules in the envelope as a function of distance from the star, using the statistical equilibrium equations. In addition, the code simultaneously solves the energy balance equation including the most relevant heating and cooling processes. Heating is dominated by collisions between the dust and gas except in the outermost parts of the envelope where the photoelectric effect effectively heats the envelope. Cooling is generally dominated by molecular line cooling from CO but adiabatic cooling due to the expansion of the envelope is also important. The excitation analysis allows for a self-consistent treatment of CO line cooling.

The observed circumstellar CO line emission is modelled taking into account 50 rotational levels in each of the fundamental and first excited vibrational states. The energy levels and radiative transition probabilities from Chandra et al. (1996) are used. The collisional rates of CO with $H_2$ by Flower (2001) have been adopted assuming an ortho-to-para ratio of 3. For temperatures above 400 K the rates from Schinke et al. (1985) were used and further extrapolated to include transitions up to $J$=50. The same set of collisional rates were used for all CO isotopomers.

The envelopes are assumed to be spherically symmetric and to expand at a constant velocity and the model includes the radiation emitted from the central star. Dust present around the star will absorb parts of the stellar radiation and re-emit it at longer wavelengths. For simplicity, the central radiation field is represented by one or two blackbodies at temperatures and luminosities given in Table 2.1 and is

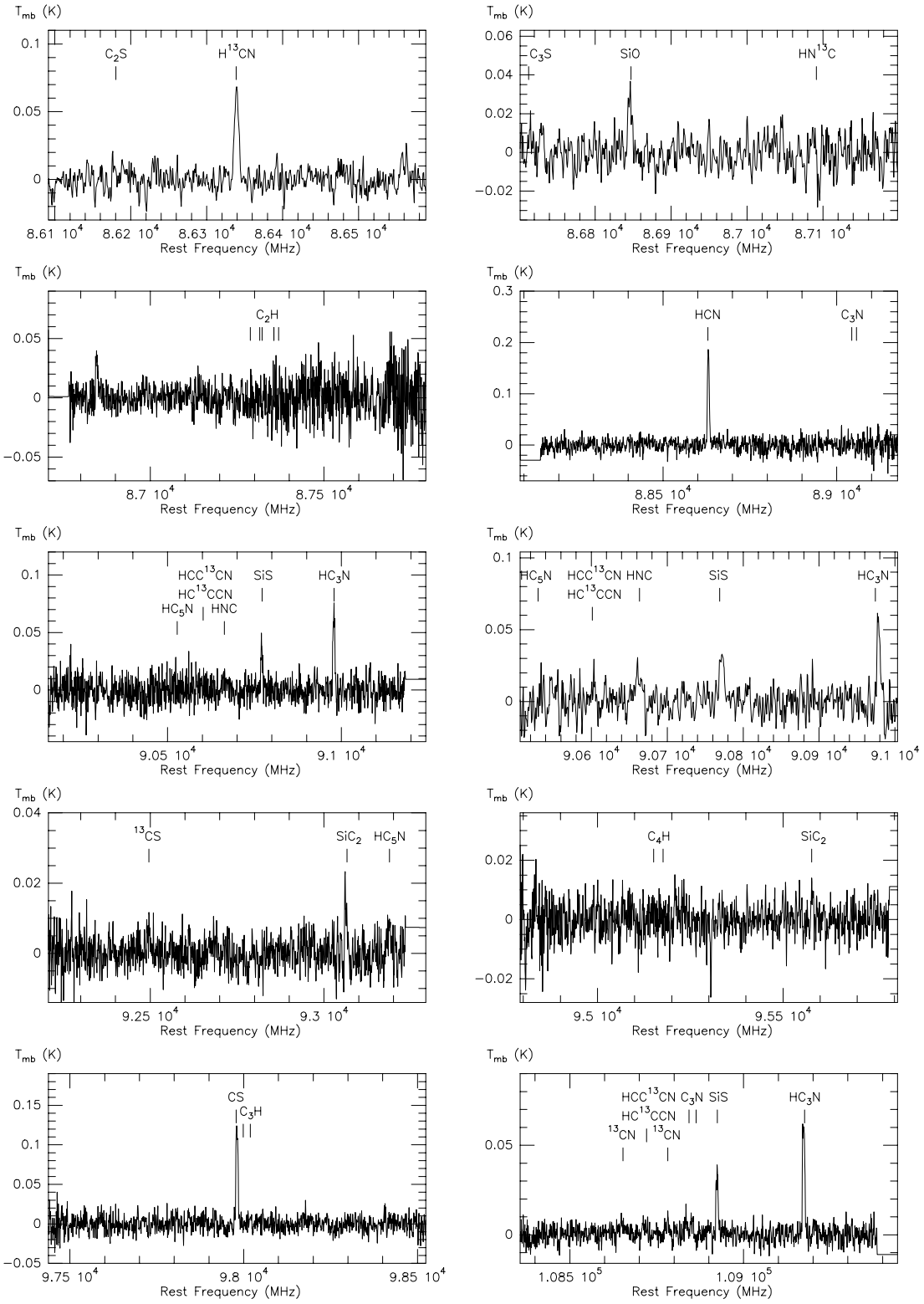


Figure 2.1: Low-resolution spectra of IRAS07454-7112, obtained with the SEST.

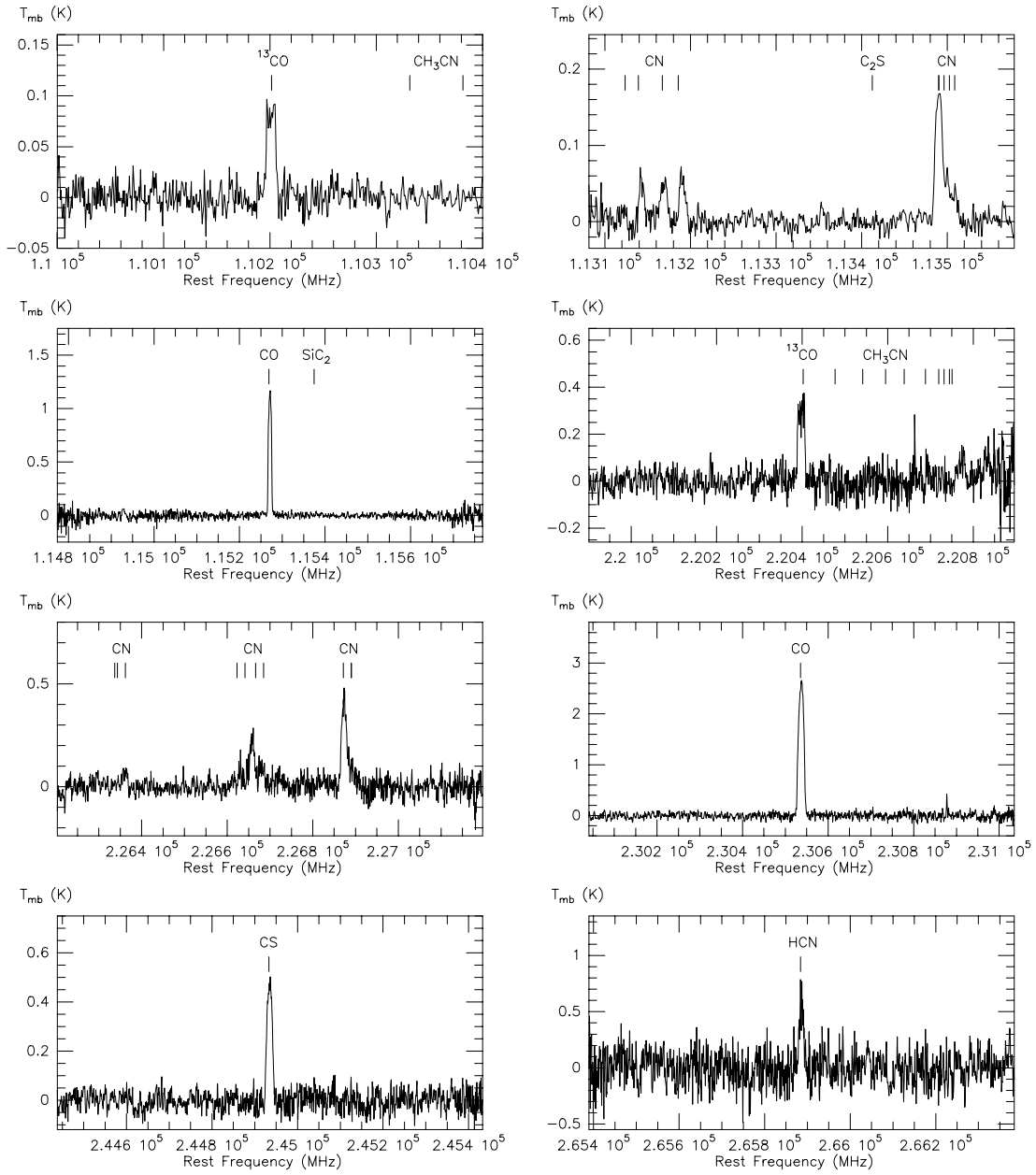


Figure 2.2: Low-resolution spectra of IRAS07454-7112, obtained with the SEST.

determined from a fit to the observed spectral energy distribution (SED). The inner radius of the circumstellar envelope is taken to reside outside that of the central blackbodies. This procedure provides a good description of the radiation field to which the envelope is subjected. A more in-depth description of the Monte Carlo-based model can be found in Schöier (2000), Schöier & Olofsson (2001) and Woods et al. (2003b).

In this modelling there are two principal free parameters, the mass-loss rate ($\dot{M}$) and the so-called $h$-parameter, which contains information about individual dust grains and controls the amount of heating through dust-gas collisions.

$$h = \left(\frac{\Psi}{0.01}\right)\left(\frac{2.0\,\mathrm{g\,cm^{-3}}}{\rho_\mathrm{d}}\right)\left(\frac{0.05\,\mu\mathrm{m}}{a_\mathrm{d}}\right), \tag{2.2}$$

where $\Psi$ is the dust-to-gas mass ratio, $\rho_\mathrm{d}$ the mass density of a dust grain, and $a_\mathrm{d}$ the size of a dust grain (assumed not to vary), and the adopted values of these parameters are also given. The mass-loss rate and the $h$-parameter were allowed to vary simultaneously.

The best fit circumstellar model for a particular source is estimated from a $\chi^2$-analysis (for details see Schöier & Olofsson 2001) using observed $^{12}$CO integrated intensities and assuming a 15–20% calibration uncertainty. The number of observational constraints used in the modelling is shown in Table 2.4, together with the reduced $\chi^2$ of the best fit model. In all the cases $\chi^2_\mathrm{red}{\sim}1$, indicating good fits.

Using the envelope parameters derived from the $^{12}$CO modelling, the abundance of $^{13}$CO was estimated using the same radiative transfer code. The derived $^{12}$CO/$^{13}$CO-ratios are presented in Table 2.4. The fits to the observed $^{13}$CO emission are good in all cases with $\chi^2_\mathrm{red}{\lesssim}1$. The quality of the fits further strengthen the adopted physical models for the envelopes. The $^{12}$CO/$^{13}$CO-ratio derived in this manner allows the assumption of optically thin emission made in Sect. 2.3.2 to be tested for those molecular species where the isotopomer containing $^{13}$C has been detected. All the sample stars, except for IRAS15194-5115 (to be discussed in Sect. 2.4.2), have inferred $^{12}$C/$^{13}$C-ratios in the range $\sim 20 - 50$.

Table 2.4: Summary of circumstellar properties derived from the CO modelling (see text for details)

| Source | $\dot{M}$ | $h$ | $N^b$ | ${\chi^2_{\rm red}}^c$ | $v_{\rm exp}$ | $\frac{(\dot{M}/v_{\rm exp})_\star}{(\dot{M}/v_{\rm exp})_{10216}}$ | $r_{\rm p}^d$ | $d$ | $\frac{^{12}{\rm CO}^e}{^{13}{\rm CO}}$ |
|---|---|---|---|---|---|---|---|---|---|
| | $[{\rm M}_\odot\,{\rm yr}^{-1}]$ | | | | $[{\rm km\,s}^{-1}]$ | | [cm] | [cm] | |
| IRAS07454-7112 | 5.0 (-6) | 1.5[a] | 2 | 0.1 | 13.0 | 0.46 | 3.0 (17) | 2.4 (16) | 17 |
| IRC+10216 | 1.2 (-5) | 1.5 | 27 | 1.4 | 14.5 | 1.00 | 3.7 (17) | 5.5 (16) | 45 |
| CIT6 | 5.0 (-6) | 2.3 | 20 | 0.8 | 17.0 | 0.36 | 1.9 (17) | 2.8 (16) | 35 |
| IRAS15082-4808 | 1.0 (-5) | 1.5[a] | 2 | 0.2 | 19.5 | 0.62 | 2.5 (17) | 3.5 (16) | 35 |
| IRAS15194-5115 | 1.2 (-5) | 2.8 | 10 | 0.9 | 21.5 | 0.67 | 3.2 (17) | 7.2 (16) | 6 |
| AFGL3068 | 2.0 (-5) | 2.5 | 4 | 1.6 | 14.0 | 1.72 | 3.8 (17) | 1.2 (17) | 30 |
| IRC+40540 | 1.5 (-5) | 1.5 | 7 | 1.0 | 14.0 | 1.29 | 4.0 (17) | 7.3 (16) | 50 |

(a) Adopted value

(b) Number of observational constraints used in the $^{12}$CO modelling

(c) Reduced $\chi^2$ of the best fit $^{12}$CO model

(d) $r_{\rm p}$ is the photodissociation radius of CO

(e) Determined from radiative transfer modelling of both $^{12}$CO and $^{13}$CO emission

The circumstellar envelopes (CSEs) of all the sample stars have similar physical properties. However, the stars presented here are losing mass at a significantly higher rate than the average carbon star: Schöier & Olofsson (2001) measure a median mass-loss rate for carbon stars of $\sim 3 \times 10^{-7}\,\mathrm{M}_{\odot}\,\mathrm{yr}^{-1}$, based on a sample of carbon stars complete within $\sim 600\,\mathrm{pc}$ from the sun. This suggests that the stars in the sample presented here are going through the super-wind phase of evolution (e.g., Vassiliadis & Wood 1993) at the end of the AGB, and will soon eject the entire stellar mantle.

### 2.3.2 Fractional abundance calculations

A full radiative transfer analysis of the wealth of molecular data presented here is beyond the scope of this work. A detailed treatment of the excitation would have to include the effects of dust emission and absorption in addition to accurate rates for collisional excitation of the molecules. Instead, abundances have been calculated for species with emission that is expected to be optically thin. In the case that the emission is optically thick, the calculated abundances under this assumption will be lower limits.

The calculation of isotope ratios of various species (as shown in Table 2.8) shows in general that many lines are optically thick (i.e., the ratio derived from observations is lower than the $^{12}\mathrm{CO}/^{13}\mathrm{CO}$ abundance ratio derived from the radiative transfer analysis). Where this is the case, the abundance of the main isotope (viz., CN, CS and $\mathrm{HC_3N}$) has been calculated by scaling the abundance of the less abundant isotope by the $^{12}\mathrm{CO}/^{13}\mathrm{CO}$-ratio. This is indicated by the bold-faced type in Table 2.7.

In the calculation of molecular abundances the circumstellar envelope is assumed to have been formed by a wind with a constant mass-loss rate and to expand with a constant velocity, such that the total density distribution follows an $r^{-2}$ law. It is further assumed that the fractional abundance of a species is constant in the radial range $r_{\mathrm{i}}$ to $r_{\mathrm{e}}$ and zero outside it. The excitation temperature was assumed to be constant throughout the emitting region. With these assumptions Olofsson et al. (1990b) have shown that for a given molecular transition,

$$\begin{aligned}\int T_{\mathrm{mb}}\mathrm{d}v \quad &= \frac{c^2}{2k\nu^2}\left[B_\nu(T_{\mathrm{ex}}) - B_\nu(T_{\mathrm{bg}})\right] \\ &\times \frac{g_u A_{ul}}{8\pi}\frac{c^3}{\nu^3}\frac{(1-e^{-h\nu/kT_{\mathrm{ex}}})}{Z}e^{-E_l/kT_{\mathrm{ex}}}\end{aligned}$$

$$\times \frac{f_{\rm X}\dot{M}_{\rm H_2}}{v_{\rm exp} m_{\rm H_2} BD} \int_{x_{\rm i}}^{x_{\rm e}} e^{-4\ln(2)x^2} {\rm d}x, \qquad (2.3)$$

where $c$ is the speed of light, $h$ the Planck constant, $k$ the Boltzmann constant, $B_\nu$ the Planck function, $T_{\rm ex}$ the excitation temperature, $T_{\rm bg}$ is taken to be the blackbody temperature of the cosmic background radiation at 2.7 K, $m_{\rm H_2}$ is the mass of an $H_2$ molecule, $v_{\rm exp}$ the expansion velocity of the circumstellar envelope, $B$ the FWHM of the telescope beam, $D$ the assumed distance, $\dot{M}_{\rm H_2}$ the mass-loss rate, $Z$ the partition function, $\nu$ the frequency of the line, $g_{\rm u}$ the statistical weight of the upper level, $A_{\rm ul}$ the Einstein coefficient for the transition, $E_{\rm l}$ the energy of the lower transition level, and $x_{\rm i,e} = r_{\rm i,e}/BD$. The integral over $x$ takes care of the beam filling. However, if $r \ll BD$, the integral can be simplified to $(r_{\rm e} - r_{\rm i})/BD$. This is the case in the furthest sources, IRAS07454-7112, CIT6 and IRAS15082-4808. However, for the CN emission from these sources, which tends to be very extended, and for the remaining four sources, the full integral is calculated. The abundance of HCN is not calculated using Eq. 2.3 since the line is certainly optically thick, but in all cases only by scaling the abundance of $H^{13}CN$ by the calculated $^{12}CO/^{13}CO$-ratio.

The following subsections describe some of the important factors in Eq. 2.3:

#### 2.3.2.1 Excitation temperature, $T_{\rm ex}$

Of importance in the radiative transfer analysis is the excitation (rotational) temperature assumed for the molecular emission. Generally, the excitation temperature will depend on the species (and transition) observed. When two or more transitions of the same molecule are observed, it is possible to make an estimate of the rotation temperature ($T_{\rm rot}$) of that molecule using Eq. 2.3. The rotation temperature is the excitation temperature for a particular rotational transition, and will generally differ from the excitation temperature assumed for all transitions. If the assumed excitation temperature is reasonable, this difference should be small. It is assumed that a molecular species is excited over the same radial range, and according to a single temperature. The results are shown in Table 2.5. It is clear that the rotational temperatures vary from source to source and between molecular species in the range $\sim 3 - 30$ K, as to be expected. Hence the average excitation temperature is 8.7 K (averaged over the individual excitation temperatures for all sources, rather than molecular species). A generic value of 10 K was assumed for all the abundances estimated.

Table 2.5: Rotation temperatures

| Source | $^{13}$CO 2–1/1–0 | CN 2–1/1–0 | CS 5–4/2–1 | $C_3N$ 11–10/10–9 | $C_4H$ 10–9/9–8 | HCN 3–2/2–1 |
|---|---|---|---|---|---|---|
| IRAS07454-7112 | 7.0 | 5.2 | 11.3 | — | — | 5.7 |
| IRC+10216 (S) | 6.3 | 3.9 | 13.7 | 17.9 | 5.3 | 7.8 |
| IRAS15082-4808 | 6.5 | 3.6 | 8.3 | — | — | 5.6 |
| IRAS15194-5115 | 5.6 | 4.0 | 9.7 | — | — | 9.7 |
| Average | 6.4 | 4.2 | 10.8 | 17.9 | 5.3 | 7.2 |

| Source | $H^{(13)}C_3N$ 12–11/10–9 | $HC_3N$ 12–11/10–9 | $HC_5N$ 34–33/32–31 | $SiC_2$ 5-4/4-3 | SiS 6–5/5–4 | Average |
|---|---|---|---|---|---|---|
| IRAS07454-7112 | 8.5 | 15.2 | — | — | 5.7 | 8.4 |
| IRC+10216 (S) | 17.8 | 10.7 | 10.0 | 11.6 | 5.8 | 10.1 |
| IRC+10216 (O) | — | — | — | — | 11.8 | 11.8 |
| IRAS15082-4808 | — | 8.9 | — | 37.1 | 5.0 | 10.7 |
| IRAS15194-5115 | 7.2 | 11.3 | — | — | 6.1 | 7.7 |
| IRC+40540 | — | — | — | — | 3.5 | 3.5 |
| Average | 11.2 | 11.5 | 10.0 | 24.4 | 6.3 | **8.7** |

#### 2.3.2.2 The partition function, $Z$

All molecules are assumed to be linear, rigid rotators, except for $SiC_2$ and $C_3H_2$ which are asymmetric tops and $CH_3CN$, which is a prolate symmetric top. Einstein A-coefficients (where available) and energy levels are taken from Chandra & Rashmi (1998) for $SiC_2$ , from Vrtilek et al. (1987) for $C_3H_2$, and from Boucher et al. (1980) for $CH_3CN$.

The partition function, $Z$, is calculated assuming that no molecules have a hyperfine structure, i.e., as having simple rotational energy diagrams. Hence the integrated intensities which are summed over all hyperfine components are used. For $C_3H_2$, $CH_3CN$ and $SiC_2$ the approximate expression for an asymmetric rotor (Townes & Schawlow 1975) is used, multiplied by 2 for $C_3H_2$, by 4 for $CH_3CN$ (to account for spin statistics) and by 1/2 for $SiC_2$ (since half of the energy levels are missing because of spin statistics). It is assumed that all levels are populated according to the same $T_{\rm ex}$.

#### 2.3.2.3 Sizes of emission regions, $r_{\rm e} - r_{\rm i}$

The chemical richness observed towards carbon stars can be qualitatively understood in terms of a photodissociation model (see the review by Glassgold 1996). Carbon-bearing molecules like CO, $C_2H_2$, HCN and CS, in addition to Si-bearing molecules like SiS and SiO, are all thought to be of photospheric origin where they are formed in conditions close to LTE. The photodissociation of these so-called parent species produces various radicals and ions that, in turn, drive a complex chemistry through ion-molecule and neutral-neutral reactions. For example, the radicals $C_2H$ and CN are the photodissociation products of $C_2H_2$ and HCN, respectively. In addition, the formation of dust in the CSE will affect the abundances of some of the species, in particular SiO and SiS, which condense onto dust grains. All other species observed in the sample of stars are thought to be products of the circumstellar chemistry.

To calculate the radial extent of the molecules HCN, CN, $C_2H$ and CS the photodissociation model of Huggins & Glassgold (1982) is adopted. The photodissociation radius of parent species ($f_{\rm X}$, viz., HCN, $C_2H_2$, CS) is determined by

$$\frac{{\rm d}f_{\rm X}}{{\rm d}r} = -\frac{G_{0,{\rm X}}}{v_{\rm exp}} {\rm e}^{-d_{\rm X}/r} f_{\rm X} \tag{2.4}$$

Table 2.6: Photodissociation rates

| Molecule | $G_0$ $[\mathrm{s}^{-1}]$ |
|---|---|
| HCN | $1.1\,10^{-9}$ |
| CN | $2.5\,10^{-10}$ |
| $C_2H_2$ | $2.1\,10^{-9}$ |
| $C_2H$ | $3.4\,10^{-10}$ |
| SiS | $6.3\,10^{-10}$ |
| CS | $6.3\,10^{-10}$ |
| SiO | $6.3\,10^{-10}$ |

and of a daughter ($f_{\mathrm{Xd}}$, viz., $C_2H$) by

$$\frac{\mathrm{d}f_{\mathrm{Xd}}}{\mathrm{d}r} = \frac{G_{0,\mathrm{X}}}{v_{\mathrm{exp}}} \mathrm{e}^{-d_{\mathrm{X}}/r} f_{\mathrm{X}} - \frac{G_{0,\mathrm{Xd}}}{v_{\mathrm{exp}}} \mathrm{e}^{-d_{\mathrm{Xd}}/r} f_{\mathrm{Xd}}. \tag{2.5}$$

$G_0$ is the unshielded photodissociation rate (see Table 2.6) and $d_{\mathrm{X}}$ is the dust shielding distance, given by:

$$d_{\mathrm{X}} = 1.4 \frac{3Q_{\mathrm{X}}}{4a_{\mathrm{d}}\rho_{\mathrm{d}}} \frac{\dot{M}_{\mathrm{d}}}{4\pi v_{\mathrm{d}}}, \tag{2.6}$$

where $Q$ is the dust absorption efficiency, $\dot{M}_{\mathrm{d}}$ the dust mass-loss rate, and $v_{\mathrm{d}}$ the expansion velocity of the dust grains (Jura & Morris 1981). Since different molecules are generally dissociated at different wavelengths the adopted value of $Q$ will depend on the species under study. However, the wavelength dependence of $Q$ in the region of interest, ∼1000–3000 Å, is weak (e.g., Suh 2000) and a generic value of 1.0 for most species of interest here is adopted. However, the shielding distance of CN is taken to be a factor of 1.2 greater than that used for HCN (Truong-Bach et al. 1987). Introducing the $h$-parameter defined in Eq. 2.2 the dust shielding distance may now be expressed as

$$d = 5.27\,10^{22} \frac{h\dot{M}}{v_{\mathrm{d}}} \quad \mathrm{cm}, \tag{2.7}$$

where the $H_2$ mass-loss rate $\dot{M}$ is given in $\mathrm{M}_\odot\,\mathrm{yr}^{-1}$ and $v_{\mathrm{d}}$ in $\mathrm{km\,s}^{-1}$. A gas-to-dust mass ratio of 0.01 was assumed.

There will generally be a drift velocity between the dust and the gas (e.g., Schöier

& Olofsson 2001)

$$v_{\rm d} - v_{\rm exp} = \sqrt{\frac{L v_{\rm exp} \langle Q \rangle}{\dot{M} c}}, \tag{2.8}$$

where $L$ is the bolometric luminosity of the star, $c$ the speed of light, and $\langle Q \rangle$ is the flux-averaged momentum transfer efficiency. The drift velocity also enters into the expression of the heating caused by dust-gas collisions. In the self-consistent treatment of the energy balance in the circumstellar envelope a value of 0.03 was assumed for $\langle Q \rangle$, which is also retained here. Photodissociation rates are taken from van Dishoeck (1988), with the assumption that SiS has the same photodissociation rate as CS (confirmed to within a factor 2 by the UMIST Ratefile[1]). The calculated shielding distances and rate coefficients are shown in Tables 2.4 and 2.6, respectively.

The photodissociation radii of species formed in the photosphere were chosen to be the e-folding radii of the initial abundances, i.e., $f_{\rm X}(r_{\rm e}) = f_{\rm X}(R_\star)/{\rm e}$, where $R_\star$ is the stellar radius. For the photodissociation products inner and outer radii are chosen to be where the abundance has dropped to 1/e of its peak value. The envelope sizes calculated by the simple photodissociation model agree relatively well with observed values in IRC+10216 and other objects, except in the case of SiS (see next paragraph). Lindqvist et al. (2000) used a detailed radiative transfer method and observed brightness distributions to derive envelope sizes of HCN and CN. For IRC+10216 and IRC+40540 they found envelope sizes of $\sim 4 \times 10^{16}$ cm for HCN and $\sim 5 \times 10^{16}$ cm for CN, in excellent agreement with the values derived here from the photodissociation model. In the case of CIT6 the observed HCN envelope size is larger than that calculated by a factor of 2. Envelope sizes and derived abundances are given in Table 2.7.

SiO and SiS are parent species with a radial extent (partially) depending on photodissociation. The calculation of the SiS photodissociation radius in IRC+10216 is not consistent with the radius observed by Bieging & Tafalla (1993). Therefore the observed radius for SiS in IRC+10216 was used in the abundance calculations, and its radius was scaled for the other objects in the sample with the factor $(\dot{M}/v_{\rm exp})_\star / (\dot{M}/v_{\rm exp})_{10216}$. This factor is proportional to the density ratio at a given radius, and also (to the first order) to the ratio of the envelope shielding distances. The outer radius calculated via the photodissociation model is actually slightly larger than that observed. This gives credence to the idea that SiS freezes out onto grains. SiO is treated in the same way as SiS since it too is likely to freeze out onto

[1] `http://www.rate99.co.uk`

grains. Hence the same envelope size as SiS was adopted for this species.

For those molecules which have their origin in a circumstellar chemistry a different approach is used. The sizes of the emission regions of HNC and $HC_3N$ have been determined interferometrically for IRC+10216 using observations by Bieging & Nguyen-Quang-Rieu (1988a), and of $SiC_2$ by Lucas et al. (1995) (see Sect. 1.6.2.5 for examples). Inner and outer radii for HNC, $HC_3N$ and $SiC_2$ are taken from observations of IRC+10216, and scaled by $(\dot{M}/v_{\rm exp})_\star/(\dot{M}/v_{\rm exp})_{10216}$ for the remaining six sample carbon stars (since molecular distributions have not been mapped in all the sample stars; see Table 2.4 for values of this ratio). Chemical modelling shows that the species $C_3H$, $C_4H$, $C_3H_2$, $C_3N$, $CH_3CN$, $HC_5N$, SO, $C_2S$ and $C_3S$ are formed via chemical reactions in the outer envelope (e.g., Millar & Herbst 1994). Furthermore, it shows that the species $C_3H$, $C_4H$, $C_3H_2$ and $C_3N$ have a similar radial distribution to HNC, and that the species $CH_3CN$ and $HC_5N$ are similarly distributed to $HC_3N$. Hence corresponding radii for these species are assumed in the calculations. SO is assumed to have a similar distribution to CN (c.f., Nejad & Millar 1988), and $C_2S$ and $C_3S$ are assumed to follow the CS distribution (c.f., Millar et al. 2001), although these latter two species are not parent molecules (and hence are given an inner radius equal to that of $HC_3N$). All isotopes (i.e., species involving $^{13}C$ and $^{34}S$) are further assumed to have the same distributions as the main isotope.

Table 2.7: Abundances and sizes of emission regions[a]

| Molecule | IRC+10216 (SEST) | | | IRC+10216 (OSO) | | | IRAS15194-5115 | | | IRAS15082-4808 | | |
|---|---|---|---|---|---|---|---|---|---|---|---|---|
| | $r_i$ [cm] | $r_e$ [cm] | $f_X$ [X]/[$H_2$] | $r_i$ [cm] | $r_e$ [cm] | $f_X$ [X]/[$H_2$] | $r_i$ [cm] | $r_e$ [cm] | $f_X$ [X]/[$H_2$] | $r_i$ [cm] | $r_e$ [cm] | $f_X$ [X]/[$H_2$] |
| CN(1–0) | 2.6 (16) | 7.1 (16) | **3.4 (-06)** | 2.6 (16) | 7.1 (16) | 2.1 (-06) | 3.5 (16) | 9.6 (16) | 2.1 (-06) | 2.0 (16) | 6.2 (16) | 3.2 (-06) |
| $^{13}$CN(1–0) | 2.6 (16) | 7.1 (16) | 7.6 (-08) | 2.6 (16) | 7.1 (16) | 4.6 (-08) | 3.5 (16) | 9.6 (16) | 3.0 (-07) | 2.0 (16) | 6.2 (16) | < 1.3 (-08) |
| CN(2–1) | 2.6 (16) | 7.1 (16) | 9.6 (-07) | 2.6 (16) | 7.1 (16) | — | 3.5 (16) | 9.6 (16) | 3.5 (-07) | 2.0 (16) | 6.2 (16) | 3.8 (-07) |
| CS(2–1) | | 4.0 (16) | **9.9 (-07)** | | 4.0 (16) | 4.6 (-07) | | 5.5 (16) | 2.3 (-06) | | 3.3 (16) | 2.2 (-06) |
| $^{13}$CS(2–1) | | 4.0 (16) | 2.2 (-08) | | 4.0 (16) | — | | 5.5 (16) | 5.0 (-07) | | 3.3 (16) | < 3.1 (-08) |
| C$^{34}$S(2–1) | | 4.0 (16) | 3.7 (-08) | | 4.0 (16) | — | | 5.5 (16) | — | | 3.3 (16) | — |
| CS(5–4) | | 4.0 (16) | 1.2 (-06) | | 4.0 (16) | — | | 5.5 (16) | 1.6 (-06) | | 3.3 (16) | 9.0 (-07) |
| $C_2$S(6,7–5,6) | 1.2 (16) | 4.0 (16) | < 4.6 (-09) | 1.2 (16) | 4.0 (16) | < 4.5 (-09) | 8.0 (15) | 5.5 (16) | < 2.4 (-08) | 7.4 (15) | 3.3 (16) | < 3.1 (-08) |
| $C_2$S(8,9–7,8) | 1.2 (16) | 4.0 (16) | < 4.1 (-09) | 1.2 (16) | 4.0 (16) | < 9.5 (-09) | 8.0 (15) | 5.5 (16) | < 3.5 (-08) | 7.4 (15) | 3.3 (16) | < 4.8 (-08) |
| $C_3$S(15-14) | 1.2 (16) | 4.0 (16) | < 1.2 (-08) | 1.2 (16) | 4.0 (16) | < 1.5 (-08) | 8.0 (15) | 5.5 (16) | < 7.2 (-08) | 7.4 (15) | 3.3 (16) | < 1.3 (-06) |
| SiO(2–1) | | 2.0 (16) | 1.3 (-07) | | 2.0 (16) | 9.6 (-08) | | 1.3 (16) | 1.7 (-06) | | 3.3 (16) | 7.2 (-07) |
| SiS(5–4) | | 2.0 (16) | 1.2 (-06) | | 2.0 (16) | 8.1 (-07) | | 1.3 (16) | 4.9 (-06) | | 3.3 (16) | 3.3 (-06) |
| SiS(6–5) | | 2.0 (16) | 9.0 (-07) | | 2.0 (16) | 9.0 (-07) | | 1.3 (16) | 4.2 (-06) | | 3.3 (16) | 2.0 (-06) |
| SO(3–2) | 2.6 (16) | 7.1 (16) | < 3.5 (-09) | 2.6 (16) | 7.1 (16) | — | 3.5 (16) | 9.6 (16) | — | 2.0 (16) | 6.2 (16) | — |
| HCN(1–0) | | 3.4 (16) | **1.4 (-05)** | | 3.4 (16) | **1.1 (-05)** | | 4.6 (16) | **1.2 (-05)** | | 2.7 (16) | **1.0 (-05)** |
| H$^{13}$CN(1–0) | | 3.4 (16) | 3.1 (-07) | | 3.4 (16) | 2.5 (-07) | | 4.6 (16) | 2.0 (-06) | | 2.7 (16) | 2.9 (-07) |
| HNC(1–0) | 2.4 (16) | 8.4 (16) | 7.2 (-08) | 2.4 (16) | 8.4 (16) | 3.8 (-08) | 1.6 (16) | 5.6 (16) | 3.3 (-07) | 1.5 (16) | 5.2 (16) | 1.6 (-07) |
| HN$^{13}$C(1–0) | 2.4 (16) | 8.4 (16) | < 1.9 (-09) | 2.4 (16) | 8.4 (16) | — | 1.6 (16) | 5.6 (16) | 1.1 (-07) | 1.5 (16) | 5.2 (16) | < 1.2 (-08) |
| $SiC_2$(4,04–3,03) | 2.4 (16) | 6.0 (16) | 1.6 (-07) | 2.4 (16) | 6.0 (16) | — | 1.6 (16) | 4.0 (16) | — | 1.5 (16) | 3.7 (16) | 3.3 (-07) |
| $SiC_2$(4,22–3,21) | 2.4 (16) | 6.0 (16) | 3.2 (-07) | 2.4 (16) | 6.0 (16) | — | 1.6 (16) | 4.0 (16) | — | 1.5 (16) | 3.7 (16) | < 1.8 (-07) |
| $SiC_2$(5,05–4,04) | 2.4 (16) | 6.0 (16) | 1.7 (-07) | 2.4 (16) | 6.0 (16) | 1.7 (-07) | 1.6 (16) | 4.0 (16) | 1.2 (-06) | 1.5 (16) | 3.7 (16) | 4.9 (-07) |
| $C_2$H(1–0) | 2.3 (16) | 5.6 (16) | 2.8 (-06) | 2.3 (16) | 5.6 (16) | 2.4 (-06) | 1.6 (16) | 4.8 (16) | 1.5 (-05) | 1.7 (16) | 4.8 (16) | 8.3 (-06) |
| $C_3$H(9/2–7/2) | 2.4 (16) | 8.4 (16) | 5.5 (-08) | 2.4 (16) | 8.4 (16) | 5.9 (-08) | 1.6 (16) | 5.6 (16) | 9.2 (-08) | 1.5 (16) | 5.2 (16) | < 1.7 (-08) |
| $C_3$N(9–8) | 2.4 (16) | 8.4 (16) | 3.0 (-07) | 2.4 (16) | 8.4 (16) | — | 1.6 (16) | 5.6 (16) | < 4.9 (-08) | 1.5 (16) | 5.2 (16) | < 1.0 (-07) |
| $C_3$N(11–10) | 2.4 (16) | 8.4 (16) | 5.9 (-07) | 2.4 (16) | 8.4 (16) | 7.6 (-07) | 1.6 (16) | 5.6 (16) | 9.2 (-07) | 1.5 (16) | 5.2 (16) | 9.5 (-07) |
| $C_4$H(9–8) | 2.4 (16) | 8.4 (16) | 3.7 (-06) | 2.4 (16) | 8.4 (16) | — | 1.6 (16) | 5.6 (16) | — | 1.5 (16) | 5.2 (16) | < 6.6 (-07) |
| $C_4$H(10–9) | 2.4 (16) | 8.4 (16) | 2.7 (-06) | 2.4 (16) | 8.4 (16) | 3.2 (-06) | 1.6 (16) | 5.6 (16) | 2.8 (-05) | 1.5 (16) | 5.2 (16) | 6.9 (-06) |
| $C_3H_2$(2,12–1,01) | 2.4 (16) | 8.4 (16) | 3.2 (-08) | 2.4 (16) | 8.4 (16) | — | 1.6 (16) | 5.6 (16) | 6.0 (-07) | 1.5 (16) | 5.2 (16) | < 9.3 (-08) |
| $HC_3$N(10–9) | 1.2 (16) | 6.0 (16) | **1.1 (-06)** | 1.2 (16) | 6.0 (16) | 4.4 (-07) | 8.0 (15) | 4.0 (16) | 1.9 (-06) | 7.4 (15) | 3.7 (16) | 2.3 (-06) |
| HCC$^{13}$CN(10–9) | 1.2 (16) | 6.0 (16) | 2.4 (-08) | 1.2 (16) | 6.0 (16) | < 2.8 (-09) | 8.0 (15) | 4.0 (16) | 3.9 (-07) | 7.4 (15) | 3.7 (16) | < 2.7 (-08) |
| HC$^{13}$CCN(10–9) | 1.2 (16) | 6.0 (16) | 2.4 (-08) | 1.2 (16) | 6.0 (16) | < 2.8 (-09) | 8.0 (15) | 4.0 (16) | 3.9 (-07) | 7.4 (15) | 3.7 (16) | < 2.7 (-08) |
| $HC_3$N(11–10) | 1.2 (16) | 6.0 (16) | 7.5 (-07) | 1.2 (16) | 6.0 (16) | — | 8.0 (15) | 4.0 (16) | — | 7.4 (15) | 3.7 (16) | — |
| $HC_3$N(12–11) | 1.2 (16) | 6.0 (16) | **1.9 (-06)** | 1.2 (16) | 6.0 (16) | — | 8.0 (15) | 4.0 (16) | 2.2 (-06) | 7.4 (15) | 3.7 (16) | 2.1 (-06) |
| HCC$^{13}$CN(12–11) | 1.2 (16) | 6.0 (16) | 4.1 (-08) | 1.2 (16) | 6.0 (16) | 1.5 (-08) | 8.0 (15) | 4.0 (16) | 2.8 (-07) | 7.4 (15) | 3.7 (16) | < 2.0 (-08) |
| HC$^{13}$CCN(12–11) | 1.2 (16) | 6.0 (16) | 4.1 (-08) | 1.2 (16) | 6.0 (16) | 1.5 (-08) | 8.0 (15) | 4.0 (16) | 2.8 (-07) | 7.4 (15) | 3.7 (16) | < 2.0 (-08) |
| $CH_3$CN(6(1)–5(1)) | 1.2 (16) | 6.0 (16) | 1.2 (-08) | 1.2 (16) | 6.0 (16) | < 2.0 (-09) | 8.0 (15) | 4.0 (16) | < 2.5 (-08) | 7.4 (15) | 3.7 (16) | < 4.3 (-08) |
| $CH_3$CN(12(0)–11(0)) | 1.2 (16) | 6.0 (16) | < 1.2 (-07) | 1.2 (16) | 6.0 (16) | — | 8.0 (15) | 4.0 (16) | < 2.4 (-06) | 7.4 (15) | 3.7 (16) | < 1.5 (-06) |
| $HC_5$N(32–31) | 1.2 (16) | 6.0 (16) | 3.9 (-06) | 1.2 (16) | 6.0 (16) | — | 8.0 (15) | 4.0 (16) | < 4.5 (-06) | 7.4 (15) | 3.7 (16) | < 3.8 (-06) |
| $HC_5$N(34–33) | 1.2 (16) | 6.0 (16) | 4.2 (-06) | 1.2 (16) | 6.0 (16) | < 7.6 (-07) | 8.0 (15) | 4.0 (16) | — | 7.4 (15) | 3.7 (16) | < 7.4 (-06) |
| $HC_5$N(35–34) | 1.2 (16) | 6.0 (16) | 1.3 (-05) | 1.2 (16) | 6.0 (16) | — | 8.0 (15) | 4.0 (16) | — | 7.4 (15) | 3.7 (16) | < 1.1 (-05) |

(a) In this table $x\,(y)$ represents $x \times 10^y$.

(b) Bold face indicates an abundance calculated by scaling the abundance of the $^{13}$C isotope of the same species by the modelled $^{12}$CO/$^{13}$CO-ratio (see Sect. 2.3.2).

Table 2.7: (*cont.*) Abundances and sizes of emission regions[a]

| Molecule | IRAS07454-7112 | | | CIT6 | | | AFGL3068 | | | IRC+40540 | | |
|---|---|---|---|---|---|---|---|---|---|---|---|---|
| | $r_i$ cm | $r_e$ cm | $f_X$ [X]/[$H_2$] | $r_i$ cm | $r_e$ cm | $f_X$ [X]/[$H_2$] | $r_i$ cm | $r_e$ cm | $f_X$ [X]/[$H_2$] | $r_i$ cm | $r_e$ cm | $f_X$ [X]/[$H_2$] |
| CN(1–0) | 1.3 (16) | 4.1 (16) | 5.3 (-06) | 1.6 (16) | 5.1 (16) | **2.0 (-05)** | 3.2 (16) | 8.3 (16) | 4.6 (-07) | 3.2 (16) | 8.3 (16) | 1.0 (-06) |
| $^{13}$CN(1–0) | 1.3 (16) | 4.1 (16) | 4.8 (-07) | 1.6 (16) | 5.1 (16) | 5.8 (-07) | 3.2 (16) | 8.3 (16) | < 2.6 (-08) | 3.2 (16) | 8.3 (16) | < 9.9 (-09) |
| CN(2–1) | 1.3 (16) | 4.1 (16) | 1.6 (-06) | 1.6 (16) | 5.1 (16) | — | 3.2 (16) | 8.3 (16) | — | 3.2 (16) | 8.3 (16) | — |
| CS(2–1) | | 2.2 (16) | 1.6 (-06) | | 2.7 (16) | 2.5 (-06) | | 4.8 (16) | 3.7 (-07) | | 4.9 (16) | 5.4 (-07) |
| $^{13}$CS(2–1) | | 2.2 (16) | < 2.9 (-08) | | 2.7 (16) | — | | 4.8 (16) | — | | 4.9 (16) | — |
| C$^{34}$S (2–1) | | 2.2 (16) | — | | 2.7 (16) | — | | 4.8 (16) | — | | 4.9 (16) | — |
| CS(5–4) | | 2.2 (16) | 1.6 (-06) | | 2.7 (16) | — | | 4.8 (16) | — | | 4.9 (16) | — |
| $C_2$S(6,7–5,6) | 5.6 (15) | 2.2 (16) | < 9.1 (-08) | 4.3 (15) | 2.7 (16) | < 1.0 (-07) | 1.6 (16) | 4.8 (16) | < 8.1 (-08) | 1.6 (16) | 4.9 (16) | < 3.0 (-08) |
| $C_2$S(8,9–7,8) | 5.6 (15) | 2.2 (16) | < 1.1 (-07) | 4.3 (15) | 2.7 (16) | < 2.0 (-07) | 1.6 (16) | 4.8 (16) | < 8.0 (-08) | 1.6 (16) | 4.9 (16) | < 5.6 (-08) |
| $C_3$S(15-14) | 5.6 (15) | 2.2 (16) | < 3.6 (-07) | 4.3 (15) | 2.7 (16) | < 2.5 (-07) | 1.6 (16) | 4.8 (16) | < 3.5 (-07) | 1.6 (16) | 4.9 (16) | < 8.9 (-08) |
| SiO(2–1) | | 9.4 (15) | 4.4 (-07) | | 7.2 (15) | 1.0 (-06) | | 2.6 (16) | < 4.7 (-08) | | 2.6 (16) | 5.6 (-08) |
| SiS(5–4) | | 9.4 (15) | 4.8 (-06) | | 7.2 (15) | 1.0 (-06) | | 2.6 (16) | 3.3 (-07) | | 2.6 (16) | 1.4 (-06) |
| SiS(6–5) | | 9.4 (15) | 3.4 (-06) | | 7.2 (15) | 5.2 (-06) | | 2.6 (16) | 1.0 (-06) | | 2.6 (16) | 4.9 (-07) |
| HCN(1–0) | | 1.8 (16) | **7.8 (-06)** | | 2.2 (16) | **1.1 (-05)** | | 4.2 (16) | **6.3 (-06)** | | 4.2 (16) | **6.5 (-06)** |
| H$^{13}$CN(1–0) | | 1.8 (16) | 5.6 (-07) | | 2.2 (16) | 3.0 (-07) | | 4.2 (16) | 2.1 (-07) | | 4.2 (16) | 1.3 (-07) |
| HNC(1–0) | 1.1 (16) | 4.0 (16) | 1.0 (-07) | 8.6 (15) | 3.0 (16) | 2.3 (-07) | 3.1 (16) | 1.1 (17) | 3.0 (-08) | 3.1 (16) | 1.1 (17) | 2.2 (-08) |
| HN$^{13}$C(1–0) | 1.1 (16) | 4.0 (16) | < 1.8 (-08) | 8.6 (15) | 3.0 (16) | < 2.1 (-08) | 3.1 (16) | 1.1 (17) | < 1.4 (-08) | 3.1 (16) | 1.1 (17) | < 4.4 (-09) |
| $SiC_2$(4,04–3,03) | 1.1 (16) | 2.8 (16) | 2.3 (-07) | 8.6 (15) | 2.2 (16) | — | 3.1 (16) | 7.8 (16) | — | 3.1 (16) | 7.8 (16) | — |
| $SiC_2$(4,22–3,21) | 1.1 (16) | 2.8 (16) | < 2.7 (-07) | 8.6 (15) | 2.2 (16) | — | 3.1 (16) | 7.8 (16) | — | 3.1 (16) | 7.8 (16) | — |
| $SiC_2$(5,05–4,04) | 1.1 (16) | 2.8 (16) | < 3.2 (-07) | 8.6 (15) | 2.2 (16) | 3.1 (-06) | 3.1 (16) | 7.8 (16) | < 7.5 (-08) | 3.1 (16) | 7.8 (16) | < 5.3 (-08) |
| $C_2$H(1–0) | 1.1 (16) | 3.2 (16) | < 4.3 (-07) | 1.4 (16) | 4.1 (16) | 6.9 (-06) | 2.8 (16) | 6.7 (16) | 5.7 (-06) | 2.7 (16) | 6.7 (16) | < 1.0 (-07) |
| $C_3$H(9/2–7/2) | 1.1 (16) | 4.0 (16) | < 3.1 (-08) | 8.6 (15) | 3.0 (16) | < 7.4 (-08) | 3.1 (16) | 1.1 (17) | < 1.4 (-08) | 3.1 (16) | 1.1 (17) | < 1.2 (-08) |
| $C_3$N(9–8) | 1.1 (16) | 4.0 (16) | < 1.6 (-07) | 8.6 (15) | 3.0 (16) | — | 3.1 (16) | 1.1 (17) | — | 3.1 (16) | 1.1 (17) | — |
| $C_3$N(11–10) | 1.1 (16) | 4.0 (16) | 7.3 (-07) | 8.6 (15) | 3.0 (16) | 2.6 (-06) | 3.1 (16) | 1.1 (17) | 5.5 (-07) | 3.1 (16) | 1.1 (17) | 1.1 (-07) |
| $C_4$H(9–8) | 1.1 (16) | 4.0 (16) | — | 8.6 (15) | 3.0 (16) | — | 3.1 (16) | 1.1 (17) | — | 3.1 (16) | 1.1 (17) | — |
| $C_4$H(10–9) | 1.1 (16) | 4.0 (16) | < 8.8 (-07) | 8.6 (15) | 3.0 (16) | < 1.7 (-06) | 3.1 (16) | 1.1 (17) | — | 3.1 (16) | 1.1 (17) | — |
| $C_3H_2$(2,12–1,01) | 1.1 (16) | 4.0 (16) | — | 8.6 (15) | 3.0 (16) | — | 3.1 (16) | 1.1 (17) | — | 3.1 (16) | 1.1 (17) | — |
| $HC_3$N(10–9) | 5.6 (15) | 2.8 (16) | 1.7 (-06) | 4.3 (15) | 2.2 (16) | 2.4 (-06) | 1.6 (16) | 7.8 (16) | 5.0 (-07) | 1.6 (16) | 7.8 (16) | **1.5 (-06)** |
| HCC$^{13}$CN(10–9) | 5.6 (15) | 2.8 (16) | 1.5 (-07) | 4.3 (15) | 2.2 (16) | < 4.9 (-08) | 1.6 (16) | 7.8 (16) | < 1.5 (-08) | 1.6 (16) | 7.8 (16) | 3.1 (-08) |
| HC$^{13}$CCN(10–9) | 5.6 (15) | 2.8 (16) | 1.5 (-07) | 4.3 (15) | 2.2 (16) | < 4.9 (-08) | 1.6 (16) | 7.8 (16) | < 1.5 (-08) | 1.6 (16) | 7.8 (16) | 3.1 (-08) |
| $HC_3$N(11–10) | 5.6 (15) | 2.8 (16) | — | 4.3 (15) | 2.2 (16) | — | 1.6 (16) | 7.8 (16) | — | 1.6 (16) | 7.8 (16) | — |
| $HC_3$N(12–11) | 5.6 (15) | 2.8 (16) | 2.4 (-06) | 4.3 (15) | 2.2 (16) | — | 1.6 (16) | 7.8 (16) | — | 1.6 (16) | 7.8 (16) | — |
| HCC$^{13}$CN(12–11) | 5.6 (15) | 2.8 (16) | 1.3 (-07) | 4.3 (15) | 2.2 (16) | 2.7 (-07) | 1.6 (16) | 7.8 (16) | < 2.9 (-08) | 1.6 (16) | 7.8 (16) | < 1.1 (-08) |
| HC$^{13}$CCN(12–11) | 5.6 (15) | 2.8 (16) | 1.3 (-07) | 4.3 (15) | 2.2 (16) | 2.7 (-07) | 1.6 (16) | 7.8 (16) | < 2.9 (-08) | 1.6 (16) | 7.8 (16) | < 1.1 (-08) |
| $CH_3$CN(6(1)–5(1)) | 5.6 (15) | 2.8 (16) | < 2.4 (-07) | 4.3 (15) | 2.2 (16) | < 1.3 (-07) | 1.6 (16) | 7.8 (16) | < 1.2 (-07) | 1.6 (16) | 7.8 (16) | < 6.4 (-08) |
| $CH_3$CN(12(0)–11(0)) | 5.6 (15) | 2.8 (16) | < 4.6 (-06) | 4.3 (15) | 2.2 (16) | — | 1.6 (16) | 7.8 (16) | — | 1.6 (16) | 7.8 (16) | — |
| $HC_5$N(32–31) | 5.6 (15) | 2.8 (16) | — | 4.3 (15) | 2.2 (16) | — | 1.6 (16) | 7.8 (16) | — | 1.6 (16) | 7.8 (16) | — |
| $HC_5$N(34–33) | 5.6 (15) | 2.8 (16) | 9.2 (-06) | 4.3 (15) | 2.2 (16) | < 1.3 (-05) | 1.6 (16) | 7.8 (16) | < 4.1 (-06) | 1.6 (16) | 7.8 (16) | < 4.5 (-06) |
| $HC_5$N(35–34) | 5.6 (15) | 2.8 (16) | < 8.8 (-06) | 4.3 (15) | 2.2 (16) | — | 1.6 (16) | 7.8 (16) | — | 1.6 (16) | 7.8 (16) | — |

(a) In this table $x\,(y)$ represents $x \times 10^y$.

(b) Bold face indicates an abundance calculated by scaling the abundance of the $^{13}$C isotope of the same species by the modelled $^{12}$CO/$^{13}$CO-ratio (see Sect. 2.3.2).

Table 2.8: Molecular isotope abundance ratios

| | IRC+10216 (S) | IRC+10216 (O) | IRAS15194 |
|---|---|---|---|
| $HC_3N/HC^{13}CCN(10–9)$ | 32.6 | — | 4.9 |
| $HC_3N/HC^{13}CCN(12–11)$ | 22.1 | — | 7.9 |
| $CS/^{13}CS(2–1)$ | 22.7 | — | 4.6 |
| $CN/^{13}CN(1–0)$ | 25.1 | 46.6 | 6.7 |
| Average | 25.6 | 46.6 | 6.0 |
| Modelling of CO (Table 2.4) | 45.0 | 45.0 | 6.0 |

| | IRAS07454 | CIT6 | IRC+40540 |
|---|---|---|---|
| $HC_3N/HC^{13}CCN(10–9)$ | 11.1 | — | 17.9 |
| $HC_3N/HC^{13}CCN(12–11)$ | 17.8 | — | — |
| $CN/^{13}CN(1–0)$ | 11.0 | 12.4 | — |
| Average | 13.3 | 12.4 | 17.9 |
| Modelling of CO (Table 2.4) | 14.0 | 35.0 | 50.0 |

### 2.3.3 Uncertainties in the abundance estimates

The assumption of optically thin emission has a systematic effect on the derived abundances, in that the true abundance will be higher if there are opacity effects. As can be seen from Table 2.8, there can be a factor of 2–3 in error from this assumption.

The accuracy of the calculated abundances is dependent on various assumptions. Due to the intrinsic difficulties in estimating distances to the objects included in the sample, the typical uncertainty in the adopted distance is a factor of $\sim$2. This influences the mass-loss rates derived in the radiative transfer modelling such that the adopted mass-loss rate will scale as $D^{1-2}$. The calculation of the limiting radii of a certain molecular distribution in the envelope is also affected by inaccuracies in the distance estimate. Where radii have been calculated by scaling observed radii in IRC+10216, there comes an error which scales as $D$. The results from the photodissociation model will have a lesser dependence, with $D$ coming into the expression for the shielding distance, via $\dot{M}$. Hence the abundance, which is trivially derived from Eq. 2.3, will vary as approximately $D^{-1-0}$, giving a factor of 2, possibly, in error.

In the present analysis an excitation temperature of 10 K was assumed for all transitions. The error in abundance estimate due to this assumption will depend on the excitation temperature of a particular transition and the assumption of LTE, and is estimated to be not more than a factor of $\sim$2.

Overall, it seems like an error of a factor of 5 is reasonable to expect in the abundances presented here, although it should be borne in mind that this could rise to an order of magnitude. In the comparison of abundance ratios in Table 2.9, any difference less than a factor of 5 is treated as insignificant with respect to error margins.

### 2.3.4 Comparison with published abundances

In comparison with Nyman et al. (1993), derived abundance ratios (Table 2.9) have increased in favour of IRAS15194-5115 by up to a factor of approximately 4. Individual abundances generally show a factor $\sim$2 increase for those in IRAS15914-5115, and a factor $\sim$2 decrease for IRC+10216, over Nyman et al. (1993).

1. In Nyman et al. (1993), the distances adopted for IRC+10216 and IRAS15194-5115 were approximately twice as large as those here; however this has little effect on calculated abundances since the distance ratio is more or less unchanged.

2. The calculated mass-loss rate of IRAS15194-5115 in Nyman et al. (1993) was larger than that of IRC+10216 by a factor of 2.5, and here the recalculated mass-loss rates are the same for these two objects. This would tend to increase the abundance ratios quoted by a similar factor.

3. The photodissociation radius depends on the mass-loss rate and the dust parameters through the dust shielding distance. Compared to Nyman et al. (1993) this work uses different mass-loss rates, a different gas-to-dust ratio (0.01 compared to 0.005), and the dust parameters are also slightly different due to the determination of the $h$–factor in the radiative transfer analysis. The scale factor that determines the inner and outer radii of the species with a origin in circumstellar chemistry depends on the ratio of the mass-loss rates.

Thus the difference in relative mass loss rates explains the factor of 4 difference in relative abundances between IRAS15914-5115 and IRC+10216 derived in this chapter compared to those derived in Nyman et al. (1993).

As discussed earlier in this chapter the outer radii of SiS and SiO are not determined through the photodissociation radius but scaled from their observed radius in IRC+10216. In this way the calculated abundances of SiO and SiS have increased in by a factor of 4–5 for IRAS15194-5115 compared to Nyman et al. (1993). For

IRC+10216 these species have the same abundance as calculated previously, and they are in reasonable agreement with those reported elsewhere in the literature. Bujarrabal et al. (1994) give $f(\mathrm{SiO}) = 5.6\,10^{-7}$ and $f(\mathrm{SiS}) = 3.9\,10^{-6}$, which are $\sim$4 times greater, using an outer radius half that quoted in this paper and a distance of 200 pc. HNC is also a factor of $\sim$6 in disagreement. Better agreement is seen for the other species which Bujarrabal et al. (1994) detect. Cernicharo et al. (2000) also calculate abundances in IRC+10216, and are within a factor 5 of those here.

Generally, it seems that IRC+10216 has lower abundances than IRAS15194-5115, IRAS15082-4808, IRAS07454-7112 and CIT6. However, it is very similar, physically and chemically, to AFGL3068 and IRC+40540.

The three northern sources observed at OSO have also been studied in the literature, and abundances derived. The Bujarrabal et al. (1994) paper includes data relating to CIT6, AFGL3068 and IRC+40540. All abundances calculated by Bujarrabal et al. in these three sources are greater than those derived here. Distances and mass-loss rates are reasonably comparable between this work and that. Generally, this means that the calculated abundances in this paper are lower by a factor of $\sim$2 in CIT6, a factor of $\sim$5 in AFGL3068, and a factor of $\sim$3 in IRC+40540 compared to those derived in Bujarrabal et al. (1994).

Table 2.9: Abundance ratios, compared to IRC+10216 observed with the SEST.

| | IRC+10216 | | IRAS15194 | IRAS15082 | IRAS07454 | CIT6 | AFGL3068 | IRC+40540 |
|---|---|---|---|---|---|---|---|---|
| Molecule | SEST | OSO | | | | | | |
| CN(1-0) | 1.0 | 1.1 | 1.1 | 1.7 | 2.8 | 3.8 | 0.2 | 0.5 |
| $^{13}$CN(1-0) | 1.0 | 0.6 | 4.0 | — | **6.3** | **7.6** | — | — |
| CN(2-1) | 1.0 | — | 0.4 | 0.4 | 1.7 | — | — | — |
| CS(2-1) | 1.0 | 0.9 | 4.6 | 4.3 | 3.2 | **5.1** | 0.7 | 1.1 |
| $^{13}$CS(2-1) | 1.0 | — | **22.7** | — | — | — | — | — |
| CS(5-4) | 1.0 | — | 1.4 | 0.8 | 1.4 | — | — | — |
| SiO(2-1) | 1.0 | 0.7 | **12.8** | **5.4** | 3.3 | **7.8** | — | 0.4 |
| SiS(5-4) | 1.0 | 0.7 | 4.0 | 2.7 | 3.9 | 0.8 | 0.3 | 1.1 |
| SiS(6-5) | 1.0 | 1.0 | 4.7 | 2.2 | 3.8 | **5.7** | 1.1 | 0.5 |
| HCN | 1.0 | 0.8 | 0.9 | 0.7 | 0.6 | 0.8 | 0.5 | 0.5 |
| H$^{13}$CN(1-0) | 1.0 | 0.8 | **6.4** | 0.9 | 1.8 | 1.0 | 0.7 | 0.4 |
| HNC(1-0) | 1.0 | 0.5 | 4.6 | 2.2 | 1.4 | 3.2 | 0.4 | 0.3 |
| $SiC_2$(4,04-3,03) | 1.0 | — | — | 2.0 | 1.5 | — | — | — |
| $SiC_2$(5,05-4,04) | 1.0 | 1.0 | **6.9** | 2.8 | — | **17.7** | — | — |
| $C_2H$(1-0) | 1.0 | 0.9 | **5.6** | 3.0 | — | 2.5 | 2.0 | — |
| $C_3H$(9/2-7/2) | 1.0 | 1.1 | 1.7 | — | — | — | — | — |
| $C_3N$(11-10) | 1.0 | 1.3 | 1.5 | 1.6 | 1.2 | 4.4 | 0.9 | 0.2 |
| $C_4H$(10-9) | 1.0 | 1.2 | **10.4** | 2.6 | — | — | — | — |
| $C_3H_2$(2,12-1,01) | 1.0 | — | **18.6** | — | — | — | — | — |
| $HC_3N$(10-9) | 1.0 | 0.6 | 2.4 | 3.0 | 2.2 | 3.1 | 0.6 | 0.7 |
| H$^{(13)}C_3N$(10-9)[a] | 1.0 | — | **16.3** | — | **6.4** | — | — | 1.3 |
| $HC_3N$(12-11) | 1.0 | — | 2.5 | 2.3 | 2.6 | — | — | — |
| H$^{(13)}C_3N$(12-11)[a] | 1.0 | 0.4 | **6.9** | — | 3.3 | **6.6** | — | — |
| $HC_5N$(34-33) | 1.0 | — | — | — | 2.2 | — | — | — |

Bold face signifies a factor of more than 5.

(a) signifies blend of HCC$^{13}$CN and HC$^{13}$CCN.

## 2.4 Discussion

### 2.4.1 Chemistry

The presence of shocks in the inner wind is discussed in Woods et al. (2003b), with a comparison to the modelling of IRC+10216 performed by Willacy & Cherchneff (1998).

#### 2.4.1.1 Photochemistry in the outer envelope

Many chemical models have been developed for the outer envelope of IRC+10216 (e.g., Millar & Herbst 1994; Doty & Leung 1998; Millar et al. 2000). The physical conditions in the outer parts of the wind ($\gtrsim 100\,\mathrm{R}_\star$) allow for the penetration of ambient ultraviolet radiation that induces a photochemistry. In Table 2.10 the derived column densities for IRC+10216 for a number of species produced in the envelope are compared to those from the photochemical model of Millar et al. (2000). In general the abundances agree well, given the uncertainties.

It is remarkable that the abundances generally show relatively little variation within the sample. Most apparent is the over-abundance of Si-bearing molecules in CIT6 (Sect. 2.4.3). Some of the abundances of IRAS15194-5115 also stand out and will be separately discussed in Sect. 2.4.2. There are no apparent trends with the stellar or circumstellar parameters. This would suggest that the physical structure in these sources indeed is much the same and that the initial atomic abundances are similar. When comparing the present sample of carbon stars to the sample of Olofsson et al. (1993a), which on the whole tend to have a low mass-loss rate ($\sim 10^{-7}\,\mathrm{M}_\odot\,\mathrm{yr}^{-1}$), the agreement in derived abundances for the star in common, CIT6, is very good: There is less than a factor 3 difference in the calculated abundances of HCN, CN and CS. However, in general, the sample of low mass-loss rate stars has calculated abundances which are systematically an order of magnitude greater than those calculated here. It must be noted that Olofsson et al. (1993a) use an excitation temperature of 20 K, twice that used in this analysis. Moreover, Schöier & Olofsson (2001) show that the mass-loss rates in the low mass-loss rate objects in Olofsson et al. (1993a) are underestimated by about a factor of 5 on average. This would explain the apparent discrepancy in calculated abundances between the high mass-loss rate objects here and the lower mass-loss rate objects in Olofsson et al. (1993a). Hence there seems not to be a marked difference in the molecular composition of high and low mass-loss carbon stars.

The large spread in the abundance of isotopomers containing $^{13}$C follows from the varying $^{12}$C/$^{13}$C-ratio among the sample sources. The $^{12}$C/$^{13}$C-ratio is related to the nucleosynthesis rather than the chemistry and reflects the evolutionary status of these stars. However, chemical fractionation may affect this ratio in certain molecules, in particular CO.

CN/HCN and HNC/HCN ratios can also be used to estimate the evolutionary status of carbon stars. CN is produced via the photodissociation of HCN by ultraviolet radiation, and as stellar radiation increases with evolution from AGB star to PPN to PN, so the CN/HCN ratio will increase (e.g., Bachiller et al. 1997a; Cox et al. 1992). HNC, formed from the dissociative recombination of $HCNH^+$, behaves in a similar way. In this sample there is a rather large spread in the CN/HCN ratio, from 0.07–0.68, and a value of 1.82 for CIT6 (see Sect. 2.4.3). This large spread is in contrast to Olofsson et al. (1993a), for example, who found a very narrow range (CN/HCN $\sim$0.65–0.70) in low mass-loss stars. However, there is excellent agreement with the results of Lindqvist et al. (2000). For the carbon stars IRC+10216, CIT6 and IRC+40540 they derive CN/HCN ratios of 0.16, 1.5 and 0.17, respectively, in comparison with the 0.22, 1.82 and 0.15 derived here. A CN/HCN ratio of $\sim$0.5 is typical in C-rich AGB stars (Bachiller et al. 1997b), increasing to $\sim$5 in PPNe. In fact, a ratio of 0.6–0.7 is predicted by the photodissociation model, with only a weak dependence on mass-loss rate (see Fig. 8 of Lindqvist et al. 2000). The HNC/HCN ratio seems to be split into two ranges in the present sample of carbon stars. IRC+10216, AFGL3068 and IRC+40540 have HNC/HCN ratios of $\leq$0.005, whilst the remaining stars have ratios of 0.01–0.03. The value derived for IRC+10216 is in agreement with that quoted in Cox et al. (1992). This seems to indicate that the sample stars are not well evolved, since a HNC/HCN ratio of $\sim$1 is expected in PPNe (e.g., Cox et al. 1992). Having said this, the HNC/HCN ratio does rapidly become of the order 1, as can be seen in models of the chemistry of PPN tori (Woods et al. 2003a).

Generally, it seems that to use the term "carbon chemistry" to refer to a paradigm of chemistry in C-rich evolved stars is reasonable. Of the sample stars here, given the variety of molecular species, there is very little difference in molecular abundances, save for two slightly curious sources, as detailed in the following subsections.

### 2.4.2 IRAS15194-5115

Of the derived abundances those obtained for IRAS15194-5115 stand out the most. In particular, the SiO and $C_4H$ abundances, in addition to the isotopomers containing $^{13}C$, appear significantly enhanced towards this source. $C_3H_2$ also appears to be greatly enhanced in this source, but, however, this molecule is only observed in one other star, IRC+10216. The $^{12}CO/^{13}CO$-ratio of 6 derived for IRAS15194-5115 is significantly lower than that of the others and that which is commonly derived for carbon stars. This value is certain, with the modelling of the CO emission being supported by intensity ratios for another four species, which agree to $\pm$30% (Table 2.8). The evolutionary status of this star is undetermined. Ryde et al. (1999) speculated that IRAS15194-5115 might be a massive (5–8 $M_\odot$) star in the last stages of evolution where its low $^{12}C/^{13}C$-ratio is the result of hot bottom burning (HBB). The increase of $^{14}N$ from the CNO cycle is a signature of HBB (Marigo 2001; Ventura et al. 2002), but so also is a decreasing C/O ratio. Given the uncertainty in the data presented here, this suggestion cannot be confirmed.

### 2.4.3 CIT6

CIT6 is another object outstanding in the sample. It has a CN/HCN ratio of $\sim$1.8, which suggests an advanced evolutionary status, but a low HNC/HCN ratio ($\sim$0.02), which suggests the contrary. Certainly the idea that CIT6 is well on its way to becoming a PPN has been put forward before (e.g., Trammell et al. 1994; Monnier et al. 2000; Začs et al. 2001; Schmidt et al. 2002).

The modelled $^{12}CO/^{13}CO$ ratio in this source agrees well with that carried out previously (Groenewegen et al. 1996; Schöier & Olofsson 2000). This ratio, however, does not agree with $^{12}C/^{13}C$ ratios derived from observations of other molecules and their $^{13}C$ isotopes, both in this paper (Table 2.8) and elsewhere (Kahane et al. 1992; Groenewegen et al. 1996).

A further point worth note is the comparative over-abundance of Si-bearing species which possibly indicates a less efficient freeze-out onto dust grains in this particular source.

## 2.5 Conclusions

The seven high mass-loss rate carbon stars presented here exhibit rich spectra at millimetre wavelengths with many molecular species readily detected. A total of

Table 2.10: Radial column densities ($cm^{-2}$) for species of circumstellar origin towards IRC+10216.

| Species | Observed[a] | MHB[b] | Obs./MHB |
|---|---|---|---|
| CN | 8.3 (14) | 1.0 (15) | 0.8 |
| HNC | 2.0 (13) | 8.4 (13) | 0.2 |
| $C_2H$ | 8.9 (14) | 5.7 (15) | 0.2 |
| $C_3H$ | 2.1 (13) | 1.4 (14) | 0.2 |
| $C_3N$ | 2.0 (14) | 3.2 (14) | 0.6 |
| $C_4H$ | 9.3 (14) | 1.0 (15) | 0.9 |
| $C_3H_2$ | 1.2 (13) | 2.1 (13) | 0.6 |
| $HC_3N$ | 9.1 (14) | 1.8 (15) | 0.5 |
| $CH_3CN$ | 9.9 (12) | 3.4 (12) | 2.9 |
| $HC_5N$ | 5.8 (15) | 7.1 (14) | 8.2 |

(a) Calculated from Tables 2.4 & 2.7.

(b) From chemical modelling by Millar et al. (2000).

47 emission lines from 24 molecular species were detected for the sample stars. The mass-loss rate and physical structure of the circumstellar envelope, such as the density and temperature profiles, was carefully estimated based upon a detailed radiative transfer analysis of CO. The determination of the mass-loss rate enables abundances for the remaining molecular species to be calculated. The derived abundances typically agree within a factor of five indicating that circumstellar envelopes around carbon stars have similar molecular compositions.

The most striking difference between the abundances are reflecting the spread in the $^{12}C/^{13}C$-ratio of about an order of magnitude between the sample stars. And, as explored in Woods et al. (2003b), the high abundance of SiO in the envelopes indicates that a shock has passed through the gas in the inner parts of the envelope. This is further corroborated by the relatively low amounts of CS and possibly HCN.

The abundances of species that are produced in the outer parts of the wind can be reasonably well explained by current photochemical models.

# Proto-planetary nebulae

In the previous chapter carbon stars were seen to be reasonably homogeneous: just asserting that a star is a carbon star is enough to imply very certain things about its chemistry – which molecules are likely to be found, and more importantly, in what abundance they are likely to be found. There are at least a couple of caveats, though, as have been seen – the $^{12}C/^{13}C$ ratio can play a role in shattering the stereotype, and also, as in the case of CIT6, when a carbon star starts to move off the AGB molecular fractional abundances can go awry.

The following three chapters show that great diversity can come from what seems to be a conformity on the AGB. Proto-planetary nebulae (PPNe) seem to be either molecule-rich or molecule-poor, but what is not clear is how this diversity begins, and how it develops.

# Chapter 3

# CRL618: A molecule-rich proto-planetary nebula

## 3.1 Introduction

This chapter deals with the modelling of a very well-known, and well-observed molecule-rich proto-planetary nebula, CRL618. A number of long carbon-chain molecules and cyanopolyynes have been detected in CRL618: a recent series of papers by Cernicharo and collaborators (Cernicharo et al. 2001a,b; Herpin & Cernicharo 2000) details detections of the carbon-based molecules $C_4H_2$, $C_6H_2$, $C_2H_4$, $CH_3C_2H$, $CH_3C_4H$, $C_6H_6$ (benzene) and the oxygen-bearing molecules OH and $H_2O$. Benzene, the simplest aromatic molecule, has not been seen in the carbon star IRC+10216, although water and OH, which are thought to arise from Kuiper Belt-like objects (Melnick et al. 2001; Ford et al. 2003) or through catalysis on metallic grain surfaces (Willacy 2004), have been detected.

The rich chemistry of CRL618 is thought to be a result of the variety of physical conditions in the object. A central photon-dominated region (PDR) is irradiated by intense UV rays from the B0-type star (Martin-Pintado et al. 1993; Fong et al. 2001) and this is surrounded by the remnant AGB envelope and bipolar lobes with a high-velocity wind (Cernicharo et al. 1989). Detailed mapping has been carried out (e.g., Hajian et al. 1996; Neri et al. 1992) and the existence of a central torus

of dust and gas seems clear (Lo & Bechis 1976). This torus is ostensibly the source of the majority of the molecular emission.

In modelling this PPN, only the molecular torus is taken into consideration. Any molecular gas in the external regions is neglected.

## 3.2 The physical model

To simplify what is a very complex source, the remnant CSE is considered to be in the form of a parcel, or slab, of gas moving away from the central star. Material between the slab and the central star is assumed to provide no extinction of the stellar UV flux. This assumption is reasonable given that dust formation does not occur after the AGB phase as well as the fact that the mass-loss rate is also (much) smaller in the PPN phase. Thus, the shielding of molecules to the internal UV field comes from the slab material itself. The external interstellar UV field is included in the model, yet is insignificant in comparison to the stellar UV field.

In a typical post-AGB object, this outwardly-moving parcel must co-exist with a fast bipolar outflow which probably has a wide opening angle, and mass-loads material from the torus. Despite the large outward radial velocity of the polar outflows, the torus moves outward slowly. Here, the torus-bipolar outflow interaction is ignored, although a recent study of such an interaction involving outflows in low-mass protostars (Viti et al. 2002) shows anomalously high abundances of $HCO^+$ which cannot be accounted for in this parcel model.

The gas density within the slab (or torus) is determined by the mass-loss rate, the expansion velocity and the initial radius at which the slab is positioned. The mass-loss is assumed to occur only for the time necessary to eject the slab. A homogeneous slab of a constant thickness, $\Delta r$, is adopted. Using mass conservation and the constraint that the slab subtends a constant solid angle, the internal density, $n(r)$, varies as $r^{-2}$, as does the intrinsic extinction, $A_{\rm V}(r)$, which is proportional to the product $n(r)\Delta r$. Assuming a thin slab means that density inhomogeneities within the slab are not considered, and that at any given time all points within the slab experience the same extinction, which is taken to be the extinction through the entire slab. This simplifies the actual situation, since density will vary with radius and with azimuthal angle. This thin slab approximation means that calculated model abundances cannot quite be considered equivalent to true (observed) column densities; this would require a more complex model which would take radial inhomogeneities into account. However, given the uncertainties in the present

knowledge of the geometrical structure of objects such as CRL618, these complexities have been neglected. It is assumed that the model gives a satisfactory snapshot picture of the object.

Detailed calculations indicate that photodissociation is extremely rapid once $A_{\rm V}$ falls to below 10 magnitudes or so. For example, the visual extinction through circumstellar matter outflowing at an expansion velocity of $15\,{\rm km\,s^{-1}}$ means that photodissociation destroys most molecules within 200 years (compare with the following chapter). The fact that molecules are detected in some PPNe implies that the expansion velocity of the slab must be low, or alternatively that the molecular gas must be in a long-lived disk. All calculations presented in this chapter use an expansion velocity of $5\,{\rm km\,s^{-1}}$. This is the velocity attributed to the expanding torus in the Red Rectangle (Jura et al. 1995; Knapp et al. 2000), a slightly more evolved object, and close to that associated with the expanding torus of the peculiar star, HD101584 (Olofsson & Nyman 1999).

Table 3.1 lists all the initial conditions for the model of CRL618; for the UV flux, an initial enhancement factor of $G/G_0$=3.2×10$^6$ over the interstellar field is adopted, following Herpin & Cernicharo (2000), who give an enhancement of 2×10$^5$ at $r$=10$^{16}$ cm. This enhancement factor becomes diluted with radius, as $1/r^2$. Calculations for even larger enhancements have been performed, but there is little sensitivity to the flux – the result of efficient dust extinction when $A_{\rm V}$ is larger than about 20 mags. The stellar UV field is modelled upon an enhanced interstellar radiation field, since tabulated photodissociation and photoionisation rates are based on the interstellar field. However, the temperature of a B-type star is not too dissimilar from the temperature of the interstellar radiation field, so that the extinction law used may introduce larger uncertainties than the choice of radiation field.

Enhanced ionisation by hard X-rays has also been considered. These can penetrate through a column density of approximately $10^{23-24}\,{\rm cm^{-2}}$ and increase the abundances of charged molecules (Glassgold et al. 1997), which are needed to enhance the speed of the chemistry. X-ray emission is a far more likely mechanism for the increased ionisation than enhanced cosmic-ray ionisation. Although both act in similar ways, the central source provides a possible source of X-rays; e.g., via accretion on a compact companion (Soker & Kastner 2002; Livio & Shaviv 1975) for which there is indirect evidence for several bipolar PPNe (Bujarrabal et al. 2001; Zijlstra et al. 2001). In contrast, the cosmic-ray intensity is mostly constant within the Galaxy, varying by no more than 30% within 15 kpc Galactocentric distance

Table 3.1: Initial physical conditions of the model.

| Parameter | Value |
|---|---|
| $\dot{M}$, ($M_\odot\,yr^{-1}$) | $3.2 \times 10^{-3}$ |
| $T$, (K) | 250 |
| Inner radius, $r_i$, (cm) | $2.5 \times 10^{15}$ |
| Expansion velocity, $v_e$, ($km\,s^{-1}$) | 5.0 |
| Initial $H_2$ density, $n(H_2)$, ($cm^{-3}$) | $1.6 \times 10^9$ |
| Initial extinction, $A_V$, (mags) | 160 |
| Slab thickness, $\Delta r$, (cm) | $9.4 \times 10^{13}$ |
| Initial UV flux enhancement, $G/G_0$ | $3.2 \times 10^6$ |
| Initial CR enhancement, $\zeta/\zeta_0$ | 500 |

(Strong & Moskalenko 1998; Hunter et al. 1997). Since cosmic-ray ionisation is already a standard component of dark-cloud chemistry, this is used to simulate X-ray ionisation. The standard model has an initial enhancement factor, $\zeta/\zeta_0$=500, which also is diluted as $1/r^2$, until it reaches the standard interstellar value of $\zeta_0$=$1.3\times10^{-17}\,s^{-1}$. The effects of varying $\zeta$ are discussed in Sect. 3.4.6. CRL618 has not (yet) been detected in X-ray emission (Guerrero et al. 2000), but it must be pointed out that soft X-rays are likely to be rapidly absorbed in material of column density $>10^{21}\,cm^{-2}$. Cox et al. (1992), following Deguchi et al. (1990), determined that the central star of CRL618 was not hot enough itself to produce the required X-ray flux (to produce the required abundance of $HCO^+$).

The temperature of the moving slab is assumed to remain constant at 250 K despite the weakening of the stellar radiation field and lowering of the ionisation rate with time. Although this simplifying assumption can be removed, most of the important chemical reactions in the network do not evince a strong temperature dependence. More detail on the effects of temperature variation is given in Sect. 3.5.2.

## 3.3 The chemical model

Since CRL618 is carbon-rich, the reaction network is based upon that which Millar et al. (2000) used to describe the chemistry in the CSE around IRC+10216. This network was primarily developed to describe the formation of large carbon chain molecules, including the cyanopolyynes with up to 23 carbon atoms. The network incorporates an extensive radical chemistry, especially involving $C_2$ and $C_2H$, the daughter products of $C_2H_2$, which are far more abundant in circumstellar envelopes

Table 3.2: Adopted initial fractional abundances of parent species, with respect to $n(H_2)$.

| Species | Initial fractional abundance |
|---|---|
| He | $1.5 \times 10^{-1}$ |
| CO | $6.0 \times 10^{-4}$ |
| $N_2$ | $2.0 \times 10^{-4}$ |
| $C_2H_2$ | $5.0 \times 10^{-5}$ |
| HCN | $8.0 \times 10^{-6}$ |
| CS | $4.0 \times 10^{-6}$ |
| $CH_4$ | $2.0 \times 10^{-6}$ |
| $NH_3$ | $2.0 \times 10^{-6}$ |
| $H_2S$ | $1.0 \times 10^{-6}$ |

than in dense interstellar clouds. Also incorporated are the rapid neutral-neutral reactions discussed in Millar & Herbst (1994). The network also contains reactions involving negative ions, which turn out to be important in IRC+10216 but are less significant here due to the lower fractional ionisation in the higher density slab adopted in the PPN model. The species $H_2O$ and OH, which have been detected in CRL618, are not included in the reaction network. In summary, the model comprises some 407 species in 6 elements (H, He, C, N, O, S) with 3880 reactions. Initial fractional abundances of parent molecules relative to $H_2$ are given in Table 3.2. These are "standard" initial abundances, in the sense that these were used for the previous model of IRC+10216, and are typical of a carbon-rich AGB star. The initial C/O ratio is $\approx$1.1. The initial abundances of the AGB phase are taken as initial abundances for the PPN phase. Self-shielding of CO is included using the approach of Mamon et al. (1988). Self-shielding of somewhat less abundant parent species is not considered, although it may play a role.

## 3.4 Results

Figure 3.1 shows the fractional abundances of several molecules relative to $n(H_2)$ as a function of radial distance from the central star. The abundances all show one of two behaviours. In the case of parent molecules, a decrease at $8.9 \times 10^{15}$ cm occurs when photodissociation finally cuts in. For simplicity, this radius will be called the Radiation Catastrophe (RC) radius. The rapid decrease in abundances is due to the fact that the radiation field is much enhanced over the interstellar field, so that the photodissociation time scales are very short at small $A_V$. For daughter

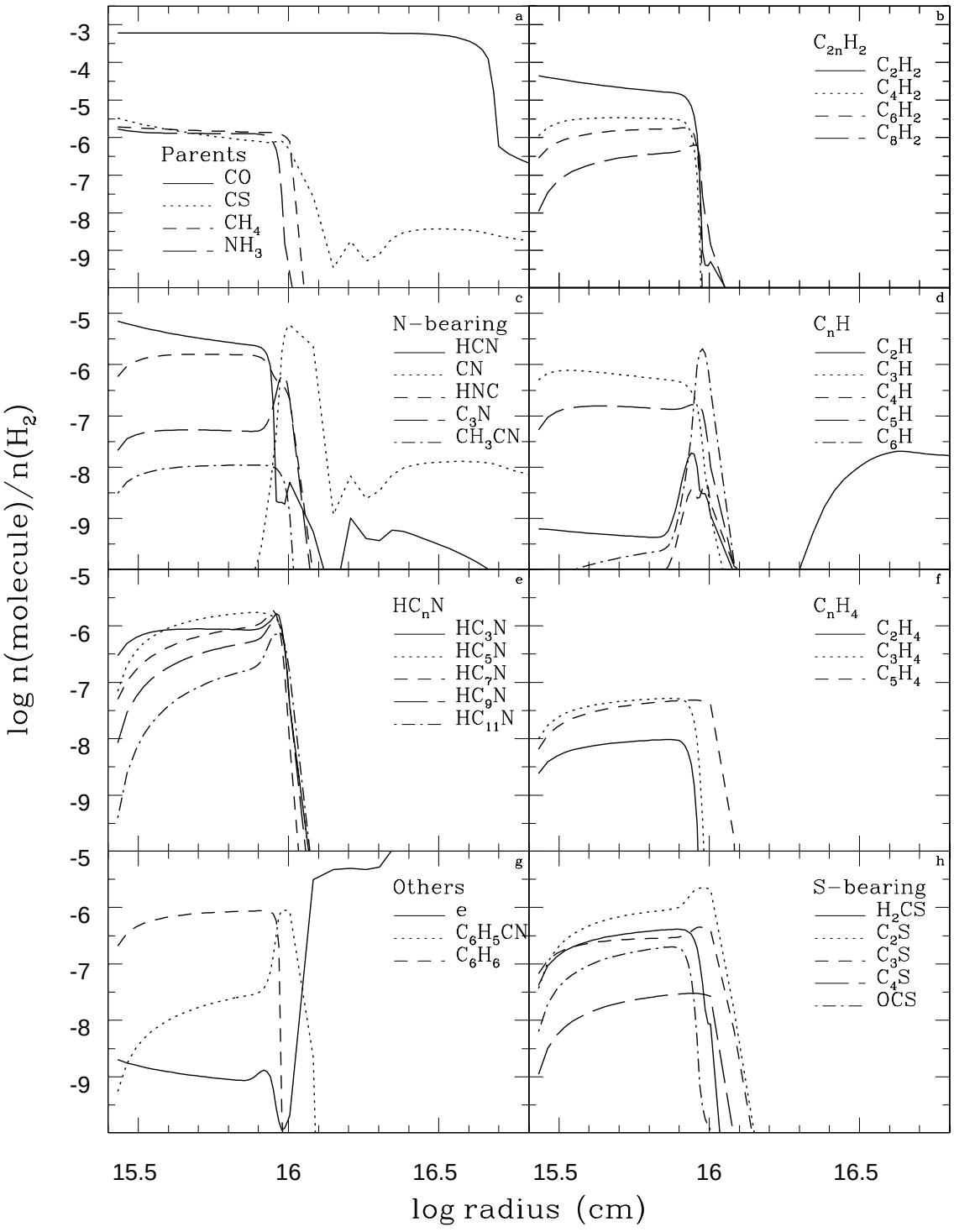


Figure 3.1: The variation of molecular abundances with radial distance in the standard PPN model, for an initial ionisation rate 500 times that of the standard interstellar value.

products, there is a rise in abundance as parents are photodissociated but again they experience a very rapid fall-off once photons dominate their destruction.

Although the fractional abundances of daughter products tend to be highest in the photodissociation region, the picture is different if one considers column densities since the overall gas density decreases with increasing radius as $r^{-2}$. In terms of column densities, those of daughter products tend to be much flatter vs. radius while those of parent species decrease strongly even before the photodissociation region. In general, the picture that emerges is that ion-molecule chemistry occurs at the smallest radii considered due to the enhanced ionisation rate. The enhanced cosmic ray (CR) ionisation rate also results in large numbers of photons induced by CR bombardment; these photons produce radicals and ions and accelerate the chemistry. The overall chemistry at small radii produces small fractional abundances of many daughter species but the column densities are enhanced by the high overall initial density. The production of large column densities happens very quickly because of the small time interval between collisions at small radii (1 s).

Molecule formation, and especially complex molecule formation, is unexpectedly efficient in the photodissociation region. For example, the cyanopolyynes up to $HC_{11}N$ all have fractional abundances above $10^{-7}$ once the slab has reached the RC radius, while benzene and its derivative, benzonitrile, $C_6H_5CN$, reach a maximum fractional abundance of about $\sim 10^{-6}$. The reactions contributing to the formation of these molecules are discussed in the following sub-sections, emphasising the dominant processes at the RC radius, which is reached in ∼425 years. This radius is approximately where the majority of species are most abundant.

### 3.4.1 Small molecules

In this section the formation routes to simple molecules such as HNC, CN and $C_2H$ and those containing sulphur are discussed.

#### 3.4.1.1 HNC

HNC is made in the dissociative recombination of $HCNH^+$, which itself is formed by proton transfer reactions with the parent molecule, HCN. The column density of HNC is less than that of HCN until the RC radius, when loss of HCN in reactions with $C_{2n}H$ ($n \geq 2$) becomes significant. HNC is also lost through analogous reactions, mostly with $C_2H$. The time at which the abundances reach equality is roughly 425 years. Herpin & Cernicharo (2000) found equal column densities of HCN and

HNC in CRL618. This equality is in contrast to the case of IRC+10216, in which HCN is much more abundant than HNC. The difference is unlikely to reflect only the age of the shell: IRC+10216 has a large shell which indicates extended mass loss. But there are other differences: (i) IRC+10216 is an AGB star with continuing mass loss, while CRL618 is a post-AGB star with a detached shell. The observed column densities in IRC+10216 are affected by LTE chemistry in the photosphere; (ii) IRC+10216 has a higher expansion velocity than the value assumed here for the torus of CRL618 which reduces the timescale available for the chemistry (CRL618 also has a very fast polar outflows which are not modelled, but the dominant molecular mass is likely to be in the shielded torus); (iii) the shell density in the wind of IRC+10216 is likely lower than in the disk of CRL618, due to the (expected) difference in expansion velocities, which results in a slower conversion of parent HCN to HNC.

The increasing HNC/HNC abundance ratio might be a useful indicator of evolution in the PPN phase. The difference with IRC+10216 suggests the possibility that it can be used to measure the product of density and expansion timescale.

#### 3.4.1.2 CN

CN is the daughter product of the parent molecule HCN. Its radial abundance distribution is rather sharply peaked at around 1–3 $\times$ $10^{16}$ cm, because it is formed by the photodissociation of HCN and HNC. Its abundance inside this radius is much less than that of HNC, also formed from HCN, because of the rapid neutral reactions it undergoes with the hydrocarbons of the type $C_{2n}H_2$, to form the cyanopolyyne chain.

#### 3.4.1.3 $C_2H$

The ethynyl radical is produced from parent $C_2H_2$ by UV and CR-induced photons. It is a very reactive radical and is involved in the creation of many other chain species. It reacts with S and CS to form $C_2S$ and $C_3S$, with $C_2H_2$ to form $C_4H_2$, and helps build larger chains by insertion reactions (see below).

#### 3.4.1.4 OCS

OCS if formed in a series of reactions initiated by the reaction:

$$S + CH_2 \longrightarrow HCS + H,$$

followed primarily by :

$$O + HCS \longrightarrow OCS + H,$$

and by the radiative association reaction:

$$S + CO \longrightarrow OCS + h\nu.$$

It has a fractional abundance of $\sim 2 \times 10^{-8}$ around the RC radius.

#### 3.4.1.5 $H_2CS$

Thioformaldehyde is formed primarily in the neutral reaction:

$$S + CH_3 \longrightarrow H_2CS + H,$$

and destroyed in proton transfer reactions, and by UV and CR-induced UV photons. Its formation is very efficient and its fractional abundance is $2.7 \times 10^{-7}$ at the RC radius.

### 3.4.2 Hydrocarbons

The formation of hydrocarbons is initiated by reactions involving the parent molecule $C_2H_2$ (acetylene) and its daughters[1] $C_2H$ and $C_2H_2^+$ (see reactions 3.1 to 3.4). These reactions can be generalised to synthesise larger, even-numbered hydrocarbons ($C_{2n}H_m$) (reactions 3.5 and 3.6).

$$C_2H + C_2H_2 \longrightarrow C_4H_2 + H \quad (3.1)$$

$$C_2H + C_2H \longrightarrow C_4H + H \quad (3.2)$$

$$C_2H_2^+ + C_2H_2 \longrightarrow C_4H_3^+ + H \quad (3.3)$$

$$C_2H_2^+ + C_2H_2 \longrightarrow C_4H_2^+ + H_2 \quad (3.4)$$

$$C_2H + C_{2n}H_2 \longrightarrow C_{2n+2}H_2 + H \quad (3.5)$$

$$C_2H_2^+ + C_{2n}H_m \longrightarrow C_{2n+2}H_{m+1}^+ + H \quad (3.6)$$

Since these reactions involve the abundant parent acetylene, the abundances of the even-numbered hydrocarbons ($C_{2n}H_2$) are generally larger than those of the odd-

[1] $C_2H_2 + h\nu \longrightarrow C_2H + H$; $C_2H_2 + h\nu \longrightarrow C_2H_2^+ + e$

numbered hydrocarbons ($C_{2n+1}H_2$). Reactions of atomic carbon (which initially comes from CR-induced photodissociation of CO) with $C_2H_2$ and $C_2H$, and other even-numbered hydrocarbons, also help increase the chain length and produce the odd-numbered species $C_{2n+1}$ and $C_{2n+1}H$. Figure 3.1 shows that the odd-numbered hydrocarbon radicals, $C_{2n+1}H$, are more abundant than their even-numbered counterparts for distances less than about $8 \times 10^{15}$ cm. This is primarily due to two reasons: (i) the $C_{2n}H$ species are destroyed more rapidly in reactions with parent HCN and $C_2H_2$, and (ii) their formation rates, which depend ultimately on the CR-induced photodissociation of $C_2H_2$, are slower than those of the odd-numbered chain, which is driven by the C + $C_2H_2$ reaction.

Methane, $CH_4$, is another parent molecule involved in hydrocarbon formation. Typically it is about ten times less abundant than acetylene in C-rich CSEs. Synthesis of larger hydrocarbons proceeds at large radii via $C^+$ insertion reactions or condensation reactions, e.g.,

$$\begin{aligned} CH_4 + C^+ &\longrightarrow C_2H_2^+ + H_2 \\ CH_4 + C^+ &\longrightarrow C_2H_3^+ + H \\ CH_4 + CH_3^+ &\longrightarrow C_2H_5^+ + H_2 \end{aligned}$$

Chain-lengthening then proceeds via further condensation reactions with $C_2H_2$ and $C_2H$, plus reactions with C and $C^+$.

### 3.4.3 Cyanopolyynes

The cyanopolyynes are synthesised via a variety of mechanisms. The first member of this family, $HC_3N$, is formed via three reactions. One important reaction to produce this species uses CN and acetylene (Howe & Millar 1990):

$$CN + C_2H_2 \longrightarrow HC_3N + H. \tag{3.7}$$

This reaction is the dominant source of $HC_3N$ in interstellar clouds. Here it also dominates throughout most of the slab. Another important reaction is the (relatively slow) process between HCN and $C_2H$:

$$HCN + C_2H \longrightarrow HC_3N + H. \tag{3.8}$$

This reaction has now been measured (Hoobler & Leone 1997) and calculated by Fukuzawa & Osamura (1997) to have a small activation energy barrier. This barrier effectively prevents reaction (3.8) at the chosen temperature of 250 K. A third important reaction is the analogous process involving HNC:

$$\mathrm{HNC} \; + \; \mathrm{C_2H} \; \longrightarrow \; \mathrm{HC_3N} \; + \; \mathrm{H}, \tag{3.9}$$

which actually becomes the dominant production method of $HC_3N$ just before photons become appreciable. After photons become appreciable, $HC_3N$ is produced mainly by the reaction between atomic nitrogen and $C_3H_2$.

There are two main routes to the production of more complex cyanopolyynes in the model. Firstly, reactions between smaller cyanopolyynes and hydrocarbon radicals serve to produce larger cyanopolyynes; viz.,

$$\begin{aligned} \mathrm{HC_{2n+1}N} \; + \; \mathrm{C_2H} \quad &\longrightarrow \quad \mathrm{HC_{2n+3}N} \; + \; \mathrm{H}, \quad n \geq 1, \\ \mathrm{HC_{2n-3}N} \; + \; \mathrm{C_4H} \quad &\longrightarrow \quad \mathrm{HC_{2n+1}N} \; + \; \mathrm{H}, \quad n \geq 2, \end{aligned}$$

by adding carbon atoms to the skeletal chain of the cyanopolyynes. Secondly, CN and HCN react with even-numbered hydrocarbons and radicals to produce the larger cyanopolyynes directly:

$$\begin{aligned} \mathrm{CN} \; + \; \mathrm{C_{2n}H_2} \quad &\longrightarrow \quad \mathrm{HC_{2n+1}N} \; + \; \mathrm{H} \\ \mathrm{HCN} \; + \; \mathrm{C_{2n}H} \quad &\longrightarrow \quad \mathrm{HC_{2n+1}N} \; + \; \mathrm{H}. \end{aligned}$$

Figure 3.1 shows that cyanopolyyne synthesis is very efficient under the conditions of our model, as it was found to be in IRC+10216, in agreement with the observations. The cyanopolyynes up to $HC_9N$ have been detected in IRC+10216; this is also the largest cyanopolyyne detected to date in a post-AGB object, in this case the PPN CRL 2688 (Truong-Bach et al. 1993). The cyanopolyyne $HC_9N$ is formed in our model at a distance of $8 \times 10^{15}$ cm by the following reactions: $C_2H$ + $HC_7N$ (58%); $C_4H$ + $HC_5N$ (17%); $C_8H$ + HCN (16%). Loss at this radius is mostly through dissociative recombination (18%), and reactions which build the larger cyanopolyynes (68%).

### 3.4.4 Organo-sulphur chains

The organo-sulphur chains, $C_2S$, $C_3S$ and $C_4S$ are included in this model. The major reactions in their formation involve atomic sulphur and parent CS:

$$\begin{aligned}
S + C_2H &\longrightarrow C_2S + H \\
CS + C_2H &\longrightarrow C_3S + H \\
S + C_4H_3^+ &\longrightarrow HC_4S^+ + H_2 \\
S + C_4H_2^+ &\longrightarrow HC_4S^+ + H \\
HC_4S^+ + e &\longrightarrow C_2S + C_2H \\
&\longrightarrow C_3S + CH \\
&\longrightarrow C_4S + H
\end{aligned}$$

The analogous reactions to form larger organo-sulphur chains have not been included in this model; Millar et al. (2001) have discussed this possibility for the case of IRC+10216. The calculated abundances for $C_2S$ and $C_3S$ are significant, that for $C_4S$ less so as it is formed in an ion-molecule, rather than neutral-neutral, reaction. Millar et al. (2001) have shown that the spin-allowed reaction:

$$S + C_4H \longrightarrow C_4S + H$$

increases the abundance of $C_4S$ in IRC+10216 by over an order of magnitude.

### 3.4.5 Benzene

Benzene formation under the adopted conditions for CRL618 is much more efficient than in interstellar clouds or cool circumstellar shells around AGB stars. The synthesis relies on relatively large fractional abundances of both $HCO^+$ and $C_2H_2$, contrary to the interstellar case (McEwan et al. 1999, see below). The former ion is only detected at very low levels in AGB star envelopes but is observed in PPNe in large abundances (Deguchi et al. 1990), which may reflect the much greater level of ionising radiation (X-rays, or cosmic ray particles) in PPNe, or the passage of shock waves.

The interstellar route to benzene formation has been studied by McEwan et al. (1999) who used laboratory measurements of three-body association reactions to infer radiative association rate coefficients involving atomic hydrogen to synthesise benzene. In CRL618, atomic hydrogen is not particularly abundant, $1 \times 10^{-7}$

relative to molecular hydrogen, and does not contribute to the formation of benzene until a distance of $10^{17}$ cm from the star (according to the model), some 50 times further out than the peak abundance of benzene, although the $C_2H_2$ abundance is so low by this distance that benzene formation is inefficient.

For the conditions adopted here a more efficient synthesis of benzene is found, with fractional abundances of $\sim 10^{-6}$ being reached. At a distance of $\sim 8 \times 10^{15}$ cm, the major route to the production of benzene is:

$$C_4H_3^+ + C_2H_2 \longrightarrow c\text{-}C_6H_5^+ + h\nu \quad (3.10)$$

$$c\text{-}C_6H_5^+ + H_2 \longrightarrow c\text{-}C_6H_7^+ + h\nu \quad (3.11)$$

$$c\text{-}C_6H_7^+ + e \longrightarrow c\text{-}C_6H_6 + H. \quad (3.12)$$

Reaction (3.10) has been measured in the laboratory by Scott et al. (1997) in the three-body limit and shown to produce cyclic $C_6H_5^+$. The corresponding radiative association rate coefficient has been included in models for some time. The radiative association rate coefficient for reaction (3.11) was determined by McEwan et al. (1999).

$C_4H_3^+$ is formed via a number of reactions, most importantly,

$$HCO^+ + C_4H_2 \longrightarrow C_4H_3^+ + CO \quad (3.13)$$

$$C_2H_2^+ + C_2H_2 \longrightarrow C_4H_3^+ + H \quad (3.14)$$

$$C_2H_3^+ + C_2H_2 \longrightarrow C_4H_3^+ + H_2 \quad (3.15)$$

where the ionised acetylene (Eq. 3.14), is produced by cosmic-ray induced photoionisation of acetylene, and $C_2H_3^+$ is formed from proton transfer reactions with acetylene:

$$HCO^+ + C_2H_2 \longrightarrow C_2H_3^+ + CO. \quad (3.16)$$

Hence the formation of $C_2H_2^+$ and $C_2H_3^+$ (Eqs. 3.14, 3.15) at small radii is highly dependent on abundances of $HCO^+$ and $H_3^+$, which in turn are dependent on the flux of ionising radiation.

$$H_3^+ + CO \longrightarrow HCO^+ + H_2 \quad (3.17)$$

$$N_2H^+ + CO \longrightarrow HCO^+ + N_2 \quad (3.18)$$

The reaction of $H_3^+$ with CO is the dominant loss-mechanism for this ion, so that the molecular abundances calculated are independent of the choice of the rate coefficient for the dissociative recombination of $H_3^+$ with electrons.

At this radius, benzene is destroyed mainly through reaction with CN, to form benzonitrile, $C_6H_5CN$, via the reaction:

$$CN \; + \; C_6H_6 \quad \longrightarrow \quad C_6H_5CN \; + \; H \tag{3.19}$$

and by proton transfer reactions followed by dissociative recombination.

### 3.4.6 Ionisation

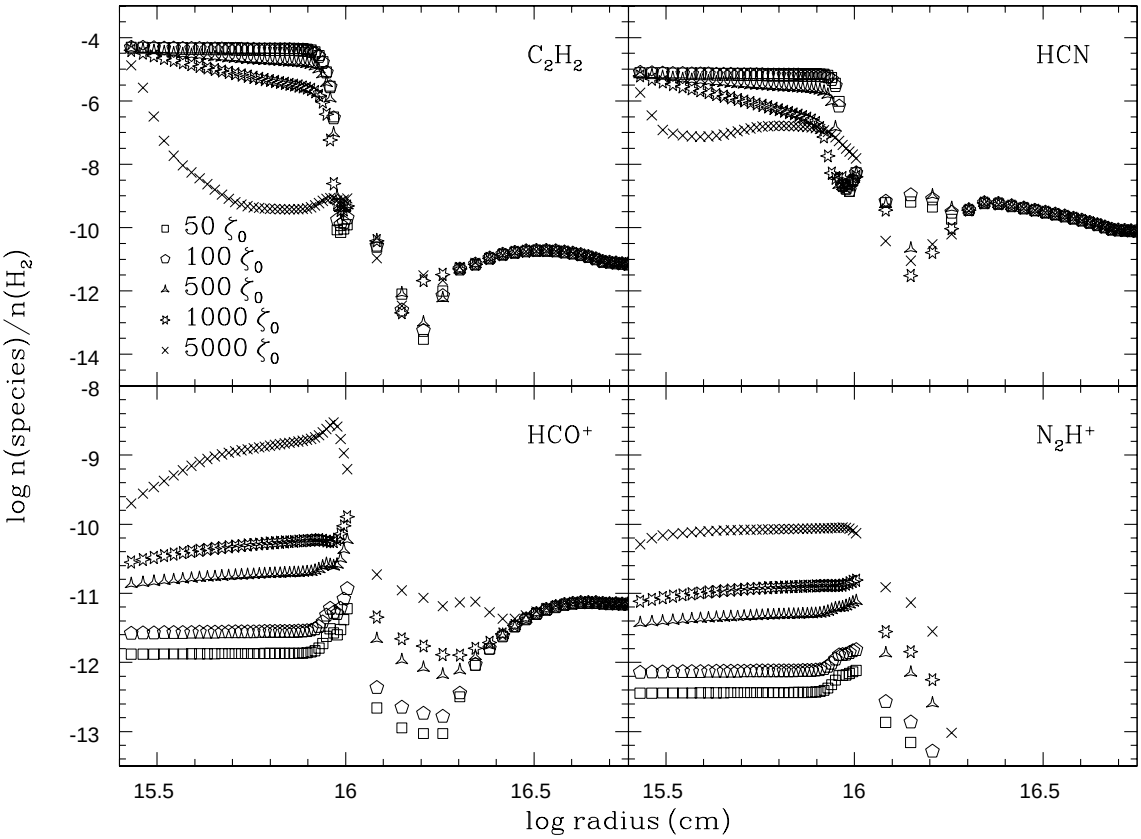


Figure 3.2: The influence of the ionisation rate on the abundances of some species is shown. Once the initial rate becomes more than about 500 times larger than the standard interstellar rate, parent molecules become destroyed rapidly.

In these models an initial ionisation rate some 500 times larger than the standard interstellar rate of $1.3{\times}10^{-17}\,s^{-1}$ has been adopted, in order to simulate the larger ionisation that may be caused by X-ray emission from the central object(s).

In order to test the sensitivity of our results to this rate, a series of models with the rate enhanced over the interstellar value by factors of 10–5 000 were run. Figure 3.2 shows the results of some of these calculations for a small number of selected species. For initial ionisation enhancement factors greater than 500, the ionisation rate becomes so large that parent molecules, such as $C_2H_2$ and HCN, are destroyed very rapidly. The figure shows, for example, that the abundance of $C_2H_2$ is reduced by over 5 orders of magnitude by the time the slab has reached about $1{\times}10^{16}$ cm (or within a time-scale of 500 years for an expansion velocity of $5\,\mathrm{km\,s^{-1}}$) with an initial ionisation enhancement of 5 000. Thus, enhancements larger than 500 are neglected, since they produce molecular slabs which are too short lived to be of interest. With the adopted ionisation rate, the precipitous drop in abundance of parent species occurs mainly in the photodissociation region at a radius of $1{\times}10^{16}$ cm.

## 3.5 The proto-planetary nebula, CRL618

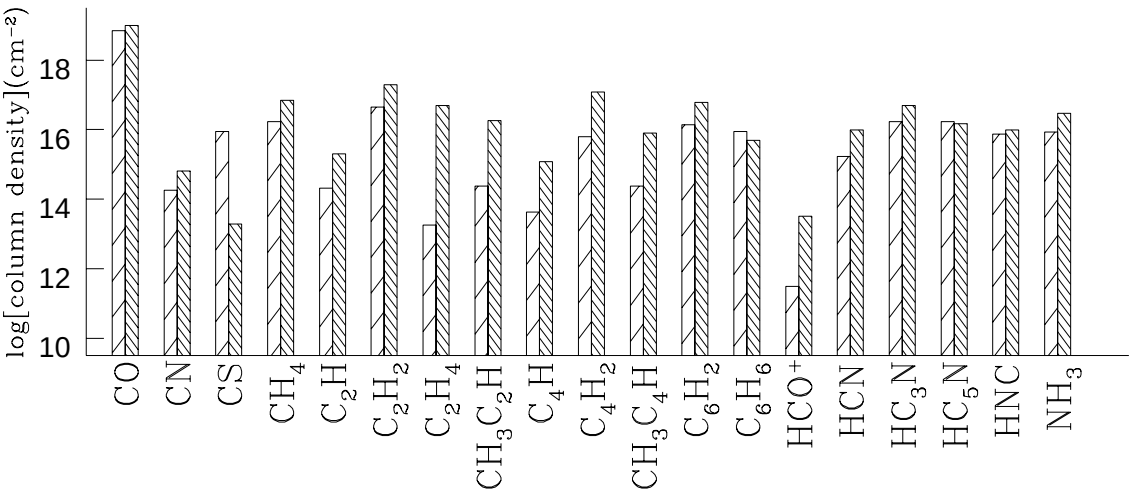


Figure 3.3: Comparison between observed (heavy hashing) and model (light hashing) column densities at $8.9 \times 10^{15}$ cm, for CRL618.

The model of PPN chemistry has been applied to the specific case of CRL618. CRL618 is a particularly well-observed PPN, with a large amount of molecular data available for study.

### 3.5.1 Comparison with CO observations

Observations of CO have been able to give structural, kinematic and mass-loss information. Various papers (e.g., Herpin & Cernicharo 2000; Meixner et al. 1998; Hajian et al. 1996; Martin-Pintado et al. 1995; Phillips et al. 1992; Neri et al. 1992) have reported quantitative sizes for structures within CRL618. Reasonable distance estimates range between 1 300 pc (e.g., Sopka et al. 1989) and 1 700 pc (e.g., Bujarrabal et al. 1988), so for simplicity CRL618 is assumed to be 1 500 pc away. The 'core' is given as 15″ (Hajian et al.) or 19″ (Meixner et al.) which corresponds to radial distances from the star of 1.7 and 2.1 $\times$ $10^{17}$ cm at 1 500 pc. At 19 km s$^{-1}$, the envelope expansion velocity attributed to CRL618 by Fuente et al. (1998), among others, this gives an expansion timescale of some 3 000–3 500 years. Also, Hajian et al. identify a region of high density subtending $\approx$3-4″, which equates to a radial distance of 3.4–4.5$\times$$10^{16}$ cm at 1 500 pc. Martín-Pintado et al. observed a dense disk, of some 1″ in extent, which surrounds a molecular 'hole' of 0.″42, which could be the edge of the HII region. In the model of a circumstellar slab, CO is predicted to be reasonably abundant out until around 5 $\times$ $10^{16}$ cm ($\sim$4.″5 on the sky), although still has abundances of $\approx$$10^{-7}$ at larger distances. Observable species (other than CO) are depleted by a radial distance of 0.9–1.3$\times$$10^{16}$ cm, which is 0.″8–1″ on the sky. The region modelled in this chapter, a disk with very slow expansion, would correspond to the dense region found by Martin-Pintado et al. (1995) in $NH_3$ emission.

### 3.5.2 Comparison with other molecular observations

To compare the calculated column densities with observed values, a radius, the RC radius, is chosen. This is close to the distance where photodissociation destroys the molecules heavily. This radial distance has some observational significance, as discussed in the previous section. At smaller distances, some daughter species have not yet achieved large abundances, although other daughters can have peaked, whilst parents are most abundant at the inner radius. At distances closer to the radius where photodestruction sets in (0.9-1.3$\times$$10^{16}$ cm), other daughter species achieve even larger column densities than at the distance chosen. Table 3.3 gives the calculated column densities at the RC radius, along with their peak values, and compares both of these to observations where available. The observational results shown in Table 3.3 are only those reported as column densities; results reported as fractional abundances are discussed separately below, and shown in Table 3.4. The

purpose of including the peak abundances is to show that if the model does not produce sufficient material at the radial distance chosen, it in all likelihood can do so at other radial distances. At the distance chosen, the calculated abundances are changing rapidly (or are about to do so at slightly larger distances), so that a truly quantitative comparison between theory and observation is difficult. In addition, it is clear that there are widely divergent values for the observed column densities of some species, notably HCN, HNC, $HC_3N$, and $HC_5N$, and that in particular the column densities derived from single-dish radio telescopes are usually much lower than those derived from the *ISO* observations. This is probably a result of both beam dilution and the fact that the millimetre-wave observations are not as sensitive to the hot dense gas as the infrared observations. A further possibility results from the complexity of the source, with the result that pointing errors could also be significant. Consider the millimetre-wave results of Bujarrabal et al. (1988, 1994), who give fractional abundances of several molecules also observed by *ISO*. Even within these two papers, differences in abundances of an order of magnitude can occur (for CS, HCN, $HC_3N$). In Bujarrabal et al. (1994), the fractional abundance of CS is given as $4.1 \times 10^{-7}$, equivalent to a column density of $4.9 \times 10^{15}\,\mathrm{cm}^{-2}$, compared to $1.9 \times 10^{13}\,\mathrm{cm}^{-2}$ derived by Bachiller et al. (1997a), also from millimetre-wave observations. At this point, it seems that the calculated abundances give a reasonable, but not perfect, match to the observed values. Certainly, and most importantly, the degree of molecular complexity seen in the *ISO* results is well reproduced here.

Looking at the individual species in Table 3.3, the calculated column densities at the RC radius are within an order of magnitude of observed values for CO, CN, $NH_3$, $CH_4$, $C_2H$, $C_2H_2$, $C_6H_2$ and $C_6H_6$. The calculated results for $HC_3N$ and $HC_5N$ lie reasonably close to the upper range of the observed values. Both HCN and HNC are within the range of observed column densities given, and fractional abundances of these species agree well with observations. There appears to be too much CS and far too little $C_2H_4$, $C_4H$, $C_4H_2$, $CH_3C_2H$, $CH_3C_4H$ and $HCO^+$. The larger molecule $HC_7N$ is also very over-abundant relative to the observed column density (Fukasaku et al. 1994) but it is noted that this is derived from single-dish observations and that the $HC_5N$ column density derived by them is a factor of 250 below the IR column density derived from the *ISO* observations. In summary, there is good agreement with 60% of observed species at the RC radius , and moreover all species are within an order of magnitude of observed column densities, save $HCO^+$, $C_2H_4$ and $C_4H$, at some radial point. A comparison of column densities is also shown in Fig. 3.3.

Table 3.3: Calculated and observed column densities $N$ ($cm^{-2}$) in CRL618. Subscripts C and P refer, respectively, to calculated values at the chosen distance and peak values. The notation $a\,(b)$ represents $a \times 10^b$.

| Species | $N_C$ | $N_P$ | $N_{OBS}$ | Species | $N_C$ | $N_P$ | $N_{OBS}$ |
|---|---|---|---|---|---|---|---|
| CN | 1.8 (14) | 5.5 (16) | 6.5 (14)[a] | HCN | 1.7 (15) | 9.0 (17) | 5.8 (14)[b]–2.0 (18)[c] |
| HNC | 7.4 (15) | 1.1 (17) | 4.2 (13)[a]–1.0 (16)[d] | $NH_3$ | 8.7 (15) | 2.2 (17) | 3.5 (16)[e,f] |
| $C_3$ | 1.9 (15) | | | $C_4$ | 2.2 (14) | | |
| $C_5$ | 1.9 (14) | | | $C_6$ | 3.4 (13) | | |
| $CH_4$ | 1.7 (16) | 2.5 (17) | 7.0 (16)[e] | $C_2H_4$ | 1.8 (13) | 4.8 (14) | 5.0 (16)[e] |
| $C_2H$ | 2.1 (14) | 2.4 (14) | 2.0 (15)[b] | $C_3H$ | 2.8 (15) | | |
| $C_4H$ | 4.2 (13) | 3.7 (13) | 1.2 (15)[b] | $C_5H$ | 2.0 (15) | | |
| $C_6H$ | 2.5 (15) | | | $C_7H$ | 3.6 (14) | | |
| $C_8H$ | 6.7 (14) | | | $C_2H_2$ | 4.4 (16) | 5.7 (18) | 2.0 (17)[g] |
| $C_3H_2$ | 9.2 (13) | | | $C_4H_2$ | 6.3 (15) | 2.3 (17) | 1.2 (17)[g] |
| $C_5H_2$ | 1.9 (15) | | | $C_6H_2$ | 1.4 (16) | 7.7 (16) | 6.0 (16)[g] |
| $C_7H_2$ | 7.5 (15) | | | $C_8H_2$ | 7.6 (15) | | |
| $C_3N$ | 1.9 (15) | | | $C_5N$ | 4.0 (14) | | |
| $HC_3N$ | 1.7 (16) | 6.0 (16) | 1.3 (14)[a]–5.0 (16)[g] | $HC_5N$ | 1.7 (16) | 5.3 (16) | 6.1 (13)[b]–1.5 (16)[g] |
| $HC_7N$ | 2.2 (16) | 2.5 (16) | <8.9 (12)[b] | $HC_9N$ | 1.4 (16) | | |
| $HC_{11}N$ | 8.2 (15) | | | $CH_3C_2H$ | 2.4 (14) | 2.4 (15) | 1.8 (16)[e] |
| $CH_3C_4H$ | 5.8 (14) | 1.7 (15) | 8.0 (15)[e] | $C_6H_5CN$ | 1.7 (15) | | |
| $C_6H_6$ | 9.0 (15) | 4.5 (16) | 5.0 (15)[g] | $H_2CS$ | 3.2 (15) | | |
| CS | 9.0 (15) | 4.2 (17) | 1.9 (13)[a] | $C_2S$ | 2.4 (16) | | |
| $C_3S$ | 4.9 (15) | | | $C_4S$ | 3.6 (14) | | |
| OCS | 2.5 (14) | | | CO | 7.1 (18) | 7.7 (19) | 1.0 (19)[h] |
| $H_3^+$ | 4.3 (10) | | | $HCO^+$ | 3.1 (11) | 1.7 (12) | 3.2 (13)[a] |

(a) Bachiller et al. (1997a); (b) Fukasaku et al. (1994); (c) Thorwirth et al. (2003); (d) Herpin & Cernicharo (2000); (e) Cernicharo et al. (2001a); (f) Martin-Pintado et al. (1993); (g) Cernicharo et al. (2001b); (h) Justtanont et al. (2000).

Since some observational data are presented as fractional abundances rather than column densities, presented in Table 3.4 is a comparison between these observed values and the fractional abundances in the model at the RC radius and also peak abundances. By comparing results in this table with column densities in the previous table, one can yet again get a sense of the large uncertainty in observed values. For example, the ratio between the calculated and observed column densities for the ion $HCO^+$ is $1\times10^{-2}$ while the corresponding ratio for fractional abundances is $1.3\times10^{-4}$! Clearly, all that can be stated is that $HCO^+$ is underproduced in both cases, although the peak column density of $HCO^+$ is only a factor of twenty less than the observed value. To produce a much higher abundance in a dense warm gas would require such a large ionisation rate that the molecular gas would be destroyed rapidly (see Sect. 3.4.6 and Fig. 3.2). It may be that most of the $HCO^+$ resides in a different region from that which is described here, or as examined by Viti et al. (2002), the high $HCO^+$ levels might be due to some wind-interaction effects which are not addressed here: Rawlings et al. (2000), in a paper which contributes results to Viti et al., show that the interaction between slow moving ($\sim$1 km s$^{-1}$) gas and a fast ($\sim$100 km s$^{-1}$) outflow can enhance the chemistry of $HCO^+$. Viti et al. show that this enhancement can mean higher abundances by an order of magnitude. The formation of $HCO^+$ in this case requires the presence of $H_2O$, which although not included in this model, is present in CRL618 (Herpin & Cernicharo 2000). Despite observational uncertainties as well as the problem that some species have rapidly changing abundances in the neighbourhood of the photodissociation distance, the general agreement is encouraging, particularly for the cyanopolyynes, HCN, and HNC. On the other hand, the calculated fractional abundances of some hydrocarbons tend to be too low.

The model results reported here are for an isothermal system at a temperature of 250 K. Two other models were also briefly considered, which start at temperatures of 250 K and 800 K , respectively, and in which the temperature decreases as the slab moves outward. Both models can be justified partially by observations: according to Herpin & Cernicharo (2000), the torus of CRL618 lies at 800 K but most of the molecular emission comes from the 250 K region. These models show that the effects of a radial temperature dependence on abundances are negligible. Note that the network of rate coefficients may not be entirely accurate at temperatures as high as 800 K.

Table 3.4: Comparison of calculated, peak and observed fractional abundances for CRL618, with respect to $n(H_2)$. The calculated values are taken at a radial distance of $8.9\times10^{15}$ cm. The notation $a\,(b)$ represents $a \times 10^b$.

| | CO | CS | $C_2H$ | $C_3H$ | $C_3H_2$ | $C_4H$ |
|---|---|---|---|---|---|---|
| $8.9\times10^{15}$ cm | 6.0 (-4) | 7.6 (-7) | 1.8 (-8) | 2.3 (-7) | 7.8 (-9) | 3.5 (-9) |
| Peak | 6.0 (-4) | 4.0 (-6) | 2.0 (-8) | 7.7 (-7) | 8.2 (-9) | 5.0 (-9) |
| Observed | 8.0 (-4)[b] | 6.0 (-8)[a] | 2.0 (-6)[a] | 4.0 (-8)[a] | 2.0 (-6)[a] | 8.0 (-8)[a] |
| | | 4.1 (-7)[b] | 2.0 (-6)[c] | | | |
| | $HCO^+$ | HCN | $HC_3N$ | $HC_5N$ | HNC | OCS |
| $8.9\times10^{15}$ cm | 2.6 (-11) | 1.4 (-7) | 1.4 (-6) | 1.5 (-6) | 6.2 (-7) | 2.1 (-8) |
| Peak | 5.9 (-11) | 8.0 (-6) | 1.6 (-6) | 1.7 (-6) | 1.6 (-6) | 2.0 (-7) |
| Observed | 2.0 (-7)[a] | 5.0 (-7)[a] | 2.0 (-7)[a] | 1.0 (-7)[a] | 1.9 (-6)[b] | $<$5.0 (-7)[a] |
| | | 4.4 (-6)[b] | 2.9 (-6)[b] | | | |
| | | 1.6 (-7)[c] | | | | |

(a) Bujarrabal et al. (1988). (b) Bujarrabal et al. (1994). (c) Fuente et al. (1998).

## 3.6 Conclusions

The model of a dense, warm gaseous slab, irradiated by an intense UV field, is able to generate very large abundances of large, complex molecules, including benzene. Assuming a dense slab/torus expanding at $5\,\mathrm{km\,s^{-1}}$, the phase during which molecules such as benzene are produced lasts 500 years, which is similar to the predicted age of CRL618. The derived column densities give a reasonable agreement with the *ISO* and millimetre-wave observations of organic molecules in CRL618, although it is often difficult to reconcile radio and IR observations of the same molecules. The physical model of a slowly expanding and uniform slab simplifies the true complexity of the source; different results would be obtained with more complex physical morphologies.

Having looked at a molecule-rich proto-planetary nebula in the previous chapter, this chapter contains observations of two PPNe which are molecule-poor. One, IRAS16594-4656, is carbon-rich, like CRL618 – what, then, makes these two PPNe so chemically different?

# Chapter 4

# Molecule-poor proto-planetary nebulae: Observational

## 4.1 Introduction

The proto-planetary stage of evolution is one of the shortest in a star's lifetime and this implies a scarcity of observable examples. Following the method of Olivier et al. (2001), the number density of proto-planetary nebulae can be estimated to be $(0.41^{+1.91}_{-0.34})\,\mathrm{kpc}^{-2}$. In comparsion, the density of AGB stars is $15\,\mathrm{kpc}^{-2}$ and of Main Sequence stars is $\sim 2\times10^{6}\,\mathrm{kpc}^{-2}$. Hence knowledge about this phase is limited. Most of current understanding of PPNe is derived from a handful of objects; mainly the carbon-rich sources CRL618 and CRL2688 and the oxygen-rich object OH231.8+4.2. All three show strong molecular lines, have axisymmetric structures and molecular tori or disks. However, several hundred PPNe candidates have been identified (see Kwok 1993, and references therein), some 34 have been confirmed as PPNe (Bujarrabal et al. 2001), and yet only a handful show such molecular "richness". The reason for the difference in molecular plenitude is far from clear.

PPNe are a favourite subject of the Hubble Space Telescope (HST), and many optical and infrared HST images have helped in the study of PPNe (e.g., see Su et al. 2001; Hrivnak et al. 2001a, 1999; Kwok et al. 1998, for details on the two PPNe described here, IRAS16594-4656 and IRAS17150-3224), although the degree to which

many of the objects discovered have been studied is minimal. Both molecule-rich PPNe and molecule-poor PPNe appear similar in images – CRL618, CRL2688, OH231.8+4.2 and both IRAS16594-4656 and IRAS17150-3224 have some degree of bipolarity, and a narrow waist. The beginnings of this bipolarity are found in the late AGB phase, where the first signs of asphericity are seen (e.g., Kastner & Weintraub 1994). The shaping of the nebula continues under the influence of a fast superwind, according to the Generalized Interacting Stellar Wind (GISW) model (Sect. 1.5.3, Balick 1987). Other effects then play a part in the developing morphology (see the review by Balick & Frank 2002), and one which may be important is the inertial confinement of the outflowing wind by a circumstellar torus or disk (Calvet & Peimbert 1983). The degree of collimation produced by this disk would depend on the mass of the disk, as well as the momentum involved in the high-speed outflow, and other, geometrical effects. This change in morphology, from something approximately spherical to something bipolar, or elliptical, occurs very rapidly at the end of the AGB phase of evolution (e.g., Schmidt et al. 2002; Kwok et al. 1996). The actual period of transition is hard to quantify, and there are inherent difficulties in estimates by dynamical means (Zijlstra et al. 2001).

In this chapter, two objects which have been imaged by the HST and show strong CO emission are studied. Both objects, IRAS16594-4656 and IRAS17150-3224 are only detected in a handful of species, including HCN and CO. These spectra are compared to other PPNe newly observed in HCN and CO – CPD-53°5736, IRAS17106-3046, IRAS17245-3951 and IRAS17441-2411 (Sect. 4.4). The molecular properties of these two PPNe are studied by calculating fractional abundances from SEST data, and comparing these fractional abundances with similar objects (Sects. 4.6.1, 5.2). Spectra are presented in Appendix B. The comparative underabundance of molecules in IRAS16594-4656 and 17150-3224 is discussed in Sect. 5.2, and arising hypotheses are confirmed by means of a chemical model (Chapter 5).

## 4.2 Observations

The observations were carried out between 1998 and 2002 with the Swedish-ESO Submillimetre Telescope (SEST), situated on La Silla, Chile. SIS receivers were used at 0.8, 1.3, 2 and 3 mm. During this period the SEST operated three acousto-optical spectrometers: one high resolution spectrometer, with a bandwidth of 86 MHz and a channel separation of 43 kHz, and two wideband spectrometers with bandwidths of about 1 GHz and a channel separation of 0.7 MHz. Typical system temperatures

Table 4.1: Positions and LSR velocities for the PPNe under study.

| IRAS No. | Other name | J2000 Co-ords. | | $v_{LSR}$ |
|---|---|---|---|---|
| | | [h:m:s] | [°:′:″] | [km s$^{-1}$] |
| 14488-5405 | CPD-53°5736 | 14:52:28.7 | −54:17:43 | −10 |
| 16594-4656 | — | 17:03:09.7 | −47:00:28 | −25 |
| 17106-3046 | — | 17:13:51.7 | −30:49:40 | 0 |
| 17150-3224 | AFGL6815S | 17:18:20.0 | −32:27:20 | +15 |
| 17245-3951 | OH348.8-2.8 | 17:28:04.8 | −39:53:44 | 0 |
| 17441-2411 | AFGL5385 | 17:47:10.3 | −24:12:54 | +110 |

above the atmosphere ranged between 150 and 800 K, depending on frequency and elevation.

Most observations were carried out with the dual beam switching method, as in Chapter 2. Beam separation was 11′.5 in azimuth. CO maps of IRAS17150-3224 were taken using the position switching method, to minimise interference from interstellar CO emission lines. The OFF position was chosen to be (-10′, -11′) from the ON position. Map spacing in all cases was 11″, which is approximately half a beamwidth at 230 GHz. Calibration was performed with the standard chopper-wheel technique, and has an uncertainty of approximately 20% (see Schöier & Olofsson 2001, for details). J2000 positions of both sources are given in Table 4.1.

Intensity scales of spectra in this chapter are given in main-beam brightness temperature, which is the corrected antenna temperature divided by the main-beam efficiency ($\eta_{\rm mb}$). Individual spectra are shown in Appendix B, and line frequencies and integrated intensities are shown in Table 4.2.

Integrated intensities of lines which were not clearly detected are calculated using the expression in Chapter 2, Eq. 2.1. Values of $I_{\rm v}$ calculated in this manner are given in Table 4.2 and indicated by a "less than" sign.

## 4.3 Sources

The two PPNe presented in this chapter are objects for which there are currently few millimetre-wavelength spectra and little or no molecular information. Both show bipolar morphology in HST images and also bright CO emission, with interesting features. These two sources were selected on the basis of previously published CO spectra (Loup et al. 1990; Hu et al. 1993). A more thorough literature survey of these objects is available in the Appendix A.

Table 4.2: Observed lines in the two PPNe.

| Molecule | Transition | Frequency | IRAS16594-4656 | | IRAS17150–3224 | |
|---|---|---|---|---|---|---|
| | | | $T_{\rm mb}$ | $\int T_{\rm mb}{\rm d}v$ | $T_{\rm mb}$ | $\int T_{\rm mb}{\rm d}v$ |
| | | GHz | K | K km s$^{-1}$ | K | K km s$^{-1}$ |
| $C_3S$ | $J$=15-14 | 86.708 | $<0.01$ | $<0.03$ | — | — |
| SiO | $J$=2-1 | 86.847 | $<0.01$ | $<0.03$ | — | — |
| $HN^{13}C$ | $J$=1-0 | 87.091 | $<0.01$ | $<0.03$ | — | — |
| $C_4H$ | $^2\Pi_{3/2}$, 19/2-17/2 | 87.372 | $<0.01$ | $<0.03$ | — | — |
| $C_2H$ | $N$=1-0 | 87.329 | $<0.01$ | $<0.03$ | — | — |
| HCN | $J$=1-0 | 88.632 | 0.02 | 0.47 | 0.02 | 0.54 |
| $C_3N$ | $N$=9-8, $J$=19/2-17/2 | 89.046 | $<0.01$ | $<0.05$ | — | — |
| $C_3N$ | $N$=9-8, $J$=17/2-15/2 | 89.064 | $<0.01$ | $<0.05$ | — | — |
| $HCO^+$ | $J$=1-0 | 89.189 | $<0.01$ | $<0.05$ | — | — |
| $HC^{13}CCN$ | $J$=10-9 | 90.593 | $<0.01$ | $<0.04$ | — | — |
| $HCC^{13}CN$ | $J$=10-9 | 90.602 | $<0.01$ | $<0.04$ | — | — |
| HNC | $J$=1-0 | 90.664 | $<0.01$ | $<0.04$ | — | — |
| SiS | $J$=5-4 | 90.772 | $<0.01$ | $<0.04$ | — | — |
| $HC_3N$ | $J$=10-9 | 90.979 | $<0.01$ | $<0.04$ | — | — |
| $CH_3CN$ | 5(1)-4(1) | 91.985 | $<0.01$ | $<0.05$ | — | — |
| $HC^{13}CCN$ | $J$=12-11 | 108.711 | $<0.01$ | $<0.06$ | — | — |
| $HCC^{13}CN$ | $J$=12-11 | 108.721 | $<0.01$ | $<0.06$ | — | — |
| $^{13}CN$ | $N$=1-0 | 108.780 | $<0.01$ | $<0.06$ | — | — |
| $C_3N$ | $N$=11-10, $J$=23/2-21/2 | 108.834 | $<0.01$ | $<0.06$ | — | — |
| $C_3N$ | $N$=11-10, $J$=21/2-19/2 | 108.853 | $<0.01$ | $<0.06$ | — | — |
| SiS | $J$=6-5 | 108.924 | $<0.01$ | $<0.06$ | — | — |
| $HC_3N$ | $J$=12-11 | 109.174 | $<0.01$ | $<0.06$ | — | — |
| $^{13}CO$ | $J$=1-0 | 110.201 | 0.04 | 0.06 | 0.04 | 0.75 |
| $CH_3CN$ | 6(1)-5(1) | 110.381 | $<0.01$ | $<0.11$ | $<0.01$ | $<0.09$ |
| $C_4H$ | $^2\Pi_{3/2}$ 23/2-21/2 | 113.266 | $<0.01$ | $<0.09$ | $<0.01$ | $<0.06$ |
| $C_2S$ | 8(7)-9(8) | 113.410 | $<0.01$ | $<0.09$ | $<0.01$ | $<0.06$ |
| CN | $N$=1-0 | 113.491 | 0.05 | 3.63 | $<0.01$ | $<0.06$ |
| $C_4H$ | $^2\Pi_{3/2}$ 21/2-19/2 | 115.217 | $<0.07$ | $<0.76$ | $<0.04$ | $<0.45$ |
| CO | $J$=1-0 | 115.271 | 0.61 | 1.78 | 0.25 | 5.05 |
| $SiC_2$ | $5_{0,5}$-$4_{0,4}$ | 115.382 | $<0.07$ | $<0.76$ | $<0.04$ | $<0.45$ |
| SiO | $J$=3-2 | 130.269 | $<0.01$ | $<0.06$ | — | — |
| $H_2CO$ | $2_{1,2}$-$1_{1,1}$ | 140.840 | $<0.01$ | $<0.07$ | — | — |
| $SiC_2$ | $6_{2,5}$-$5_{2,4}$ | 140.920 | $<0.01$ | $<0.07$ | — | — |
| $H^{13}CCCN$ | $J$=16-15 | 141.062 | $<0.01$ | $<0.07$ | — | — |
| CS | $J$=3-2 | 146.969 | $<0.01$ | $<0.04$ | — | — |
| $CH_3CN$ | 8(0)-7(0) | 147.175 | $<0.01$ | $<0.04$ | — | — |
| $^{13}CO$ | $J$=2-1 | 220.399 | 0.10 | 1.34 | 0.13 | 2.91 |
| $CH_3CN$ | 12(0)-11(0) | 220.747 | $<0.01$ | $<0.16$ | $<0.01$ | $<0.17$ |
| CN | $N$=2-1 | 226.875 | 0.11 | 9.91 | $<0.01$ | $<0.10$ |
| CO | $J$=2-1 | 230.538 | 1.75 | 32.60 | 0.65 | 12.84 |
| $CO^+$ | $J$=2-1 | 235.790 | $<0.01$ | $<0.12$ | — | — |
| SiS | $J$=13-12 | 235.961 | $<0.01$ | $<0.12$ | — | — |
| $CH_3CN$ | 13(0)-12(0) | 239.138 | $<0.01$ | $<0.16$ | — | — |
| $CH_3C_2H$ | 14(0)-13(0) | 239.252 | $<0.01$ | $<0.16$ | — | — |
| $C_3H_2$ | $4_{4,1}$-$3_{3,0}$ | 265.759 | $<0.02$ | $<0.36$ | — | — |
| HCN | $J$=3-2 | 265.886 | 0.11 | 2.85 | — | — |
| $H^{13}CN$ | $J$=4-3 | 345.340 | $<0.04$ | $<0.80$ | $<0.06$ | $<1.28$ |
| $HC_3N$ | $J$=38-37 | 345.610 | $<0.04$ | $<0.80$ | $<0.06$ | $<1.28$ |
| CO | $J$=3-2 | 345.796 | 2.05 | 41.20 | 0.78 | 18.19 |

### 4.3.1 IRAS16594-4656

IRAS16594-4656 is a proto-planetary nebula which has a mixed chemistry. In its infrared spectrum there are strong and rarely observed features at 12.6 and 13.4 $\mu$m, thought to be due to polycyclic aromatic hydrocarbons (PAHs) with a high degree of hydrogenation, and further PAH features in the range 3-13 $\mu$m (García-Lario et al. 1999). An emission feature between 19 and 23 $\mu$m, associated with C-rich PPNe by Kwok & Hrivnak (1989), also suggests that this source is carbon rich. However, there are also indications of crystalline silicates (pyroxenes), with weak features around 34 $\mu$m (García-Lario et al. 1999), and a 10 $\mu$m silicate feature (Olnon et al. 1986). This suggests that until recently this object was oxygen-rich, becoming carbon-rich shortly before the transition to the post-AGB phase (García-Lario et al. 1999), which occurred some 370 years ago (van der Veen et al. 1989). This hypothesis was strengthened by the lack of a detection in OH (te Lintel Hekkert et al. 1991; Silva et al. 1993) and no SiO maser emission (Nyman et al. 1998). In evolved stars with this mixed chemistry the silicates are found in a torus and the PAHs in the polar flow (Matsuura et al. 2004).

Several authors describe HST images of this PPN (Hrivnak et al. 1999, 2000; García-Lario et al. 1999), which show the presence of a bright , B7-type (van de Steene et al. 2000) central star, surrounded by a multiple–axis bipolar nebulosity with a complex morphology.

The only CO spectrum of this source previously published is a CO ($J$=1-0) spectrum from Loup et al. (1990), who detected broad CO emission corresponding to that from a circumstellar shell expanding with a velocity of 16 km s$^{-1}$.

### 4.3.2 IRAS17150-3224

IRAS17150-3224 (AFGL6815S) is a young PPN which left the AGB some 150 (Hu et al. 1993) to 210 (Meixner et al. 2002) years ago (van der Veen et al. 1989, give a dynamic timescale of 800 yr for this object.) Structurally, it is a bipolar nebula, with a nearly edge-on (82°) dusty torus (Kwok et al. 1996), expanding at 11 km s$^{-1}$ (Weintraub et al. 1998) around a G2-type central star. A newly-discovered equatorial loop seen in near-infrared, but not optical, images, is discussed by Su et al. (2003). A faint halo (AGB mass-loss remnant) can be seen in images from Kwok et al. (1998).

IRAS17150-3224 shows molecular hydrogen emission, but not hydrogen recombination, indicating that the degree of ionisation is small (García-Hernández et al.

2002). The emission is likely due to shock-excitation, as is often seen in strongly bipolar nebulae. This object is similar to CRL2688 (Sahai et al. 1998) in that it has $H_2$ emission, and a spectral type later than A (CRL2688 has a spectral type of F2, Cohen & Kuhi 1977). IRAS17150-3224 also shows OH maser emission (Hu et al. 1994), but not SiO maser emission (Nyman et al. 1998). It also has been detected in the 3.1 $\mu$m water line (van der Veen et al. 1989), but not in $H_2O$ maser emission (Zuckerman & Lo 1987).

Previous CO observations are limited to the paper of Hu et al. (1993), who present both CO ($J$=1-0) and ($J$=2-1) spectra.

## 4.4 CO observations

### 4.4.1 IRAS16594-4656

The CO ($J$=2-1) and ($J$=3-2) line profiles presented in Fig. 4.1a are affected by interstellar emission in the OFF position (between -12 and -5 $\mathrm{km\,s^{-1}}$ approximately). The CO ($J$=3-2) profile is taken in dual beamswitch mode whereas the CO ($J$=2-1) profile was taken in position switch mode with an OFF position -30″ away in R.A. in order to minimise the effect of the interstellar line. Despite this, a high signal-to-noise ratio affords some indication of structure in this source, shown by features in the line profile. A roughly parabolic profile and a source size comparable to the beam shows that the CO emission is probably optically thick. An outflowing wind of 14 $\mathrm{km\,s^{-1}}$ is indicated by the line profile, and there seems to be an appreciable line wing on the blue side, possibly indicating a second wind of up to 25 $\mathrm{km\,s^{-1}}$. The CO ($J$=2-1) map of this source (Fig. 4.3) shows a reasonably symmetric pattern of emission. The red/blue-shifted emission contour plot (Fig.4.2) does not show the red-shifted emission, due to the interstellar interference. The blue-shifted emission, taken in the interval [-50,-35] $\mathrm{km\,s^{-1}}$, lies directly on top of the centre emission, taken in the interval [-35,-12] $\mathrm{km\,s^{-1}}$, indicating that there is little or no separation in emission regions. There is some emission at ±20″ in right ascension (R.A.), and an elliptical Gaussian fit to the integrated intensity map shows that the FWHM ellipse has a major axis of ∼25″ and a minor axis of ∼22.5″ (position angle of 57°), very similar to the size of the SEST beam (23″) at 230 GHz. Hence the source is on the limit of being resolved.

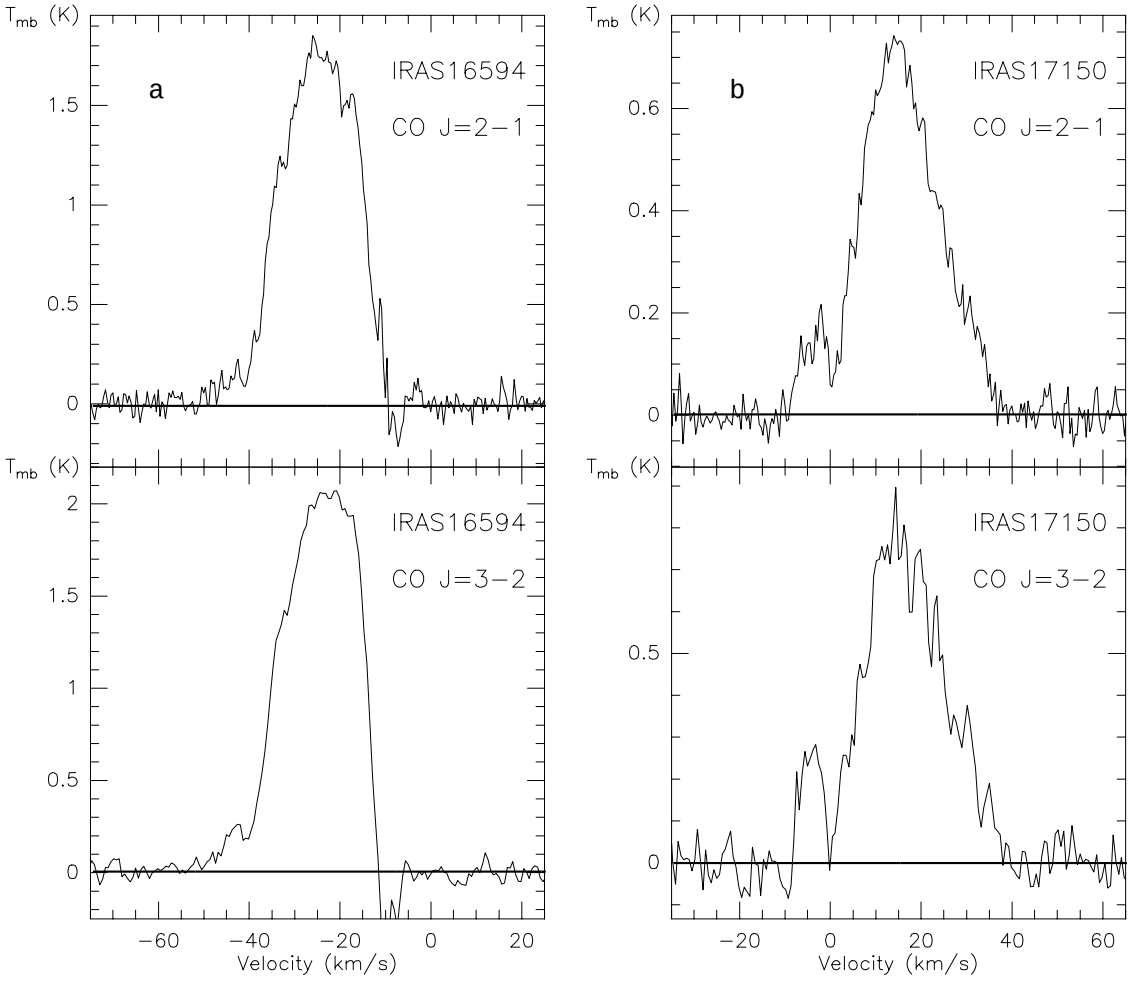


Figure 4.1: **A. Top.** A position-switched high-resolution CO ($J$=2-1) spectrum toward IRAS16594-4656. **Bottom.** A beam-switched CO ($J$=3-2) spectrum toward IRAS16594-4656. **B. Top.** A position-switched high-resolution CO ($J$=2-1) spectrum toward IRAS17150-3224. **Bottom.** A beam-switched CO ($J$=3-2) spectrum toward IRAS17150-3224.

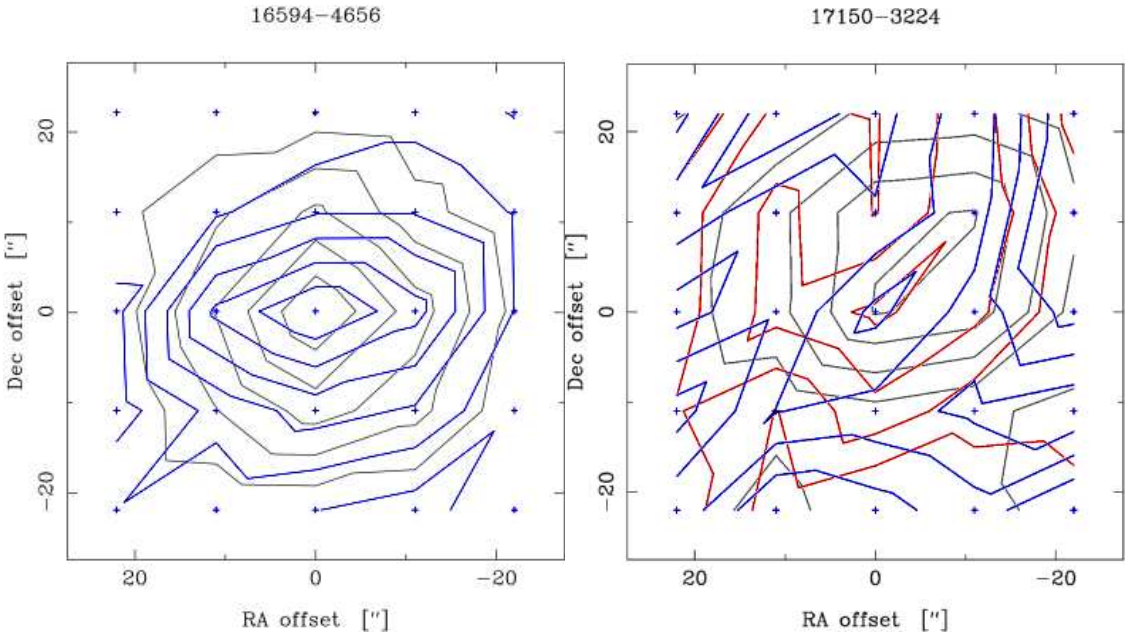


Figure 4.2: Position-position contour emission maps of IRAS16594-4656, and IRAS17150-3224. Blue contours show blue-shifted emission, black contours emission from the centre of the line profile, and red contours red-shifted emission.

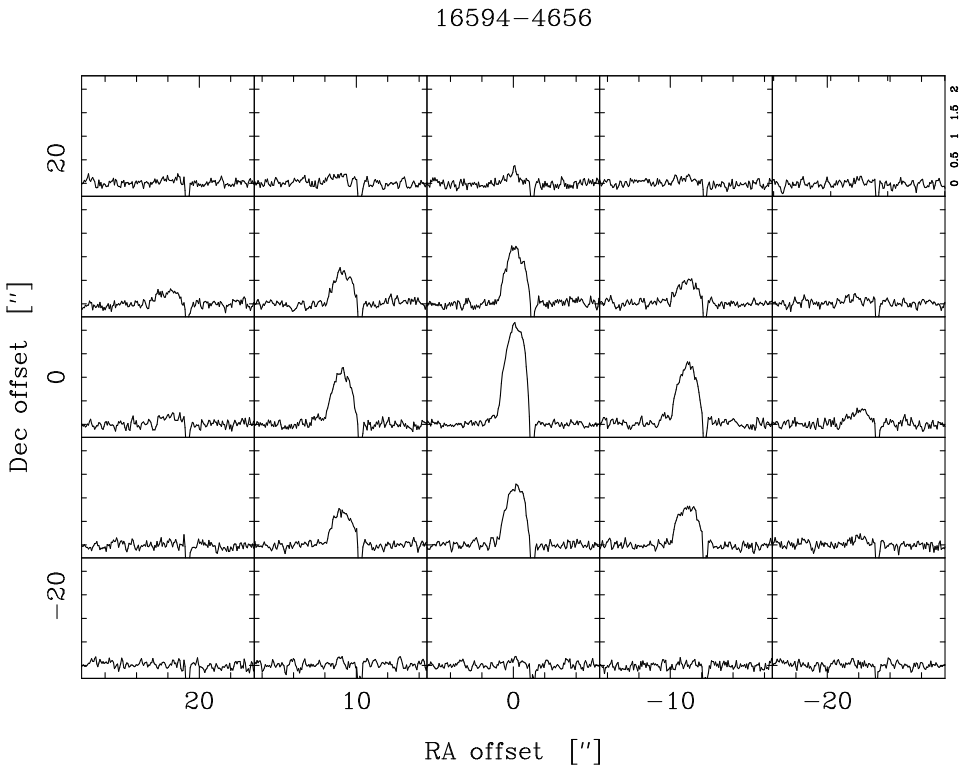


Figure 4.3: A map of the CO ($J$=2-1) line around IRAS16954-4656. The beam-spacing is 11″. The spectra are affected by interstellar line contamination in the red-shifted line wing.

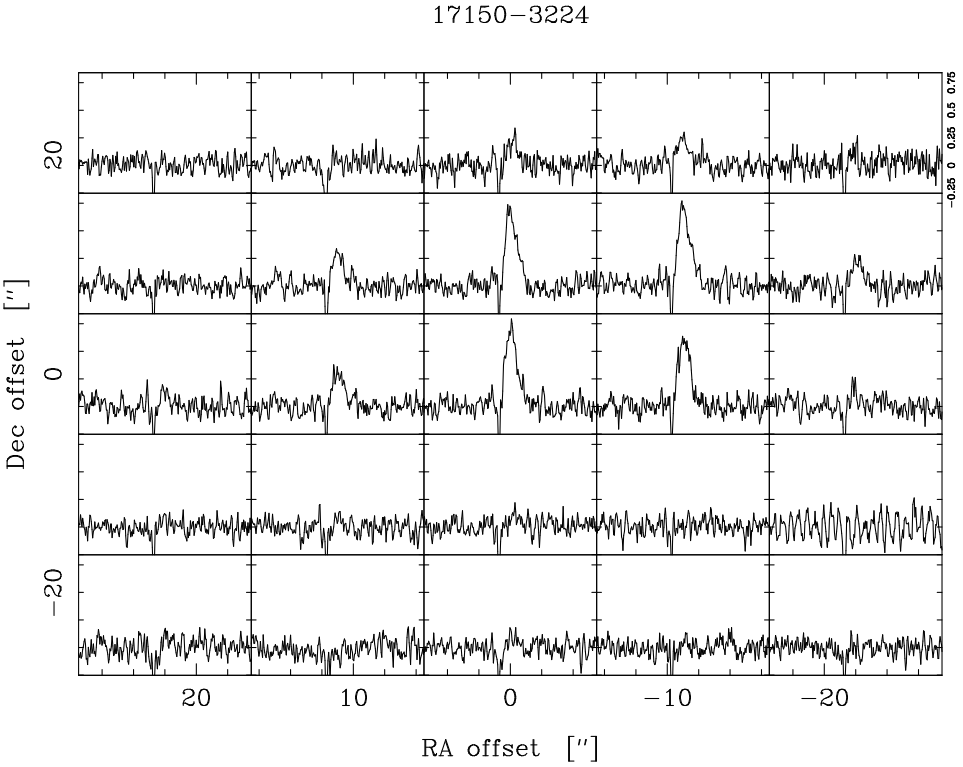


Figure 4.4: A map of the CO ($J$=2-1) line around IRAS17150-3224, taken in beam-switch mode. The beam-spacing is 11″. The spectra are affected by interstellar line contamination in the blue-shifted line wing.

### 4.4.2 IRAS17150-3224

The CO ($J$=2-1) spectrum (Fig. 4.1b) of IRAS17150-3224 was taken in position switch mode, with an OFF position of +45″ in R.A. The CO ($J$=3-2) was taken in beamswitch mode. Both CO line profiles of IRAS17150-3224 shown in Fig. 4.1b are distinctly triangular in shape, similar to those shown by 89 Her, the Red Rectangle, and M2-9 (Alcolea & Bujarrabal 1991) (and also IRAS17441-2411, presented in this chapter). Here the triangular shape is affected by an interstellar line in the blue-shifted wing (between 0 and 10 $\mathrm{km\,s^{-1}}$ approximately). The CO lines indicate a wind of some 30 $\mathrm{km\,s^{-1}}$ coming from the source, and yet a parabolic fit to the line indicates a wind of 14.5 $\mathrm{km\,s^{-1}}$. This latter wind is ostensibly the AGB wind of the star, with the higher velocity emission probably coming from an inner swept-up shell, moving at a velocity intermediate to the AGB wind and a post-AGB or super-wind.

The CO ($J$=2-1) emission map (Fig. 4.4) is taken in position switch mode to minimise the effects of the interstellar interference, and although hampered slightly by poor pointing, seems to show a reasonably symmetric distribution which does not appear to be resolved by the telescope beam. The contour map (Fig. 4.2) does not show any separation in the source. The red-shifted emission was taken from the interval [30,40] $\mathrm{km\,s^{-1}}$, the centre emission from [5,30] $\mathrm{km\,s^{-1}}$ and the blue-shifted emission from [-18,-6] $\mathrm{km\,s^{-1}}$. A two-dimensional elliptical Gaussian fit to the centre emission gives an extent of ∼20″×26″ (position angle of -160°) for this source. Again, this is similar to the size of the SEST beam at 230 GHz.

### 4.4.3 Other sources observed in CO

Spectra of sources which have been hitherto unobserved and/or unpublished in the CO ($J$=2-1) line are presented in Fig. 4.5. HCN ($J$=1-0) spectra have also been taken (not presented), and CO/HCN intensity ratios are derived (Table 4.3).

*CPD-53°5736.* Although not fully clear from the noisy spectrum, CPD-53°5736 seems to show the presence of a wind expanding at 15 $\mathrm{km\,s^{-1}}$.

*IRAS17106-3046.* This object shows a strange profile: some low-level emission, perhaps a wind of ∼15 $\mathrm{km\,s^{-1}}$, and a thin, narrow spike. This narrow spike (of width ∼2 $\mathrm{km\,s^{-1}}$) could correspond in some way to the circumstellar disk observed by Kwok et al. (2000). The narrow feature seems to be offset from the centre of the broad feature, although the signal-to-noise ratio is low.

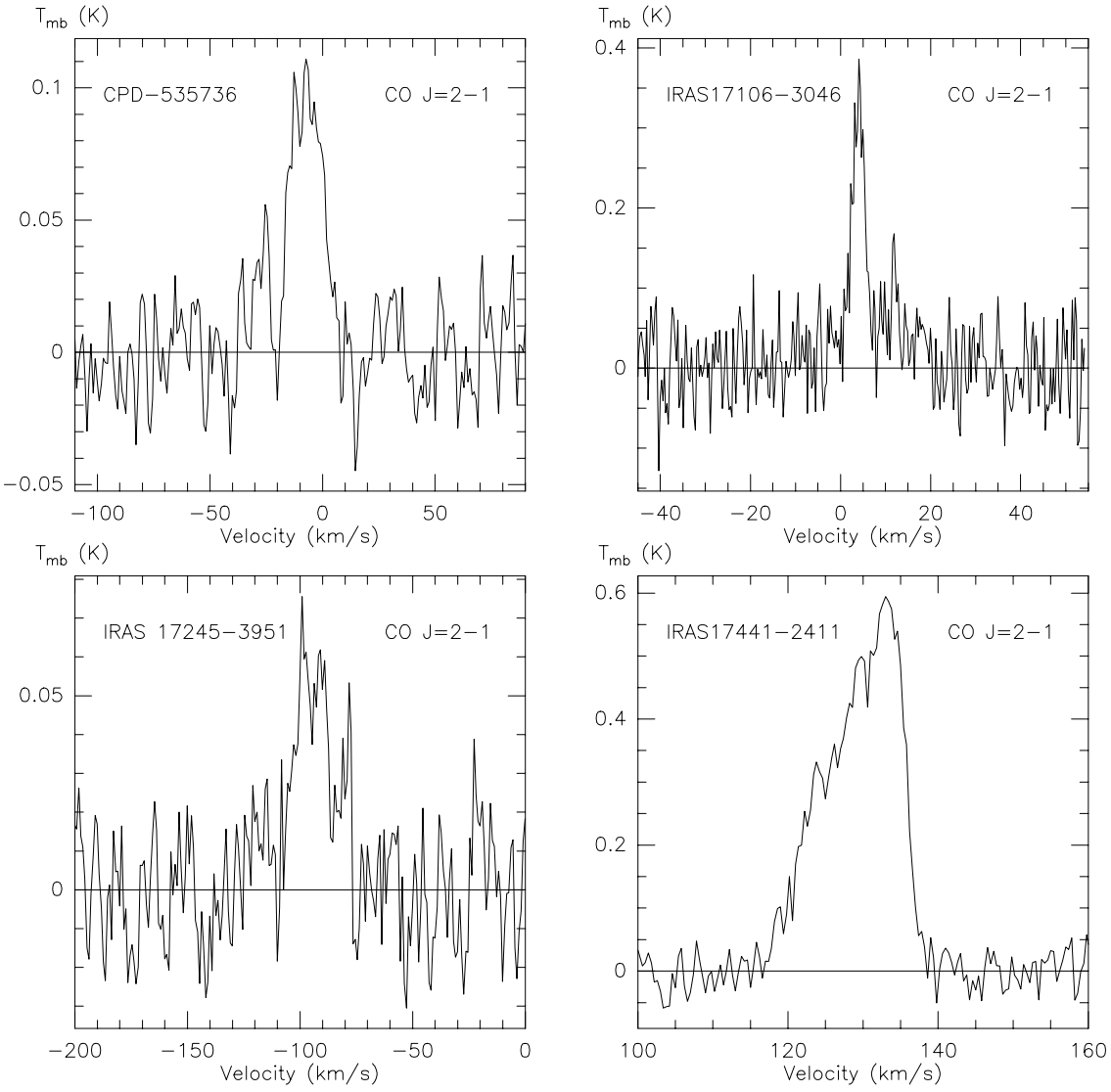


Figure 4.5: CO ($J$=2-1) spectra of PPNe candidates, named in the upper left-hand corner of each spectrum.

Table 4.3: Observed lines in the four PPNe candidates.

| Molecule | CPD-53°5736 | | IRAS16594-4656 | | IRAS17106-3046 | |
|---|---|---|---|---|---|---|
| | $T_{\rm mb}$ K | $\int T_{\rm mb}{\rm dv}$ K km s$^{-1}$ | $T_{\rm mb}$ K | $\int T_{\rm mb}{\rm dv}$ K km s$^{-1}$ | $T_{\rm mb}$ K | $\int T_{\rm mb}{\rm dv}$ K km s$^{-1}$ |
| HCN($J$=1-0) | — | $<0.07$ | 0.02 | 0.47 | — | — |
| CO($J$=2-1) | 0.09 | 2.07 | 1.75 | 32.60 | 0.30 | 1.84 |
| $I_{HCN}/I_{CO}$ | | $<0.04$ | | 0.01 | | — |

| Molecule | IRAS17150-3224 | | IRAS17245-3951 | | IRAS17441-2411 | |
|---|---|---|---|---|---|---|
| | $T_{\rm mb}$ K | $\int T_{\rm mb}{\rm dv}$ K km s$^{-1}$ | $T_{\rm mb}$ K | $\int T_{\rm mb}{\rm dv}$ K km s$^{-1}$ | $T_{\rm mb}$ K | $\int T_{\rm mb}{\rm dv}$ K km s$^{-1}$ |
| HCN($J$=1-0) | 0.02 | 0.54 | — | $<0.09$ | 0.05 | 0.32 |
| CO($J$=2-1) | 0.65 | 12.84 | 0.04 | 0.58 | 0.57 | 6.24 |
| $I_{HCN}/I_{CO}$ | | 0.04 | | $<0.15$ | | 0.05 |

*IRAS17245-3951.* Low signal-to-noise means that this profile is hard to qualify. The profile suggests an expansion velocity of 15 km s$^{-1}$, but this value does have a considerable uncertainty.

*IRAS17441-2411.* This source has a triangular lineshape, similar to IRAS17150-3224. It is somewhat asymmetric, and quite narrow in velocity (20 km s$^{-1}$ in width). There are no appreciable line wings.

#### 4.4.3.1 $I_{HCN}/I_{CO}$ ratios

The $I_{HCN}/I_{CO}$ ratios shown in Table 4.3 look to be reasonably consistent throughout the sample of PPN candidates. To put these figures into context, a sample of oxygen stars selected by Lindqvist et al. (1988) has an average $I_{HCN}/I_{CO}$ ratio of 0.124, whereas the carbon star sample of Olofsson et al. (1990b) has an average $I_{HCN}/I_{CO}$ ratio of 0.623. Both these samples were made up of AGB stars; the values for PPNe seem to be smaller. IRAS07134+1005 and IRAS19500-1709, both C-rich PPNe, have $I_{HCN}/I_{CO}$ ratios of 0.15 and 0.08, respectively (Bujarrabal et al. 1992). Evolved PNe generally have $I_{HCN}/I_{CO}$ ratios of less than 0.1 (c.f., Bachiller et al. 1997a).

## 4.5 CO line modelling

The radiative transfer model explained in the Chapter 2 is used here also. For IRAS16594-4656 a CO fractional abundance of $1 \times 10^{-3}$ (which is typical of a C-rich AGB envelope) is used, whereas for the O-rich object IRAS17150-3224 a value

Table 4.4: Adopted and derived modelling parameters of the two PPNe.

| IRAS No. | $D$ [kpc] | $L$ [$L_\odot$] | $f_{CO}$ | $\dot{M}$ [$M_\odot\,yr^{-1}$] | $v_{exp}$ [$km\,s^{-1}$] | $R_e$ [cm] | $h$ | $\frac{^{12}CO}{^{13}CO}$ |
|---|---|---|---|---|---|---|---|---|
| 16594-4656 | 1.80[a] | 4 900 | $1\times10^{-3}$ | $1\times10^{-5}$ | 14.0 | $2.9\times10^{17}$ | 10.0 | 30 |
| 17150-3224 | 2.42[b] | 11 000 | $2\times10^{-4}$ | $3\times10^{-5}$ | 14.5 | $2.4\times10^{17}$ | 1.8 | 7 |

(a) van der Veen et al. (1989).

(b) Bujarrabal et al. (2001).

of $2 \times 10^{-4}$ is adopted. The derived envelope properties such as the mass loss rate ($\dot{M}$), expansion velocity ($v_{exp}$), extent of the CO envelope ($R_e$) and $^{12}CO/^{13}CO$-ratio are reported in Table 4.4 together with the adopted distance ($D$), luminosity ($L$) and initial CO fractional abundances ($f_{CO}$). Also shown is the $h$-parameter that determines the amount of heating in the envelope due to momentum transfer due to dust-gas collisions (see Eq. 2.2 and Schöier & Olofsson 2001, for details).

There is a high degree of confidence in the model fits: the total integrated intensities in the lines are well reproduced as are the overall line profiles. There is confusion due to interstellar lines at the red-shifted edge of the line profiles of IRAS16594-4656. Also, on the blue-shifted edge there are signs of a second weak component, possibly a higher velocity wind due to the present-day mass loss. The $^{12}CO$ spectra for IRAS17150-3224 show signs of excess emission at larger expansion velocities possibly indicating the presence of a faster moving wind. However, the blue side of the emission is confused by interstellar line contamination.

The $h$-parameter of 10 derived for IRAS16594-4656 is significantly larger than that of IRAS17150-3224 and that which is typically derived for high mass-loss rate AGB-stars, $h \sim 1-2$, (Schöier & Olofsson 2001, and Chapter 2). Such a large discrepancy is hard to explain in terms of, for example, uncertainties in the adopted distance, and could instead indicate that the properties of the dust grains are different in IRAS16594-4656. A further possibility is that the spectra are contaminated by a second, warmer component such as the bipolar present day mass-loss seen in optical images at smaller spatial scales.

The winds of these PPNe are assumed to resemble those of their progenitor AGB-stars, i.e., spherical symmetry and a constant expansion velocity are assumed. Given that both sources left the AGB ~200-400 yr ago this assumption should be valid for distances $\gtrsim 1 \times 10^{16}$ cm, since the material outside this radius would once have made up the AGB wind. However, there is the possibility that a high velocity bipolar wind is penetrating this remnant AGB shell. The CO emission from the

Table 4.5: Calculated fractional abundances, with respect to $n(H_2)$.

| Molecule | Transition | IRAS16594-4656 | | |
|---|---|---|---|---|
| | | $r_i$ | $r_e$ | $f_X$ |
| | | cm | cm | |
| $^{13}CO^a$ | $J$=1-0 | — | 1.0 (17) | 1.0 (-5) |
| $^{13}CO^a$ | $J$=2-1 | — | 1.0 (17) | 2.0 (-5) |
| $^{13}CO^b$ | — | — | 2.9 (17) | 3.3 (-5) |
| HCN | $J$=1-0 | — | 2.3 (16) | 1.0 (-6) |
| HCN | $J$=3-2 | — | 2.3 (16) | 1.9 (-7) |
| CN | $N$=1-0 | 1.7 (16) | 5.1 (16) | 9.6 (-6) |
| CN | $N$=2-1 | 1.7 (16) | 5.1 (16) | 2.5 (-6) |
| Molecule | Transition | IRAS17150-3224 | | |
| | | $r_i$ | $r_e$ | $f_X$ |
| | | cm | cm | |
| $^{13}CO^a$ | $J$=1-0 | — | 2.8 (17) | 2.7 (-5) |
| $^{13}CO^a$ | $J$=2-1 | — | 2.8 (17) | 9.5 (-6) |
| $^{13}CO^b$ | — | — | 2.4 (17) | 2.9 (-5) |
| HCN | $J$=1-0 | — | 4.4 (16) | 3.8 (-7) |

(a) $^{13}CO$ fractional abundances derived using the simple photochemical model.

(b) $^{13}CO$ fractional abundance derived using CO line modelling (Sect. 4.5).

lower rotational transitions observed here are formed mostly at distances larger than $5 \times 10^{16}$ cm and thus mainly probe the outer, AGB-type, wind. For other molecular species contributions from the present-day wind might become significant.

However, a more detailed treatment of the wind characteristics will require high-resolution, multi-transition, observations. Also, the effect of dust emission in the excitation of the molecules, which is not taken into account in the present analysis, needs to be investigated.

## 4.6 Fractional abundances

### 4.6.1 Calculation of fractional abundances

Fractional abundances are calculated assuming that all lines are optically thin. A constant excitation temperature of 25 K is assumed throughout the emitting region. The expression used to calculate fractional abundances is Eq. 2.3 in Chapter 2, and the results are shown in Table 4.5. Upper limits to fractional abundances are given in Table 4.6, and are calculated using the integrated intensity from Eq. 2.1.

Inner and outer radii of molecular distributions are determined in much the same way as in the Chapter 2, using the simple photodissociation model. Here, however, there is not the benefit of good interferometric data. Hence simplifying assumptions have to be made about certain molecular distributions. The distribution of all parent species, with the exception of CO, is calculated from the photodissociation model (observed parent species are HCN, CS, SiO, SiS). The distribution of CO comes from the radiative transfer modelling, as described in Sect. 4.5. Self-shielding of CO is taken into account, in the manner of Mamon et al. (1988). All ionisation products or products of the circumstellar chemistry are assumed to take on the distribution of $C_2H$, with the exception of CN, which has a slightly more expansive distribution. This should not have too great an effect on results since there is only a linear dependence on the difference between inner and outer radius. These are very straightforward assumptions, which ignore effects of circumstellar chemistry, and freeze-out onto grains (which were important for SiO and SiS, as seen in Chapter 2), for example. Again, isotopomers are assumed to have the same distribution as their more abundant forms.

Table 4.6: Calculated upper limits to fractional abundances, with respect to $n(H_2)$.

| | IRAS16594-4656 | IRAS17150-3224 |
|---|---|---|
| Molecule | $f_X$ | $f_X$ |
| $CO^+$ | 1.1 (-8) | — |
| $HCO^+$ | 1.2 (-7) | — |
| $H_2CO$ | 1.1 (-6) | — |
| CS | 6.5 (-8) | — |
| $C_2S$ | 3.4 (-7) | 9.5 (-8) |
| $C_3S$ | 4.1 (-7) | — |
| SiO | 5.1 (-8) | — |
| SiS | 3.2 (-7) | — |
| $SiC_2$ | 4.7 (-7) | 2.1 (-6) |
| CN | Det.[a] | 1.1 (-8) |
| $^{13}CN$ | 5.0 (-7) | — |
| $H^{13}CN$ | 2.4 (-8) | 1.3 (-8) |
| HNC | 1.8 (-7) | — |
| $HN^{13}C$ | 1.9 (-7) | — |
| $HC_3N$ | 2.7 (-7) | — |
| $H^{(13)}C_3N$[b] | 2.7 (-7) | — |
| $H^{13}CCCN$ | 2.0 (-7) | — |
| $C_3N$ | 4.2 (-7) | — |
| $CH_3CN$ | 8.2 (-8) | 5.3 (-8) |
| $C_2H$ | 3.1 (-6) | — |
| $CH_3C_2H$ | 3.5 (-6) | — |
| $C_3H_2$ | 2.5 (-7) | — |
| $C_4H$ | 4.5 (-6) | 1.4 (-6) |

(a) signifies a detection has been made of that particular line in that particular source (see Table 4.5).

(b) signifies a blend of $HCC^{13}CN$ and $HC^{13}CCN$.

Table 4.7: Comparison with fractional abundances in other PPNe, arranged in order of decreasing stellar temperature.

| C-rich PPNe: | IRAS16594-4656 | M1-16 | CRL618 | CRL2688 | IRAS19500-1709 | IRC+10216 |
|---|---|---|---|---|---|---|
| $^{13}$CO | 3.3 (-5)[a] | | 2.4 (-5)[b] | 5.2 (-5)[b] | 2.0 (-5)[k] | |
| HCN | 6.1 (-7)[a] | 1.0 (-7)[j] | 4.4 (-6)[b]–5.0 (-7)[d] | 2.1 (-5)[b]–4.0 (-7)[d] | 1.5 (-7)[k] | 1.3 (-5)[r] |
| CN | 6.0 (-6)[a] | 8.5 (-7)[j] | 2.1 (-6)[c] | 1.0 (-6)[c] | | 2.2 (-6)[r] |
| H$^{13}$CN | $<$ 2.4 (-8)[a] | | 6.3 (-8)[e] | $>$ 4.0 (-6)[g]–5.1 (-7)[e] | | 2.8 (-7)[r] |
| HNC | $<$ 1.8 (-7)[a] | | 1.9 (-6)[b]–1.9 (-7)[e] | 1.8 (-7)[h]–5.0 (-8)[g] | | 5.5 (-8)[r] |
| HC$_3$N | $<$ 2.7 (-7)[a] | | 4.4 (-7)[e]–1.9 (-7)[b] | 1.5 (-7)[e,g] | | 1.0 (-6)[r] |
| HCO$^+$ | $<$ 1.2 (-7)[a] | 9.3 (-8)[j] | 2.0 (-7)[d] | | | |
| CS | $<$ 6.5 (-8)[a] | $<$ 8.8 (-8)[j] | 4.1 (-7)[b]–6.0 (-8)[d] | 2.1 (-6)[b] | | 8.8 (-7)[r] |
| C$_2$H | $<$ 3.1 (-6)[a] | | 2.0 (-6)[d] | 9.3 (-6)[f] | | 2.6 (-6)[r] |
| C$_4$H | $<$ 4.5 (-5)[a] | | 2.9 (-6)[b]–8.0 (-8)[d] | | | 3.2 (-6)[r] |
| SiO | $<$ 5.1 (-8)[a] | $<$ 2.4 (-8)[j] | $<$ 5.5 (-7)[b] | | | 1.1 (-7)[r] |
| SiS | $<$ 3.2 (-7)[a] | $<$ 4.2 (-8)[j] | | 4.0 (-8)[g] | | 9.5 (-7)[r] |
| O-rich PPNe: | IRAS17150-3224 | M1-92 | HD101584 | IRAS19114+0002 | OH17.7-2.0 | OH231.8+4.2 |
| $^{13}$CO | 2.9 (-5)[a] | | 5.0 (-4)[q] | 3.8 (-4)[b] | 4.2 (-6)[b] | 1.0 (-4)[l]–2.2 (-5)[b] |
| HCN | 3.8 (-7)[a] | $<$ 2.0 (-7)[o,p] | $<$ 1.7 (-6)[q] | $<$ 4.5 (-6)[b] | $<$ 1.6 (-7)[b] | 4.4 (-6)[b]–5.2 (-8)[m] |
| CN | $<$ 1.1 (-8)[a] | | | | | $<$ 2.0 (-7)[c,l] |
| H$^{13}$CN | $<$ 1.3 (-8)[a] | | | | | 4.8 (-8)[l] |
| C$_4$H | $<$ 1.4 (-6)[a] | $<$ 3.6 (-7)[q] | | $<$ 1.4 (-6)[b] | $<$ 4.7 (-8)[b] | |

(a) This work. (b) Bujarrabal et al. (1994) (c) Bachiller et al. (1997b) (d) Bujarrabal et al. (1988) (e) Sopka et al. (1989) (f) Fuente et al. (1998) (g) Nguyen-Q-Rieu & Bieging (1990) (h) Kasuga et al. (1997) (j) Sahai et al. (1994) (k) Using the results of Bujarrabal et al. (1992, 2001). (l) Morris et al. (1987) (m) Sanchez Contreras et al. (1997) (n) Omont et al. (1993b) (o) Lindqvist et al. (1992) (p) Nercessian et al. (1989) (q) Using the results of Olofsson & Nyman (1999). (r) Woods et al. (2003b)

### 4.6.2 Errors

As discussed in Chapter 2, there are inherent uncertainties in the approach taken here. Typical distance estimates can vary by up to a factor 2, and this influences the mass-loss rate derived from the radiative transfer modelling (see Sect. 4.5). When combined with the uncertainties in the choice of inner and outer radii for the molecular distributions, the overall error in fractional abundance varies with $\sim D^{-1-0}$, where $D$ is the distance. Given also that there are likely to be errors introduced by the choice of excitation temperature, an overall error of a factor 5 or so is to be expected in fractional abundance estimates. Moreover, some species other than CO are expected to be optically thick, most notably HCN, and the optically thin approximation would give systematically too low fractional abundances in those cases.

As mentioned in Sect. 4.5 contribution to the line intensities from the present-day, non-spherically symmetric, high-velocity, mass loss might become significant for some molecules. A full treatment of this problem, including the effects of radiative excitation due to dust emission, will require high spatial resolution observations of a large number of molecules.

With this caveat molecular fractional abundances are believed to be order of magnitude estimates. However, the properties of the outer wind, probed by the CO emission, should to be accurate to within a factor of two. The $^{12}$CO/$^{13}$CO ratio should be even better constrained.

## 4.7 Discussion

### 4.7.1 Comparison of observations with other observations

IRAS16594-4656 is very under-abundant in molecules in comparison to C-rich AGB stars. Generally, fractional abundances derived here, and presented in Table 4.5 (and the upper limits shown in Table 4.6), are an order of magnitude deficient when compared to C-rich AGB stars, such as those surveyed in Bujarrabal et al. (1994) and in Chapter 2. Two exceptions to this are CN and $^{13}$CO, which show good agreement with the fractional abundances derived for IRC+10216.

The lack of detection of SiO would seem to confirm that this object is C-rich, and that any silicate grains present (see García-Lario et al. 1999) are not being destroyed by shocks because either shocks might not be present, or the shocks which are present are not strong enough (c.f., van de Steene & van Hoof 2003).

Another explanation may be that the shocked regions are very small, in which case high abundances of SiO would be localised, and SiO emission diluted by the beam.

Conversely, IRAS17150-3224 seems (chemically) very much like an O-rich AGB star, such as those observed by Bujarrabal et al. (1994), or Lindqvist et al. (1988), for example. Although the fractional abundances of only two molecules, $^{13}$CO and HCN, in IRAS17150-3224 are suitable for comparison, they are very similar to the O-rich AGB stars in both AGB-star samples. In this case the SEST $^{13}$CO spectra presented here are not effected by the interstellar lines which plague the $^{12}$CO spectra. Values of the fractional abundance of $^{13}$CO are nearly identical between the simple photochemical model and the radiative transfer model, implying that the lines are optically thin.

So, IRAS16594-4656 and IRAS17150-3224 seem different breeds of PPNe from each other, and both seem far from the well-known molecule-rich PPNe, like CRL618, CRL2688 and OH231.8+4.2. IRAS16594-4656, supposedly a C-rich object, is poor in molecules and, as can be seen from Table 4.7, is at least an order of magnitude less abundant than CRL618 and CRL2688 in many molecules. However, IRAS16594-4656 has generally higher fractional abundances than M1-16, which is widely accepted to be a standard planetary nebula (PN). An exception to this is CN - a fractional abundance of CN similar to those in CRL618 and CRL2688 may indicate that IRAS16594-4656 is a somewhat evolved PPN, but not quite part of the PN regime yet. The theoretical work in Chapter 3 shows that fractional abundances of CN can remain high for a period of $\sim$100 years in the PPNe phase, whilst other molecules are destroyed, if molecular material is to be found in the shielded environment of a circumstellar torus.

Using the fractional abundance of HCN derived from the $J$=1-0 line, since this line is least likely of the two observed to be optically thick, a CN/HCN ratio of $< 10$ is derived for IRAS16594-4656. This value is quite uncertain, and dependent very much on the uncertainties discussed in Sect. 4.6.2. A full radiative transfer treatment of the HCN($J$=1-0) line does in fact predict a fractional abundance 2–3 times larger than that derived via the simple photodissociation model (Sect. 4.6.2), implying that IRAS16594-4656 could have a CN/HCN ratio as low as $\sim$3–5. In this case the CN/HCN ratio seems to indicate that IRAS16594-4656 is just starting the post-AGB phase. Other PPNe have a CN/HCN ratio up to an order of magnitude smaller, e.g., for CRL618, CN/HCN$\sim$0.5 and for CRL2688, CN/HCN$\sim$0.2. IRC+10216 has a smaller CN/HCN ratio yet, and the more evolved object NGC7027 has a CN/HCN ratio of about 10.

Both IRAS16594-4656 and IRAS17150-3224 have very low HCN/CO ratios compared to CRL618, CRL2688 and OH231.8+4.2. IRAS16594-4656 has an HCN/CO ratio of $6\times10^{-4}$, whereas CRL618 and CRL2688 have ratios of $6\times10^{-3}$ and $3\times10^{-2}$ respectively (Bujarrabal et al. 1994). IRAS17150-3224 has an HCN/CO ratio of $2\times10^{-3}$, which is again smaller than the $2\times10^{-2}$ of OH231.8+4.2 (Bujarrabal et al. 1994).

From Table 4.7, IRAS17150-3224 is similar to OH231.8+4.2 in $^{13}$CO, and HCN (despite the spread in observed values). The relatively high fractional abundance of HCN (only half that of the C-rich object IRAS16594-4656) would imply that IRAS17150-3224 is at a stage before heavy ionisation of the molecular matter occurs (and the CN fractional abundance rises), i.e., IRAS17150-3224 is at a less evolved stage than IRAS16594-4656.

### 4.7.2 Chemical evolution from the AGB

One has to ask why there seem to be two differing evolutionary paths for PPNe: why are some PPNe molecule-rich, like CRL618, and why are some molecule-poor, like the two objects discussed here. Visually, IRAS16594-4656 and IRAS17150-3224 are not very different from CRL618. All three have a similar bipolar structure, with a pinched waist indicating an equatorial density enhancement and possibly a collimating mechanism. In the case of CRL618, this mechanism could very well be a circumstellar torus, the presence of which has been implied from observations (see Herpin & Cernicharo 2000, and references therein). Hence it does not seem too exotic to consider similar structures for IRAS16594-4656 and IRAS17150-3224. Many of the PPNe identified do have such structures which have been directly observed (e.g., IRAS17106-3046 – Kwok et al. (2000), IRAS17245-3951 – Hrivnak et al. (1999), IRAS04296+3429 – Sahai (1999), Hen 401 – Sahai et al. (1999a), IRAS17441-2411 – Su et al. (1998); Kwok et al. (1996)) and there is strong evidence from polarimetry (Su et al. 2000) that a circumstellar disk or torus does exist around IRAS16594-4656.

CRL618 owes its molecular richness, in a large part, to the shielding effects of its torus. This can clearly be seen in the chemical model detailed in Chapter 3 – the high levels of radiation are only abated by high initial densities and a slow torus expansion velocity, and when the density, or essentially the extinction, becomes too low, complex molecules are destroyed. One obvious implication that this has for PPNe such as IRAS16594-4656 and IRAS17150-3224 is that their collimating

torus must not be dense enough to synthesise and protect complex molecules. This brings in an interesting interplay between the column density of material required to produce the degree of collimation seen and the column density of material required to shield complex molecules from the often very intense UV fields, cosmic rays and possibly also X-rays. One of the prevalent results from the previous chapter is that incident UV radiation starts to destroy molecules when the optical depth reaches approximately 10 magnitudes of extinction. This equates to a column density of $\sim$1.6 $10^{22}\,\mathrm{cm}^{-2}$. For the particular model of CRL618, the density at the innermost part of the torus is $\sim 10^{9}\,\mathrm{cm}^{-3}$. Typically an average AGB star during the superwind phase at the end of AGB evolution (e.g., $\dot{M} = 10^{-4}\,\mathrm{M}_{\odot}\,\mathrm{yr}^{-1}$ and $\mathrm{v}_{\mathrm{exp}} = 15\,\mathrm{km\,s}^{-1}$) would have a density of around $10^{8}\,\mathrm{cm}^{-3}$ at a similar radial distance ($10^{15}\,\mathrm{cm}$). Numerical models (e.g., Ignace et al. 1996) show that only an equatorial density enhancement of 2 or more over the polar direction is enough to produce asphericity (bipolarity) in a wind-compressed disk situation.

# Chapter 5

# Molecule-poor proto-planetary nebulae: Modelling

## 5.1 Introduction

To investigate the changes in fractional abundance of species during the late AGB and PPN phases, in a region of no particular density enhancement (e.g., a torus, clump or disk), a chemical model of the circumstellar envelope was used. Results of this model are shown in Fig. 5.2. The chemical model of IRC+10216 constructed by Millar et al. (2000, MHB) was adapted to investigate the chemistry as an AGB star finishes its phase of mass loss, and moves into the PPN phase. Several simplifying assumptions are made, and the MHB model has been changed to include X-rays, and a minimal X-ray chemistry.

### 5.1.1 Model parameters and simplifying assumptions

Nine parcels of gas and dust in the circumstellar envelope (CSE) of an AGB star are assumed to flow outward at a uniform velocity of $14\,\mathrm{km\,s^{-1}}$, from initial radial distances of 1, 2, 4 and $7\times10^{15}$, 1, 4 and $7\times10^{16}$ and 1 and 4 $\times10^{17}\,\mathrm{cm}$ from the central star. A mass-loss rate of $1\times10^{-5}\,\mathrm{M}\odot\,\mathrm{yr}^{-1}$ is chosen, in accordance with the molecular line modelling in Table 4.4. A spherical geometry implies that the density of the homogeneous outflow drops as $r^{-2}$. Mass-loss is assumed to end with

the start of the model.

*Envelope heating.* During the expansion, the "kinetic temperature" of the parcels varies according to $T{=}T_0(r_0/r)^{0.79}$, where $T_0$ increases from 100 K to 1 000 K over the first 1 000 yr of the model (chosen to represent the PPN phase). This heating is due to the increasing temperature of the central star as it evolves towards a white dwarf.

*Stellar UV field.* Following the increase in stellar temperature, the intensity of the stellar UV field also increases. An ionisation rate similar to that of the interstellar UV field is assumed at the start of the model. At the end of the first 1 000 yr this value has increased by a factor of 100 at $10^{16}$ cm; this is very small compared to $2{\times}10^5$ times the interstellar field assumed by Herpin & Cernicharo (2000), however IRAS16594-4656 (presently) has an effective temperature three times lower than CRL618. Furthermore, as the results below show, this enhancement is enough to prove the point in hand.

### 5.1.2 X-rays

X-rays from the central star or companion (Woods et al. 2002) are treated in a very simple way in this model. The X-ray extinction law of Deguchi et al. (1990) is used (see their Eq. B3), and an X-ray energy of 1.2 keV is assumed ($\lambda \sim$1 nm). X-rays only play an ionising role in the chemical reaction network, and these reactions are given the same rate coefficients as the equivalent cosmic-ray reactions. A very low ionisation rate of $10^{-17}\,\mathrm{s}^{-1}$ is chosen initially; this rises to a rate of $10^{-13}\,\mathrm{s}^{-1}$ by the end of the model run.

### 5.1.3 Chemical reaction network

The reaction network is the same as that used in the next chapter, with the addition of a small number of X-ray ionisation reactions. Now the network includes 3897 reactions among 407 species in 6 elements. Initial fractional abundances are determined via the use of an AGB steady-state model, with a mass-loss rate of $1{\times}10^{-5}\,\mathrm{M}_\odot\,\mathrm{yr}^{-1}$ and expansion velocity of $14\,\mathrm{km\,s}^{-1}$. For example, a parcel starting at a radius of $1{\times}10^{16}$ cm in the model presented here will have initial abundances which are the same as a parcel of "AGB" material at the same radial distance. The adopted AGB envelope is shown in Fig. 5.1. Initial abundances of parent molecules for the AGB model are chosen to represent a carbon-rich environment, and values are taken from MHB.

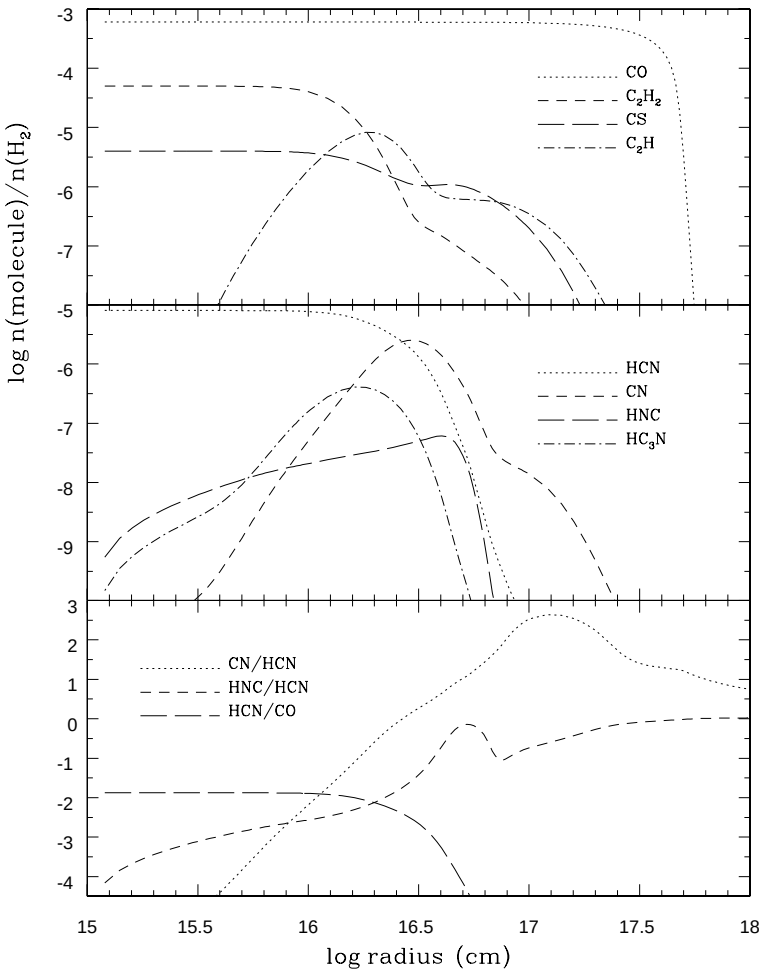


Figure 5.1: Steady-state AGB model showing the fractional abundances used as inputs to the parcel model of IRAS16594-4656. The bottom panel shows the radial variation of selected ratios through the AGB circumstellar envelope. A mass-loss rate of $1\times10^{-5}\,\mathrm{M}\odot\,\mathrm{yr}^{-1}$, an expansion velocity of $14\,\mathrm{km\,s}^{-1}$ and initial fractional abundances appropriate for a carbon-rich envelope were used.

## 5.2 Discussion

### 5.2.1 Comparison of observations with chemical model

The chemical model generally shows good agreement with the fractional abundances derived in the previos chapter. Both HCN and CN reach the calculated fractional abundances for IRAS16594-4656 and IRAS17150-3224 during the first 100 yr of the model. However, by 500 yr these two species are drastically depleted. Upper limits for other observed species (e.g., HNC, $HC_3N$, $C_2H$ and $C_4H$) are also in agreement with the model in this region.

The model shows how few species survive at observable levels after, say, 1 000 yr

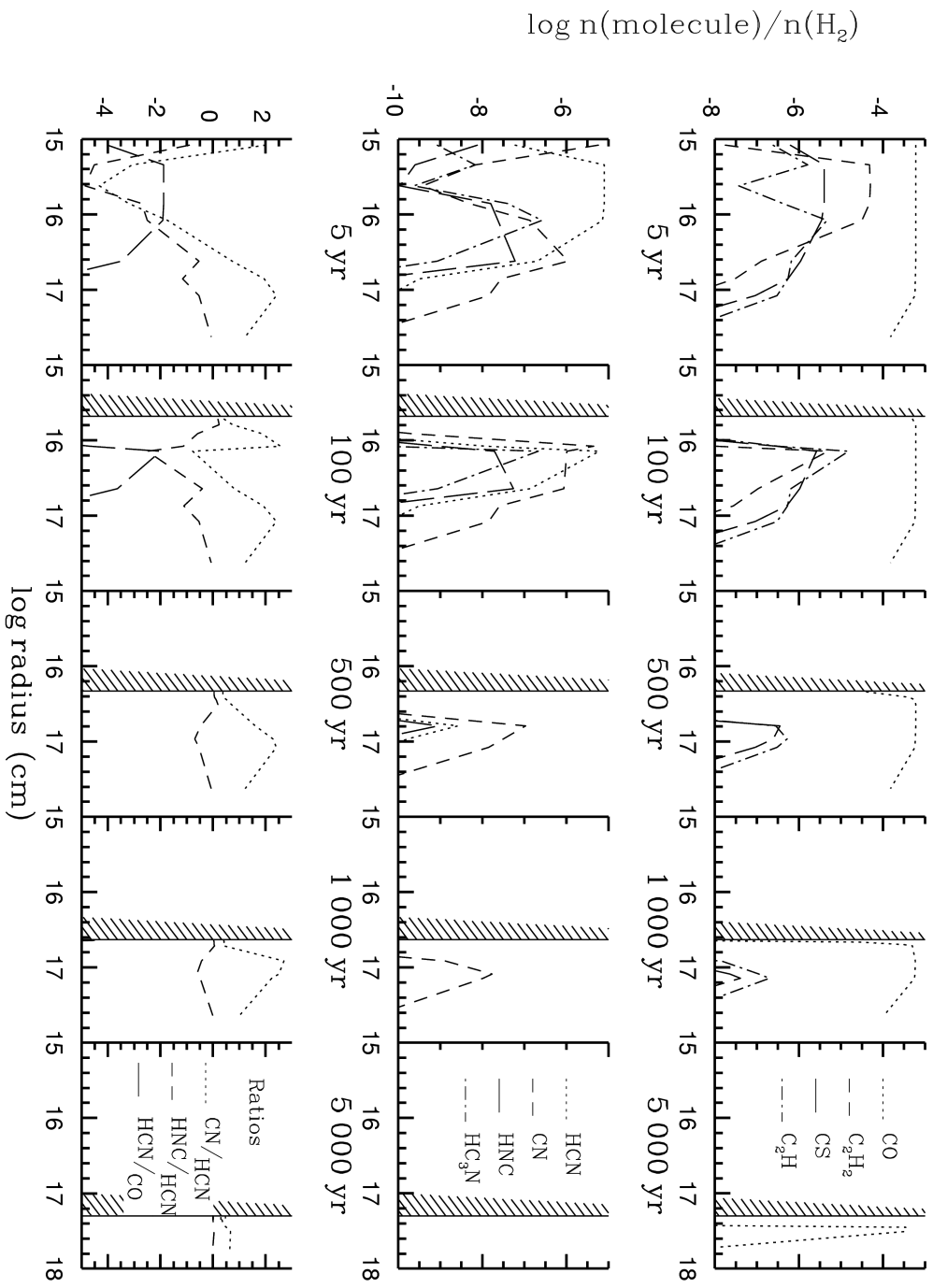


Figure 5.2: Results of the chemical model of IRAS16594-4656. The figure shows the variation of the fractional abundances (or ratios, in the lower row of axes) of selected species radially through the expanding circumstellar envelope at different points in time (measured in years since the cessation of mass-loss). The shading marks the passage of the inner edge of the circumstellar envelope. As can be seen at long times (5 000 yr), only CO is reasonably abundant.

of post-AGB evolution. Of those shown in Fig. 5.2 only CO, CS, $C_2H$ and CN are seen to survive 1 000 yr, and only CO remains at the 5 000 yr mark.

Perhaps the most interesting result of the model is the variation of the CN/HCN, HNC/HCN and HCN/CO ratios. As expected, the CN/HCN ratio is seen to rise during the early post-AGB evolution (taking a mean through the envelope). Similarly, the HNC/HCN ratio also increases. The HCN/CO ratio slowly decreases with evolutionary age. When these three behaviours are combined, a reasonably accurate age can be given. This approach is taken later, in Sect. 4.7.2.

Again, the sharp drop-offs in fractional abundance are seen in the outer parts of the envelope, similar (although not as steep) to those seen in the chemical model of a PPN torus (Chapter 3).

### 5.2.2 Chemical evolution from the AGB

To support the hypothesis that these two PPNe are low in fractional abundances due to low envelope density, a chemical model was constructed to follow the evolution of a star along the AGB phase and into the PPNe phase. The model shows that within $\sim$500 yr of the cessation of mass-loss UV photons from the star start to ionise the molecular material at a very high rate, and molecular matter is destroyed rapidly. As an example, HCN loses three orders of magnitude in fractional abundance in the 500 or so years after mass-loss stops (Fig. 5.2). CO, which self-shields in the model, would survive at least 10 000 yr after the end of mass-loss at detectable levels. Hence for molecules other than CO to survive through the PPN phase and into the PN phase, they must either i) benefit from heavy UV shielding ($\gtrsim$10 mag) from the very end of the AGB phase or ii) be reformed, either constantly or when conditions are more favourable. Which of these options is correct is currently open for debate, with some siding for the conveyance of clumps throughout the entire post-AGB phase (e.g., Redman et al. 2003), and some siding against (e.g., Huggins & Mauron 2002).

### 5.2.3 Post-AGB ages of IRAS16594-4656 and IRAS17150-3224

Using the fractional abundances calculated from observations (Chapter 4) and the chemical model presented here, an approximate post-AGB age for IRAS16594-4656 can be estimated. IRAS16594-4656 seems to be older than IRAS17150-3224, with quite a high CN fractional abundance and also a high CN/HCN ratio. Through

comparison with Fig. 5.2 in particular, the figure of 370 yr, named by van der Veen et al. (1989), seems a good upper limit. IRAS17150-3224 is slightly more difficult to qualify, since there is no detection of CN. However, this does suggest that the CN/HCN ratio is low. The HCN/CO is high (higher than IRAS16594-4656) and hence a post-AGB age of 150–210 yr for IRAS17150-3224 (Hu et al. 1993; Meixner et al. 2002) seems likely, with the estimate of van der Veen et al. (1989), 800 yr, appearing to be much too long to be an accurate post-AGB age for this object.

It is not clear whether IRAS16594-4656 and IRAS17150-3224 are older or younger than CRL618 and CRL2688. The lack of signs of ionisation suggest that they are younger; the reasonably high CN/HCN ratios and low HCN/CO ratios suggest that they are older. Certainly, IRAS16594-4656 fits into the " evolutionary sequence" (of post-AGB objects) of Bachiller et al. (1997a) between CRL618 and the young PN, NGC7027. The age estimates of van der Veen et al. (1989), Hu et al. (1993) and Meixner et al. (2002), above, in comparison with the results of Bujarrabal et al. (2001) also tend to favour IRAS16594-4656 and IRAS17150-3224 being older, since Bujarrabal et al. (2001) give post-AGB ages for CRL618 and CRL2688 as 110 and 200 yr, respectively.

## 5.3 Conclusions from Chapters 4 and 5

Two proto-planetary nebulae, IRAS16594-4656 and IRAS17150-3224, were observed in a wide range of molecular lines, but only detected in a few. Calculating fractional abundances and upper limits from these lines shows that these two sources are molecule-poor in relation to other PPNe such as CRL618 and OH231.8+4.2. As a reason for this apparent difference the degree of density of the circumstellar torus (or disk) is suggested, with molecule-rich PPNe having dense, protective and nurturing tori, and molecule-poor PPNe having tenuous, or no, tori. To substantiate this, a model of the chemistry in a late–AGB/early–PPN circumstellar envelope, with no particular density enhancements (such as a torus), is used. As expected, it shows that very few molecules reach high fractional abundances in the post-AGB phase, and agrees well with fractional abundances calculated from observations. This is in stark contrast to the model in Chapter 3 of a dense circumstellar torus in the PPN phase. The usefulness of HCN/CO, HNC/HCN and particularly CN/HCN ratios in determining evolutionary age is discussed, and using these tools, post-AGB ages for IRAS16594-4656 and IRAS17150-3224 are given.

# Planetary nebulae

This look at AGB and post-AGB chemistry would not be complete without a study of planetary nebulae. Although the following section is cursory, leaving much to be explored, it serves well enough to illumine some chemically interesting aspects of the final stage of stellar evolution.

# Chapter 6

# Molecules in young planetary nebulae

## 6.1 Introduction

The planetary nebula (PN) phase of evolution is marked by a hot ($\sim$100 000 K) central star, an ionised region and diffuse matter, which makes the detection of molecules surprising. Molecules such as CO, HCN, HNC, CN and $C_2H$ are thought to survive (Bachiller et al. 1997a; Josselin & Bachiller 2003) from the Asymptotic Giant Branch (AGB), through the proto-planetary nebula (PPN) stage, and into the PN stage of evolution through being shielded from the intense radiation from the central star and the much less intense radiation from the interstellar medium (ISM). Clumps are such a method of shielding. Indeed, clumps have been observed in young PNe (such as IC4406, O'Dell et al. 2003, 2002; López 2003), where the clumps are seen in the neutral material, and in more evolved objects (such as the Helix nebula, Huggins et al. 2002), where the ionisation front has overtaken them, and cometary tails are seen. Without this enhanced shielding such molecules could not be observed: The modelling of a dense torus and an increasingly diffuse circumstellar shell with no density enhancements in the previous chapters has shown that very few molecules survive - in fact, only CO survives until long times, and this is most likely due to its high fractional abundance and self-shielding properties.

Clumps in AGB stars are generally of the size of a stellar radius ($\approx 10^{13}$ cm), have a density of $10^7$ cm$^{-3}$, a temperature of a few hundred degrees Kelvin, and a visual extinction ($A_V$) of 100 or less (taken from the model of Redman et al. 2003). The cometary globules in the Helix (planetary) nebula are somewhat less dense ($4.5\times10^5$ cm$^{-3}$, Meaburn et al. 1992), although it seems that the clumps envisaged in AGB stars are not massive enough ($\geq 10^{-5}$ M$_\odot$) to be cometary globule precursors (Huggins & Mauron 2002).

In this chapter three planetary nebulae are observed: IC4406, NGC6072 and NGC6563. These three objects are described in more detail in Sect. 6.2. A number of molecules are detected, and two molecules, formaldehyde ($H_2CO$) and carbon sulphide (CS), are detected for the first time in a planetary nebula – $H_2CO$ in both IC4406 and NGC6072, and CS in IC4406. Maps of CO, $^{13}$CO, HCN and CN emission are also made, and show the distribution of these molecules in these particular sources. Finally, fractional abundances are calculated, and show that all three PNe are reasonably abundant in molecules.

## 6.2 Objects

### 6.2.1 IC4406

IC4406 is a bipolar planetary nebula (Corradi & Schwarz 1995), with an equatorial disk (Sahai et al. 1991; Scarrott & Scarrott 1995; Gruenwald et al. 1997). HST images of IC4406 (O'Dell et al. 2003) show that the nebula has a cylindrical shape, with a diameter of 35″ (Phillips 2002; Zhang 1995, see Appendix A.3.1). Shocked $H_2$ emission marks the boundary of the ionised inner region and the outer, molecular region (Storey 1984).

The nebula is seen to contain clumps (López 2003) or knots (O'Dell et al. 2003, 2002), close to the ionisation front of the nebula (some 0.1 pc from the central star), but within the neutral material. The knots do not appear directional since they have no tails (O'Dell et al. 2003); instead, they form a "lacy" pattern. The position of these knots, not yet inside the ionised region, indicates that this object is reasonably young, although O'Dell et al. (2002) derive a dynamic age of 9 000 yr from the expansion velocity of CO (11.5 km s$^{-1}$, Sahai et al. 1991). A much larger dynamical age of 27 000 yr is calculated if the expansion velocity from optical data is used.

Few molecules have been detected previous to this work: the CO ($J$=2-1) transi-

tion was mapped by Cox et al. (1991), and Sahai et al. (1991) map both the ($J$=1-0) and ($J$=2-1) transitions of CO. Cox et al. (1992) report detections of $^{13}$CO, CN, $HCO^+$, HCN and HNC. However, they fail to detect $N_2H^+$, $C_2H$ and $HC_3N$. The CN ($N$=3-2) transition was detected by Bachiller et al. (1997b). According to Huggins et al. (1996), there is more molecular matter than ionised (0.25 $M_\odot$ compared to 0.18 $M_\odot$), and a large proportion of the molecular matter is contained within the cylindrical cavity (Sahai et al. 1991).

The stellar temperature is estimated to be 79 250 K (Stanghellini et al. 1993) or 94 000 K (Liu et al. 1995), and the luminosity is low, some 800 $L_\odot$ (Stanghellini et al. 1993).

### 6.2.2 NGC6072

NGC6072 is also a bipolar planetary nebula. It has a visible waist, which shows the brightest $H_2$ emission, where the $H_2$ is probably shock-excited (Kastner et al. 1996).

NGC6072 has been observed in CO ($J$=2-1) by Huggins & Healy (1989). It was then mapped in this line by Healy & Huggins (1990) and also by Cox et al. (1991). More recently Balser et al. (2002) observed both the $^{12}$CO and $^{13}$CO ($J$=2-1) lines in order to derive a $^{12}C/^{13}C$ ratio. Their calculation resulted in $^{12}C/^{13}C = 6.9 \pm 0.3$. Other molecular observations are limited to the detection of CN ($N$=3-2) by Bachiller et al. (1997b) and $^{13}$CO, CN, $HCO^+$, HCN and HNC by Cox et al. (1992). Small maps in CN ($N$=1-0), HCN ($J$=1-0) and $HCO^+$ ($J$=1-0) with the SEST by Cox et al. (1992) reveal that the nebula is extended, and that the distribution of these molecules approximately follows that of CO ($J$=2-1).

In contrast to IC4406, NGC6072 has predominantly more ionised material than molecular. Healy & Huggins (1990) give the ratio of molecular to ionised gas (by mass) as 0.29:0.73; (Huggins & Healy 1989) give 0.54:0.69 – these values vary with the adopted fractional abundance of CO. Also, NGC6072 has a much hotter central star than IC4406, with the stellar temperature given as 147 910 K (Stanghellini et al. 1993), or 150 000 K (Zhang & Kwok 1993), whilst the luminosity is 220 $L_\odot$ (Stanghellini et al. 1993), or 400 $L_\odot$ (Zhang & Kwok 1993).

Expansion velocities differ depending on whether derived from molecular or ionic observations. A value of 10 km s$^{-1}$ is taken from observations of the ionised gas (Gussie & Taylor 1994), whilst 15.5 km s$^{-1}$ is taken from the CO data of Cox et al. (1991).

Table 6.1: PNe co-ordinates and other data.

| Object | IRAS number | J2000 Co-ords. [h:m:s °:′:″] | $v_{\rm LSR}$ [km s$^{-1}$] | Distance [kpc] | Mass-loss rate $M_\odot$ yr$^{-1}$ |
|---|---|---|---|---|---|
| IC4406 | 14192-4355 | 14:22:25.8 −44:09:00 | −50 | 1.7[a] | $1.7\times10^{-5}$[c] |
| NGC6072 | 16097-3606 | 16:12:58.8 −36:13:38 | 0 | 1.8[a] | $2.0\times10^{-5}$[c] |
| NGC6563 | 18087-3352 | 18:12:02.6 −33:52:05 | −25 | 0.7[b] | $4.0\times10^{-6}$[c] |

(a) Sabbadin (1986). (b) Maciel & Pottasch (1980). (c) Cox et al. (1991).

### 6.2.3 NGC6563

The third of the planetary nebulae selected from the southern sky is NGC6563. This is an elliptical ring nebula with a brightening on its minor axis (Huggins et al. 1996). The stellar temperature is reported to be 136 500 K by Cazetta & Maciel (2000), again, much higher than IC4406.

Very little information is available on the molecular content and structure of this object. A detection of CO ($J$=2-1) is made by Huggins & Healy (1989), and this was followed up with a small map of the same transition (Cox et al. 1991). Huggins et al. (1996) use the same data to derive a mass of molecular material: 0.021 $M_\odot$, which gives a ratio to the ionised material of 0.93.

Again, a discrepancy between the expansion velocity derived from optical and molecular (CO) data is evident. CO data indicates an envelope expanding at 20 km s$^{-1}$, whilst optical data gives 11 km s$^{-1}$ (Huggins et al. 1996).

## 6.3 Observations

Observations were made with the 15 m SEST, located on Cerro La Silla, Chile, during 2000 and the early part of 2002. J2000 co-ordinates of the three planetary nebulae are listed in Table 6.1, along with the local standard of rest (LSR) velocities used for the observations. Distances are adopted from values given in the literature (Sabbadin 1986; Maciel & Pottasch 1980) and mass-loss rates are from Cox et al. (1991). Instrumentation at the SEST comprised of four SIS receivers, at 0.8, 1.3, 2 and 3 mm, and three spectrometers: one high resolution, and two wideband. The observation method was that which is described in Chapter 2, with the dual beam switching method employed for the point observations. Mapping was also performed with the dual beam switching method, with beam separations that varied according to source (although never more than 11″, half a beamwidth at 230 GHz).

Table 6.2: Detected lines in the three PNe.

| Molecule | Transition | Frequency | IC4406 | | NGC6072 | | NGC6563 | |
|---|---|---|---|---|---|---|---|---|
| | | | $T_{\rm mb}$ | $\int T_{\rm mb}{\rm dv}$ | $T_{\rm mb}$ | $\int T_{\rm mb}{\rm dv}$ | $T_{\rm mb}$ | $\int T_{\rm mb}{\rm dv}$ |
| | | GHz | K | K km s$^{-1}$ | K | K km s$^{-1}$ | K | K km s$^{-1}$ |
| $C_2H$ | $N$=1-0 | 87.329 | 0.01 | 0.51 | 0.03 | 2.27 | — | — |
| HCN | $J$=1-0 | 88.632 | 0.08 | 2.33 | 0.11 | 3.74 | 0.04 | 0.72 |
| $HCO^+$ | $J$=1-0 | 89.189 | 0.06 | 2.23 | 0.13 | 3.09 | 0.04 | 0.82 |
| HNC | $J$=1-0 | 90.664 | 0.03 | 0.53 | 0.06 | 1.36 | — | — |
| $^{13}CO$ | $J$=1-0 | 110.201 | 0.02 | 0.41 | — | — | 0.03 | 0.33 |
| CN | $N$=1-0 | 113.491 | 0.10 | 7.81 | 0.22 | 13.92 | 0.09 | 8.49 |
| CO | $J$=1-0 | 115.271 | 0.36 | 8.33 | 0.73 | 14.21 | 0.19 | 6.25 |
| $H_2CO$ | $2_{1,2}$-$1_{1,1}$ | 140.840 | 0.03 | 0.74 | 0.05 | 0.29 | — | — |
| CS | $J$=3-2 | 146.969 | 0.01 | 0.23 | — | — | — | — |
| $^{13}CO$ | $J$=2-1 | 220.399 | 0.17 | 2.21 | — | — | — | — |
| CN | $N$=2-1 | 226.875 | 0.34 | 14.22 | 0.36 | 10.68 | 0.13 | 5.43 |
| CO | $J$=2-1 | 230.538 | 1.55 | 29.00 | 2.33 | 35.60 | 0.74 | 16.29 |
| HCN | $J$=3-2 | 265.886 | 0.23 | 4.11 | — | — | — | — |
| $HCO^+$ | $J$=3-2 | 267.558 | 0.18 | 2.76 | 0.18 | 0.24 | — | — |

Detected lines are shown in Table 6.2, with detected intensities shown in main beam temperature, which accounts for telescope beam (in)efficiencies.

## 6.4 CO spectra

CO ($J$=1-0) and ($J$=2-1) spectra are shown in Fig. 6.1. The spectra from all three sources have features worthy of note:

Figure 6.1 shows CO spectra of IC4406, with two main peaks at -23 and -60 $\mathrm{km\,s^{-1}}$, and a profile width of $\approx$64 $\mathrm{km\,s^{-1}}$. In all likelihood the separation of the two main peaks will give a better representation of the expansion velocity of the shell, and hence $v_{exp}$=18.5 $\mathrm{km\,s^{-1}}$. There is also a less intense peak, seen more clearly in the CO ($J$=2-1) spectrum – a small feature in the centre of the profile has a width of 5 $\mathrm{km\,s^{-1}}$. In addition, an appreciable line wing on the blueshifted side, and a less obvious wing on the redshifted side of the CO ($J$=2-1) profile can be seen.

The main peaks of the CO profiles towards NGC6072 (Fig. 6.1) occur at -2 and 30 $\mathrm{km\,s^{-1}}$, giving an expansion velocity of 16 $\mathrm{km\,s^{-1}}$. The width of the profile is different for CO ($J$=1-0) and ($J$=2-1): In the first case it is 55.6 $\mathrm{km\,s^{-1}}$, in the second only 46.5 $\mathrm{km\,s^{-1}}$ – i.e., the less excited CO gas seems to be expanding 4.5 $\mathrm{km\,s^{-1}}$ faster. Interstellar emission is seen in the profiles at 5.4 $\mathrm{km\,s^{-1}}$ and also 14.4 $\mathrm{km\,s^{-1}}$.

The CO ($J$=1-0) profile towards NGC6563 does not show the two distinct peaks which are seen in the ($J$=2-1) spectrum because the beamsize is larger at the lower frequency. These peaks are at -4 and -45 $\mathrm{km\,s^{-1}}$, indicating a shell expanding at $\approx$20 $\mathrm{km\,s^{-1}}$. There is a less intense feature shown in the CO ($J$=2-1) spectrum peaking at -16 $\mathrm{km\,s^{-1}}$ which is too wide ($\approx$10 $\mathrm{km\,s^{-1}}$) to be interstellar.

## 6.5 Molecular distributions

The maps displayed in Figs. 6.2–6.5 show the distribution of molecules in the three PNe by means of intensity of emission. Maps on the same page share the same scale.

IC4406, as can be seen from the images in Sect. A.3.1, has a cylindrical shape. The two other PNe are also likely to be cylindrical, or ellipsoidal in shape. This can be seen in the maps of the nebulae, where the doubly-peaked line profiles are a result of more intense emission from the "walls" of the cylinder. The CO ($J$=1-0)

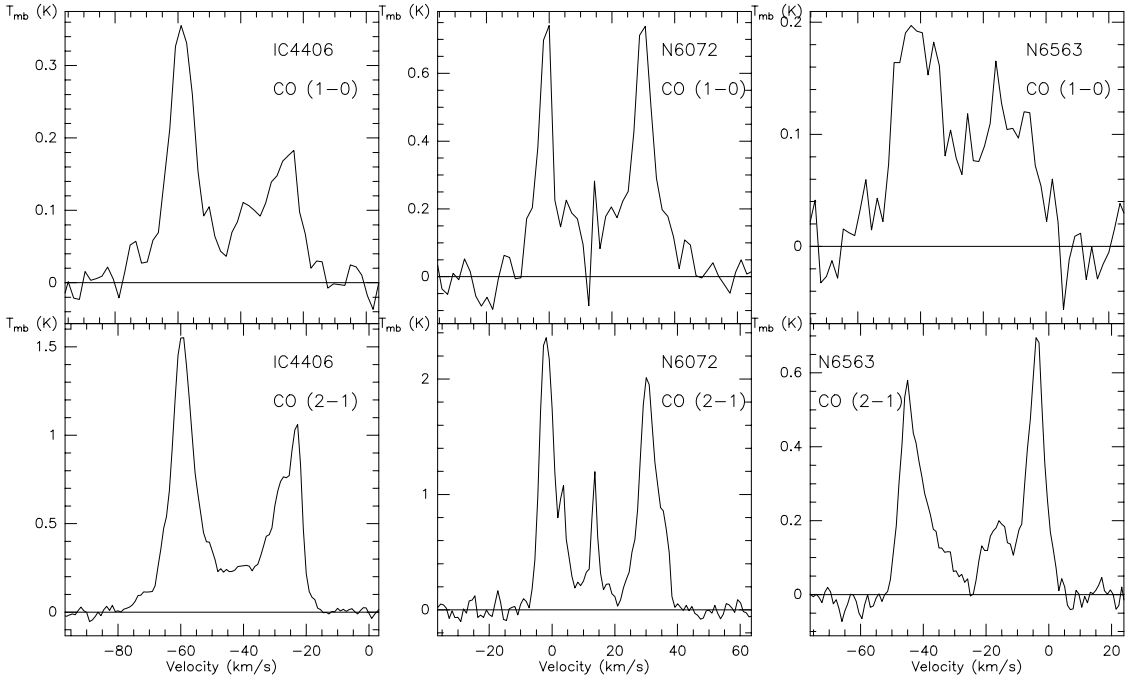


Figure 6.1: CO ($J$=1-0) and CO ($J$=2-1) spectra of the three sample PNe.

map of NGC6563 does not show double peaked profiles due to the reason stated above.

The fact that two peaks are seen indicates that the emission is optically thin, and the difference in intensity of the peaks is probably due largely to geometrical effects rather than optical depth effects. Thus it seems reasonable to assume that the more intense the emission, the greater abundance of that particular species.

All mapped emission seems to be most intense in the centre of the map; the "bright" region is spread over a number of telescope pointings in most of the maps, indicating that the molecular matter is not concentrated in the very centre of these objects. In fact, in most, if not all, of the objects, molecular emission is detected at distances of $\pm 33''$ from the central star. In most cases this emission is CO, but in the case of IC4406 both HCN and CN are detected at these distances too.

Figure 6.6 and Table 6.3 show Gaussian fits to the map spectra, and give some indication of the distribution of molecules in these three sources. The CO ($J$=1-0) emission, usually taken as a tracer for molecular hydrogen, marks the limits of the former AGB envelopes, which through expansion outward, now form a "halo".

IC4406 has a visual size of about $85''\times30''$ (Strasbourg-ESO catalogue, Acker et al. 1992), quite different to the size calculated from the CO ($J$=1-0) map, of $\approx 60''\times65''$. From their CO ($J$=2-1) map, Cox et al. (1991) give a half power size of

Table 6.3: Full width half maximum (FWHM) of the Gaussian fits to the integrated intensity of the map spectra. Numbers in brackets are the position angle of the elliptical fit. See also Fig. 6.6

| Line | IC4406 | NGC6072 | NGC6563 |
|---|---|---|---|
| HCN(1-0) | $51.3'' \times 64.5''$ (213°) | — | — |
| CN(1-0) | $33.4'' \times 41.8''$ (34°) | — | — |
| CO(1-0) | $60.6'' \times 65.8''$ (−11.5°) | $59.5'' \times 54.7''$ (38.6°) | $54.6'' \times 63.3''$ (0.3°) |
| CO(2-1) | $34.9'' \times 45.7''$ (−7.6°) | $67.0'' \times 47.4''$ (−0.6°) | $55.9'' \times 49.9''$ (−6.4°) |

$35'' \times 25''$, some $10''$ smaller than that which is determined here. This may be due to developments in the sensitivity of the SEST instrumentation over the ten year period between the two observing runs.

NGC6072 has a visual size of $87'' \times 65''$ (ESO/SRC Southern Sky survey), much larger than the size determined from the CO ($J$=1-0) map fit ($60'' \times 55''$). Again, Cox et al. (1991) give a half power size which is smaller than that which is determined from the CO ($J$=2-1) map presented here.

NGC6563 is a visually small planetary nebula (Strasbourg-ESO catalogue, Acker et al. 1992), of size $50'' \times 38''$. The CO ($J$=1-0) emission marks out a half power size of at least $55'' \times 60''$, and the CO ($J$=2-1) emission $55'' \times 50''$.

Interestingly, it can be seen that the CO ($J$=2-1) emission region lies almost on top of the CO ($J$=1-0) emission region in both NGC6072 and NGC6563, whereas for IC4406 it is much smaller. This could be due to a more dense dust shell around IC4406, providing a higher extinction (permitting less exciting radiation).

## 6.6 Molecular abundances

Molecular abundances are calculated in the same way as in Chapter 2 – however, since this simplistic method is open to error in distance, mass-loss rate and resolution effects (especially in the case of PNe, where matter is likely to be clumpy, or fragmented), abundance ratios are given in relation to HCN, which is detected in all three objects. Abundance ratios are more robust than simple fractional abundances. Non-detections are given in Table 6.5. The derived abundances are more for comparison with the study of Cox et al. (1992) rather than any particular significance in the values themselves.

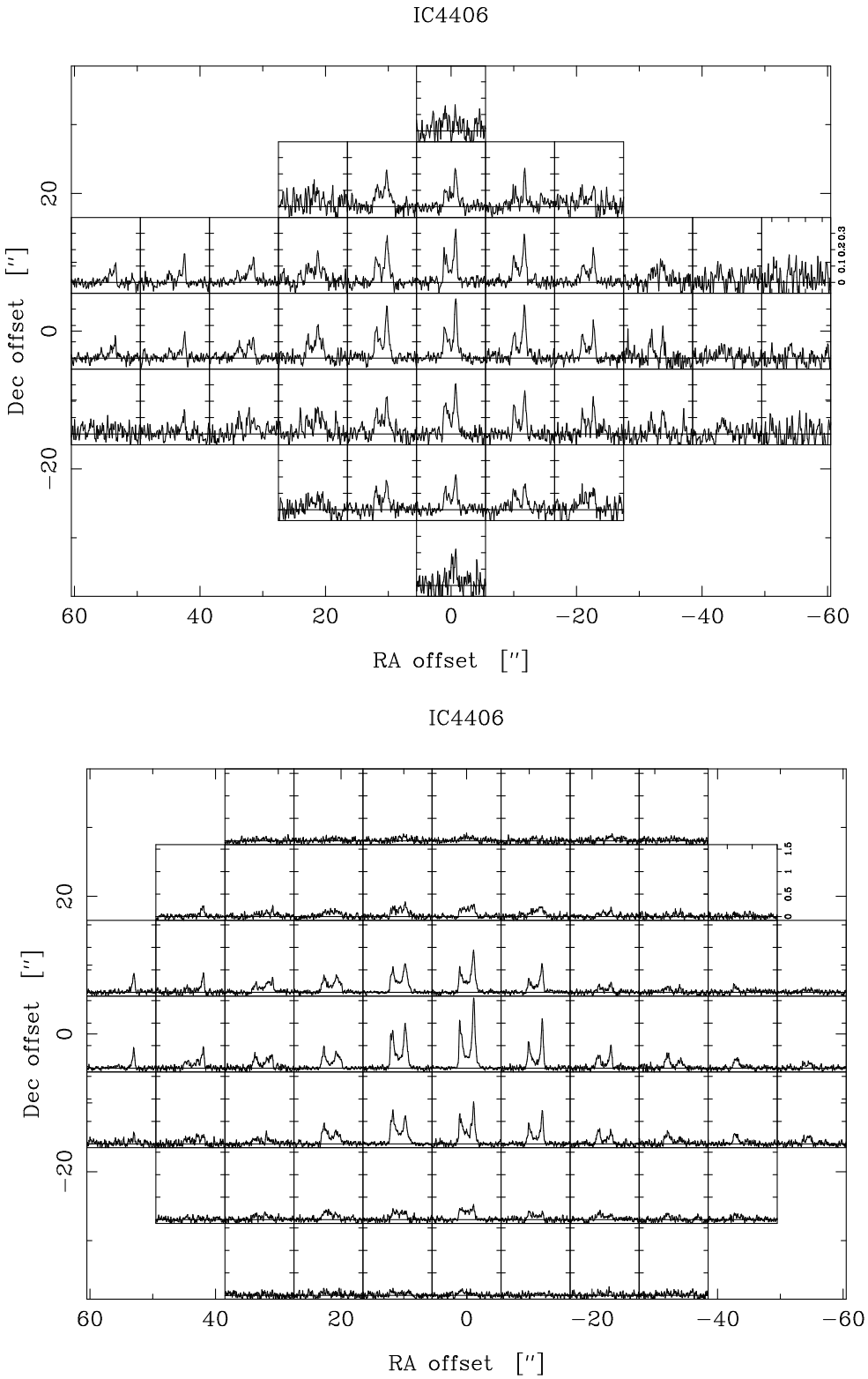


Figure 6.2: **Top**. A map of the CO ($J$=1-0) emission towards IC4406. **Bottom**. A map of the CO ($J$=2-1) emission towards IC4406.

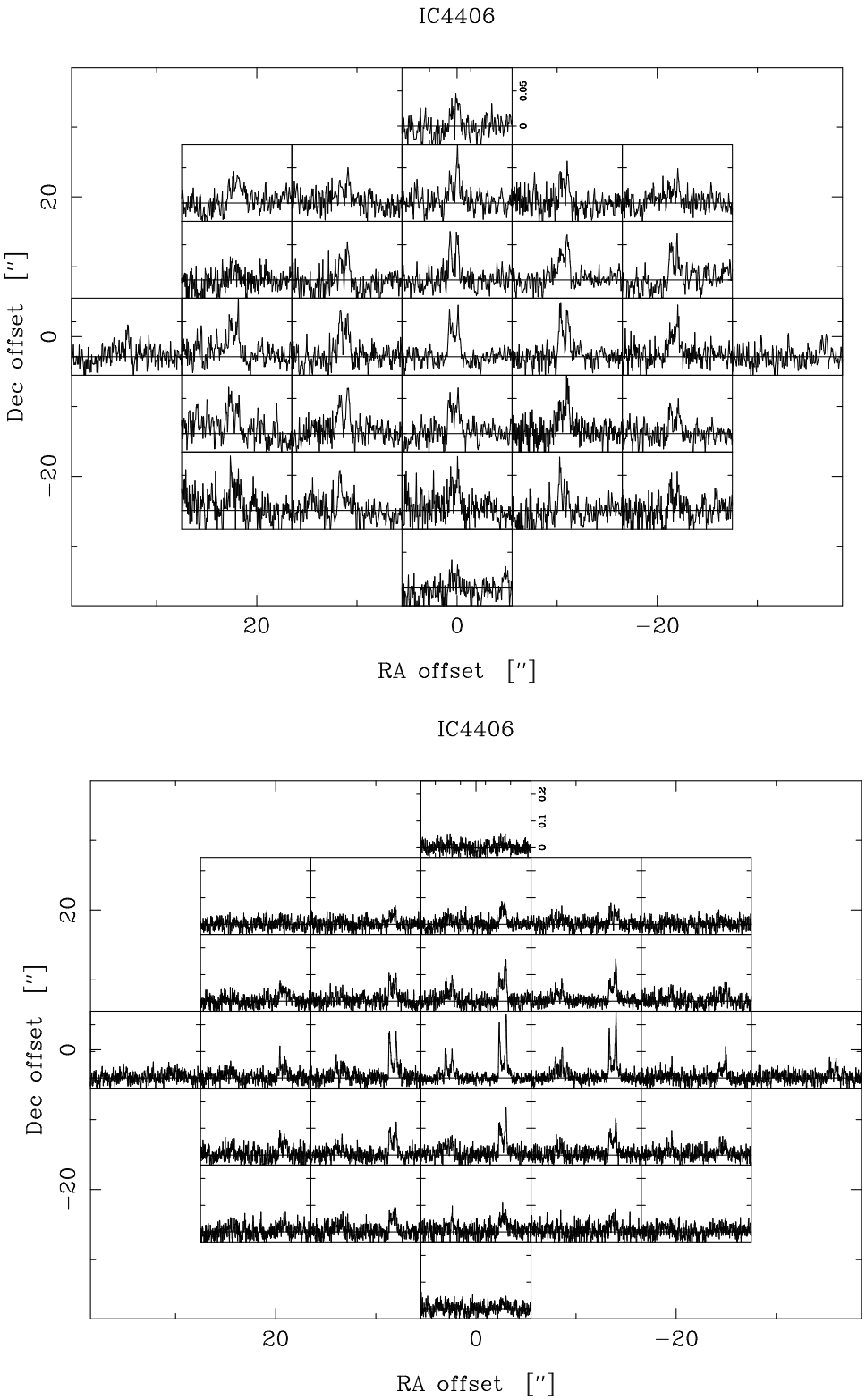


Figure 6.3: **Top**. A map of the HCN ($J$=1-0) emission towards IC4406. **Bottom**. A map of the CN ($N$=2-1) emission towards IC4406. Only the two strongest components of the hyperfine splitting are shown.

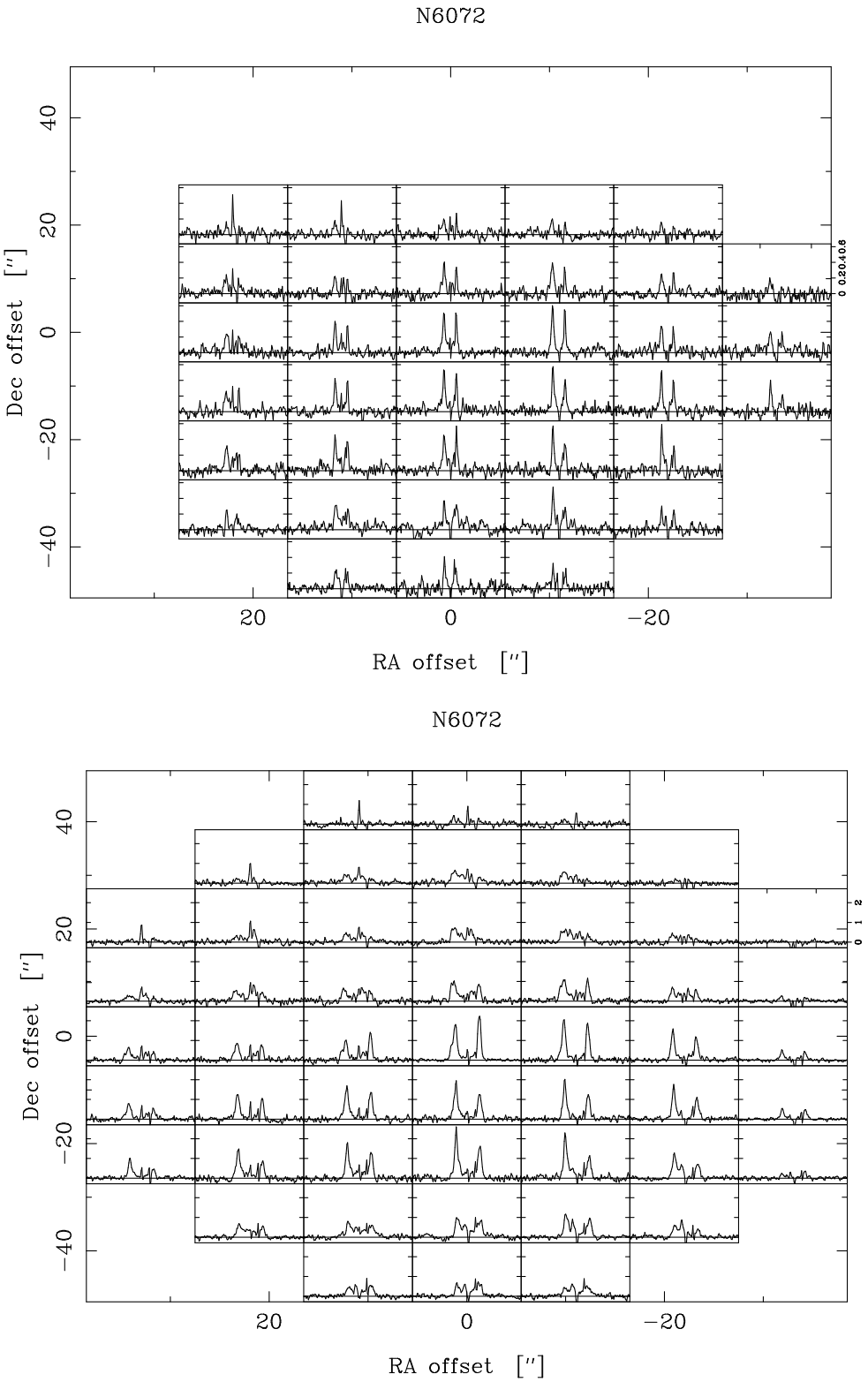


Figure 6.4: **Top**. A map of the CO ($J$=1-0) emission towards NGC6072. **Bottom**. A map of the CO ($J$=2-1) emission towards NGC6072. Both maps show signs of interstellar lines, more clearly visible in the outermost spectra.

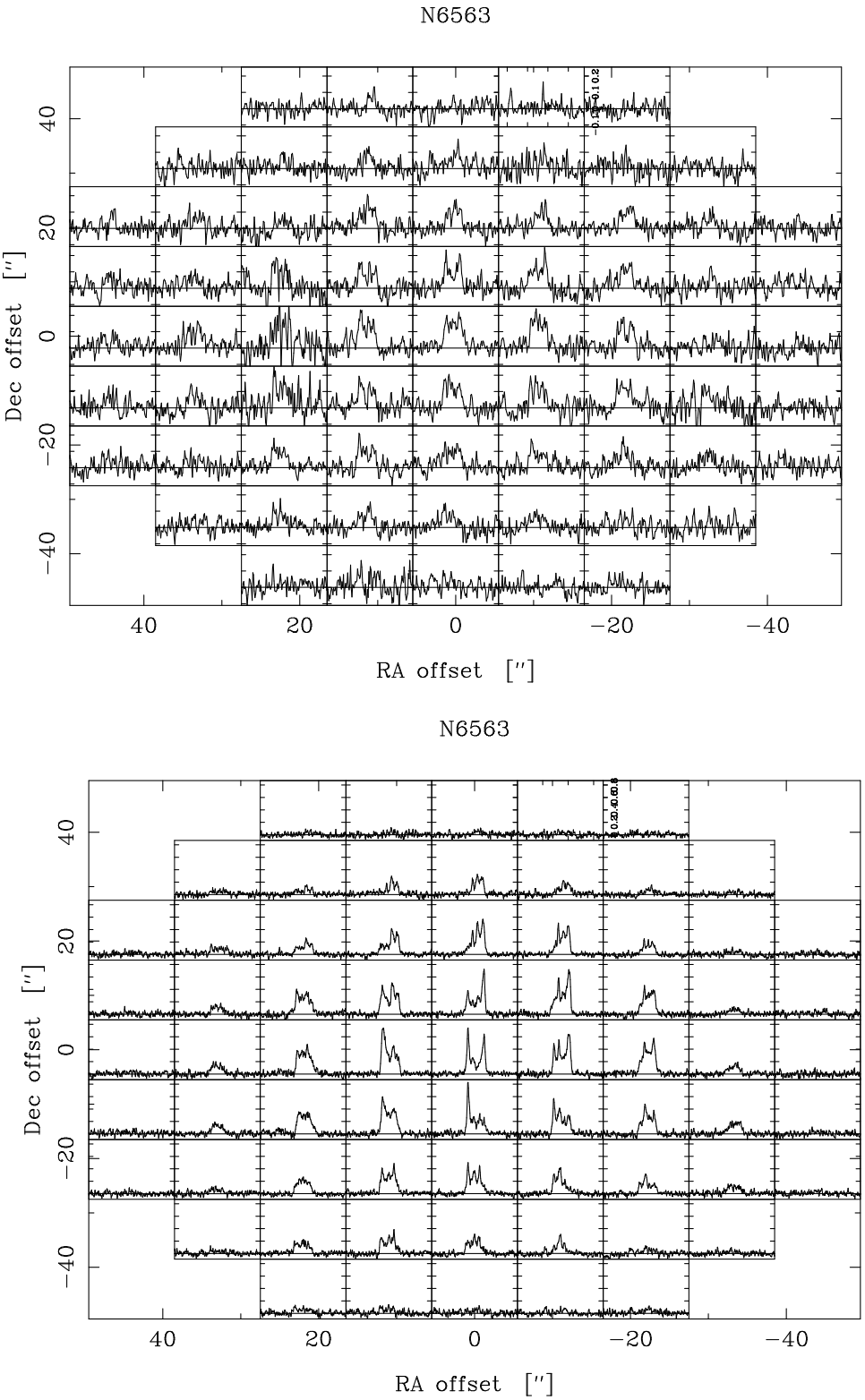


Figure 6.5: **Top**. A map of the CO ($J$=1-0) emission towards NGC6563. **Bottom**. A map of the CO ($J$=2-1) emission towards NGC6563.

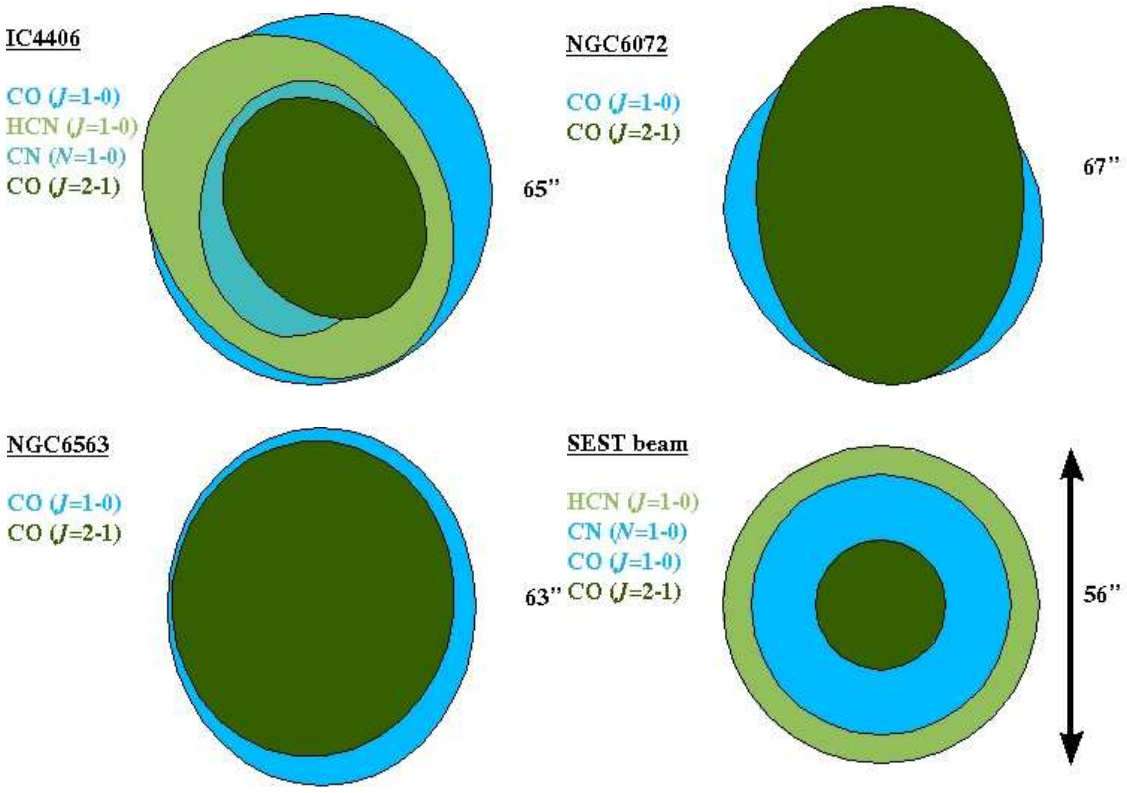


Figure 6.6: This figure shows the distribution of molecular emission in the three sources IC4406, NGC6072 and NGC6563 and the SEST beam at various wavelengths. The edges of the ellipses mark the FWHM of the two-dimensional Gaussian fit made to the maps shown in Figures 6.2–6.5, and the FWHM of the SEST beam, respectively (assuming a Gaussian beamshape).

Table 6.4: Fractional abundances with respect to $f$(HCN) derived from the ($J$=1-0) transition.

| | | IC4406 | NGC6072 | NGC6563 |
|---|---|---|---|---|
| Molecule | Transition | $f_X/f_{HCN}$ | $f_X/f_{HCN}$ | $f_X/f_{HCN}$ |
| CO | $J$=1-0 | 244 | 280 | 630 |
| $^{13}$CO | $J$=1-0 | 14.4 | — | 40.7 |
| CO | $J$=2-1 | 76.7 | 64.6 | 152 |
| $^{13}$CO | $J$=2-1 | 6.92 | — | U.L.[a] |
| CN | $N$=1-0 | 3.59 | 3.53 | 7.78 |
| CN | $N$=2-1 | 0.615 | 0.256 | 0.481 |
| $C_2H$ | $J$=1-0 | 2.82 | 6.95 | — |
| $H_2CO$ | $2_{1,2}$-$1_{1,1}$ | 1.15 | 0.256 | — |
| $HCO^+$ | $J$=1-0 | 0.333 | 0.256 | 0.252 |
| $HCO^+$ | $J$=3-2 | 0.0115 | 0.000549 | — |
| HNC | $J$=1-0 | 0.159 | 0.232 | — |
| HCN | $J$=3-2 | 0.0538 | U.L.[a] | U.L.[a] |
| CS | $J$=3-2 | 0.0359 | U.L.[a] | — |

(a) signifies a non-detection, but the calculation of an upper limit to the fractional abundance has been made (see Table 6.5).

Table 6.5: Calculated upper limits with respect to $n(H_2)$.

| Molecule | Transition | IC4406 | | NGC6072 | | NGC6563 | |
|---|---|---|---|---|---|---|---|
| | | rms noise | $f_X$ | rms noise | $f_X$ | rms noise | $f_X$ |
| | | mK | | mK | | mK | |
| SiO | $J$=2-1 | 1.7 | 1.3 (-7) | — | — | — | — |
| $HN^{13}C$ | $J$=1-0 | 1.7 | 1.2 (-7) | 4.9 | 4.0 (-7) | — | — |
| SiS | $J$=5-4 | 3.0 | 8.2 (-7) | 3.8 | 1.4 (-6) | — | — |
| $HC_3N$ | $J$=10-9 | 3.0 | 2.7 (-7) | 3.8 | 3.9 (-7) | — | — |
| $N_2H^+$ | $J$=1-0 | 1.5 | 6.7 (-8) | 2.6 | 1.3 (-7) | — | — |
| SiO | $J$=3-2 | — | — | 3.5 | 6.8 (-8) | — | — |
| SO | $J$=4-3 | 1.9 | 9.7 (-8) | 3.7 | 2.2 (-7) | — | — |
| CS | $J$=3-2 | — | Det.[a] | 5.1 | 1.8 (-7) | — | — |
| $HCNH^+$ | $J$=2-1 | 2.8 | 2.9 (-6) | 3.8 | 4.5 (-6) | — | — |
| $^{13}CO$ | $J$=2-1 | — | Det.[a] | — | Det.[a] | 4.6 | 8.9 (-6) |
| HCN | $J$=3-2 | — | Det.[a] | 16.3 | 5.8 (-8) | 20.6 | 1.3 (-7) |
| $HCO^+$ | $J$=3-2 | — | Det.[a] | — | Det.[a] | 32.1 | 4.0 (-8) |

(a) signifies a detection, given in Table 6.4.

It can be seen from Table 6.4 that fractional abundances derived from the higher transitions (e.g., HCN ($J$=3-2), $HCO^+$ ($J$=3-2)) are very different from those derived from the lower transitions. This is, in all likelihood, a limitation of the method of calculation. Fig. 6.6 shows that molecules at different excited levels do occupy different regions, and also that the telescope beam is much smaller than the higher-transition regions; the method of calculation assumes an unresolved source, with molecules having the same distributions. Despite this, Table 6.4 shows that IC4406 and NGC6072 are very similar chemically. NGC6563 looks somewhat chemically different – either under-abundant in HCN (and $HCO^+$), or over-abundant in CO and CN, in comparison. However, again, this could be an optical depth effect.

### 6.6.1 $H_2CO$ and CS

The detections of $H_2CO$ in IC4406 and NGC6072 and CS in IC4406 are the first detections of these molecules in PNe. Indeed, $H_2CO$ is reasonably abundant, on a par with HCN, and CS, although less so, is within two orders of magnitude of HCN in IC4406.

Formaldehyde is only usually seen in oxygen-rich environments, where it is formed by the neutral-neutral reactions,

$$\begin{aligned} OH + CH_2 &\longrightarrow H_2CO + H \\ O + CH_3 &\longrightarrow H_2CO + H \end{aligned}$$

(Willacy & Millar 1997). Its presence here, in what are obstensibly carbon-rich sources, could be a result of oxygen-rich material surviving from the AGB phase. This would also indicate that these two stars became carbon-rich quite late on in the AGB phase.

However, formaldehyde has recently been detected in the carbon star, IRC+10216 (Ford 2002), at a fractional abundance of $1.1\times10^{-8}$. Here it is explained as a result of cometary activity, the same reason given for the presence of OH (Ford et al. 2003) and $H_2O$ (Melnick et al. 2001) in this object. Willacy (2004) argues that the detection of these three molecules does not necessarily indicate comets. Her work on the (Fischer-Tropsch) catalytic effects of iron and nickel in circumstellar grains also predicts abundances of $H_2O$ and OH very similar to those observed. Moreover, $H_2CO$ can be formed by the photodissociation of methanol, which could be formed by Fischer-Tropsch catalysis (Latter & Charnley 1996).

So, at present it seems hard to conclude anything definite about the implications

of $H_2CO$ for these two PNe. If oxygen-rich material is present, one would expect formaldehyde to survive until the PN phase only with heavy shielding, perhaps in clumps or dense regions in a disk or torus. With the added surprise of a detection of CS, possibly this seems more likely (see Redman et al. 2003, for CS in clumps).

CS is a parent molecule in carbon-rich AGB stars and is seen in steadily decreasing abundances as the post-AGB phase progresses (see Fig. 5 of Bachiller et al. 1997a). However, given the right conditions (e.g., those of the "PPN" clump model, see below), it would be possible to form CS in a cycle such as:

$$\begin{aligned} C^+ + S &\longrightarrow S^+ + C \\ S^+ + C_2 &\longrightarrow CS^+ + C \\ S^+ + CH &\longrightarrow CS^+ + H \\ CS^+ + H_2 &\longrightarrow HCS^+ + H \\ HCS^+ + e &\longrightarrow CS + H \end{aligned}$$

Further work should be done to exclude the possibility that $H_2CO$ and CS are not present in IC4406 and NGC6072 entirely due to chemical (reformation) effects, as suggested for the case of the young PN NGC7027 by Hasegawa et al. (2000)

The new detections of CS and $H_2CO$ beg the question, why have these two molecules not been detected before? Both the survey of Bachiller et al. (1997a) (five PNe – see also Thronson & Bally 1986, for NGC7027) and the study of M1-16 by Sahai et al. (1994) proved negative in their search for CS. Thronson & Bally (1986) also drew a negative result in their search for $H_2CO$ in NGC7027. Of these six PNe, all would be expected to have clumpy material, and yet none show detections of these two molecules.

## 6.7 Simple clump model

In order to establish limits upon the survival of molecules in a shielded environment in a post-AGB envelope, a simple model of a clump was used. This model assumes a constant density semi-infinite slab geometry, with physical parameters taken from the literature.

Three scenarios were used, representative of the three stages of AGB and post-AGB evolution. These three scenarios are labelled AGB, PPN and PN for convenience, and physical conditions for each scenario are given in Table 6.6. In the AGB

Table 6.6: Clump model input parameters

| | AGB | PPN | PN |
|---|---|---|---|
| $n$ ($\mathrm{cm^{-3}}$) | $10^7$ | $10^6$ | $10^5$ |
| $r_\mathrm{i}$ (cm) | $10^{16}$ | $10^{17}$ | $10^{18}$ |
| $T$ (K) | 20 | 20 | 20 |
| $A_\mathrm{V}$ ($^\mathrm{m}$) | 2 | 1 | 0.5 |
| $v_\mathrm{exp}$ ($\mathrm{km\,s^{-1}}$) | 15 | 15 | 15 |
| $G$ ($\mathrm{G_0}$) | 1 | 10 | 25 |

scenario, the density of the clump is taken to be $10^{-7}\,\mathrm{cm^{-3}}$, which is similar to the density of the inter-clump matter at a radius of $10^{16}\,\mathrm{cm}$. In actuality, it seems that the density of a clump is $\sim$10 times greater than the inter-clump matter (Huggins & Mauron 2002). The initial radius is chosen to be similar to the radius at which clumps are observed in IRC+10216 (Huggins & Mauron 2002), and a clump size of $10^{14}\,\mathrm{cm}$ is adopted, to give a visual extinction through the clump of $\sim$2 magnitudes. The only shielding of molecules is due to the material of the clump itself; there is assumed to be no intervening matter between the clump and the central star.

In PNe clumps (or knots, or globules) are larger in size, having a radius on the order of $10^{15-16}\,\mathrm{cm}$. They also have a lower density, and hence a lower $\mathrm{A_V}$ (Meaburn et al. 1998). The parameters for the PN scenario are chosen to reflect this, and an increase in the UV ionisation rate is made to account for the hot central star. The PPN scenario is an intermediate between the other two scenarios.

Results in the AGB scenario show that parent molecules such as CO, CS and HCN can survive $\sim10^5$ yr (equivalent in length to the thermally pulsing AGB phase) in a clumpy environment such as that adopted in the model. Current thinking (Young et al. 2003), however, holds that clumps only form at the very end of the AGB phase. The fractional abundance of these three species after $10^5$ yr in the model is $\sim10^{-4}$, $10^{-7}$ and $10^{-7}$ respectively. Photodissociation products are not very abundant, peaking before 1 000 yr has passed (e.g., CN, $\mathrm{C_2H}$), and parent molecules are destroyed by neutral-neutral reactions rather than by photon-interaction, as seen in models of AGB chemistry (Millar & Herbst 1994).

In the PPN scenario those molecules detected in Chapter 4 – CO, HCN, and CN – are abundant, although only for 100 years or so in the case of HCN. CO and CN survive for long times in this environment, as does CS. The UV field used in the model is some twenty times less than that in the CRL618 model (Chapter 3) at the same radius, and the cosmic ray ionisation rate 500 times less, which may account for the difference in molecular complexity seen.

Table 6.7: Fractional abundance ranges for PNe (with respect to HCN)

| Molecule | Abundance range | |
|---|---|---|
| | PNe | Compact PNe |
| CN | 3.5–12 | 0.5–5 |
| HNC | 0.16–0.7 | 13–91 |
| $HCO^+$ | 0.25–1 | 0.13–2.5 |
| CS | <0.09 | — |

In the PN scenario, several non-parent molecules reach high ($10^{-5}$–$10^{-7}$) fractional abundances (e.g., $C_2H$, HNC, $HC_3N$) but only for very short periods, on the order of a year or so. Long-lived molecules include CO, $C_2$, CS and CN.

Note that throughout all these different scenarios, "complex" molecules do not survive ("complex" in this case meaning with more than two or three atoms). The simplest cyanopolyyne, $HC_3N$, although it becomes abundant in clumps in the AGB scenario, does so only for 1 000 years. This was also found by Howe et al. (1992).

## 6.8 Discussion

The observational results of Cox et al. (1992) are generally in good agreement with the fractional abundances derived here; there is a minor disagreement in the CN/HCN ratio (a factor of 3–4) and a slightly larger disagreement in CO/HCN ratio (a factor of 4–6). They calculate an integrated $^{12}CO/^{13}CO$ intensity ratio of 20±3 for IC4406, which is comparable with the 14±3 calculated from this data. In comparison, NGC6563 data indicates an integrated $^{12}CO/^{13}CO$ intensity ratio of ∼16. This is fairly standard for evolved PNe, for which the ratio tends to be in the range 10–25 (Bachiller et al. 1997a). Compiling the results of Bachiller et al. (1997a) (who observe the evolved PNe NGC6720, M4-9, NGC6781 and NGC7293), Sahai et al. (1994) (M1-16), Josselin & Bachiller (2003) (who observe the compact PNe BV5-1, K3-94, M1-13, M1-17, K3-24, IC5117 and NGC7027) and the data here, the abundance ranges given in Table 6.7 can be specified.

The modelling of clumps, albeit in a simple manner, is enough to show that molecules can survive through the AGB and PPN phases and into the PN phase, as suggested by some authors (e.g., Dyson et al. 1989). This does not exclude the possible post-AGB re-formation of the molecules seen in PNe, and indeed some molecules (e.g., CS) increase slightly in abundance even in clumps. There seems to be some indication that the chemistry of the neutral envelope (of, say, PPNe and

PNe) is different to that occurring in clumps: complex molecules are not noticeably abundant in the clump models, and yet in PPNe they can be present at high abundances. When it comes to chemistry in clumps, small molecules are the order of the day (see also Howe et al. 1994). Even in PNe, where few molecules are seen, clumps cannot provide the required amounts of HCN, HNC, $C_2H$ and even CN. The high degrees of $HCO^+$ seen in planetary nebulae probably do not exist in clumps. These molecules are presumably shielded from the stellar radiation field in some manner, and one must invoke alternative suggestions in the search for explanations. "Shadowing" may be a viable solution, where clumps shield molecules as a parasol would shield a person on a sunny day (Canto et al. 1998).

Redman et al. (2003) study clumps in post-AGB environments in a much more comprehensive manner, and come up with a different result, that large molecules are present in the clumps themselves and survive long enough to enter the inter-stellar medium. As an example of this they use the benzene molecule, which has a fractional abundance of $\sim 10^{-8}$ in their model for over 10,000 yr. However, it seems that this is unlikely, given that fractional abundances of $HCO^+$ are consistently extremely low (c.f., Chapter 3) and large molecules are rapidly destroyed. They do note that their benzene chemistry, which is based upon $2C_3H_3 \longrightarrow C_6H_6$, may be incomplete. The two other large molecules reaching high fractional abundances in the model of Redman et al. (2003) are $C_4H_4$ and $C_4H_5$, which are not included in the reaction set used here. Apart from this, the models presented here and that of Redman et al. (2003) are very similar – clumps allow small molecules such as CO, CS and $C_2$ to survive for long times, in contrast to molecules in the inter-clump material which do not survive.

## 6.9 Conclusions

In a molecular line survey of three PNe, eight species were detected: CO, $^{13}CO$, CN, $C_2H$, $H_2CO$, $HCO^+$, HNC and CS. Of these species, CS and $H_2CO$ have not been detected in PNe previously. In general, fractional abundances seem high, although the simplistic method used to calculate them is probably not accurate to more than an order of magnitude. Two transitions of CO were mapped in all three PNe, as well as HCN and CN in IC4406.

A model of a clump has illustrated that some molecules may survive from the AGB to the PN phase without being destroyed. CO and CS are two such molecules. However, other molecules seen in (these) PNe are not abundant for a prolonged time

in the clump model. This leads to suggest that these molecules are shielded in some other way, or that some unaccounted-for effect leads to an increase in the complexity of molecules within a clump.

# Chapter 7

# Conclusions and further work

## 7.1 Summary

This study of the chemistry of mainly carbon-rich AGB and post-AGB objects has looked at the three main stages (AGB, PPN, PN) and the complex AGB to PPN transition in some detail.

### 7.1.1 Carbon chemistry on the AGB

Chapter 2 investigated the chemistry of seven high mass-loss rate carbon stars in both the northern and southern skies. Nearly 200 emission lines were detected from 24 molecular species. Mass-loss rates and density and temperature profiles of the circumstellar envelope were determined using the observed CO emission and a detailed radiative transfer code. Fractional abundances were derived using this data, and it was found that fractional abundances generally vary between the sources by no more than a factor of five, indicating that circumstellar envelopes around carbon stars with high mass-loss rates have similar chemical compositions. Furthermore, through comparison with surveys of stars with lower mass-loss rates, it seems that carbon stars in general have very similar chemical compositions. However, there are some notable exceptions. The most striking difference between fractional abundances is the spread in the $^{12}C/^{13}C$-ratio of about an order of magnitude between the sample stars, which mainly shows the results of nucleosynthesis. The abun-

dance of SiO also shows a variation of more than an order of magnitude between the sources, and as shown in Woods et al. (2003b), this is can be explained by the passage of pulsation-driven shock through the inner part of the wind. The chemistry occurring in the outer envelope is consistent with current photochemical models, such as that of Millar et al. (2000).

Further avenues of work in this field lie in high-resolution (interferometric) mapping of molecular distributions in carbon stars, and the detection of new molecules, both of which will help to constrain chemical models. The arrival of ALMA in the near-to-mid future should improve sensitivity and resolution immensely. Development of chemical models will probably lead away from the (physically) simplistic approaches taken, for example in Millar et al. (2000), which deal with the chemistry in these environments quite successfully, on the whole. The present models make simplifications about hydrodynamics, dust, geometry, etc., which may be important considerations to take into account.

### 7.1.2 Carbon chemistry in a PPN torus

Chapter 3 looked at the molecule-rich PPN CRL618, and in particular, the chemistry occurring in a dense shell of outwardly expanding gas, chosen to represent a carbon-rich circumstellar disk or torus. Despite the high flux of UV photons from the central star, the intrinsic dust extinction in the shell is found to prevent rapid photodissociation and allows chemical reactions to make a variety of gas-phase species, some of which are complex. Chemical evolution ends when the intrinsic extinction falls below about 10 magnitudes, since at this point rapid photodissociation occurs. For many species (including benzene) good agreement between the model and observations is obtained, despite the complexity of the source and the difficulties in reconciling millimetre and infra-red data.

A formation mechanism for benzene was discovered which differs from that which is efficient in interstellar clouds. Atomic hydrogen is not abundant in the dense torus of CRL618, so production of benzene is initiated by the reaction of $HCO^+$ with acetylene, followed by reactions of the products with further acetylene.

Again, high resolution observations of molecules in PPNe would help the understanding of these objects greatly. Knowing, for instance, where the $HCO^+$ resides in CRL618 would indicate whether the boundary layer effects studied by Viti et al. (2002), for example, were important in this specific situation.

### 7.1.3 Chemistry in molecule-poor PPNe

In contrast to the preceding chapter, Chapter 4 looks at two molecule-poor PPNe, IRAS16594-4656 and IRAS17150-3224. IRAS16594-4656 is carbon-rich, appearing to have become so very late on the AGB; IRAS17150-3224 is oxygen-rich. Both objects are detected in CO, $^{13}$CO and HCN, and IRAS16594-4656 is also detected in CN. The CO($J$=2-1) and CO($J$=3-2) line profiles are compared to those of other PPN which were observed in the same transitions: CPD-53°5736, IRAS17106-3046, IRAS17245-3951 and IRAS17441-2411. Fractional abundances of all detected molecules (except CO) are calculated using the results of CO line modelling and a simple photodissociation model, as in Chapter 2. Comparisons between these fractional abundances and those of other PPNe show that IRAS16594-4656 and IRAS17150-3224 are quite under-abundant when compared to molecule-rich sources like CRL618, CRL2688 and OH231.8+4.2. As a reason for this deficit, the difference in circumstellar envelope/torus density between the molecule-rich sources and the molecule-poor sources is proposed. Finally, the post-AGB ages of these two objects are estimated using CN/HCN and HCN/CO ratios and both ages are found to be in agreement with previous figures cited in the literature, IRAS17150-3224 being the younger of the two PPNe.

Chapter 5 supports the results of Chapter 4 by means of a chemical model which follows the transition of a circumstellar envelope through the AGB phase and into the PPN phase of evolution. The model includes the effects of UV radiation, cosmic rays and also X-rays, but no density enhancements (such as a torus, or clumps).

Additional observations of molecular lines in other PPNe would be useful to determine how clear-cut this distinction between molecule-rich and molecule-poor PPNe is. If there is some sharp boundary, then identifying characteristics for the two classes could be determined, whereas if there is no boundary, it may be easier to confirm/discover the factors on which molecular-richness relies.

### 7.1.4 Chemistry in PNe

The final chapter moves on to look briefly at the PN stage of evolution. Three PNe are observed, and detected in several lines. Most notably, $H_2CO$ and CS are detected for the first time in a PN. Fractional abundances are calculated in the usual manner and a comparison between these three PNe and a number of others shows that PNe as a group also have a very similar chemical composition. A simple model shows that molecules such as CO and CS may survive from the AGB phase

in a clump. However, this method is ineffective for other molecules such as $C_2H$, HNC and HCN, suggesting that some other form of shielding may be active.

Further observations of clumps in PNe such as those by Huggins et al. (2002, 1992), O'Dell et al. (2002) and Speck et al. (2003) cannot fail to help the study of chemistry in PNe, and molecular line studies of these clumps in particular would help understanding of the processes occurring. $H_2$ and CO have already been detected in the clumps in the Helix nebula (Huggins et al. 2002); detections of HCN, HNC and $C_2H$ will identify important missing elements in the modelling carried out in this chapter.

## 7.2 Conclusions

Overall, it seems that the final stages of stellar evolution for low- and intermediate-mass stars bring a change from chemical "conformity" to chemical diversity, and back once again to conformity. This assumes that the progenitor to CRL618 was a carbon star, and not, say, a molecule-poor symbiotic star (which would perhaps be more interesting!) and, of course, there may be selection effects: many PNe have been identified, but only a small percentage have been detected in CO (or other molecules). Those detected could have been "CRL618"s in previous lives; those remaining undetected could easily be "IRAS16594"s. Either way, there is still some degree of conformity: a molecule-rich PPN will become a molecule-rich PN, and a molecule-poor PPN will become one of many PNe undetected in CO. This distinction in PNe may also say something about clumps – whether they are ubiquitous in PNe, with distance making the detection of CO emission difficult, or whether clumps are solely specific to a certain group of PNe. There is already some evidence that (large) clumps are not ubiquitous in PNe (Huggins & Mauron 2002), but that some small-scale structure is present in over half of all PNe (Gonçalves et al. 2001). Nevertheless, it remains clear that the transition from AGB star to PN is chemically very interesting, and with the variety of conditions and molecules in PPNe, a very difficult transition to model accurately.

## 7.3 Future work

The two main unanswered questions arising from this research concern polycyclic aromatic hydrocarbons (PAHs) and clumps: Does the formation of benzene in

CRL618 have implications for PAH formation, and at what stage of stellar evolution do clumps form?

Firstly, PAHs have been detected in many post-AGB objects, and are assumed to be responsible for many of the unidentified features and lines seen in infra-red and millimetre spectra. The building blocks which go into the formation of PAHs are small cyclic molecules such as phenyl and benzene, which are thought to form in high density, high temperature (900–1 100 K) shocked regions very close to the atmosphere of carbon-rich AGB stars (Cherchneff et al. 1992). The study of PAH formation is preliminary, with some pieces of the puzzle coming together neatly (for example, once a benzene ring is formed, larger PAHs can then be built via a simple three-step process, see Cherchneff et al. 1992) and other pieces being more difficult (how do carbonaceous dust particles form from PAHs? Cau 2002). Now, however, the detection of benzene in a PPN, and evidence that it can be formed in the gas phase in the right circumstances (Chapter 3) – without the need for shocks, or high temperatures – may throw new light on the whole PAH formation process.

Clumps are expected to form at the end of the AGB phase (or perhaps in the early PPN phase, Young et al. 2003) close to the emerging ionisation front (O'Dell et al. 2002), but have not actually been observed there (Huggins & Mauron 2002). Globules are seen in many PNe (O'Dell et al. 2002), but it is not clear whether these globules are AGB-type clumps grown large, or whether AGB-type clumps are also present in PNe, but invisibly. Searches for the precursors of such globules in the envelopes of AGB stars and young PNe have been negative (Huggins & Mauron 2002). In order to understand the chemistry in post-AGB objects, where UV shielding is important, it is important to understand clumps in more detail, and discover when, where and how they form.

# Postscript

In five billion years or so, when the effective radius of the Sun engulfs the present orbit of Venus, we might finally get conclusive proof of what happens in the huge clouds of gas and dust around a red giant star. Provided we aren't incinerated first, of course. Until then we are left with postulation, hypothesis and educated guesswork in our attempts to understand circumstellar chemistry. We rely on light which has travelled further than our wildest imaginations, which has been affected by unknown electromagnetic fields, which has passed through matter we cannot even experience on Earth. Looking at it like this, the "science" of astronomy can all seem rather tenuous (no pun intended), and one has to wonder, well, why do we bother?

Maybe the first response that springs to mind is that to understand ourselves, we must understand the stuff – physical, mental and spiritual – of which we are composed. A part of that stuff, the carbon, oxygen, and all other atoms of which we are made, was once spewn out from the inside of a red giant star somewhere in our galaxy. As Joni Mitchell says, we are all made of a billion year old carbon. For those to whom this explanation appeals, just think of this thesis as having used astronomy to trace your roots...

Others, realising our relative insignificance as we sit in our chairs atop a spinning ball of rock, three stepping-stones out from a somewhat ordinary star, might look further out and see so much more. So much more than concerns us, light which we haven't even seen yet, myriads of concepts which are presently inconceivable to us. By observing and modelling these things, astronomy lets us ask 'How?'. And however imperfect the responses telescope data and numerical simulations are, surely something is better than nothing? Because knowing something, or thinking we know something, removes one of the obstacles in the way of thinking about the real question, the ultimate question, the big 'Why?'. If that appeals, just think of this thesis as one of the 'How?'s in amongst the tumult.

# Appendix A

# Individual sources

Table A.1: Stars studied in this thesis

| IRAS No. | Other catalogue name | Evolutionary stage | J2000 Co-ords. (Source: SIMBAD) | Dist. (kpc) | $V_{\rm lsr}$ ($\rm km\,s^{-1}$) | $V_{\rm exp}$ ($\rm km\,s^{-1}$) |
|---|---|---|---|---|---|---|
| $04395+3601$ | CRL618 | PPN | 04:42:53.6 +36:06:54 | 1.50 | $-21$ | 19.5 |
| $07454-7112$ | AFGL4078 | AGB | 07:45:25.7 −71:12:19 | 0.71 | $-39$ | 13.0 |
| $09452+1330$ | IRC+10216 | AGB | 09:47:57.4 +13:16:44 | 0.12 | $-26$ | 14.5 |
| $10131+3049$ | CIT6 | AGB | 10:16:02.3 +30:34:19 | 0.44 | $-\ 2$ | 17.0 |
| $14192-4355$ | IC4406 | PN | 14:22:25.8 −44:09:00 | 1.80 | $-50$ | 11.5 |
| $15082-4808$ | AFGL4211 | AGB | 15:11:41.9 −48:20:01 | 0.64 | $-\ 3$ | 19.5 |
| $15194-5115$ | | AGB | 15:23:05.0 −51:25:58 | 0.60 | $-15$ | 21.5 |
| $16097-3606$ | NGC6072 | PN | 16:12:58.8 −36:13:38 | 1.00 | 0 | 15.5 |
| $16594-4656$ | | PPN | 17:03:09.7 −47:00:28 | 1.80 | $-25$ | 14.0 |
| $17150-3224$ | AFGL6815 | PPN | 17:18:20.0 −32:27:20 | 2.42 | $+15$ | 14.5 |
| $18087-3352$ | NGC6563 | PN | 18:12:02.6 −33:52:05 | 2.24 | $-25$ | 20.0 |
| $23166+1655$ | AFGL3068 | AGB | 23.19.12.4 +17:11:35 | 0.82 | $-31$ | 14.0 |
| $23320+4316$ | IRC+40540 | AGB | 23:34:28.0 +43:33:02 | 0.63 | $-15$ | 14.0 |

# A.1 AGB stars

## A.1.1 IRC+10216

IRC+10216 is *the* most studied late-type star. This is largely because of its proximity, 100 – 200 pc away. To review all the observations and studies would be a hefty undertaking. However, a recent paper by Men'shchikov et al. (2001) does a very good job of giving a broad overview of observational work.

Becklin et al. (1969) were the first group to study IRC+10216: It is the brightest source in the IR sky, and hence drew early investigation. Its spectral energy distribution (SED) is virtually featureless; its brightness varies by 2 mag every ∼600 days. IRC+10216 is an extended source with an opaque dust shell, possibly in the early post-AGB stage of evolution.

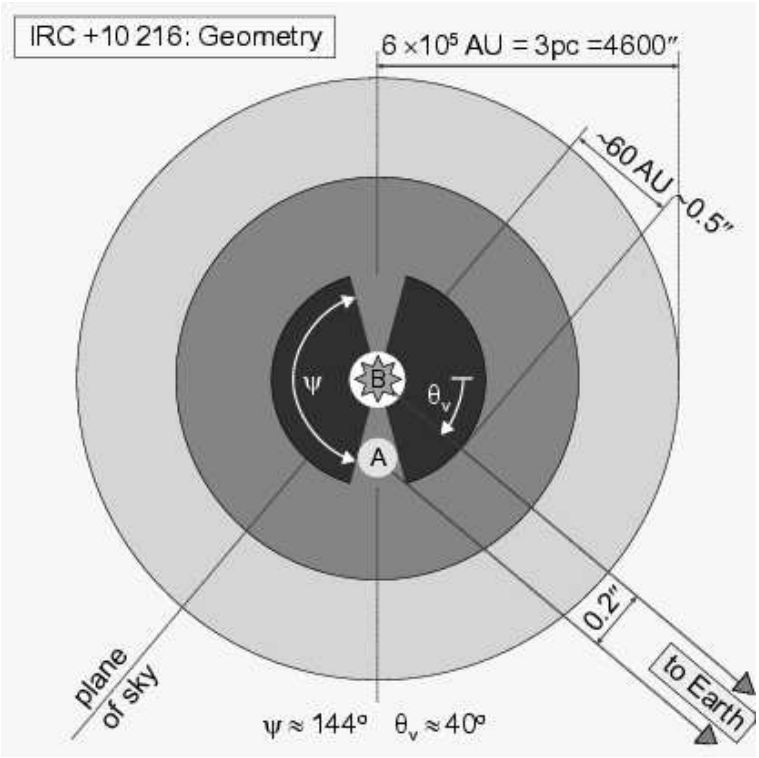


Figure A.1: Geometry of the circumstellar envelope of IRC+10216, taken from Men'shchikov et al. (2001). Three regions are indicated: the dense core, with bipolar cavities (dark colour); the less dense envelope where molecules are observed (medium colour); and the extended outer envelope (light colour).

With such an obscured source, the dust properties are well studied – some thirteen papers have presented dust continuum models (e.g. Ivezic & Elitzur 1996; Groenewegen 1997). All models assume a spherically symmetric envelope (see Fig-

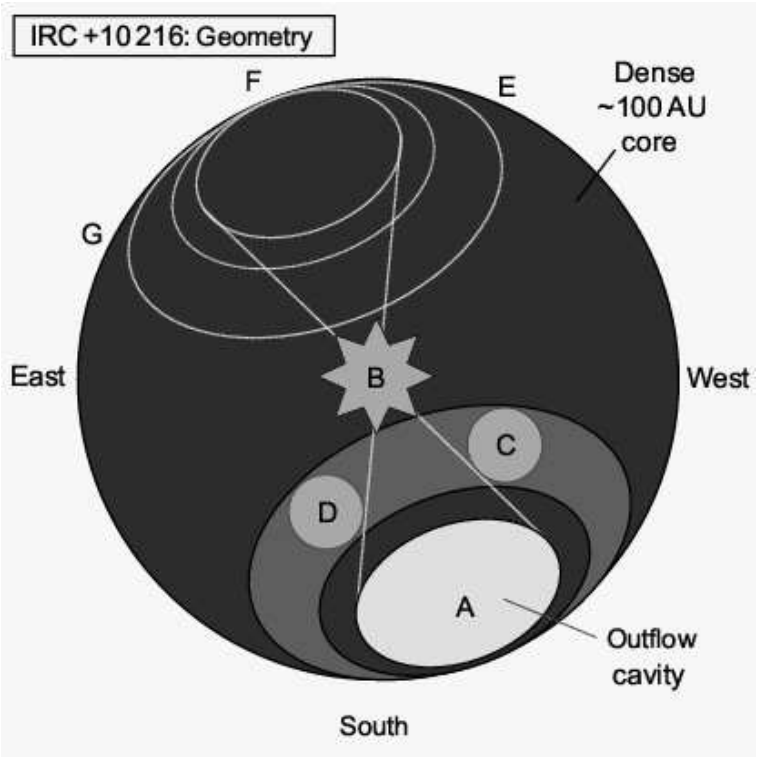


Figure A.2: Three-dimensional representation of the inner, dense core of IRC+10216 (Men'shchikov et al. 2001). Components A–D were observed by Weigelt et al. (1998), and E–G by Osterbart et al. (2000). B is the position of the star, A is the position of the brightest emission. Components C–G are irregularities due to inhomogeneities in the dust density.

ures A.1 and A.2), and also a uniform density law, which may not be accurate in reality:

Optical and near–IR polarisation measurements (Dyck et al. 1971; Capps & Knacke 1976) suggest departures from spherical symmetry. Also, speckle observations (e.g. Danchi et al. 1994) and recent high–resolution observations (e.g. Osterbart et al. 2000; Tuthill et al. 2000) show that the inner dust shell of IRC+10216 is non-symmetric and clumpy. Various other departures from spherical symmetry have been suggested: a weakly–bipolar reflection nebula (Kastner & Weintraub 1994), a geometrically thick disk (Dyck et al. 1987) or a dusty torus (Skinner et al. 1998), all inclined toward the observer.

In addition to departures from spherical geometry, there are departures from the often-assumed $\rho \propto r^{-2}$ density distribution, although again, both on small and large scales. For instance, see McCarthy et al. (1980); Bieging et al. (1984); Fazio et al. (1980); Harvey et al. (1991); Keady & Ridgway (1993). Near–IR speckle interferometry by Ridgway & Keady (1988), for example, shows density enhancements

around the stellar equator. This clumpy structure seems to be varying on timescales of a few years (Weigelt et al. 1998; Haniff & Buscher 1998). See also the recent results of Chandrasekhar & Mondal (2001), which show the clumpy structure. The deep optical images of Crabtree et al. (1987) and Mauron & Huggins (1999) give direct evidence of higher densities in a series of concentric shells at radii of $\sim$15–60″ (indicating mass-loss variations on timescales of 200–800 years ). See also Groenewegen et al. (1997) for further observations and Meijerink et al. (2003) for related modelling. Thus the challenge lies open for the development of multidimensional radiative transfer codes. These recent, high quality observations show how much simple models are lacking.

Estimates of mass-loss rate vary, and since they are dependent on distance, can vary in quite a range. However, Men'shchikov et al. (2001) do a survey of estimated mass-loss rates and scale the surveyed results for a distance of 130 pc (see their Table 5). From dust continuum modelling, estimates of mass-loss rate vary from $1.1\,10^{-5}$ (Le Bertre 1997) to $6.1\,10^{-5}\,\mathrm{M_\odot\,yr^{-1}}$ (Winters et al. 1994). From molecular line modelling estimates are less varied: from $0.8\,10^{-5}$ (Kwan & Hill 1977) to $2.4\,10^{-5}\,\mathrm{M_\odot\,yr^{-1}}$ (Crosas & Menten 1997). Hence it is fairly certain that the rate of mass-loss from IRC+10216 is on the order of $10^{-5}\,\mathrm{M_\odot\,yr^{-1}}$.

Measurements of outflow velocity depend on the molecule observed. For instance, Betz et al. (1979) detected $NH_3$ moving at $14\,\mathrm{km\,s^{-1}}$. CO observations usually indicate a faster outflow than this, for example, Knapp & Morris (1985) observe CO at $15.2\,\mathrm{km\,s^{-1}}$, Knapp et al. (1982) measure $17\,\mathrm{km\,s^{-1}}$.

Dust composition is likely to be silicon carbide (due to the 11$\mu$m emission feature, Treffers & Cohen 1974), with some carbonaceous content. A broad emission in the far–IR at 24$\mu$m was proposed by Goebel & Moseley (1985) to be due to magnesium sulphide dust. Grain sizes are hard to determine, and various authors have come up with different values. Treffers & Cohen (1974) suggest radii, $a \ll 1\mu$m. Witteborn et al. (1980) think smaller, $a \lesssim 0.25\mu$m, and Jura (1983) thinks even smaller still, $a \approx 0.05\mu$m. However, Jura later changes his mind (Jura 1994) and decides that there are no medium-sized particles ($a \lesssim 0.015\mu$m, $a \gtrsim 0.5\mu$m).

From a chemical point of view, IRC+10216 is the richest late-type star known. Some 50–60 species have been detected in the circumstellar envelope (Glassgold 1999; Olofsson 1996b). Since these papers, SiCN has been detected by Guélin et al. (2000), $SiC_3$ has been detected by Apponi et al. (1999) and AlNC has been detected by Ziurys et al. (2002). In addition, various oxygen-bearing species have been detected – OH (Ford et al. 2003), $H_2O$ (Melnick et al. 2001) and formaldehyde,

Table A.2: Species detected in IRC+10216, from Glassgold (1999). The information has been updated with the addition of $H_2CO$, $H_2O$, OH, AlNC, SiCN and $SiC_3$. Species are grouped in rough "families" and decrease in abundance, from the top down.

| | | | | | |
|---|---|---|---|---|---|
| CO | $C_2H_2$ | HCN | SiS | CS | AlCl |
| C | $C_2H$ | CN | $SiC_2$ | $C_2S$ | AlF |
| $HCO^+$ | $C_4H$ | $HC_3N$ | SiO | $C_3S$ | NaCN |
| — | $C_3$ | $C_3N$ | SiC | $H_2S$ | MgNC |
| $H_2CO$ [a] | $C_6H$ | $HC_5N$ | SiN | | CP |
| | $C_5$ | HNC | $SiC_4$ | | NaCl |
| | $l$-$C_3H$ | $HC_7N$ | — | | MgCN |
| $CH_4$ | $c$-$C_3H_2$ | $HC_9N$ | $SiC_3$ [a] | | KCl |
| $SiH_4$ | $C_5H$ | $HC_2NC$ | | | SiCN |
| $NH_3$ | $C_8H$ | $CH_3CN$ | | | AlNC |
| | $C_7H$ | $C_5N$ | $H_2O$ | | |
| | $c$-$C_3H$ | | OH | | |
| $H_2C_4$ | — | | | | |
| $HC_2N$ | $C_2$ [a] | | | | |
| $H_2C_3$ | | | | | |

(a) These species are of undetermined abundance.

$H_2CO$ (Ford 2002). See Table A.2 for details.

IRC+10216 is the most active carbon–star maser source, although due to the nature of carbon stars, maser lines are weak. Weak maser emission was discovered in the $J$=1–0 and $J$=5–4 rotational lines of SiS (Nguyen-Q-Rieu et al. 1984; Carlström et al. 1990) and also recently in CS (Highberger et al. 2000). HCN is the most active masering molecule, with three transitions detected. The first two by Lucas & Cernicharo (1989) and the last by Schilke et al. (2000). An HCN laser is detected by Schilke & Menten (2003).

Good reviews of the chemistry in this source are given by Glassgold (1996) and Millar (1988). Of great interest are the long-chain molecules, and the idea that fullerenes may be contained in the CSE of IRC+10216 (Hinkle & Bernath 1993). Cyanopolyynes of up to $HC_9N$ (Matthews et al. 1985), and possibly $HC_{11}N$ (Bell et al. 1982; Travers et al. 1996) have been detected. A summary of the chemistry of IRC+10216 is given in the introduction to this thesis, Sect. 1.6.

### A.1.2 IRAS07454-7112

IRAS07454-7112 was detected in the IRAS survey and classified as a carbon star in Stephenson's *General catalogue of cool carbon stars*. It was observed (seemingly with great difficulty) by Skinner & Griffin (1989). It is very faint optically, and highly reddened, but bright in the IR. The observed energy distribution between 0.1 and 100$\mu$m was modelled by Chan & Kwok (1990), with a mass-loss rate of $5.9\,10^{-6}$. IRAS fluxes are given in the paper by Egan & Leung (1991) and photometry in J, H, K, L, M bands by Fouque et al. (1992).

Papers by Groenewegen (Groenewegen et al. 1992, 1996) give the distance to this star as 0.53 kpc, $v_{exp}$ as $13.5\mathrm{km\,s^{-1}}$ and $v_{lsr}$ as $-36.5\mathrm{km\,s^{-1}}$. The mass-loss rate of gas is estimated at $1.62\,10^{-5}\,\mathrm{M_\odot\,yr^{-1}}$, that of dust $1.88\,10^{-8}\,\mathrm{M_\odot\,yr^{-1}}$ (Groenewegen et al. 2002). Skinner & Griffin (1989) class IRAS07454-7112 as an extreme carbon star (by which they meant...), with a mass-loss rate of something around $10^{-5}\,\mathrm{M_\odot\,yr^{-1}}$.

IRAS07454-7112 was not detected in the SiO maser survey of Haikala (1990), but was detected in CO by Nyman et al. (1992) and also by Groenewegen et al. (1996). In addition, its detection in SiC (Skinner & Griffin 1989; Egan & Leung 1991; Kwok et al. 1997) confirmed to its classification as a carbon star.

Olofsson et al. (1998), who detected CO, CS, HCN, SiO and SiS, note that IRAS07454-7112 has very low HCN/CO and SiO/CO ratios for a carbon star. They assume a distance of 750 pc.

### A.1.3 CIT6

CIT6 is a Mira-type carbon star (misclassified as an SRa Barnbaum & Hinkle 1995) with a period of approximately 640 days (Alksnis & Khozov 1975; Alksnis 1995; Taranova & Shenavrin 1999). Using the period-luminosity relation of Groenewegen & Whitelock (1996) ($m_{\rm bol} = -2.59\log P + 2.02$, where $P$ is the pulsation period), CIT6 has a luminosity of $9\,700\,\mathrm{L_\odot}$. The distance in this case would be 440 pc (Cohen & Hitchon 1996). It was discovered in the Caltech infrared survey (Ulrich et al. 1966) and since has been well-observed. It was identified as a carbon star using its near-IR CN bands (Wisniewski et al. 1967; Gaustad et al. 1969) and its thick carbon-rich dust shell (e.g., Strecker & Ney 1974).

This star has a similarly wide variety of circumstellar molecular species to IRC+10216. Detections include CO, HCN, CN, HNC, $HC_3N$, $HC_5N$, $C_3N$, SiS, $C_2$ and $C_3$ (Jewell & Snyder 1982; Henkel et al. 1985; Sopka et al. 1989; Olofsson

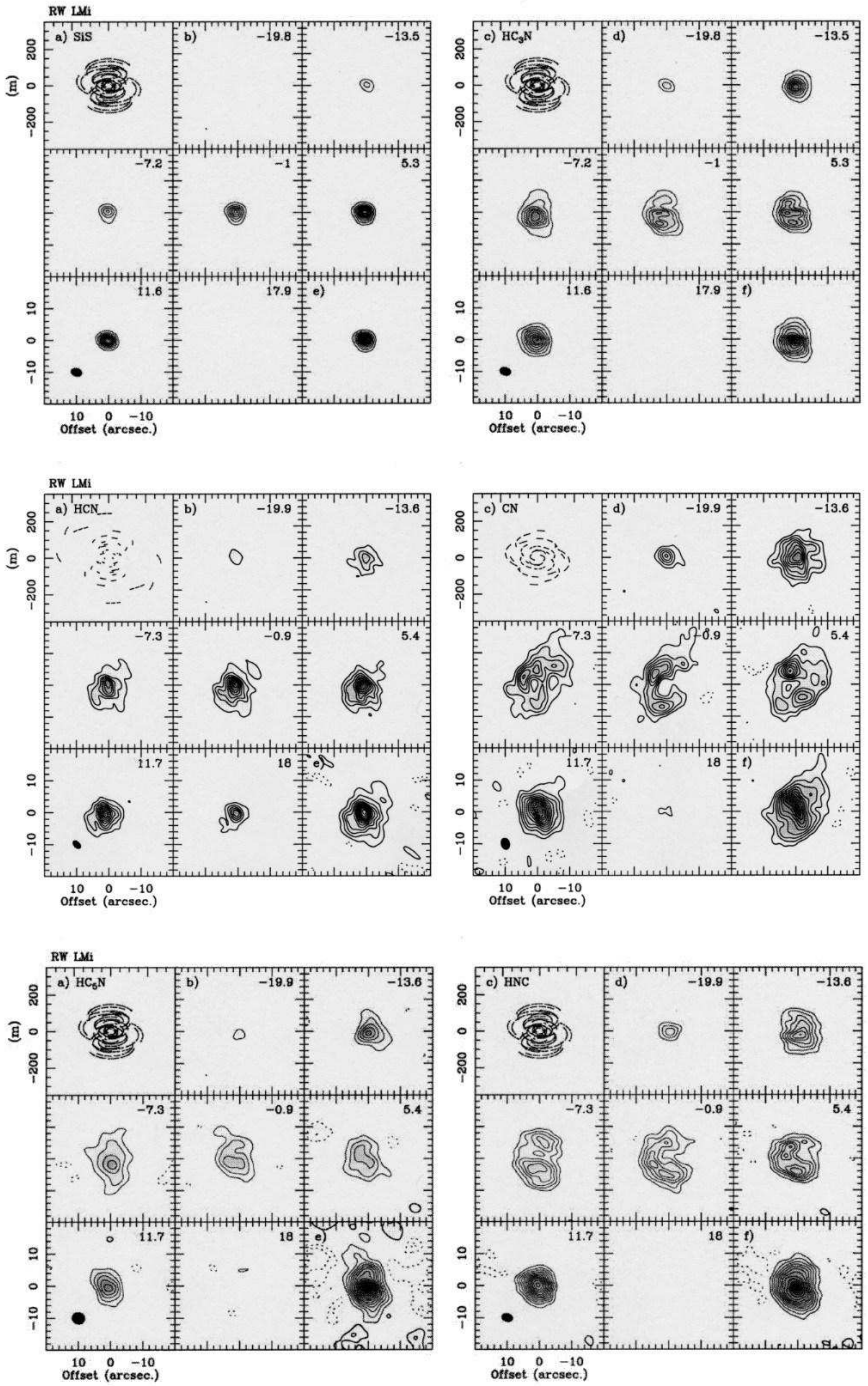


Figure A.3: Maps of the molecular envelope around CIT6, from Lindqvist et al. (2000). Six species are mapped: SiS ($J = 5 - 4$), $HC_3N$ ($J = 10 - 9$), HCN ($J = 1 - 0$), CN ($N = 1 - 0$), $HC_5N$ ($J = 34 - 33$) and HNC ($J = 1 - 0$). The top–left panel in each case shows the *uv*-plane coverage for the observations. The bottom–right panel shows the complete velocity-integrated map. The remaining panels show maps at the central LSR velocity shown in the upper right-hand corner of each panel. See Lindqvist et al. for more details.

et al. 1993a,b; Fukasaku et al. 1994; Zacs 1997) but no CI (Knapp et al. 2000). Guilloteau et al. (1987) discovered a strong HCN ($J$=1–0) maser, and Lewis et al. (1995) report SiO maser activity. Schilke & Menten (2003) detect an HCN laser at 891 GHz (HCN $J$=10–9), and conclude it must arise from the inner regions of the CSE.

From infrared and visible data, CIT6 appears slightly asymmetric (Monnier et al. 2000) and has a clumpy structure (Meixner et al. 1998), with fluxes and polarisations which are variable (Kruszewski 1968, 1971, 1973; Dyck et al. 1971; Trammell et al. 1994). Specifically, there is an unusual light variability in the near IR and red, but a complete lack of periodicity in the blue (Zacs 1997). This behaviour, which may be linked to the excess UV flux and the unusual emission lines which have been observed, could be due to a hot invisible companion (Alksnis et al. 1988) or circumstellar shocks (Cohen 1980; Cohen & Schmidt 1982). Further infrared data (photometry, etc.) is available in Olivier et al. (2001). Surprisingly, CIT6 is easily observed in the optical regime, despite its heavy shroud (Alksnis 1995). The slight asymmetry seen by Monnier et al. (2000) and the similarity of the blue spectrum to the young PPN CRL2688 (Začs et al. 2001) may be indicative that CIT6 is coming to the end of the AGB. Some authors believe that this object is well on its way to becoming a PN (Trammell et al. 1994). Schmidt et al. (2002) suggest that they have detected the nascent bipolar planetary nebula, and believe that it has only developed within the last few hundred years. Radio continuum emission is too weak to imply the presence of an HII region (Knapp et al. 1995).

The only high-resolution imaging to date of this source is presented by Monnier et al. (2000). However, Lindqvist et al. (2000) present brightness maps of six species: HCN ($J$=1–0), CN ($N$=1–0), SiS ($J$=5–4), HNC ($J$=1–0), $HC_3N$ ($J$=10–9) and $HC_5N$ ($J$=34–33): see Figure A.3. Meixner et al. (1998) present CO maps. Dyck et al. (1984) present IR speckle interferometry results and Lipman (1998) and Tuthill et al. (2000) also have performed interferometric measurements of CIT6.

The ratio $^{12}C/^{13}C$ is an intriguing property for this star. Observations of the $^{12}CO/^{13}CO$ ratio give values of 13–16 (Kahane et al. 1992; Groenewegen et al. 1996), yet modelling of the ratio $^{12}C/^{13}C$ produces uniformly higher values of 31–35 (Groenewegen et al. 1996; Schöier & Olofsson 2000). This seems to be due to optical depth effects.

For an extreme carbon star, CIT6 has a low mass-loss rate of approximately $5\,10^{-6}\,M_\odot\,yr^{-1}$ (Ivezic & Elitzur 1995). At the centre of the source is a C4,3 type star (Cohen 1979; Carlström et al. 1990).

### A.1.4 IRAS15082-4808

IRAS15082-4808 is not a tremendously well-observed star. It was first classified as a carbon star by Little-Marenin et al. (1987) (using IRAS low-resolution data), after having been discovered in the AFGL survey (hence its designation as AFGL 4211; Persi & Ferrari-Toniolo 1984). It was first detected in CO by Knapp et al. (1989), and despite being part of two SiO maser surveys (Haikala 1990; Hall et al. 1990), remained undetected in both. New detections of CS, SiO and SiS were made by Olofsson et al. (1998), in addition to a previous detection of HCN. IRAS fluxes are given in the paper of Egan & Leung (1991) and photometry in J, H, K, L, and M bands in Fouque et al. (1992). The dust of this star was modelled (Lorenz-Martins et al. 2001; Lorenz-Martins & Lefevre 1994) and was found to contain a high degree of amorphous carbon grains. Ivezic & Elitzur (1996) identified it as "one of the best candidates for the resolution of dust condensation zones in future observations".

IRAS15082-4808 is an extreme carbon star, with a mass-loss rate of approximately $10^{-5}\,\mathrm{M}_{\odot}\,\mathrm{yr}^{-1}$ (Groenewegen et al. 1992, 2002) or $10^{-6}\,\mathrm{M}_{\odot}\,\mathrm{yr}^{-1}$ (Netzer & Elitzur 1993; Knapp et al. 1989). Its circumstellar wind expands with a velocity of $20.5\,\mathrm{km\,s}^{-1}$ (Young et al. 1993) and has a centre velocity of $-3.3\,\mathrm{km\,s}^{-1}$ (Nyman et al. 1992). It lies at a distance between 0.3 and 0.7 kpc (Loup et al. 1993).

### A.1.5 IRAS15194-5115

This object is well studied, and has several papers devoted to it (Ryde et al. 1999; Lopez et al. 1993; Nyman et al. 1993; Meadows et al. 1987). It was discovered in the IRAS survey (Olnon et al. 1986), and also seen in the ESO–Valinhos 2.2 $\mu$m sky survey (Epchtein et al. 1987). It became classed as a C-star following the interpretation of optical and infrared spectra by Meadows et al. (1987). IRAS15194-5115 is the third brightest C-star at 12$\mu$m, and is the brightest known in the southern sky. However, according to Chen & Kwok (1993) and Olofsson et al. (1998), it might better be classified as an S-star. Photometry in J, H, K, L, M bands is presented by Epchtein et al. (1987) and Le Bertre (1992).

IRAS15194-5115 is often compared to the prototypical C-star, IRC+10216, and it is indeed very similar. However, there is a striking difference in that the $^{12}\mathrm{C}/^{13}\mathrm{C}$ ratio is extremely low (Schöier & Olofsson 2000) - at least five times lower than IRC+10216 (Nyman et al. 1993). Ryde et al. (1999) suggest that this is due to either IRAS15194-5115 being a J-star for which the $^{12}\mathrm{C}/^{13}\mathrm{C}$ ratio has remained low, or to it being a reasonably massive star that has just become a carbon star

after the cessation of hot bottom burning (Frost et al. 1998a). Schöier & Olofsson (2000) suggest that this is due to IRAS15194-5115 being low in mass, so that the CNO cycle produces a low $^{12}C/^{13}C$ ratio, and the temperature of the star is too low for efficient conversion of $^{12}C$ to $^{14}N$.

The dust properties of these two stars appear to be different. IRAS15194-5115 has a low (SiC)/(amorphous carbon) ratio (0.03–0.04, Groenewegen 1995; Lorenz-Martins & Lefevre 1993). This low ratio is in some way connected to a high mass-loss rate (Lorenz-Martins et al. 2001). Dust modelling has been carried out by Lopez et al. (1993), amongst others (Lorenz-Martins et al. 2001; Groenewegen et al. 1998; Groenewegen 1995; Lorenz-Martins & Lefevre 1993; Chen & Kwok 1993).

This star is a long–period variable with a period of 580 days, and a change in magnitude of less than 1 mag (Le Bertre 1992, 1997). Ryde et al. (1999) derive a luminosity of 8770 $L_\odot$ using the period-luminosity relation of Groenewegen & Whitelock (1996).

IRAS15194-5115 was first detected in CO by Booth et al. (1989) and Knapp et al. (1989). Since then it has been detected in 29 transitions of 14 molecular species and various isotopes by Nyman et al. (1993). Fong et al. (2001) have detected IRAS15194-5115 in C II and derive upper limits for various metals (Fe I, Fe II, Si II). Observations tend to be difficult because of the presence of a molecular cloud in the line-of-sight, situated some 2.9 kpc behind the star (Nyman et al. 1987).

This star lies at a distance of approximately 0.6 kpc (Fong et al. 2001). Mass-loss is estimated to occur at a rate of approximately $1\,10^{-5}\,M_\odot\,yr^{-1}$ (e.g. Ryde 2000). IRAS15194-5115, an extreme carbon star, has an optically thick circumstellar shell, with some degree of asymmetry (Lorenz-Martins & Lefevre 1994). However the shell does not appear extended (Young et al. 1993).

### A.1.6 AFGL3068

The much-studied star AFGL3068 is also known by the IRAS designation IRAS 23166+1655 and the name LL Pegasus. Estimates of this star's distance range from 570 pc (Fukasaku et al. 1994) to 1.2 kpc (Meixner et al. 1999), with most authors taking a distance of approximately 1 kpc.

AFGL3068 is an extreme carbon star, slightly more evolved than the generic carbon star IRC+10216 (CW Leo). It has no optical counterpart down to a very high magnitude limit (Volk et al. 2000), but is well observed in the infrared and in the millimetre band. It is identified by its low IRAS colour temperatures. AFGL3068

has a very red IR continuum which is devoid of strong emission features, suggesting strong circumstellar extinction (Kwok et al. 1997). From IR spectra Jones et al. (1978) found (i) a strong absorption feature at 3.1$\mu$m, (ii) the absence of a silicate feature at 9.7$\mu$m and (iii) a spectral break at 10.5$\mu$m. The first two of these factors strongly suggest that the star is heavily dust enshrouded. Absorption and emission features of the circumstellar dust have been well investigated. The presence of a weak absorption feature due to SiC (Speck et al. 1999) and emission well fitted by models of SiC (Smith et al. 2000) suggest silicon-based grain composition. Similarly, strong emission in the 30$\mu$m band has been attributed to either pure MgS or graphite grains with a thick MgS coating (Szczerba et al. 1999). The strong feature in the 30$\mu$m band has also been observed in other extreme carbon-rich stars (Yamamura et al. 1997), as well as proto-planetary nebulae (Omont et al. 1995) and planetary nebulae (Forrest et al. 1981). Also, the flatness of the IR spectra may suggest pure amorphous carbon grains (Kwok et al. 1997; Smith et al. 2000; Suh 2000).

Thermal lines from $HC_3N$ were first observed by Jewell & Snyder (1984). Since then HCN, CO, $^{13}$CO, H$^{13}$CN, $HC_3N$ and HNC have been observed by Sopka et al. (1989), as have CCH, $HC_5N$, $C_4H$ and SiS by Fukasaku et al. (1994) and Fuente et al. (1998). Indications of OH or water have not been found (Lewis 2000, 1996).

Physically, AFGL3068 is a pulsating star (Bagnulo et al. 1998; Lewis 1996) with an optical depth that varies (Le Bertre et al. 1995) over its period of approximately 700 days (Whitelock et al. 1994). CO scans show an asymmetry in the central, compact region, with a detached and strongly bipolar outer circumstellar nebulosity (Neri et al. 1998). The mass-loss rate is on the order of $10^{-5}\,M_\odot\,yr^{-1}$ (Greaves & Holland 1997; Ivezic & Elitzur 1995), with an envelope expansion velocity of $14.1\,km\,s^{-1}$(Sopka et al. 1989). The local standard of rest velocity is usually taken as -31 $km\,s^{-1}$(Groenewegen et al. 1996).

### A.1.7 IRC+40540

IRC+40540 is a very red Mira variable, of spectral type C8, 3.5 (Sloan et al. 1998), with a period of 628 days (Cohen & Hitchon 1996). It has a luminosity of approximately 9400 $L_\odot$, and hence a distance of 630 pc (Lindqvist et al. 2000). Schöier & Olofsson (2000) use CO data to derive a mass-loss rate of $1.5\,10^{-5}\,M_\odot\,yr^{-1}$. It has a wind expansion velocity of $14.0\,km\,s^{-1}$. Thus this star is very similar to IRC+10216, or CIT6. An effective stellar temperature of 2040 K is given by Bergeat et al. (2001).

IRC+40540 has been detected in HCN and CN by Lindqvist et al. (2000), and also by Sopka et al. (1989), who add $H^{13}CN$ to the list. Lindqvist et al. (2000) also map and model the distribution of HCN and CN. The CO emission of IRC+40540 has been well-observed, for example by Neri et al. (1998), Groenewegen et al. (1996), Zuckerman et al. (1986) and Knapp & Morris (1985). Stanek et al. (1995) present a very nice map of CO ($J$=3–2) emission. The map shows a slight elongation NE-SW, with possible jetlike structures. Schöier & Olofsson (2000) calculate a $^{12}C/^{13}C$ ratio of 55, slightly higher than the 43 of Wannier et al. (1991) and Wannier & Sahai (1987). Bujarrabal et al. (1994) calculate abundances from observations of $^{13}CO$, HCN, HNC, SiS, SiO, CS, $HC_3N$ and SO (upper limit). Also, a sensitive line search of CSEs by Nguyen-Quang-Rieu et al. (1988) revealed detections of HCN, $H^{13}CN$ and SiO. They also derive upper limits for seven other species, including $HC_5N$. Jewell & Snyder (1984) were the first to detect $HC_3N$ (in three transitions). Fuente et al. (1998) calculate the abundance of $C_2H_2$ from $C_2H$ observations. Sahai et al. (1984) detect the $J$=7–6 transition of SiS.

Maser activity surveys for the following molecules have been negative: $H_2O$ (Lewis 1997; Takaba et al. 1994); SiO (Takaba et al. 1994); HCN (Lucas et al. 1988; Bieging 2001).

The dust properties of this object are well-studied. The SED has been modelled by Suh (2000), Bagnulo et al. (1998) and Groenewegen et al. (1998). Dust composition is studied by Speck et al. (1999, 1997). The 30$\mu$m emission due to MgS is observed by Jiang et al. (1999). 11.2$\mu$m emission from SiC is used to calculate the mass-loss rate ($2.4\,10^{-5}\,M_\odot\,yr^{-1}$) by Skinner & Whitmore (1988b).

Photometric measurements (in J, H, K, L or M bands) are presented by Bagnulo et al. (1998), Groenewegen et al. (1993), Jones et al. (1990), Cohen & Kuhi (1977) and Lockwood (1974). IRAS fluxes are given in Egan & Leung (1991) and Rowan-Robinson et al. (1986).

## A.2 Proto-planetary nebulae

### A.2.1 CRL618

CRL618 is a highly observed object, and justly so since it provides a very wide range of physical conditions in which to study some very interesting chemistry. Generally classed as a proto-planetary nebula (although classed by some as a planetary nebula since it does show the prescence of a central ionised region; Kwok & Bignell 1984),

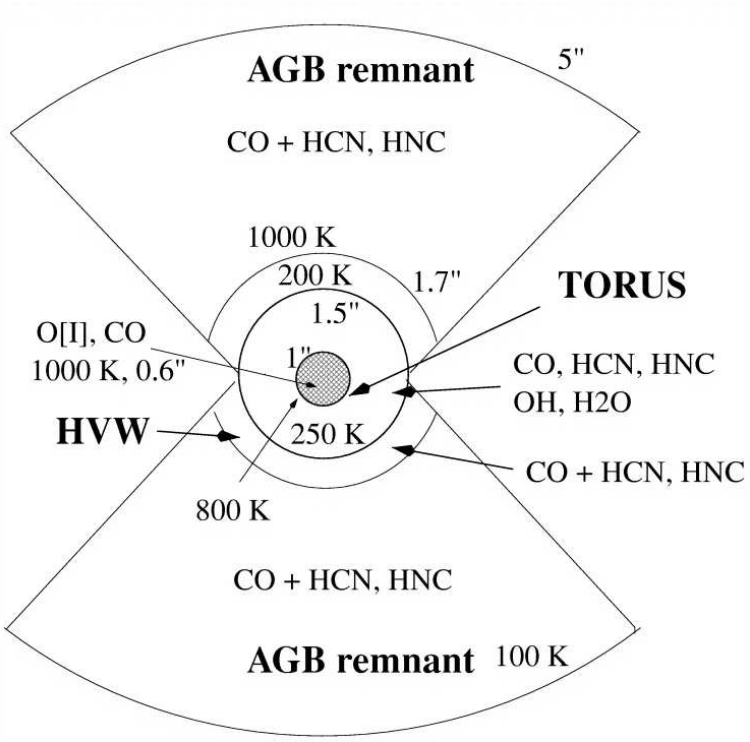


Figure A.4: Simple view of the structure of CRL618, taken from Herpin & Cernicharo (2000). Similar but more complex diagrams are presented in Phillips et al. (1992); Burton & Geballe (1986).

the effect of intense radiation and shock chemistry make this star a complex subject for study.

This object was first discovered by the CRL rocket flight, which searched for infrared sources (Walker & Price 1975). First detailed examinations were made in the infrared by Westbrook et al. (1975), and a broad CO emission line was observed by Lo & Bechis (1976).

CRL618 is observed at optical, radio and infrared wavelengths (Carsenty & Solf 1982; Bujarrabal et al. 1988; Hora et al. 1996) as a bipolar nebula. It is worth quoting from the paper of Neri et al. (1992),

> The simplest and most plausible interpretation of the ensemble of the radio, infrared, and optical data presently available is that CRL618 has just reached a stage where its stellar wind is scraping through the star's dense cocoon and starts to propel pockets of gas into the outer regions. Strong shocks between the wind and envelope fragments and between the wind and the outer envelope material, give rise to high excitation, high velocity emission in a variety of atomic and molecular lines.

Largely the optical and near-infrared radiation from the lobes is reflected from the central source (Westbrook et al. 1975; Latter et al. 1992), although Goodrich (1991) holds that some of the optical light, at least, must be generated within the lobes themselves. Goodrich (1991) compares the optical spectrum of the east lobe to spectra of Herbig-Haro objects (objects found in the vicinity of young pre-main-sequence stars), and finds that they are very similar.

Physically, the PPN consists of an invisible B0-type central star surrounded by a compact HII region (Wynn-Williams 1977) with a thick bipolar envelope outermost. Figure A.4 is taken from Herpin & Cernicharo (2000), who base this diagram on observations from Weintraub et al. (1998), Burton & Geballe (1986), Neri et al. (1992) and Carsenty & Solf (1982). The physical parameters relating to the geometry of CRL618 have been investigated by Martin-Pintado et al. (1995), Meixner et al. (1998) and Hajian et al. (1996). The three main features of CRL618 are: (i) a central torus with a photon dominated region, (ii) the extended AGB remnant envelope ($\sim$70″ diameter; Phillips et al. 1992) and (iii) the bipolar lobes (the easternmost of which is brighter). The medium is most likely clumpy (e.g., Meixner et al. 1998; Hajian et al. 1996; Neri et al. 1992), and, in fact, Ueta et al. (2001) find CO clumps moving at $>200\,\mathrm{km\,s^{-1}}$, corresponding to the near-IR "bullets" they also see. These IR structures are thought to be the locations of interactions at the clump/circumstellar shell interface. There is a cool dust shell at a very large radius of 400″, with enhanced rings of emission at $\sim$ 160″ and $\sim$275″ (Speck et al. 2000). The rings of enhanced emission in the ISOPHOT spectra are thought to be remnants of thermal pulse activity (and hence episodic mass–loss) on the AGB.

The bipolar outflows have been the subject of much recent research, along the lines of Cox et al. (2000), in dealing with CRL2688, the Egg nebula. Closest to the central star, Kastner et al. (2001) find the highest velocity molecular material, and attribute a velocity of over $150\,\mathrm{km\,s^{-1}}$ to it. Cernicharo et al. (1989) also (see also Gammie et al. 1989) observe a high speed ($\approx$200 $\mathrm{km\,s^{-1}}$ in CO) dense molecular outflow. Different molecules are contained in this wind, with differing lineshapes and widths. Many, though, are at a similar speed to the velocity of CO. For example, $\Delta_v = 152.0\,\mathrm{km\,s^{-1}}$ in $HCO^+$ ($J$=3–2). Both Cox et al. (2000) and Kastner et al. (2001) find all $H_2$ emission along the polar axis of the nebula, which is different from other PPNe and PNe, where most is detected along the equatorial axis (e.g., Kastner et al. 1996). Trammell & Goodrich (2002) analyse HST data in H$\alpha$, and show at least three (probably four) highly collimated outflows, which are interacting with the neutral envelope around CRL 618. These structures seem to

be simultaneous outflows, rather than a precessing jet. These same jets are seen in the infra-red, in $H_2$ emission, and show many of the same features (Cox et al. 2003, Fig. A.5).

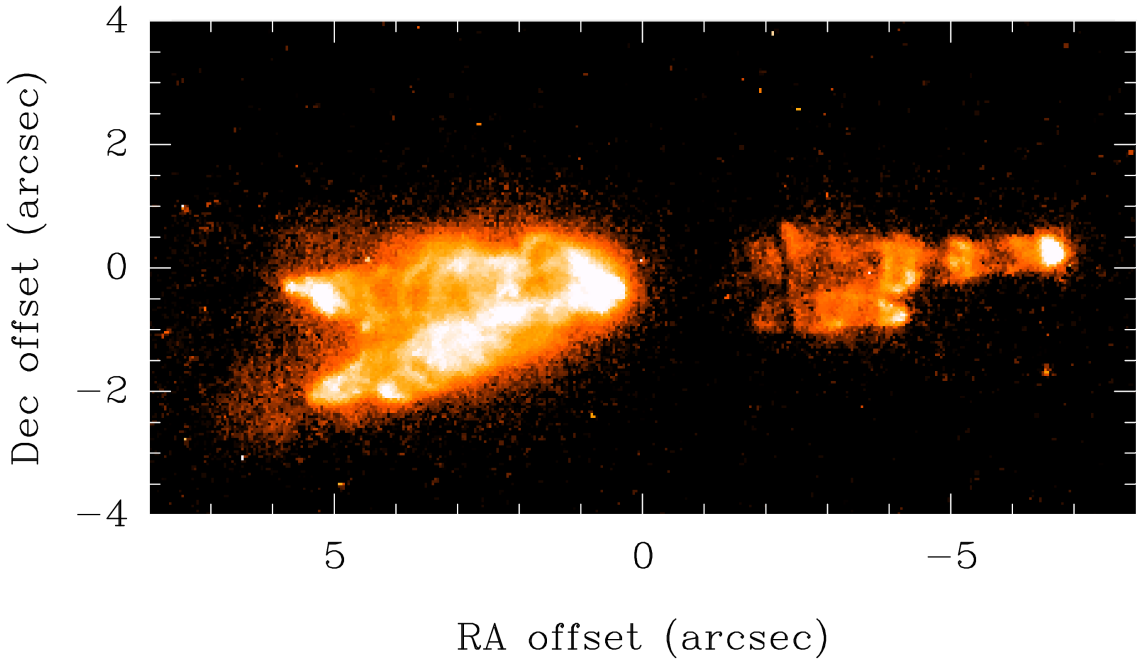


Figure A.5: BEAR image of CRL618 in $H_2$ emission (Cox et al. 2003).

A hydrodynamical model of PPNe & young PNe, and in particular CRL618, has been constructed by Lee & Sahai (2003). Their model shows the effect of a collimated fast wind (CFW) upon the spherical AGB wind. For a 1000km s$^{-1}$ fast wind, a bowlike structure is seen at the interacting region, and X-ray emission is expected. Lee & Sahai (2003) calculate an X-ray luminosity of $L_X$=1.5×10$^{29}$ ergs s$^{-1}$ for CRL618, about ten times lower than the upper limit of X-ray flux determined from observations ($L_X$ >1.7×10$^{30}$ ergs s$^{-1}$).

One of the interesting qualities of CRL618 is its rapid evolution. The rarity of the transition stage between AGB star and PN represented by CRL618 argues for a short lifetime of this stage. Several authors note changes in brightness, even over as short a period as a few years (e.g. Baessgen et al. 1997). Gottlieb & Liller (1976) attest to a tenfold increase in luminosity of two nebulosities found on either side of the central IR source in the last fifty years. CRL618 is a radio continuum source (Wynn-Williams 1977; Sanchez Contreras et al. 1998), and Kwok & Feldman (1981) note the rapid change in radio flux due to the expansion of the ionisation front over a 2–3 year period. Spergel et al. (1983) found that the radio brightening

of Kwok & Feldman had slowed only two years after it was reported. This suggests that the ionisation front also is slowing, whilst passing through a CSE of decreasing density. The first detection of radio recombination lines was made by Martin-Pintado et al. (1988), who detected the H41$\alpha$, H35$\alpha$ and H30$\alpha$ lines. Further, high angular resolution observations were also made (Martin-Pintado et al. 1995). Since then, the Br$\gamma$ line of atomic hydrogen has been detected by van de Steene et al. (2000).

The variety of chemical species is worthy of note. Most interestingly, the first detection of benzene outside of the solar system was made in this object, by Cernicharo et al. (2001b), using ISO, the *Infrared Space Observatory* is questioned by (although this is questioned by Kaiser et al. 2001, who would have expected to see indications of the presence of methylbenzene (toluene) and also ortho- and para-dimethylbenzene in the ISO spectra, along with benzene.) They also report first–time detections of $C_4H_2$ and $C_6H_2$, at high abundances. In their companion Letter, Cernicharo et al. (2001a), observed many small hydrocarbons, including $C_2H_4$, $CH_3C_2H$, $CH_3C_4H$, among others, and $NH_3$ (For further details of observations of $NH_3$ see Martin-Pintado et al. 1995, 1993, 1988; Martin-Pintado & Bachiller 1992). Herpin & Cernicharo (2000) also report ISO observations of water vapour, OH, and the fine structure lines of OI in the spectral region of 43-197 $\mu$m. This is extremely unusual in a C-rich star. In addition, they made observations of $^{12}$CO ($J$=14–13 to 41–40) and $^{13}$CO ($J$=14–13 to $J$=19–18). The fine structure lines of [OI] at 63 $\mu$m and 145 $\mu$m indicate that the processing of AGB-remnant CO molecules has begun. Detections of $H_2CO$ (Cernicharo et al. 1989) and $HCO^+$ (Bujarrabal et al. 1988) confirm this.

Cernicharo et al. (1989) detect the high excitation lines of $HC_3N$ ($J$=25–24) and HCN and $HCO^+$ ($J$=3–2) in addition to three lines of $H_2CO$, the first time this oxygen-rich compound has been observed in a carbon-rich envelope. Vibrationally excited HNC has been detected in CRL618; this is the first reported detection in space (Schilke et al. 2003). A further two Letters by the same authors detail the detection of HCN lines in absorption against the bright HII continuum of CRL618 (Thorwirth et al. 2003) and the detection of vibrationally excited $HC_3N$ (Wyrowski et al. 2003). These authors give $N$(HCN)=$2\times10^{18}$ cm$^{-2}$, $N$($HC_3N$)=(3-6)$\times10^{17}$ cm$^{-2}$, respectively.

Detections of the cyanopolyynes $HC_3N$, $HC_5N$ and $HC_7N$ are reported by Fukasaku et al. (1994). Bujarrabal et al. (1988) observed 14 species in CRL618, including $HC_3N$ (several transitions, one of which is mapped), $HC_5N$ (two transitions), HCN,

CCH, $C_3N$ and $HCO^+$ (for the first time in a C-rich object). Truong-Bach et al. (1996) report a tentative detection of $HC_9N$. No sulphur-bearing species have been detected (Omont et al. 1993b), apart from CS (Bujarrabal et al. 1988). Bright CN emission was detected by Bachiller et al. (1997b). MgNC was detected in CRL618 by Highberger et al. (2000) (see also Highberger & Ziurys 2003) and this is discussed further in Dunbar & Petrie (2002).

For further observations of HCN, the paper of Neri et al. (1992) should be consulted. They analyse the HCN $J$=1–0 line, and are able to determine three regions with three distinct velocities, from different parts of the line profile. Using the IRAM interferometer they produce detailed and varied maps of HCN distribution. HCN seems to be the result of post-shock chemistry (similarly $HCO^+$, $HC_3N$ and CO Neri et al. 1992). Mapping of CO is carried out by Phillips et al. (1992). These authors study the core and halo of CRL618 in some depth. The CO $J$=1–0 and $J$=2–1 maps of Bachiller et al. (1988) show essentially spherical symmetry, with a slight elongation east-west (see also Hora et al. 1996). Shibata et al. (1993) also map CRL618 in CO. Kastner et al. (2001) map $H_2$ in the near-infrared and make conclusions about the gas kinematics in CRL618. Yamamura et al. (1994) attempt to use $^{13}CO$ interferometric observations to model CRL618 in three dimensions.

The rotational transitions of CO have been highly observed in this object: Justtanont et al. (2000) observed rotational lines from ($J$=14–13) up to ($J$=37–36) in CO (see also Herpin & Cernicharo 2000). They use their observations to determine the heating and cooling mechanisms present in CRL618, since high rotational lines cannot be produced by a simple constant velocity, spherical wind. Both far-UV photons (and hence a PDR) and shocks are considered as sources of heating, since the early-type central star produces many high-energy photons, and the morphology of this object is complex enough for high-velocity shocks to form. However, Justtanont et al. (2000) conclude that a PDR is most likely, since a shock velocity of $\geq$150 km s$^{-1}$ would be necessary to reproduce the observed CO line profiles. A stellar temperature of 30 000 K has been estimated (Justtanont et al. 2000). For a discussion of shocks in CRL618, see Beckwith et al. (1984). A paper on CO isotopes in PNe (Balser et al. 2002), calculates $N(^{13}CO)=6.8\,10^{15}$, and $N(^{12}CO)=3.2\,10^{16}$ with a $^{12}CO/^{13}CO$ ratio of 5 for this object.

Another first (in addition to those previously mentioned) was the detection of the 3.4 $\mu$m absorption band attributed to the C—H stretching vibrational mode in hydrogenated carbon compounds (Lequeux & Jourdain de Muizon 1990; Chiar et al. 1998). This was the first time that particular band had been detected in a

CSE. These authors also report the identification of the 12 $\mu$m absorption band of SiC, and they conclude that since there is an apparent lack of PAH in CRL618, that PAHs are formed from amorphous carbon, of which there is a lack in CRL618. Justtanont et al. (1996), who study the spectrum of CRL618 between 8 and 24 $\mu$m in great detail, detect an absorption feature that they suggest is due to a large column of highly-hydrogenated PAH-type species.

The age of CRL618 as a PPN is an intriguing property. Kwok & Bignell (1984) calculate an age of 200 years. Bujarrabal et al. (1988) also calculate an age of 200 years, when considering the transit time between AGB star and planetary nebula to be 1000 years. Spergel et al. (1983) calculate that the age of a proto-planetary nebula is ≈500 years, on average. Carsenty & Solf (1982) opt for a slightly longer time of 600 years in this transition stage, using the expansion speed of the lobes. Yet Zijlstra et al. (2001) argue for a longer age than is evident from calculations based on dynamical expansion timescales.

### A.2.2 IRAS16594-4656

IRAS16594-4656 is a proto-planetary nebula which lies almost in the plane of the Galaxy ($b = -3\overset{\circ}{.}3$, van de Steene & van Hoof 2003) and has a mixed chemistry. In its infrared spectrum there are strong and rarely observed features at 12.6 and 13.4 $\mu$m, thought to be due to polycyclic aromatic hydrocarbons (PAHs) with a high degree of hydrogenation, and further PAH features in the range 3-13 $\mu$m (García-Lario et al. 1999; Buss et al. 1990, 1993; Geballe et al. 1992). An emission feature between 19 and 23 $\mu$m, associated with C-rich PPNe by Kwok & Hrivnak (1989), also suggests that this source is carbon rich. However, there are also indications of crystalline silicates (pyroxenes), with weak features around 34 $\mu$m (García-Lario et al. 1999), and a 10 $\mu$m silicate feature (Olnon et al. 1986). This suggests that until recently this object was oxygen-rich, becoming carbon-rich shortly before the transition to the post-AGB phase (García-Lario et al. 1999), which occurred some 370 years ago (van der Veen et al. 1989). This hypothesis was strengthened by the lack of a detection in OH (te Lintel Hekkert et al. 1991; Silva et al. 1993) and no SiO maser emission (Nyman et al. 1998). In evolved stars with this mixed chemistry the silicates are found in a torus and the PAHs in the polar flow (Matsuura et al. 2004).

Several authors describe HST images of this PPN (Hrivnak et al. 1999, 2000; García-Lario et al. 1999), which show the presence of a bright , B7-type (van de

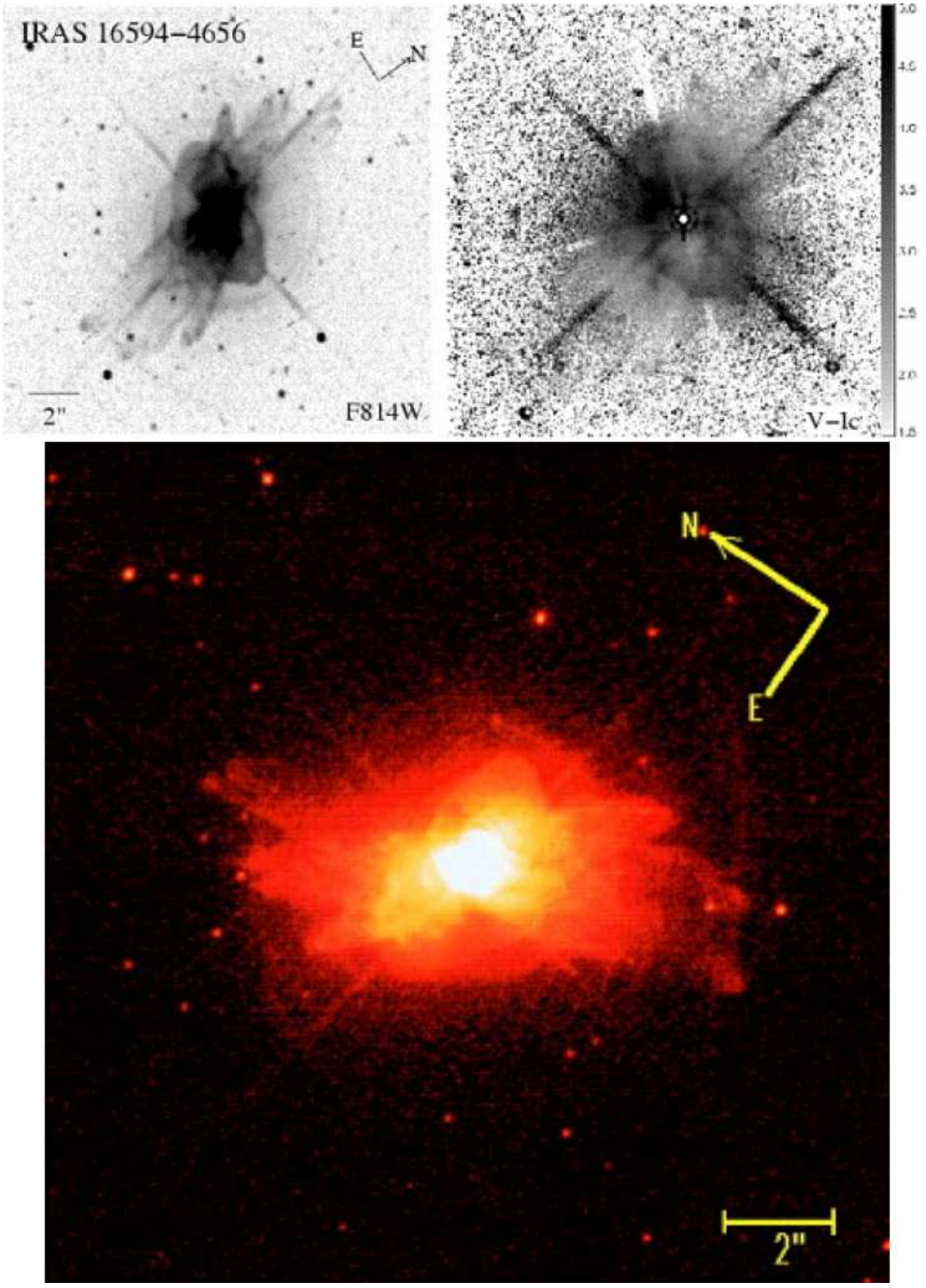


Figure A.6: HST images of IRAS16594-4656 from Su et al. (2001, top) and Hrivnak et al. (1999, bottom).

Steene et al. 2000) central star, surrounded by a multiple–axis bipolar nebulosity with a complex morphology. The nebula is seen at an intermediate inclination, rather than edge-on. The optical size of the nebula is given as $5'' \times 11''$(García-Lario et al. 1999). A further paper, Su et al. (2001), describes three "petals" (see Fig. A.6)

Recently, a paper by Hrivnak et al. (2001a) has recorded observations of four arcs around the central star. Similar arcs have been observed around three PNe, and three other PPNe (including IRAS17150-3224), as well as around IRC+10216 (Mauron & Huggins 1999). Despite the bipolar morphology of IRAS16594-4656, the arcs appear to be concentric and circular in the HST images. The arcs are thought to be regions of enhanced dust and gas that scatter light from the central star.

The only CO spectrum of this source previously published is a CO ($J$=1-0) spectrum from Loup et al. (1990), who detected broad CO emission corresponding to that from a circumstellar shell expanding with a velocity of $16\,\mathrm{km\,s^{-1}}$.

### A.2.3 IRAS17150-3224

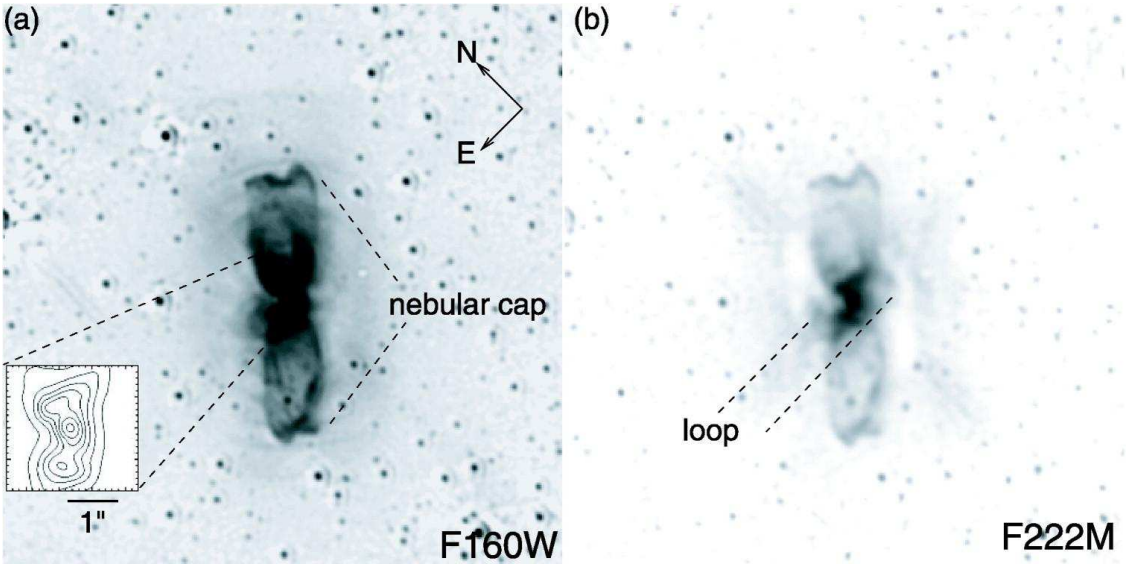


Figure A.7: HST images of IRAS17150-3224 from Su et al. (2003)

IRAS17150-3224 (AFGL6815S) is a young PPN which left the AGB some 150 (Hu et al. 1993) to 210 years ago, and possibly came from a high-mass progenitor (Meixner et al. 2002). Note however, that van der Veen et al. (1989) give a dynamic timescale of 800 yr for this object. Structurally, it is a bipolar nebula, with a nearly

edge-on (82°) dusty torus (Kwok et al. 1996), expanding at $11\,\mathrm{km\,s^{-1}}$ (Weintraub et al. 1998) around a G2-type central star. The optical size of the nebula is approximately $12'' \times 9''$ (Hu et al. 1993; Kwok et al. 1996; García-Hernández et al. 2002). A newly-discovered equatorial loop seen in near-infrared, but not optical, images, is discussed by Su et al. (2003). A faint halo (AGB mass-loss remnant) can be seen in images from Kwok et al. (1998). Around the nebula 8 concentric arcs are reasonably uniformly spaced (Kwok et al. 1998). The arcs are not two-dimensional circular features on the plane of the sky, but are projections of limb-brightened spherical shells (Hrivnak et al. 2001a). The expansion velocity of the rings is given as $15\,\mathrm{km\,s^{-1}}$, which means that they have a separation of about 200–300 yr (González Delgado et al. 2001). The method of ejecting these arcs from the star is not clear; however it seems certain that the chaotic motions in the surface of circumstellar envelopes cannot account for the regularity in spacing seen (i.e. they are not thermal-pulse induced; Soker 2000). The bipolar lobes themselves are comparable in size and brightness, and extend NW/SE. The inner structure of the nebula seems point-symmetric (Ueta et al. 2000), although a departure from axisymmetry in the optical regime is discussed by Soker & Hadar (2002).

IRAS17150-3224 shows molecular hydrogen emission, but not hydrogen recombination, indicating that the degree of ionisation is small (García-Hernández et al. 2002). The emission is likely due to shock-excitation, as is often seen in strongly bipolar nebulae. This object is similar to CRL2688 (Sahai et al. 1998) in that it has $H_2$ emission, and a spectral type later than A (CRL2688 has a spectral type of F2, Cohen & Kuhi 1977). IRAS17150-3224 also shows OH maser emission (Hu et al. 1994), but not SiO maser emission (Nyman et al. 1998). It also has been detected in the $3.1\,\mu$m water line (van der Veen et al. 1989), but not in $H_2O$ maser emission (Zuckerman & Lo 1987).

Previous CO observations are limited to the paper of Hu et al. (1993), who present both CO ($J$=1-0) and ($J$=2-1) spectra.

Dust grains are large, akin to the Red Rectangle, and a gas-to-dust ratio of 280 is derived by Meixner et al. (2002). This dust is in the form of amorphous silicate grains - absorption at $9.8\,\mu$m is discussed by Meixner et al. (1999).

IRAS17150-3224 shows molecular hydrogen emission, but not recombination, indicating that the degree of ionisation is small. The emission is likely due to shock-excitation, as often seen in strongly bipolar nebulae. This object is similar to CRL 2688 (Sahai et al. 1998) in that it has $H_2$ emission, and a spectral type later than A. IRAS17150-3224 also shows OH maser emission (Hu et al. 1994), but

not SiO maser emission (Nyman et al. 1998). The OH maser emission is strongly circularly-polarised, indicating a large (0.2 kG) magnetic field on the stellar surface (Hu et al. 1993). It also has been detected in the 3.1 $\mu$m water line (van der Veen et al. 1989), but not in $H_2O$ maser emission (Zuckerman & Lo 1987).

Distances in the literature vary widely, from 1.6 kpc (van der Veen et al. 1989), to 1.8 kpc (Phillips 2000), to 2.42 kpc (Bujarrabal et al. 2001) or even 2.9 kpc (Weintraub et al. 1998).

## A.3 Planetary nebulae

### A.3.1 IC4406

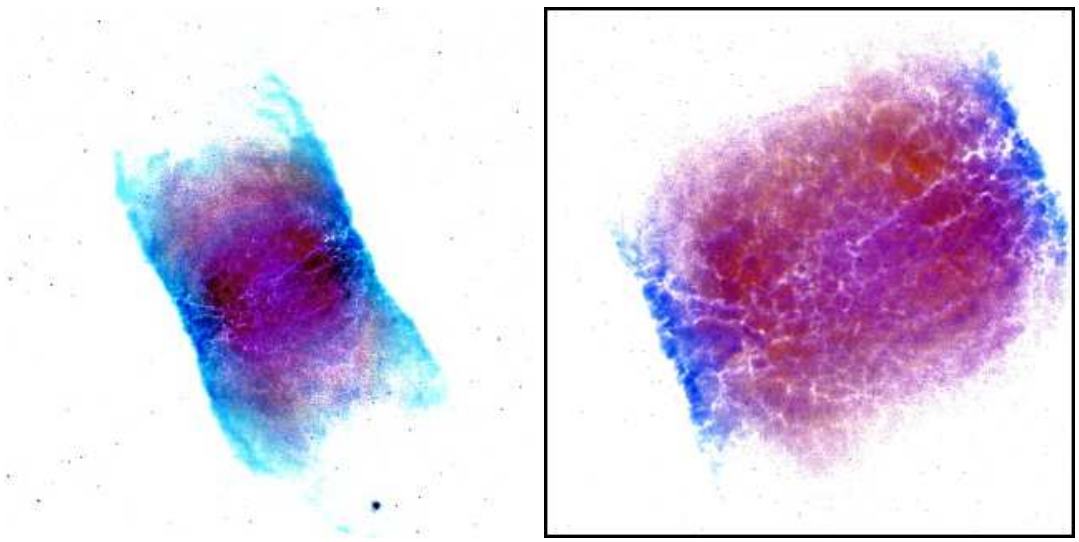

Figure A.8: HST images of IC4406 from O'Dell et al. (2002). The right-hand image is a close-up of the central region in order to show some of the structure.

IC4406 is a bipolar planetary nebula (Corradi & Schwarz 1995), with an equatorial disk (Sahai et al. 1991; Scarrott & Scarrott 1995; Gruenwald et al. 1997), possibly containing an binary star system (Soker 1997), of which one star may be a Wolf-Rayet type (Phillips 2000). HST images of IC4406 (O'Dell et al. 2003, , see Fig. A.8) show that the nebula has a cylindrical shape, with a diameter of 35″ (Phillips 2002; Zhang 1995). Shocked $H_2$ emission marks the boundary of the ionised inner region and the outer, molecular region (Storey 1984).

The nebula is seen to contain clumps (López 2003) or knots (O'Dell et al. 2003, 2002), close to the ionisation front of the nebula (some 0.1 pc from the central star), but within the neutral material. The knots do not appear directional since

they have no tails (O'Dell et al. 2003); instead, they form a "lacy" pattern. The position of these knots, not yet inside the ionised region, indicates that this object is reasonably young, and O'Dell et al. (2002) derive a dynamic age of 9 000 yr from the expansion velocity of CO (11.5 $\mathrm{km\,s^{-1}}$, Sahai et al. 1991). A much larger dynamical age of 27 000 yr is calculated if the expansion velocity from optical data is used.

Distance estimates vary from 0.81 kpc (Hua et al. 1998) to 3.1 kpc (Liu et al. 2001), with most authors settling for something in the region of 1.8 kpc (e.g. van de Steene & Zijlstra 1994). The stellar temperature is estimated to be 79 250 K (Stanghellini et al. 1993) or 94 000 K (Liu et al. 1995), and the luminosity is low, some 800 $\mathrm{L_\odot}$ (Stanghellini et al. 1993).

Few molecules have been detected previous to this work: the CO ($J$=2-1) transition was mapped by Cox et al. (1991), and Sahai et al. (1991) map both the ($J$=1-0) and ($J$=2-1) transitions of CO. Cox et al. (1992) report detections of $^{13}$CO, CN, $HCO^+$, HCN and HNC. However, they fail to detect $N_2H^+$, $C_2H$ and $HC_3N$. The CN ($N$=3-2) transition was detected by Bachiller et al. (1997b). According to Huggins et al. (1996), there is more molecular matter than ionised (0.25 $\mathrm{M_\odot}$ compared to 0.18 $\mathrm{M_\odot}$), and a large proportion of the molecular matter is contained within the cylindrical cavity (Sahai et al. 1991).

### A.3.2 NGC6072

NGC6072 is also a bipolar planetary nebula, with a diameter of some 70″ (Balser et al. 2002; Phillips 1998). At a distance of 1 kpc, this means a nebula radius of 0.171 pc (e.g. Huggins et al. 1996). However, as ever with PNe, distance estimates vary, with in this case 0.8 kpc (Zhang 1995) and 1.8 kpc (Healy & Huggins 1990) indicating the suggested range. The nebula has a visible waist, and this part shows the brightest $H_2$ emission, where the $H_2$ is probably shock-excited (Kastner et al. 1996). There has been a suggestion of binarity in this object (Soker 1997).

This object has been observed in CO ($J$=2-1) by Huggins & Healy (1989). It was then mapped in this line by Healy & Huggins (1990) and also by Cox et al. (1991). More recently Balser et al. (2002) observed both the $^{12}$CO and $^{13}$CO ($J$=2-1) lines in order to derive a $^{12}\mathrm{C}/^{13}\mathrm{C}$ ratio, which resulted in $^{12}\mathrm{C}/^{13}\mathrm{C} = 6.9\pm0.3$. Other molecular observations are limited to the detection of CN ($N$=3-2) by Bachiller et al. (1997b) and $^{13}$CO, CN, $HCO^+$, HCN and HNC by Cox et al. (1992). Small maps in CN ($N$=1-0), HCN ($J$=1-0) and $HCO^+$ ($J$=1-0) with the SEST by Cox et al. (1992) reveal that the nebula is extended, and that the distribution of these

molecules approximately follows that of CO ($J$=2-1).

The mass of CO makes up around 0.14 $M_\odot$ (Liu et al. 2001) of the 0.29 $M_\odot$ (Healy & Huggins 1990) or 0.54 $M_\odot$ (Huggins & Healy 1989) of molecular gas. Ionised gas makes up 0.73 $M_\odot$ or 0.69 $M_\odot$, respectively. These values vary with the adopted fractional abundance of CO. Stellar mass is estimated to be 0.644 $M_\odot$ (Zhang & Kwok 1993) or 0.91 $M_\odot$ (Gorny et al. 1997), and the Main Sequence mass of the central star has been calculated to be 4.2 $M_\odot$ (Balser et al. 2002).

Expansion velocities differ depending on whether derived from molecular or ionic observations. A value of 10 $km\,s^{-1}$ is taken from observations of the ionised gas (Gussie & Taylor 1994), whilst 15.5 $km\,s^{-1}$ is taken from the CO data of Cox et al. (1991).

The stellar temperature is given as 147 910 K (Stanghellini et al. 1993), or 150 000 K (Zhang & Kwok 1993), whilst the luminosity is 220 $L_\odot$ (Stanghellini et al. 1993), or 400 $L_\odot$ (Zhang & Kwok 1993).

### A.3.3 NGC6563

The third of the planetary nebulae selected from the southern sky is NGC6563. This is an elliptical ring nebula with a brightening on its minor axis (Huggins et al. 1996). Phillips (1998) gives a nebular radius of $\sim$22″, which at a distance of 2.24 kpc is 0.24 pc. Cazetta & Maciel (2000) give a distance of 2.6 kpc whilst Huggins et al. (1996) use a very low distance of 0.7 kpc, which gives a nebular radius of only 0.077 pc. The stellar temperature is reported to be 136 500 K by Cazetta & Maciel (2000).

Very little information is available on the molecular content and structure of this object. A detection of CO ($J$=2-1) is made by Huggins & Healy (1989), and this was followed up with a small map of the same transition (Cox et al. 1991). Huggins et al. (1996) use the same data to derive a mass of molecular material: 0.021 $M_\odot$, which gives a ratio to the ionised material of 0.93.

Again, the discrepancy between the expansion velocity derived from optical and molecular (CO) data is mentioned. CO data indicates an envelope expanding at 20 $km\,s^{-1}$, whilst optical data indicates an outflow of 11 $km\,s^{-1}$ (Huggins et al. 1996).

# Appendix B

# Collected spectra

## B.1 Carbon stars

Molecular line spectra of all the carbon stars in this thesis have been published by Astronomy & Astrophysics, and can be found via their website, at: `http://www.edpsciences.org/articles/aa/full/2003/17/aah4004/aah4004.html`.

## B.2 Proto-planetary nebulae

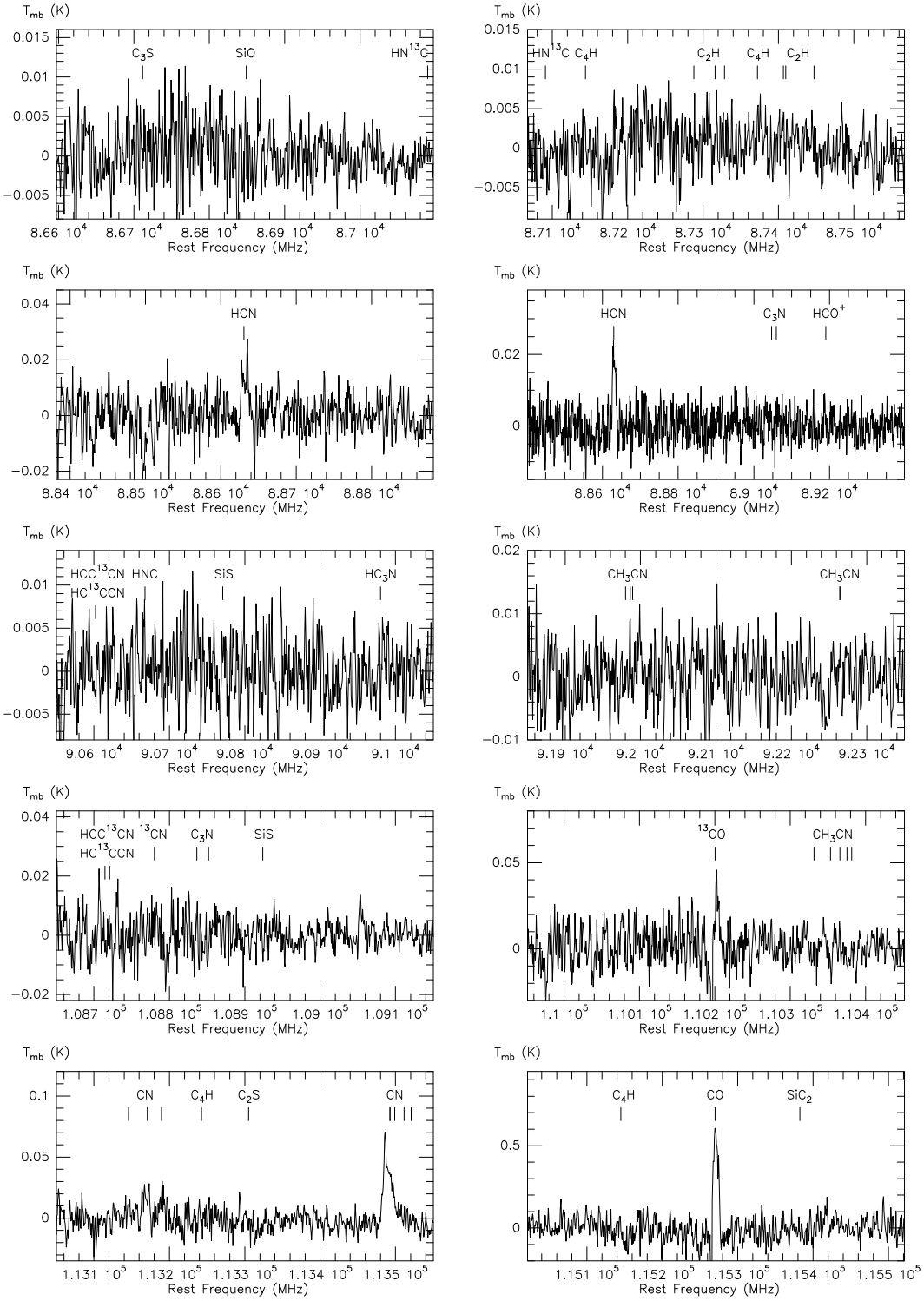


Figure B.1: Molecular line observations of IRAS16594-4656.

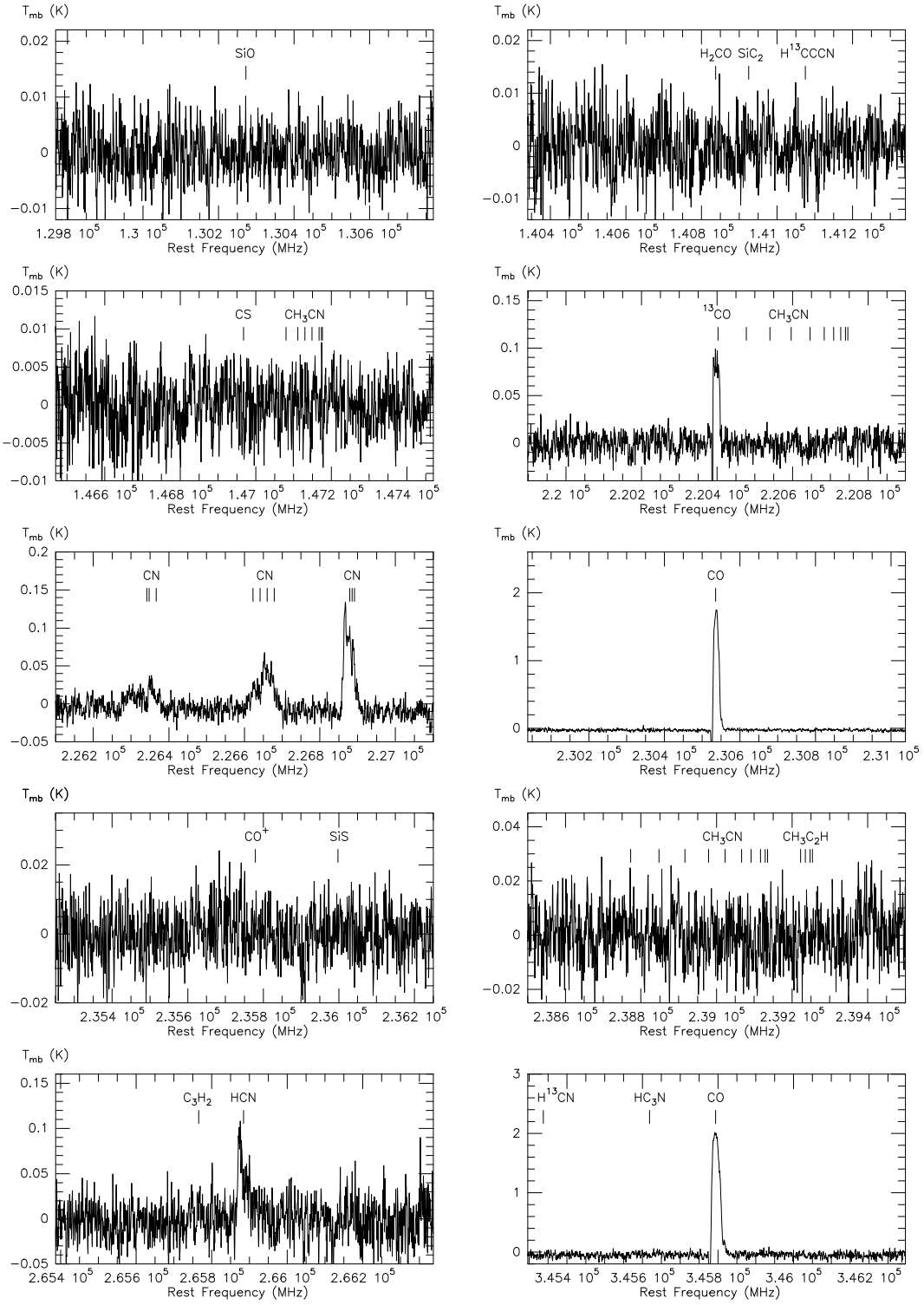


Figure B.1: (*cont.*) Molecular line observations of IRAS16594-4656.

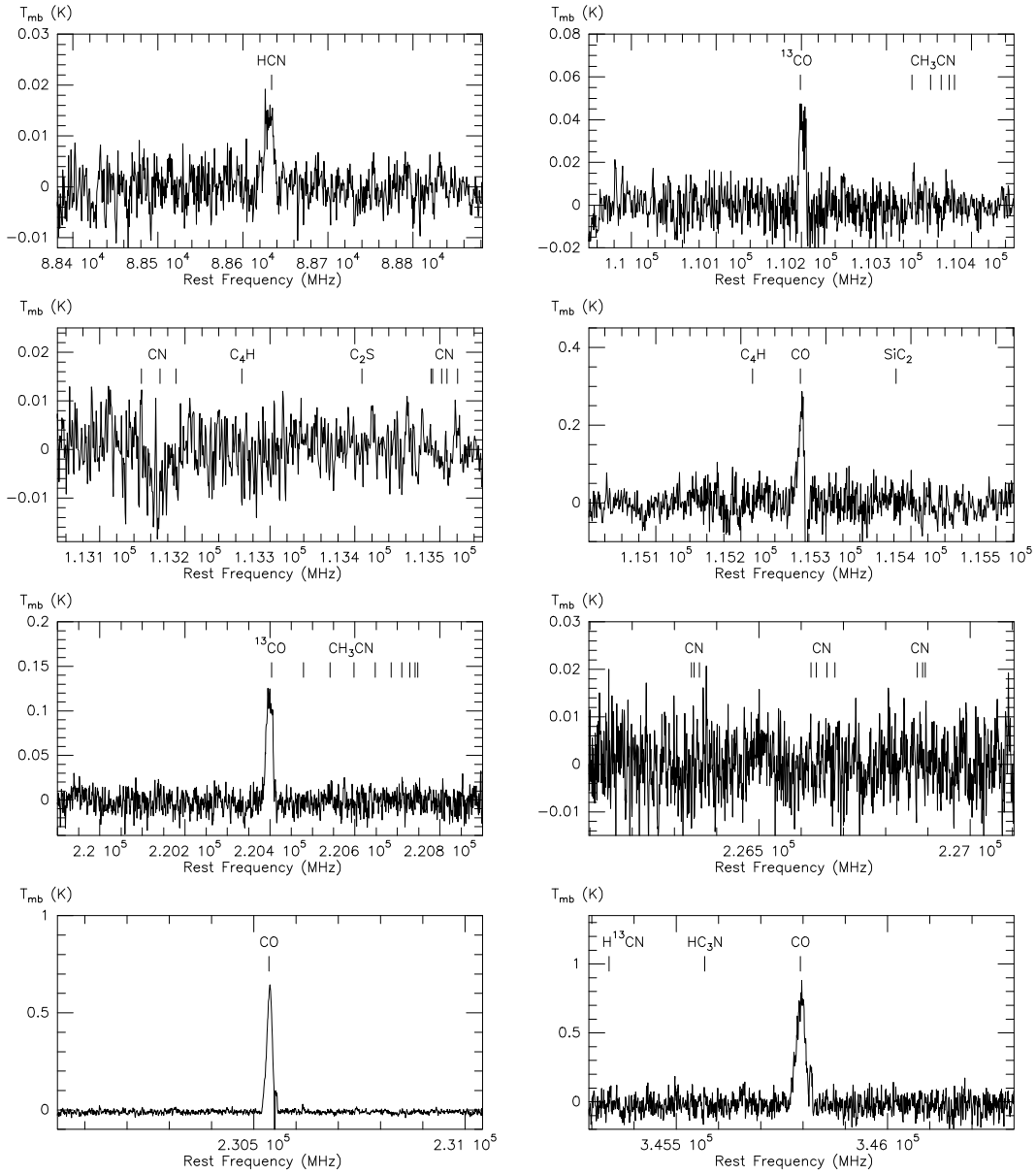


Figure B.2: Molecular line observations of IRAS17150-3224.

## B.3 Planetary nebulae

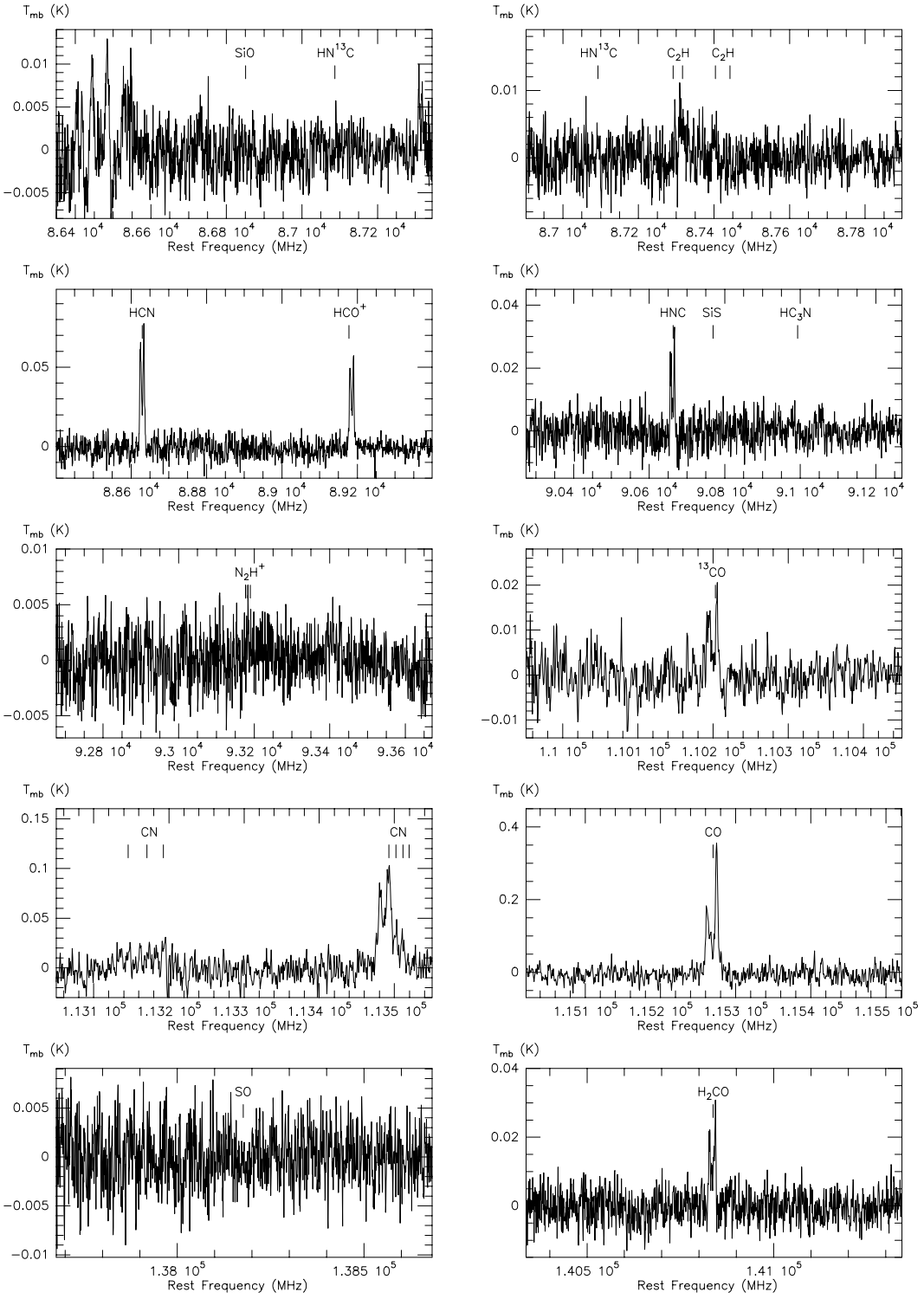


Figure B.3: Molecular line observations of IC4406.

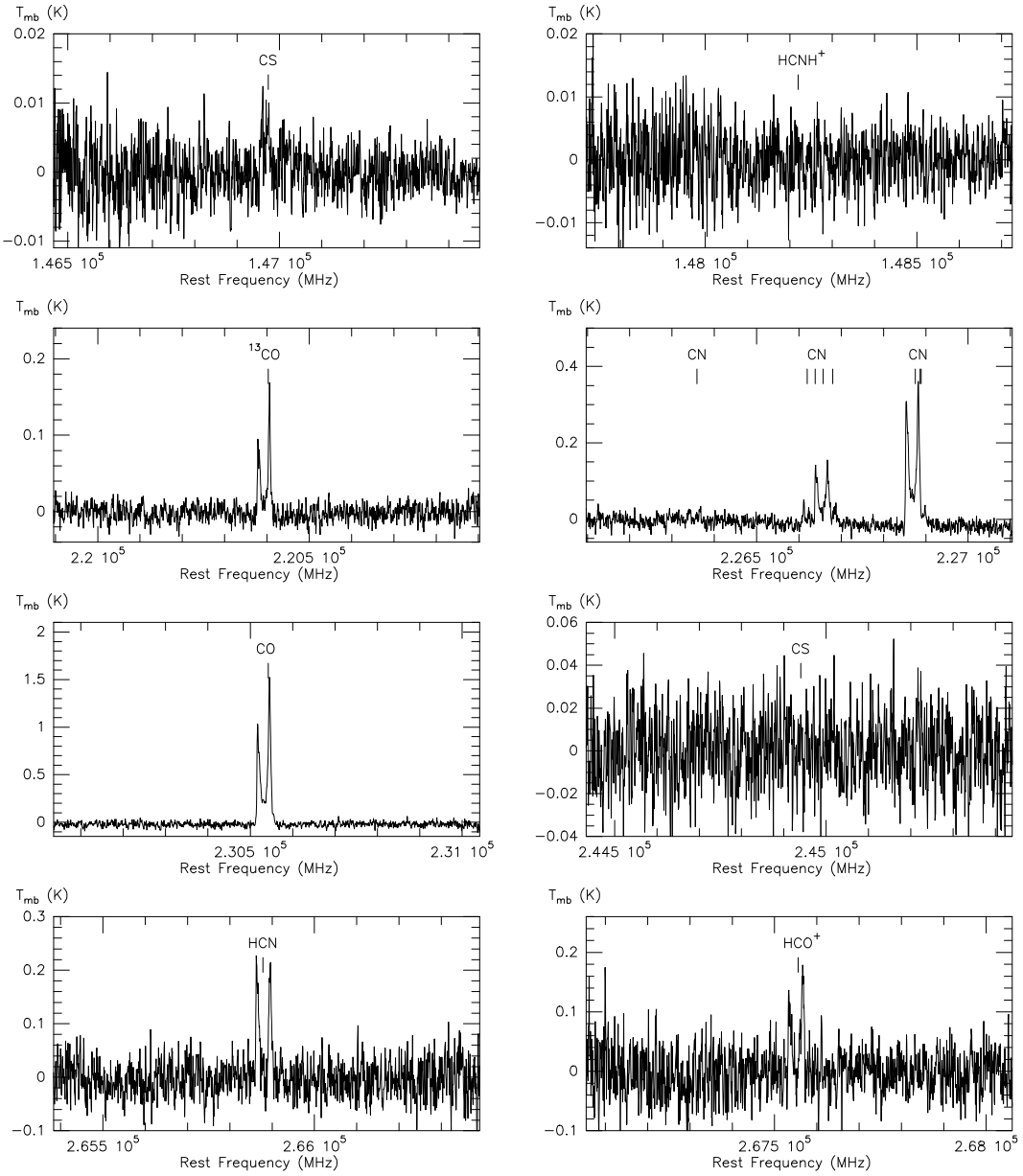


Figure B.3: (*cont.*) Molecular line observations of IC4406.

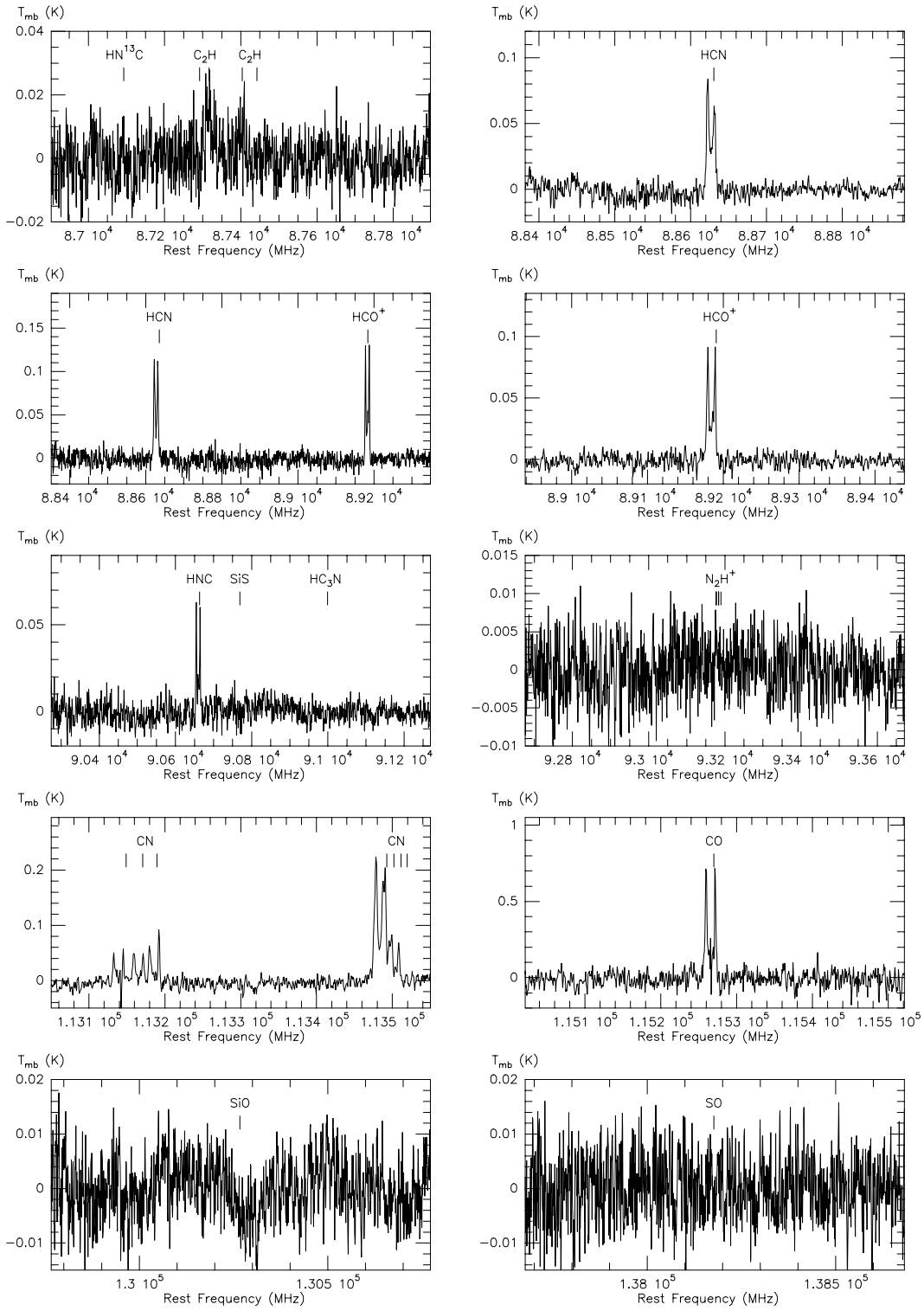


Figure B.4: Molecular line observations of NGC6072.

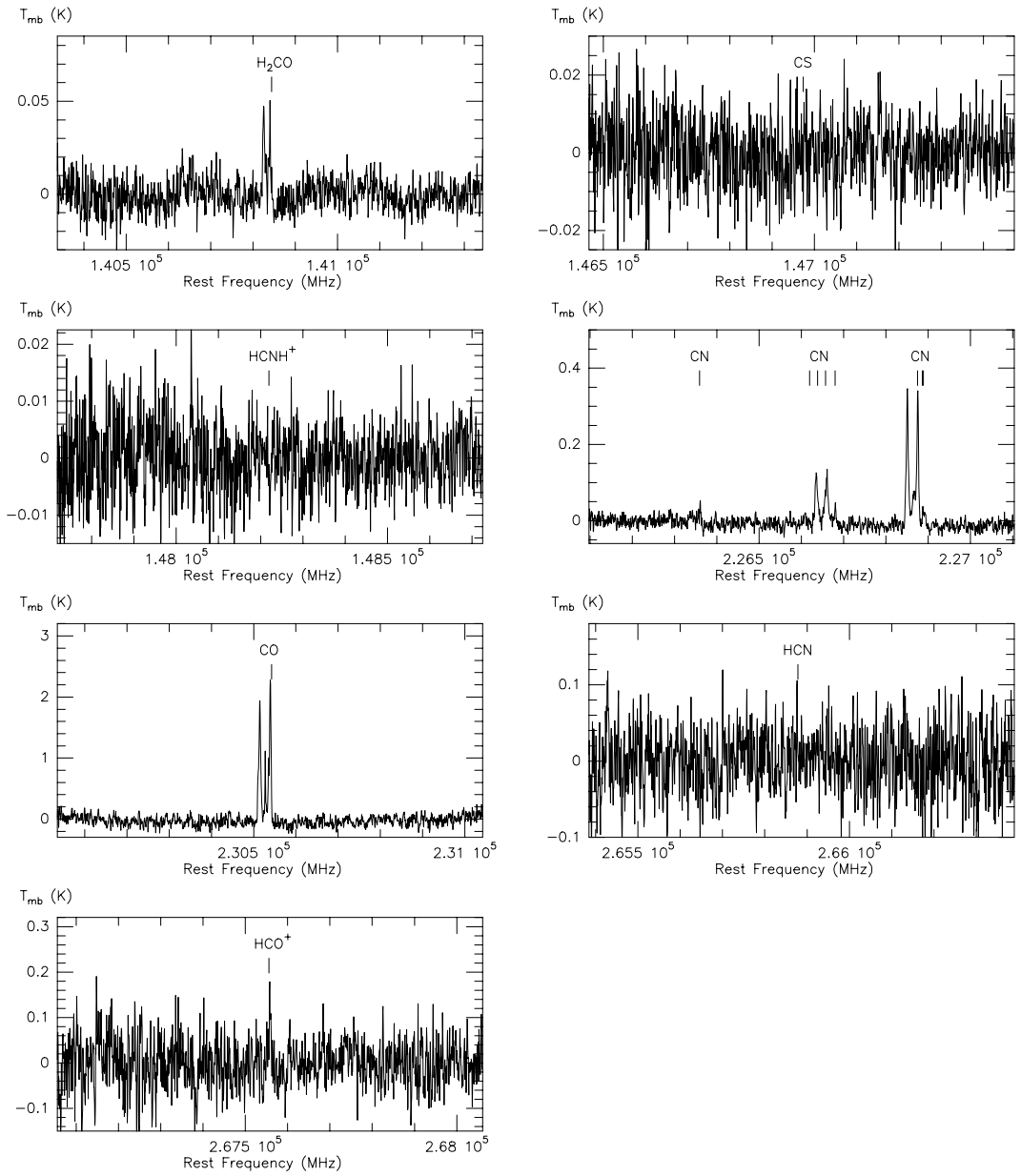


Figure B.4: (*cont.*) Molecular line observations of NGC6072.

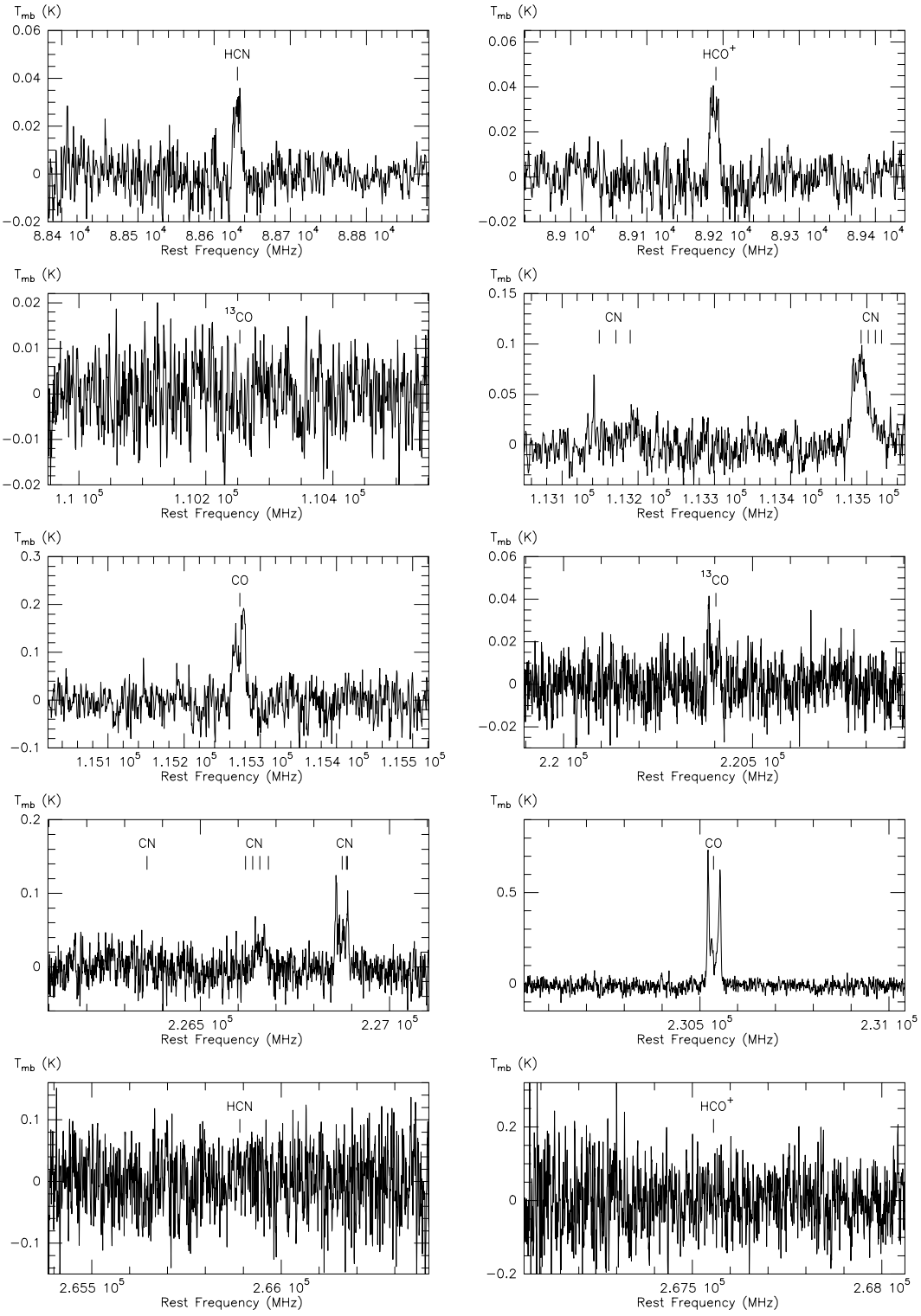


Figure B.5: Molecular line observations of NGC6563.

# Bibliography

Acker, A., Marcout, J., Ochsenbein, F., Stenholm, B., & Tylenda, R. 1992, Strasbourg - ESO catalogue of galactic planetary nebulae. Part 1; Part 2 (Garching: European Southern Observatory, 1992)

Alcolea, J. & Bujarrabal, V. 1991, A&A, 245, 499

Ali, A., Shalabiea, O. M., El-Nawawy, M. S., & Millar, T. J. 2001, MNRAS, 325, 881

Alksnis, A. 1995, Baltic Astronomy, 4, 79

Alksnis, A. A., Zacs, L., Kopylov, I. M., & Somov, N. N. 1988, Soviet Astronomy Letters, 14, 352

Alksnis, A. K. & Khozov, G. V. 1975, Soviet Astronomy Letters, 1, 144

Apponi, A. J., McCarthy, M. C., Gottlieb, C. A., & Thaddeus, P. 1999, ApJ, 516, L103

Bachiller, R. 1997, Ap&SS, 251, 63

Bachiller, R., Forveille, T., Huggins, P. J., & Cox, P. 1997a, A&A, 324, 1123

Bachiller, R., Fuente, A., Bujarrabal, V., et al. 1997b, A&A, 319, 235

Bachiller, R., Gomez-Gonzalez, J., Bujarrabal, V., & Martin-Pintado, J. 1988, A&A, 196, L5

Bachiller, R., Planesas, P., Martin-Pintado, J., Bujarrabal, V., & Tafalla, M. 1989, A&A, 210, 366

Baessgen, M. & Grewing, M. 1989, A&A, 218, 273

Baessgen, M., Hopfensitz, W., & Zweigle, J. 1997, A&A, 325, 277

Bagnulo, S., Doyle, J. G., & Andretta, V. 1998, MNRAS, 296, 545

Balick, B. 1987, AJ, 94, 671

Balick, B. & Frank, A. 2002, ARA&A, 40, 439

Balick, B., Wilson, J., & Hajian, A. R. 2001, AJ, 121, 354

Balser, D. S., McMullin, J. P., & Wilson, T. L. 2002, ApJ, 572, 326

Barnbaum, C. & Hinkle, K. H. 1995, AJ, 110, 805

Barnbaum, C., Zuckerman, B., & Kastner, J. H. 1991, AJ, 102, 289

Becker, S. A. & Iben, I. 1980, ApJ, 237, 111

Becklin, E. E., Frogel, J. A., Hyland, A. R., Kristian, J., & Neugebauer, G. 1969, ApJ, 158, L133+

Beckwith, S., Beck, S. C., & Gatley, I. 1984, ApJ, 280, 648

Bedijn, P. J. 1987, A&A, 186, 136

Bell, M. B., Avery, L. W., & Feldman, P. A. 1993, ApJ, 417, L37+

Bell, M. B., Avery, L. W., MacLeod, J. M., & Matthews, H. E. 1992, ApJ, 400, 551

Bell, M. B., Feldman, P. A., Kwok, S., & Matthews, H. E. 1982, Nature, 295, 389

Bergeat, J., Knapik, A., & Rutily, B. 2001, A&A, 369, 178

Bernes, C. 1979, A&A, 73, 67

Betz, A. L., McLaren, R. A., & Spears, D. L. 1979, ApJ, 229, L97

Bidelman, W. P. 1956, Vistas in Astronomy, 2, 1428

Bieging, J. H. 2001, ApJ, 549, L125

Bieging, J. H., Chapman, B., & Welch, W. J. 1984, ApJ, 285, 656

Bieging, J. H. & Nguyen-Quang-Rieu. 1988a, ApJ, 329, L107

—. 1988b, ApJ, 324, 516

—. 1996, AJ, 112, 706

Bieging, J. H. & Tafalla, M. 1993, AJ, 105, 576

Bohlin, R. C., Savage, B. D., & Drake, J. F. 1978, ApJ, 224, 132

Bond, H. E. 2000, in ASP Conf. Ser. 199: Asymmetrical Planetary Nebulae II: From Origins to Microstructures, 115–+

Booth, R. S., Delgado, G., Hagstrom, M., et al. 1989, A&A, 216, 315

Boothroyd, A. I., Sackmann, I.-J., & Ahern, S. C. 1993, ApJ, 416, 762

Boucher, D., Burie, J., Bauer, A., Dubrulle, A., & Demaison, J. 1980, J. Phys. Chem. Ref. Data, 9, 659

Bowen, G. H. 1988, ApJ, 329, 299

Bowen, G. H. & Willson, L. A. 1991, ApJ, 375, L53

Bowers, P. F. 1991, ApJS, 76, 1099

—. 1992, ApJ, 390, L27

Bujarrabal, V., Alcolea, J., & Planesas, P. 1992, A&A, 257, 701

Bujarrabal, V., Castro-Carrizo, A., Alcolea, J., & Sánchez Contreras, C. 2001, A&A, 377, 868

Bujarrabal, V., Fuente, A., & Omont, A. 1994, A&A, 285, 247

Bujarrabal, V., Gomez-Gonzalez, J., Bachiller, R., & Martin-Pintado, J. 1988, A&A, 204, 242

Buonanno, R., Corsi, C. E., Buzzoni, A., et al. 1994, A&A, 290, 69

Burton, M. G. & Geballe, T. R. 1986, MNRAS, 223, 13P

Buss, R. H., Cohen, M., Tielens, A. G. G. M., et al. 1990, ApJ, 365, L23

Buss, R. H., Tielens, A. G. G. M., Cohen, M., et al. 1993, ApJ, 415, 250

Calvet, N. & Peimbert, M. 1983, Revista Mexicana de Astronomia y Astrofisica, 5, 319

Canto, J., Raga, A., Steffen, W., & Shapiro, P. 1998, ApJ, 502, 695

Capps, R. W. & Knacke, R. F. 1976, PASP, 88, 224

Capriotti, E. R. 1973, ApJ, 179, 495

Carlström, U., Olofsson, H., Johansson, L. E. B., Nguyen-Q-Rieu, & Sahai, R. 1990, in From Miras to Planetary Nebulae: Which Path for Stellar Evolution?, 170–+

Carsenty, U. & Solf, J. 1982, A&A, 106, 307

Cau, P. 2002, A&A, 392, 203

Cazetta, J. O. & Maciel, W. J. 2000, Revista Mexicana de Astronomia y Astrofisica, 36, 3

Cernicharo, J. 2004, ApJ, preprint

Cernicharo, J., Guélin, M., & Kahane, C. 2000, A&AS, 142, 181

Cernicharo, J. & Guelin, M. 1987, A&A, 183, L10

—. 1996, A&A, 309, L27

Cernicharo, J., Guelin, M., Menten, K. M., & Walmsley, C. M. 1987, A&A, 181, L1

Cernicharo, J., Guelin, M., Penalver, J., Martin-Pintado, J., & Mauersberger, R. 1989, A&A, 222, L1

Cernicharo, J., Heras, A. M., Pardo, J. R., et al. 2001a, ApJ, 546, L127

Cernicharo, J., Heras, A. M., Tielens, A. G. G. M., et al. 2001b, ApJ, 546, L123

Chan, S. J. & Kwok, S. 1990, A&A, 237, 354

Chandra, S., Maheshwari, V. U., & Sharma, A. K. 1996, A&AS, 117, 557

Chandra, S. & Rashmi. 1998, A&AS, 131, 137

Chandrasekhar, T. & Mondal, S. 2001, MNRAS, 322, 356

Chen, P. S. & Kwok, S. 1993, ApJ, 416, 769

Cherchneff, I., Barker, J. R., & Tielens, A. G. G. M. 1992, ApJ, 401, 269

Chiar, J. E., Pendleton, Y. J., Geballe, T. R., & Tielens, A. G. G. M. 1998, ApJ, 507, 281

Chu, Y., Guerrero, M. A., & Gruendl, R. A. 2001, in Two Years of Science with Chandra, Abstracts from the Symposium held in Washington, DC, 5-7 September, 2001.

Cohen, M. 1979, MNRAS, 186, 837

—. 1980, ApJ, 238, L81

Cohen, M. & Hitchon, K. 1996, AJ, 111, 962

Cohen, M. & Kuhi, L. V. 1977, ApJ, 213, 79

Cohen, M. & Schmidt, G. D. 1982, ApJ, 259, 693

Corradi, R. L. M., Sánchez-Blázquez, P., Mellema, G., Gianmanco, C., & Schwarz, H. E. 2004, A&A, 417, 637

Corradi, R. L. M., Schönberner, D., Steffen, M., & Perinotto, M. 2003, MNRAS, 340, 417

Corradi, R. L. M. & Schwarz, H. E. 1995, A&A, 293, 871

Cox, P., Huggins, P. J., Bachiller, R., & Forveille, T. 1991, A&A, 250, 533

Cox, P., Huggins, P. J., Maillard, J.-P., et al. 2003, ApJ, 586, L87

Cox, P., Lucas, R., Huggins, P. J., et al. 2000, A&A, 353, L25

Cox, P., Lucas, R., Huggins, P. J., & Maillard, J. 2001, in Post-AGB Objects as a Phase of Stellar Evolution, 387–+

Cox, P., Omont, A., Huggins, P. J., Bachiller, R., & Forveille, T. 1992, A&A, 266, 420

Crabtree, D. R., McLaren, R. A., & Christian, C. A. 1987, in ASSL Vol. 132: Late Stages of Stellar Evolution, 145–+

Crosas, M. & Menten, K. M. 1997, ApJ, 483, 913

Danchi, W. C., Bester, M., Degiacomi, C. G., Greenhill, L. J., & Townes, C. H. 1994, AJ, 107, 1469

Dayal, A. & Bieging, J. H. 1993, ApJ, 407, L37

—. 1995, ApJ, 439, 996

de Jong, T. 1989, A&A, 223, L23+

Degioia-Eastwood, K., Hackwell, J. A., Grasdalen, G. L., & Gehrz, R. D. 1981, ApJ, 245, L75

Deguchi, S. 1997, in IAU Symp. 180: Planetary Nebulae, 151–+

Deguchi, S., Izumiura, H., Kaifu, N., et al. 1990, ApJ, 351, 522

Deguchi, S., Izumiura, H., Nguyen-Q-Rieu, et al. 1992, ApJ, 392, 597

Doty, S. D. & Leung, C. M. 1998, ApJ, 502, 898

Duari, D., Cherchneff, I., & Willacy, K. 1999, A&A, 341, L47

Dunbar, R. C. & Petrie, S. 2002, ApJ, 564, 792

Dyck, H. M., Forbes, F. F., & Shawl, S. J. 1971, AJ, 76, 901

Dyck, H. M., Howell, R. R., Zuckerman, B., & Beckwith, S. 1987, PASP, 99, 99

Dyck, H. M., Zuckerman, B., Leinert, C., & Beckwith, S. 1984, ApJ, 287, 801

Dyson, J. E., Hartquist, T. W., Pettini, M., & Smith, L. J. 1989, MNRAS, 241, 625

Egan, M. P. & Leung, C. M. 1991, ApJ, 383, 314

Epchtein, N., Le Bertre, T., Lepine, J. R. D., et al. 1987, A&AS, 71, 39

Fazio, G. G., Stier, M. T., Wright, E. L., & McBreen, B. 1980, ApJ, 237, L39

Ferch, R. L. & Salpeter, E. E. 1975, ApJ, 202, 195

Flower, D. R. 2001, J. Phys. B: Mol. Opt. Phys., 34, 1

Fong, D., Meixner, M., Castro-Carrizo, A., et al. 2001, A&A, 367, 652

Ford, K. E. S. 2002, Bulletin of the American Astronomical Society, 34, 1263

Ford, K. E. S., Neufeld, D. A., Goldsmith, P. F., & Melnick, G. J. 2003, ApJ, 589, 430

Forrest, W. J., Houck, J. R., & McCarthy, J. F. 1981, ApJ, 248, 195

Fouque, P., Le Bertre, T., Epchtein, N., Guglielmo, F., & Kerschbaum, F. 1992, A&AS, 93, 151

Frank, A. 1999, New Astronomy Review, 43, 31

Frank, A. & Mellema, G. 1994, A&A, 289, 937

Frost, C. A., Cannon, R. C., Lattanzio, J. C., Wood, P. R., & Forestini, M. 1998a, A&A, 332, L17

Frost, C. A., Lattanzio, J. C., & Wood, P. R. 1998b, ApJ, 500, 355

Fuente, A., Cernicharo, J., & Omont, A. 1998, A&A, 330, 232

Fukasaku, S., Hirahara, Y., Masuda, A., et al. 1994, ApJ, 437, 410

Fukuzawa, K. & Osamura, Y. 1997, ApJ, 489, 113

Gammie, C. F., Knapp, G. R., Young, K., Phillips, T. G., & Falgarone, E. 1989, ApJ, 345, L87

García-Hernández, D. A., Manchado, A., García-Lario, P., et al. 2002, A&A, 387, 955

García-Lario, P., Manchado, A., Ulla, A., & Manteiga, M. 1999, ApJ, 513, 941

Garcia-Segura, G. 1997, ApJ, 489, L189+

García-Segura, G., Langer, N., Różyczka, M., & Franco, J. 1999, ApJ, 517, 767

Gaustad, J. E., Gillett, F. C., Knacke, R. F., & Stein, W. A. 1969, ApJ, 158, 613

Geballe, T. R., Tielens, A. G. G. M., Kwok, S., & Hrivnak, B. J. 1992, ApJ, 387, L89

Gensheimer, P. D., Likkel, L., & Snyder, L. E. 1995, ApJ, 439, 445

Gilman, R. C. 1969, ApJ, 155, L185+

Glassgold, A. E. 1996, ARA&A, 34, 241

Glassgold, A. E. 1999, in IAU Symp. 191: Asymptotic Giant Branch Stars, 337–+

Glassgold, A. E. & Huggins, P. J. 1983, MNRAS, 203, 517

Glassgold, A. E., Mamon, G. A., Omont, A., & Lucas, R. 1987, A&A, 180, 183

Glassgold, A. E., Najita, J., & Igea, J. 1997, ApJ, 480, 344

Goebel, J. H. & Moseley, S. H. 1985, ApJ, 290, L35

Gonçalves, D. R., Corradi, R. L. M., & Mampaso, A. 2001, ApJ, 547, 302

González Delgado, D., Olofsson, H., Schwarz, H. E., Eriksson, K., & Gustafsson, B. 2001, A&A, 372, 885

Goodrich, R. W. 1991, ApJ, 376, 654

Gorny, S. K., Stasinska, G., & Tylenda, R. 1997, A&A, 318, 256

Gottlieb, E. W. & Liller, W. 1976, ApJ, 207, L135

Greaves, J. S. & Holland, W. S. 1997, A&A, 327, 342

Groenewegen, M. A. T. 1995, A&A, 293, 463

—. 1997, A&A, 317, 503

Groenewegen, M. A. T., Baas, F., de Jong, T., & Loup, C. 1996, A&A, 306, 241

Groenewegen, M. A. T., de Jong, T., & Baas, F. 1993, A&AS, 101, 513

Groenewegen, M. A. T., de Jong, T., van der Bliek, N. S., Slijkhuis, S., & Willems, F. J. 1992, A&A, 253, 150

Groenewegen, M. A. T., Sevenster, M., Spoon, H. W. W., & Pérez, I. 2002, A&A, 390, 511

Groenewegen, M. A. T., van der Veen, W. E. C. J., Lefloch, B., & Omont, A. 1997, A&A, 322, L21

Groenewegen, M. A. T. & Whitelock, P. A. 1996, MNRAS, 281, 1347

Groenewegen, M. A. T., Whitelock, P. A., Smith, C. H., & Kerschbaum, F. 1998, MNRAS, 293, 18

Gruenwald, R., Viegas, S. M., & Broguiere, D. 1997, ApJ, 480, 283

Guélin, M., Lucas, R., Neri, R., Bremer, M., & Broguiere, D. 2000, in Astrochemistry: From Molecular Clouds to Planetary, 365–+

Guelin, M., Lucas, R., & Cernicharo, J. 1993, A&A, 280, L19

Guelin, M., Lucas, R., & Neri, R. 1996, in IAU Symp. 170: CO: Twenty-Five Years of Millimeter-Wave Spectroscopy, Vol. 170, 359

Guerrero, M. A., Chu, Y., & Gruendl, R. A. 2000, ApJS, 129, 295

Gueth, F., Guilloteau, S., & Bachiller, R. 1998, A&A, 333, 287

Guilloteau, S., Omont, A., & Lucas, R. 1987, A&A, 176, L24

Gussie, G. T. & Taylor, A. R. 1994, PASP, 106, 500

Habing, H. J. 1996, A&A Rev., 7, 97

Habing, H. J., van der Veen, W., & Geballe, T. 1987, in ASSL Vol. 132: Late Stages of Stellar Evolution, 91–95

Haikala, L. K. 1990, A&AS, 85, 875

Hajian, A. R., Phillips, J. A., & Terzian, Y. 1996, ApJ, 467, 341

Hall, P. J., Allen, D. A., Troup, E. R., Wark, R. M., & Wright, A. E. 1990, MNRAS, 243, 480

Haniff, C. A. & Buscher, D. F. 1998, A&A, 334, L5

Hartquist, T. W., Dalgarno, A., & Oppenheimer, M. 1980, ApJ, 236, 182

Harvey, P. M., Lester, D. F., Brock, D., & Joy, M. 1991, ApJ, 368, 558

Hasegawa, T., Volk, K., & Kwok, S. 2000, ApJ, 532, 994

Hasegawa, T. I. & Kwok, S. 2001, ApJ, 562, 824

Healy, A. P. & Huggins, P. J. 1990, AJ, 100, 511

Heap, S. R., Boggess, A., Holm, A., et al. 1978, Nature, 275, 385

Henkel, C., Matthews, H. E., Morris, M., Terebey, S., & Fich, M. 1985, A&A, 147, 143

Herman, J. & Habing, H. J. 1985a, Phys. Rep., 124, 257

—. 1985b, A&AS, 59, 523

Herpin, F. & Cernicharo, J. 2000, ApJ, 530, L129

Herpin, F., Goicoechea, J. R., Pardo, J. R., & Cernicharo, J. 2001, in The Promise of the Herschel Space Observatory. Eds. G.L. Pilbratt, J. Cernicharo, A.M. Heras, T. Prusti, & R. Harris. ESA-SP 460, p. 249, 249–+

Herpin, F., Goicoechea, J. R., Pardo, J. R., & Cernicharo, J. 2002, ApJ, 577, 961

Herwig, F. 2001, Ap&SS, 275, 15

Highberger, J. L., Savage, C., & Ziurys, L. M. 2000, Bulletin of the American Astronomical Society, 32, 683

Highberger, J. L. & Ziurys, L. M. 2003, ApJ, 597, 1065

Hinkle, K. H. & Bernath, P. F. 1993, in ASP Conf. Ser. 41: Astronomical Infrared Spectroscopy: Future Observational Directions, 125–+

Hollenbach, D. & Natta, A. 1995, ApJ, 455, 133

Hoobler, R. J. & Leone, S. R. 1997, J. Geophys. Res., 102, 28717

Hora, J. L., Deutsch, L. K., Hoffmann, W. F., & Fazio, G. G. 1996, AJ, 112, 2064

Houk, N. 1963, AJ, 68, 253

Howe, D. A., Hartquist, T. W., & Williams, D. A. 1994, MNRAS, 271, 811

Howe, D. A. & Millar, T. J. 1990, MNRAS, 244, 444

Howe, D. A., Millar, T. J., & Williams, D. A. 1992, MNRAS, 255, 217

Hrivnak, B. J., Kwok, S., & Su, K. Y. L. 1999, ApJ, 524, 849

—. 2001a, AJ, 121, 2775

Hrivnak, B. J., Kwok, S., & Su, K. Y. L. 2001b, in Post-AGB Objects as a Phase of Stellar Evolution, 197–+

Hrivnak, B. J., Volk, K., & Kwok, S. 2000, ApJ, 535, 275

Hu, J. Y., Slijkhuis, S., Nguyen-Q-Rieu, & de Jong, T. 1993, A&A, 273, 185

Hu, J. Y., te Lintel Hekkert, P., Slijkhuis, F., et al. 1994, A&AS, 103, 301

Hua, C. T., Dopita, M. A., & Martinis, J. 1998, A&AS, 133, 361

Huggins, P. J., Bachiller, R., Cox, P., & Forveille, T. 1992, ApJ, 401, L43

—. 1996, A&A, 315, 284

Huggins, P. J., Forveille, T., Bachiller, R., & Cox, P. 2003, in IAU Symp. 209: Planetary nebulae: Their evolution and role in the Universe, 277–+

Huggins, P. J., Forveille, T., Bachiller, R., et al. 2002, ApJ, 573, L55

Huggins, P. J. & Glassgold, A. E. 1982, ApJ, 252, 201

Huggins, P. J. & Healy, A. P. 1989, ApJ, 346, 201

Huggins, P. J. & Mauron, N. 2002, A&A, 393, 273

Huggins, P. J., Olofsson, H., & Johansson, L. E. B. 1988, ApJ, 332, 1009

Hunter, S. D., Bertsch, D. L., Catelli, J. R., et al. 1997, ApJ, 481, 205

Iben, I. 1975, ApJ, 196, 525

Iben, I. 1977, in Saas-Fee Advanced Course 7: Advanced Stages in Stellar Evolution, 3–+

—. 1984, ApJ, 277, 333

Iben, I. & MacDonald, J. 1995, in LNP Vol. 443: White Dwarfs, 48–+

Iben, I. & Renzini, A. 1983, ARA&A, 21, 271

Iben, I. J. 1967, ARA&A, 5, 571

Ignace, R., Cassinelli, J. P., & Bjorkman, J. E. 1996, ApJ, 459, 671

Ivezic, Z. & Elitzur, M. 1995, ApJ, 445, 415

—. 1996, MNRAS, 279, 1011

Jewell, P. R. & Snyder, L. E. 1982, ApJ, 255, L69

—. 1984, ApJ, 278, 176

Jiang, B. W., Szczerba, R., & Deguchi, S. 1999, A&A, 344, 918

Jones, B., Merrill, K. M., Puetter, R. C., & Willner, S. P. 1978, AJ, 83, 1437

Jones, T. J., Bryja, C. O., Gehrz, R. D., et al. 1990, ApJS, 74, 785

Josselin, E. & Bachiller, R. 2003, A&A, 397, 659

Jura, M. 1983, ApJ, 267, 647

—. 1986, Irish Astronomical Journal, 17, 322

—. 1987, ApJ, 313, 743

—. 1994, ApJ, 434, 713

Jura, M., Balm, S. P., & Kahane, C. 1995, ApJ, 453, 721

Jura, M. & Morris, M. 1981, ApJ, 251, 181

Justtanont, K., Barlow, M. J., Skinner, C. J., et al. 1996, A&A, 309, 612

Justtanont, K., Barlow, M. J., Tielens, A. G. G. M., et al. 2000, A&A, 360, 1117

Kahane, C., Cernicharo, J., Gomez-Gonzalez, J., & Guelin, M. 1992, A&A, 256, 235

Kahane, C., Gomez-Gonzalez, J., Cernicharo, J., & Guelin, M. 1988, A&A, 190, 167

Kahn, F. D. 1983, in IAU Symp. 103: Planetary Nebulae, 305–315

Kaiser, R. I., Nguyen, T. L., Le, T. N., & Mebel, A. M. 2001, ApJ, 561, 858

Kastner, J. H. 1990, Ph.D. Thesis

Kastner, J. H. & Weintraub, D. A. 1994, ApJ, 434, 719

Kastner, J. H., Weintraub, D. A., Gatley, I., & Henn, L. 2001, ApJ, 546, 279

Kastner, J. H., Weintraub, D. A., Gatley, I., Merrill, K. M., & Probst, R. G. 1996, ApJ, 462, 777

Kasuga, T., Yamamura, I., & Deguchi, S. 1997, A&A, 320, 575

Keady, J. J. & Ridgway, S. T. 1993, ApJ, 406, 199

Knapp, G. R., Bowers, P. F., Young, K., & Phillips, T. G. 1995, ApJ, 455, 293

Knapp, G. R., Crosas, M., Young, K., & Ivezić, Ž. 2000, ApJ, 534, 324

Knapp, G. R. & Morris, M. 1985, ApJ, 292, 640

Knapp, G. R., Phillips, T. G., Leighton, R. B., et al. 1982, ApJ, 252, 616

Knapp, G. R., Sutin, B. M., Phillips, T. G., et al. 1989, ApJ, 336, 822

Kruszewski, A. 1968, PASP, 80, 560

—. 1971, AJ, 76, 576

—. 1973, Informational Bulletin on Variable Stars, 781, 1

Kwan, J. & Hill, F. 1977, ApJ, 215, 781

Kwan, J. & Linke, R. A. 1982, ApJ, 254, 587

Kwok, S. 1982, ApJ, 258, 280

Kwok, S. 1983, in IAU Symp. 103: Planetary Nebulae, 293–302

—. 1993, ARA&A, 31, 63

Kwok, S. 2001, in Post-AGB Objects as a Phase of Stellar Evolution, 3–71453

Kwok, S. & Bignell, R. C. 1984, ApJ, 276, 544

Kwok, S. & Feldman, P. A. 1981, ApJ, 247, L67

Kwok, S. & Hrivnak, B. J. 1989, in Infrared Spectroscopy in Astronomy, 363–366

Kwok, S., Hrivnak, B. J., & Su, K. Y. L. 2000, ApJ, 544, L149

Kwok, S., Hrivnak, B. J., Zhang, C. Y., & Langill, P. L. 1996, ApJ, 472, 287

Kwok, S., Purton, C. R., & Fitzgerald, P. M. 1978, ApJ, 219, L125

Kwok, S., Su, K. Y. L., & Hrivnak, B. J. 1998, ApJ, 501, L117+

Kwok, S., Volk, K., & Bidelman, W. P. 1997, ApJS, 112, 557

López, J. A. 2003, in Revista Mexicana de Astronomia y Astrofisica Conference Series, 7–11

Lattanzio, J. & Forestini, M. 1999, in IAU Symp. 191: Asymptotic Giant Branch Stars, 31–+

Lattanzio, J. C. 1993, in IAU Symp. 155: Planetary Nebulae, 235–+

Latter, W. B. & Charnley, S. B. 1996, ApJ, 463, L37+

Latter, W. B., Maloney, P. R., Kelly, D. M., et al. 1992, ApJ, 389, 347

Le Bertre, T. 1992, A&AS, 94, 377

—. 1997, A&A, 324, 1059

Le Bertre, T., Gougeon, S., & Le Sidaner, P. 1995, A&A, 299, 791

Lee, C. & Sahai, R. 2003, ApJ, 586, 319

Lequeux, J. & Jourdain de Muizon, M. 1990, A&A, 240, L19

Lewis, B. M. 1989, ApJ, 338, 234

—. 1990, AJ, 99, 710

—. 1991, AJ, 101, 254

—. 1996, ApJ, 462, 786

—. 1997, AJ, 114, 1602

—. 2000, ApJ, 533, 959

Lewis, B. M., David, P., & Le Squeren, A. M. 1995, A&AS, 111, 237

Lindqvist, M., Nyman, L.-A., Olofsson, H., & Winnberg, A. 1988, A&A, 205, L15

Lindqvist, M., Olofsson, H., Winnberg, A., & Nyman, L.-A. 1992, A&A, 263, 183

Lindqvist, M., Schöier, F. L., Lucas, R., & Olofsson, H. 2000, A&A, 361, 1036

Lipman, E. A. 1998, Ph.D. Thesis

Little-Marenin, I. R. 1986, ApJ, 307, L15

Little-Marenin, I. R., Ramsay, M. E., Stephenson, C. B., Little, S. J., & Price, S. D. 1987, AJ, 93, 663

Liu, X.-W., Barlow, M. J., Cohen, M., et al. 2001, MNRAS, 323, 343

Liu, X.-W., Barlow, M. J., Danziger, I. J., & Clegg, R. E. S. 1995, MNRAS, 273, 47

Liu, X.-W., Barlow, M. J., Nguyen-Q-Rieu, et al. 1996, A&A, 315, L257

Livio, M. & Pringle, J. E. 1997, ApJ, 486, 835

Livio, M. & Shaviv, G. 1975, Nature, 258, 308

Lo, K. Y. & Bechis, K. P. 1976, ApJ, 205, L21

Lockwood, G. W. 1974, ApJ, 192, 113

Lopez, B., Perrier, C., Mekarnia, D., Lefevre, J., & Gay, J. 1993, A&A, 270, 462

Lorenz-Martins, S., de Araújo, F. X., Codina Landaberry, S. J., de Almeida, W. G., & de Nader, R. V. 2001, A&A, 367, 189

Lorenz-Martins, S. & Lefevre, J. 1993, A&A, 280, 567

—. 1994, A&A, 291, 831

Loup, C., Forveille, T., Omont, A., & Nyman, L.-A. 1990, A&A, 227, L29

Loup, C., Forveille, T., Omont, A., & Paul, J. F. 1993, A&AS, 99, 291

Lucas, R. & Cernicharo, J. 1989, A&A, 218, L20

Lucas, R. & Guélin, M. 1999, in IAU Symp. 191: Asymptotic Giant Branch Stars, Vol. 191, 305

Lucas, R., Guelin, M., Kahane, C., Audinos, P., & Cernicharo, J. 1995, Ap&SS, 224, 293

Lucas, R., Omont, A., & Guilloteau, S. 1988, A&A, 194, 230

Maciel, W. J. & Pottasch, S. R. 1980, A&A, 88, 1

Malin, D. F. 1982, S&T, 63, 22

Mamon, G. A., Glassgold, A. E., & Huggins, P. J. 1988, ApJ, 328, 797

Mamon, G. A., Glassgold, A. E., & Omont, A. 1987, ApJ, 323, 306

Marigo, P. 2001, A&A, 370, 194

Martin-Pintado, J. & Bachiller, R. 1992, ApJ, 391, L93

Martin-Pintado, J., Bujarrabal, V., Bachiller, R., Gomez-Gonzalez, J., & Planesas, P. 1988, A&A, 197, L15

Martin-Pintado, J., Gaume, R., Bachiller, R., & Johnson, K. 1993, ApJ, 419, 725

Martin-Pintado, J., Gaume, R. A., Johnston, K. J., & Bachiller, R. 1995, ApJ, 446, 687

Mastrodemos, N. & Morris, M. 1999, ApJ, 523, 357

Mathews, W. G. 1966, ApJ, 144, 206

Matsuura, M., Zijlstra, A. A., Molster, F. J., et al. 2004, ApJ, 604, 791

Matthews, H. E., Friber, P., & Irvine, W. M. 1985, ApJ, 290, 609

Mauron, N. & Huggins, P. J. 1999, A&A, 349, 203

—. 2000, A&A, 359, 707

McCarthy, D. W., Howell, R., & Low, F. J. 1980, ApJ, 235, L27

McEwan, M. J., Scott, G. B. I., Adams, N. G., et al. 1999, ApJ, 513, 287

Meaburn, J., Clayton, C. A., Bryce, M., et al. 1998, MNRAS, 294, 201

Meaburn, J., Walsh, J. R., Clegg, R. E. S., et al. 1992, MNRAS, 255, 177

Meadows, P. J., Good, A. R., & Wolstencroft, R. D. 1987, MNRAS, 225, 43P

Meijerink, R., Mellema, G., & Simis, Y. 2003, A&A, 405, 1075

Meixner, M., Campbell, M. T., Welch, W. J., & Likkel, L. 1998, ApJ, 509, 392

Meixner, M., Ueta, T., Bobrowsky, M., & Speck, A. 2002, ApJ, 571, 936

Meixner, M., Ueta, T., Dayal, A., et al. 1999, ApJS, 122, 221

Melnick, G. J., Neufeld, D. A., Ford, K. E. S., Hollenbach, D. J., & Ashby, M. L. N. 2001, Nature, 412, 160

Men'shchikov, A. B., Balega, Y., Blöcker, T., Osterbart, R., & Weigelt, G. 2001, A&A, 368, 497

Millar, T. J. 1988, in ASSL Vol. 146: Rate Coefficients in Astrochemistry, 287–+

Millar, T. J., Flores, J. R., & Markwick, A. J. 2001, MNRAS, 327, 1173

Millar, T. J. & Herbst, E. 1994, A&A, 288, 561

Millar, T. J., Herbst, E., & Bettens, R. P. A. 2000, MNRAS, 316, 195

Mitchell, G. F. 1984, ApJ, 287, 665

Mitchell, G. F. & Watt, G. D. 1985, A&A, 151, 121

Monnier, J. D., Tuthill, P. G., & Danchi, W. C. 2000, ApJ, 545, 957

Morris, M. 1987, PASP, 99, 1115

Morris, M., Guilloteau, S., Lucas, R., & Omont, A. 1987, ApJ, 321, 888

Nejad, L. A. M. & Millar, T. J. 1987, A&A, 183, 279

—. 1988, MNRAS, 230, 79

Nercessian, E., Omont, A., Benayoun, J. J., & Guilloteau, S. 1989, A&A, 210, 225

Neri, R., Garcia-Burillo, S., Guelin, M., et al. 1992, A&A, 262, 544

Neri, R., Kahane, C., Lucas, R., Bujarrabal, V., & Loup, C. 1998, A&AS, 130, 1

Netzer, N. & Elitzur, M. 1993, ApJ, 410, 701

Netzer, N. & Knapp, G. R. 1987, ApJ, 323, 734

Nguyen-Q-Rieu & Bieging, J. H. 1990, ApJ, 359, 131

Nguyen-Q-Rieu, Bujarrabal, V., Olofsson, H., Johansson, L. E. B., & Turner, B. E. 1984, ApJ, 286, 276

Nguyen-Quang-Rieu, Deguchi, S., Izumiura, H., et al. 1988, ApJ, 330, 374

Nyman, L.-A., Booth, R. S., Carlstrom, U., et al. 1992, A&AS, 93, 121

Nyman, L.-A., Hall, P. J., & Olofsson, H. 1998, A&AS, 127, 185

Nyman, L.-A., Olofsson, H., Johansson, L. E. B., et al. 1993, A&A, 269, 377

Nyman, L.-A., Thaddeus, P., Bronfman, L., & Cohen, R. S. 1987, ApJ, 314, 374

O'Dell, C. R., Balick, B., Hajian, A. R., Henney, W. J., & Burkert, A. 2002, AJ, 123, 3329

O'Dell, C. R., Balick, B., Hajian, A. R., Henney, W. J., & Burkert, A. 2003, in Revista Mexicana de Astronomia y Astrofisica Conference Series, 29–33

Olivier, E. A., Whitelock, P., & Marang, F. 2001, MNRAS, 326, 490

Olnon, F. M., Raimond, E., Neugebauer, G., et al. 1986, A&AS, 65, 607

Olofsson, H. 1989, in IAU Colloq. 106: Evolution of Peculiar Red Giant Stars, 321–+

Olofsson, H. 1990, in Nordic-Baltic Astronomy Meeting. Proceedings of a Meeting Held at the Astronomical Observatory of the Uppsala University, June 17-21, 1990, Celebrating the 250th. Anniversary of the Celsius Observatory. Editors, C.-I. Lagerkvist, D. Kiselman, M. Lindgren; Publisher, Uppsala Universiter, Uppsala, Sweden, 1990. LC # QB1 .N67 1990. ISBN # 9150608444. P. 223, 1990, 223–+

Olofsson, H. 1996a, in IAU Symp. 178: Molecules in Astrophysics: Probes & Processes, 457–+

Olofsson, H. 1996b, in IAU Symp. 178: Molecules in Astrophysics: Probes & Processes, 457–+

Olofsson, H., Bergman, P., Eriksson, K., & Gustafsson, B. 1996, A&A, 311, 587

Olofsson, H., Bergman, P., Lucas, R., et al. 2000, A&A, 353, 583

Olofsson, H., Carlstrom, U., Eriksson, K., Gustafsson, B., & Willson, L. A. 1990a, A&A, 230, L13

Olofsson, H., Eriksson, K., & Gustafsson, B. 1990b, A&A, 230, 405

Olofsson, H., Eriksson, K., Gustafsson, B., & Carlstroem, U. 1993a, ApJS, 87, 305

Olofsson, H., Eriksson, K., Gustafsson, B., & Carlstrom, U. 1993b, ApJS, 87, 267

Olofsson, H., Lindqvist, M., Nyman, L.-A., & Winnberg, A. 1998, A&A, 329, 1059

Olofsson, H. & Nyman, L.-Å. 1999, A&A, 347, 194

Omont, A. 1985, in ASSL Vol. 117: Mass Loss from Red Giants, 269–289

Omont, A. 1991, in NATO ASIC Proc. 323: Chemistry in Space, 171–+

Omont, A., Loup, C., Forveille, T., et al. 1993a, A&A, 267, 515

Omont, A., Lucas, R., Morris, M., & Guilloteau, S. 1993b, A&A, 267, 490

Omont, A., Moseley, S. H., Cox, P., et al. 1995, ApJ, 454, 819

Osterbart, R., Balega, Y. Y., Blöcker, T., Men'shchikov, A. B., & Weigelt, G. 2000, A&A, 357, 169

Palla, F., Bachiller, R., Stanghellini, L., Tosi, M., & Galli, D. 2000, A&A, 355, 69

Persi, P. & Ferrari-Toniolo, M. 1984, A&AS, 55, 165

Phillips, J. P. 1998, A&A, 340, 527

—. 2000, AJ, 119, 342

—. 2002, A&A, 385, 1008

Phillips, J. P., Williams, P. G., Mampaso, A., & Ukita, N. 1992, A&A, 260, 283

Rawlings, J. M. C., Taylor, S. D., & Williams, D. A. 2000, MNRAS, 313, 461

Redman, M. P., Viti, S., Cau, P., & Williams, D. A. 2003, MNRAS, 345, 1291

Renzini, A. 1981, in ASSL Vol. 88: Physical Processes in Red Giants, 431–446

Ridgway, S. & Keady, J. J. 1988, ApJ, 326, 843

Rowan-Robinson, M., Lock, T. D., Walker, D. W., & Harris, S. 1986, MNRAS, 222, 273

Rozyczka, M. & Franco, J. 1996, ApJ, 469, L127+

Ruffle, D. P., Bettens, R. P. A., Terzieva, R., & Herbst, E. 1999, ApJ, 523, 678

Ryde, N. 2000, PASP, 112, 1277

Ryde, N., Schöier, F. L., & Olofsson, H. 1999, A&A, 345, 841

Sabbadin, F. 1986, A&AS, 64, 579

Sackmann, I. J. & Boothroyd, A. I. 1991, in IAU Symp. 145: Evolution of Stars: the Photospheric Abundance Connection, 275–+

Sackmann, I.-J., Boothroyd, A. I., & Kraemer, K. E. 1993, ApJ, 418, 457

Sahai, R. 1999, ApJ, 524, L125

Sahai, R., Bujarrabal, V., & Zijlstra, A. 1999a, ApJ, 518, L115

Sahai, R., Hines, D. C., Kastner, J. H., et al. 1998, ApJ, 492, L163+

Sahai, R., Wootten, A., & Clegg, R. E. S. 1984, ApJ, 284, 144

Sahai, R., Wootten, A., Schwarz, H. E., & Clegg, R. E. S. 1991, A&A, 251, 560

Sahai, R., Wootten, A., Schwarz, H. E., & Wild, W. 1994, ApJ, 428, 237

Sahai, R., Zijlstra, A., Bujarrabal, V., & Te Lintel Hekkert, P. 1999b, AJ, 117, 1408

Sanchez Contreras, C., Alcolea, J., Bujarrabal, V., & Neri, R. 1998, A&A, 337, 233

Sanchez Contreras, C., Bujarrabal, V., & Alcolea, J. 1997, A&A, 327, 689

Scarrott, S. M. & Scarrott, R. M. J. 1995, MNRAS, 277, 277

Schöier, F. L. 2000, PhD thesis, Stockholm Observatory, SE-133 36 Saltsjöbaden, Sweden

Schöier, F. L. & Olofsson, H. 2000, A&A, 359, 586

—. 2001, A&A, 368, 969

Schönberner, D. & Steffen, M. 2001, in Post-AGB Objects as a Phase of Stellar Evolution, 85–+

Schilke, P., Comito, C., & Thorwirth, S. 2003, ApJ, 582, L101

Schilke, P., Mehringer, D. M., & Menten, K. M. 2000, ApJ, 528, L37

Schilke, P. & Menten, K. M. 2003, ApJ, 583, 446

Schinke, R., Engel, V., Buck, U., Meyer, H., & Diercksen, G. H. F. 1985, ApJ, 299, 939

Schmidt, G. D., Hines, D. C., & Swift, S. 2002, ApJ, 576, 429

Schmidt-Voigt, M. & Koppen, J. 1987, A&A, 174, 223

Schoenberner, D. 1990, in From Miras to Planetary Nebulae: Which Path for Stellar Evolution?, 355–367

Schutte, W. A. & Tielens, A. G. G. M. 1989, ApJ, 343, 369

Scott, G. B. I., Fairley, D. A., Freeman, C. G., et al. 1997, J. Phys. Chem., 101, 4973

Shibata, K. M., Deguchi, S., Hirano, N., Kameya, O., & Tamura, S. 1993, ApJ, 415, 708

Silva, A. M., Azcarate, I. N., Poppel, W. G. L., & Likkel, L. 1993, A&A, 275, 510

Skinner, C. J. & Griffin, I. P. 1989, MNRAS, 240, 189

Skinner, C. J., Meixner, M., & Bobrowsky, M. 1998, MNRAS, 300, L29

Skinner, C. J. & Whitmore, B. 1988a, MNRAS, 231, 169

—. 1988b, MNRAS, 234, 79P

Sloan, G. C., Little-Marenin, I. R., & Price, S. D. 1998, AJ, 115, 809

Smith, C. H., Wright, C. M., Aitken, D. K., Roche, P. F., & Hough, J. H. 2000, MNRAS, 312, 327

Soker, N. 1996, ApJ, 468, 774

—. 1997, ApJS, 112, 487

—. 1998a, ApJ, 496, 833

—. 1998b, MNRAS, 299, 1242

—. 2000, MNRAS, 312, 217

Soker, N. & Clayton, G. C. 1999, MNRAS, 307, 993

Soker, N. & Hadar, R. 2002, MNRAS, 331, 731

Soker, N. & Harpaz, A. 1999, MNRAS, 310, 1158

Soker, N. & Kastner, J. H. 2002, ApJ, 570, 245

Soker, N. & Livio, M. 1994, ApJ, 421, 219

Sopka, R. J., Olofsson, H., Johansson, L. E. B., Nguyen, Q.-R., & Zuckerman, B. 1989, A&A, 210, 78

Speck, A. K., Barlow, M. J., & Skinner, C. J. 1997, MNRAS, 288, 431

Speck, A. K., Hofmeister, A. M., & Barlow, M. J. 1999, ApJ, 513, L87

Speck, A. K., Meixner, M., Jacoby, G. H., & Knezek, P. M. 2003, PASP, 115, 170

Speck, A. K., Meixner, M., & Knapp, G. R. 2000, ApJ, 545, L145

Spergel, D. N., Giuliani, J. L., & Knapp, G. R. 1983, ApJ, 275, 330

Stanek, K. Z., Knapp, G. R., Young, K., & Phillips, T. G. 1995, ApJS, 100, 169

Stanghellini, L., Corradi, R. L. M., & Schwarz, H. E. 1993, A&A, 279, 521

Sternberg, A. & Dalgarno, A. 1995, ApJS, 99, 565

Storey, J. W. V. 1984, MNRAS, 206, 521

Strecker, D. W. & Ney, E. P. 1974, AJ, 79, 1410

Strong, A. W. & Moskalenko, I. V. 1998, ApJ, 509, 212

Su, K. Y. L., Hrivnak, B. J., & Kwok, S. 2001, AJ, 122, 1525

Su, K. Y. L., Hrivnak, B. J., Kwok, S., & Sahai, R. 2003, AJ, in press

Su, K. Y. L., Kwok, S., & Hrivnak, B. J. 2000, American Astronomical Society Meeting, 197, 0

Su, K. Y. L., Volk, K., Kwok, S., & Hrivnak, B. J. 1998, ApJ, 508, 744

Suh, K. 2000, MNRAS, 315, 740

Szczerba, R., Henning, T., Volk, K., Kwok, S., & Cox, P. 1999, A&A, 345, L39

Takaba, H., Ukita, N., Miyaji, T., & Miyoshi, M. 1994, PASJ, 46, 629

Taranova, O. G. & Shenavrin, V. I. 1999, Astronomy Letters, 25, 750

te Lintel Hekkert, P., Caswell, J. L., Habing, H. J., et al. 1991, A&AS, 90, 327

Terzian, Y. & Hajian, A. R. 2000, in ASP Conf. Ser. 199: Asymmetrical Planetary Nebulae II: From Origins to Microstructures, 33–+

Thorwirth, S., Wyrowski, F., Schilke, P., et al. 2003, ApJ, 586, L338

Thronson, H. A. & Bally, J. 1986, ApJ, 300, 749

Tielens, A. G. G. M. 1983, ApJ, 271, 702

Townes, C. H. & Schawlow, A. L. 1975, Microwave Spectroscopy (New York: Dover)

Trammell, S. R., Dinerstein, H. L., & Goodrich, R. W. 1994, AJ, 108, 984

Trammell, S. R. & Goodrich, R. W. 2002, ApJ, 579, 688

Trams, N. R., Waters, L. B. F. M., Waelkens, C., Lamers, H. J. G. L. M., & van der Veen, W. E. C. J. 1989, A&A, 218, L1

Travers, M. J., McCarthy, M. C., Kalmus, P., Gottlieb, C. A., & Thaddeus, P. 1996, ApJ, 469, L65+

Treffers, R. & Cohen, M. 1974, ApJ, 188, 545

Truong-Bach, Graham, D., & Nguyen-Q-Rieu. 1993, A&A, 277, 133

—. 1996, A&A, 312, 565

Truong-Bach, Nguyen-Q-Rieu, Morris, D., & Deguchi, S. 1990, A&A, 230, 431

Truong-Bach, Nguyen-Q-Rieu, Omont, A., Olofsson, H., & Johansson, L. E. B. 1987, A&A, 176, 285

Tsuji, T. 1973, A&A, 23, 411

Tuthill, P. G., Monnier, J. D., Danchi, W. C., & Lopez, B. 2000, ApJ, 543, 284

Ueta, T., Fong, D., & Meixner, M. 2001, ApJ, 557, L117

Ueta, T., Meixner, M., & Bobrowsky, M. 2000, ApJ, 528, 861

Ukita, N. 1982, A&A, 112, 167

Ulrich, B. T., Neugebauer, G., McCammon, D., et al. 1966, ApJ, 146, 288

van de Steene, G. C. & van Hoof, P. A. M. 2003, A&A, 406, 773

van de Steene, G. C., Wood, P. R., & van Hoof, P. A. M. 2000, in ASP Conf. Ser. 199: Asymmetrical Planetary Nebulae II: From Origins to Microstructures, 191–+

van de Steene, G. C. & Zijlstra, A. A. 1994, A&AS, 108, 485

van der Veen, W. E. C. J. 1989, A&A, 210, 127

van der Veen, W. E. C. J., Habing, H. J., & Geballe, T. R. 1989, A&A, 226, 108

van Dishoeck, E. F. 1988, in ASSL Vol. 146: Rate Coefficients in Astrochemistry, ed. T. J. Millar & D. A. Williams (Kluwer Academic Publishers), 49

van Winckel, H. 1999, in IAU Symp. 191: Asymptotic Giant Branch Stars, 465–+

Vassiliadis, E. & Wood, P. R. 1993, ApJ, 413, 641

Ventura, P., D'Antona, F., & Mazzitelli, I. 2002, A&A, 393, 215

Viti, S., Natarajan, S., & Williams, D. A. 2002, MNRAS, 336, 797

Volk, K. & Kwok, S. 1985, A&A, 153, 79

Volk, K., Kwok, S., & Woodsworth, A. W. 1993, ApJ, 402, 292

Volk, K., Xiong, G., & Kwok, S. 2000, ApJ, 530, 408

Volk, K. M. & Kwok, S. 1989, ApJ, 342, 345

von Helden, G., Tielens, A. G. G. M., van Heijnsbergen, D., et al. 2000, Science, 288, 313

Vrtilek, J. M., Gottlieb, C. A., & Thaddeus, P. 1987, ApJ, 314, 716

Walker, R. G. & Price, S. D. 1975, AFCRL Infrared Sky Survey, Tech. Rep. Vol. 1, No. 522, Air Force Cambridge Research Laboratory

Wallerstein, G. & Knapp, G. R. 1998, ARA&A, 36, 369

Wannier, P. G., Andersson, B.-G., Olofsson, H., Ukita, N., & Young, K. 1991, ApJ, 380, 593

Wannier, P. G. & Sahai, R. 1987, ApJ, 319, 367

Weidemann, V. & Koester, D. 1983, A&A, 121, 77

Weigelt, G., Balega, Y., Bloecker, T., et al. 1998, A&A, 333, L51

Weintraub, D. A., Huard, T., Kastner, J. H., & Gatley, I. 1998, ApJ, 509, 728

Wentzel, D. G. 1976, ApJ, 204, 452

Westbrook, W. E., Willner, S. P., Merrill, K. M., et al. 1975, ApJ, 202, 407

Whitelock, P., Menzies, J., Feast, M., et al. 1994, MNRAS, 267, 711

Willacy, K. 2004, ApJ, 600, L87

Willacy, K. & Cherchneff, I. 1998, A&A, 330, 676

Willacy, K. & Millar, T. J. 1997, A&A, 324, 237

Willems, F. J. & de Jong, T. 1986, ApJ, 309, L39

Wing, R. F., ed. 2000, The Carbon Star Phenomenon

Winters, J. M., Dominik, C., & Sedlmayr, E. 1994, A&A, 288, 255

Wisniewski, W. Z., Wing, R. F., Spinrad, H., & Johnson, H. L. 1967, ApJ, 148, L29+

Witteborn, F. C., Strecker, D. W., Erickson, E. F., et al. 1980, ApJ, 238, 577

Woods, P. M., Millar, T. J., Herbst, E., & Zijlstra, A. A. 2003a, A&A, 402, 189

Woods, P. M., Millar, T. J., Zijlstra, A. A., & Herbst, E. 2002, ApJ, 574, L167

Woods, P. M., Schöier, F. L., Nyman, L.-A., & Olofsson, H. 2003b, A&A, 402, 617

Woolf, N. J. & Ney, E. P. 1969, ApJ, 155, L181+

Wynn-Williams, C. G. 1977, MNRAS, 181, 61P

Wyrowski, F., Schilke, P., Thorwirth, S., Menten, K. M., & Winnewisser, G. 2003, ApJ, 586, 344

Yamamura, I., de Jong, T., Justtanont, K., Cami, J., & Waters, L. B. F. M. 1997, Ap&SS, 255, 351

Yamamura, I., Shibata, K. M., Kasuga, T., & Deguchi, S. 1994, ApJ, 427, 406

Yan, M., Federman, S. R., Dalgarno, A., & Bjorkman, J. E. 1999, ApJ, 515, 640

Young, K., Phillips, T. G., & Knapp, G. R. 1993, ApJ, 409, 725

Young, K., Serabyn, G., Phillips, T. G., et al. 1992, ApJ, 385, 265

Young, P. A., Highberger, J. L., Arnett, D., & Ziurys, L. M. 2003, ApJ, 597, L53

Zacs, L. 1997, Ap&SS, 251, 289

Začs, L., Alksnis, A., & Spëlmanis, R. 2001, in Post-AGB Objects as a Phase of Stellar Evolution, 289–+

Zhang, C. Y. 1995, ApJS, 98, 659

Zhang, C. Y. & Kwok, S. 1993, ApJS, 88, 137

Zijlstra, A. A., Chapman, J. M., te Lintel Hekkert, P., et al. 2001, MNRAS, 322, 280

Ziurys, L. M. & Friberg, P. 1987, ApJ, 314, L49

Ziurys, L. M., Savage, C., Highberger, J. L., et al. 2002, ApJ, 564, L45

Zuckerman, B., Dyck, H. M., & Claussen, M. J. 1986, ApJ, 304, 401

Zuckerman, B. & Lo, K. Y. 1987, A&A, 173, 263

Zuckermann, B. & Maddalena, R. J. 1989, A&A, 223, L20